**Title**
Prediction and Understanding of Functional Topological and Spintronic Materials from First Principles

**Permalink**
https://escholarship.org/uc/item/9xg621xw

**Author**
Weber, Sophie Frances Liss

**Publication Date**
2021

Peer reviewed|Thesis/dissertation

# Prediction and Understanding of Functional Topological and Spintronic Materials from First Principles

by

Sophie Frances Liss Weber

A dissertation submitted in partial satisfaction of the

requirements for the degree of

Doctor of Philosophy

in

Physics

in the

Graduate Division

of the

University of California, Berkeley

Committee in charge:

Professor Jeffrey B. Neaton, Chair
Professor Steven G. Louie
Professor Mark Asta

Spring 2021

# Prediction and Understanding of Functional Topological and Spintronic Materials from First Principles

# Abstract

# Prediction and Understanding of Functional Topological and Spintronic Materials from First Principles

by

Sophie Frances Liss Weber

Doctor of Philosophy in Physics

University of California, Berkeley

Professor Jeffrey B. Neaton, Chair

In this thesis we use first-principles density functional theory (DFT) and related methods to predict and understand the properties of two categories of materials with particular promise for technological applications: topological semimetals, and antiferromagnets whose magnetic order can be controlled by electrical current.

Topological semimetals (TSMs), a subset of topological materials which are the particular focus of the first part of this thesis, have robust band crossings in reciprocal space protected by crystalline symmetries and characterized by mathematical invariants. They exhibit a variety of exotic phenomena such as ultrahigh mobility of electrons, giant magnetoresistance, and chiral anomalies. Moreover, analogously to the better known topological insulators (TIs), the "bulk-boundary correspondence", related to the change in topological invariant in going from material to vacuum, implies the existence of electronic states localized at the compound surface which can differ significantly from the semimetallic bulk states in TSMs. The development of group-theoretical methods to identify TSMs and TIs have revealed that TSMs are far more ubiquitous than initially hypothesized; to date over 10000 candidates have been identified. While this might seem to imply that the goal of harnessing properties of TSMs for practical purposes is a solved problem, most candidate materials have one or more features which make experimental manipulation and detection of the topological properties difficult if not impossible. If the symmetry-protected band crossings occur at energies far from the Fermi level, or if they are obscured by other trivial bands at the same energy, the topological signatures will be obscured. Thus, the identification of specific materials, structural motifs, and possible tuning parameters through which one can realize "functional" TSMs is highly desirable.

The first section of this thesis describes a set of studies focused on the interplay of symmetry, orbital character and magnetism in yielding electronic structures with controllable TSM features near the Fermi level and free from interfering trivial bands. First, we use a combination of DFT and tight-binding to examine the electronic structure of a previously synthesized

compound, TiRhAs. We find that TiRhAs hosts a topological nodal line protected by a mirror plane nearly exactly at the Fermi level, with no other energetically degenerate trivial bands. Next, in combination with experimental ARPES data which confirmed our DFT findings, we investigate the transition metal dichalcogenide (TMD) $NiTe_2$, and find that is a Dirac semimetal with a bulk tilted Dirac cone and topological surface states. While previous isostructural $MX_2$ (M = Pd, Pt: X = Te, Se) compounds have been shown to host similar "ladders" of topologically protected bulk and surface states, the features of interest occur at large binding energies which render their topological properties irrelevant to transport. We show that the increased hybridization between Ni d and Te p states as compared to the other $MX_2$ compounds is responsible for tuning the Dirac cone very close to the Fermi level; thus substitution of the transition metal element is an effective method for designing functional TSMs within this class of TMDs. Finally, we examine the possibility of realizing TSM features in compounds isostructural to the multiferroic hexagonal manganites. This was motivated by the numerous order parameters in multiferroic compounds which can be controlled by external fields; thus, a multiferroic compound with TSM features in a particular phase would provide an opportunity to switch from nontrivial to trivial topology by tuning of the ferroic order parameters. We find through our DFT calculations that by enforcing a metastable ferromagnetic order in the nonpolar centrosymmetric phase, hexagonal $YCrO_3$ and $YVO_3$ become topological nodal line semimetals, in contrast to the insulating band structures that occur with the ground state antiferromagnetic order of the transition metal ions.

The second section of this thesis focuses on first-principles characterization of "functional materials" in which the feature to leverage for functionality is magnetic, rather than topological, order. We focus on antiferromagnetic (AFM) materials. There has been a recent surge of interest in using AFMs rather than their traditional ferromagnetic (FM) counterparts for spintronic devices whose magnetic order can be manipulated by an electrical current. The vanishing bulk magnetization of AFMs makes them particularly robust to magnetic field perturbations, and the limiting rate of spin dynamics (i.e. the rate at which spins can rotate) in AFMs is order $\sim$ THz as opposed to $\sim$ GHz for FMs.

Our studies focus on one example, the iron-intercalated TMD, $Fe_{1/3}NbS_2$. The triangular lattice of Fe ions has an antiferromagnetic (AFM) order which can be manipulated with electrical pulses of very low current density. While numerous experimental characterizations have been performed on this compound, ambiguities regarding the magnetic ground state, spin exchange constants, and the specifics of the current-induced magnetization dynamics, remain. In one study, we calculate the nearest-neighbor Heisenberg exchange constants in $Fe_{1/3}NbS_2$ and find that competition between strong nearest-neighbor interplanar and intraplanar Fe exchange constants is responsible for an observed half-magnetization plateau. In the second part of our first-principles characterization of $Fe_{1/3}NbS_2$, we explore the working hypothesis that the current-induced manipulation of AFM order, which is detected by changes in electrical resistance, is due to a repopulation of three energetically equivalent AFM domains on the triangular lattice. Based on calculated conductivity tensors within a constant relaxation time approximation with experimentally proposed AFM magnetic orders, we verify that the transport parallel to the Fe layers is anisotropic, a necessary condition for the domain repopulation hypothesis. Finally, by comparing our ab-initio transport with experimental changes in resistance for specific pulse directions, we infer the likely current-domain response for $Fe_{1/3}NbS_2$, that is, which domains are favored for a given current direction.

To my mother, Ellen Liss

For being my primary educator from birth until college, and for countless other sacrifices made for my betterment, I owe whatever I have accomplished in large part to you. Thank you for your love, strength and unwavering support.

# Contents

# List of Figures

# List of Tables

# Acknowledgments

This is it. After completing the equivalent of "22nd grade" (I think), I can finally answer in the negative to old friends and acquaintances who ask sympathetically, "So, you're still in school?" and then ask, "What happened!!?"

First and foremost, I would like to thank my advisor, Jeff Neaton, for making my six years at Berkeley as wonderful as they were. You are without exaggeration the busiest person I have ever known, yet inevitably when we meet you have a welcoming smile and are excited to talk about science (or anything else I want to ramble about). In working with you I have learned countless things about a wide variety of topics in solid state physics. More fundamentally however, you have been instrumental in the way I think *about* science, from prioritizing good research over sexy results, to the role of our work in society at large. I also greatly appreciate your steadfast faith in my abilities (and those of everyone in your group), even when my own self-confidence has faltered. Thank you for your incredible mentorship, and for never getting angry the times when I've sent you ten emails in the span of two days.

To my collaborators and in some cases, mentors, inside and outside of Jeff's group: Ru Chen and Qimin Yan in Chapter 4, Saumya Mukherjee, Sungwon Jung and Timur Kim in Chapter 5, Sinéad Griffin in Chapter 6, and Shannon Haley, Dan Parker, Tessa Cookmeyer, Joel Moore, and James Analytis in Chapter 8. Thank you to Eran Maniv and Shan Wu for fruitful insight and explanations of the ridiculously complex experimental results regarding $Fe_{1/3}NbS_2$ in Chapter 9. Thanks in particular to Ru, who was my first mentor in the Neaton group and was essential in helping me get my footing.

Every person with whom I overlapped during my time in the Neaton group has brightened my PhD in some way, and one of my biggest personal regrets stemming from the COVID pandemic has been the loss of daily interactions with such vibrant, supportive colleagues. There are a few individuals in particular whom I must acknowledge by name. Thank you to Jonah, for the joy you have brought to everyone else in the group. Your brilliance, inexhaustible willingness to help others with their research, and extreme humility are a rare combination in a human. Academia would be happier, better place with more people like you. Thank you to Liz, for your confusing mixture of incredible kindness and extreme sass. Chatting with you about research and life over the past several years has always been a pleasure. Thanks also for organizing my bachelorette party!! Thanks to Marina, for the new ideas, energy and happiness you brought to the Neaton group during your postdoc here. You and your husband Tony were almost singularly responsible for the exponential increase in group happy hours in the 2018-2019 years, for which we are all grateful. Thanks to Stephanie for helping me out and being so supportive when I first joined the group, at a time when it was very post-doc heavy and having a friendly face in another graduate student meant a lot. Finally, thanks to Alex, my officemate. I wasn't very happy when I learned another person was going to share the space, having had the office to myself for four years. But my grumpiness dissipated as soon as we first spoke (plus, you don't type very loudly, which was my main fear). I really value the conversations and laughs we had, and I am very sorry we didn't get a chance to know each other better in the last year due to COVID.

Moving on from my academic family to my actual family, I have my parents to thank in large part for this thesis and everything it represents. Thank you to my mom, Ellen Liss, to whom this thesis is dedicated. Looking back, the amount of work you put into my education while homeschooling me from birth until college is just mind boggling. From the experiment kits we got from the museum of science, to reading first-hand accounts of history rather than conventional textbooks, you went above and beyond to ensure that my education was enriching and thought-provoking. You taught me that my interests should dictate my education, and not the other way around, and I think this philosophy has served me well in life. Thank you also for being one of my best friends in addition to being my mom; I treasure the times we have spent together talking, crafting, and playing games. I love you so much.

Thank you to my dad, Mark Weber. You are one of my great heroes both from an academic and personal perspective. Your scientific knowledge, interpersonal skills, stoicism and kindness are all life skills I aspire to. Thank you for contributing so much time and energy, along with mom, to make sure I had as many opportunities as possible. Thanks also for instilling in me a lifelong enjoyment of running, even if my talent for it leaves something to be desired compared to you in your younger years.

Finally, thank you Tobias; love of my life, and soon-to-be husband. You have supported me through the darkest of times, and shared in my joy during the best of times. I could never have imagined such an incredible partner to go through life with, and I am so excited for new adventures with you. Thank you for everything that you are.

# Chapter 1

# Introduction

Condensed matter is the largest and possibly most varied branch of physics (skim through the scientific program for any given American Physical Society March Meeting and this quickly becomes evident). One likely reason for this is the ubiquity of solid-state materials in our everyday lives. From the diamonds in jewelry to the silicon chips in our computers, crystals show up everywhere. Every material (amorphous or crystalline) can be described at its core by the same quantum mechanical Hamiltonian, described in Chapter 2, which is simply the sum of kinetic and Coulomb energies for each electron and each nucleus. It is quite incredible then that by simply varying the elemental species and/or changing the geometric arrangement of atoms, an effectively infinite variety of materials can be generated. The diversity of electronic, magnetic, and optical properties that can be realized implies that the discovery, characterization and eventual synthesis of materials is the main bottleneck in the development of technological applications.

Traditionally, the theoretical side of materials research has focused on understanding phenomena using simplified, "model Hamiltonians" which, while useful for understanding general phenomena, can lack the power to predict real materials made in a lab. In the last few decades however, materials understanding and discovery has exploded due to the advent of density functional theory (DFT), the formalism used in this thesis, and other electronic structure methods such as embedded cluster models, dynamical mean field theory, and Quantum Monte Carlo to name a few [83]. These realistic, quantum mechanical modeling methods, combined with exponential increase in computing power starting in the second half of the 20th century, allow for the prediction and study of promising functional materials even before their successful synthesis in a lab. This thesis focuses on DFT-based studies of two material subcategories: topological semimetals (TSMs) and electrically controllable antiferromagnets (AFMs). TSMs and electrically controlled AFMs hold great promise for device applications in electronics, memory storage, magnetic sensing, quantum computing and even catalysis [169, 77, 177, 164].

TSMs are materials with robust, usually linear band crossings protected by a combination of crystalline symmetries and topology. In general a semimetal can be thought of as an "edge case" of an insulator, for which the energy gap closes only at specific points or lines and and the energy disperses linearly away from the band touchings [207]. TSMs can be either zero-dimensional (e.g. discrete band crossing points) or one-dimensional, if the band crossing points form closed loops in reciprocal space. Analogously to the better-known topological insulators, TSMs can be characterized by mathematical invariants that define topologically distinct phases, in contrast to the more universal Landau theory which describes phase transitions by symmetry breaking [71]. Attractive properties of TSMs for technological purposes include ultrahigh electron mobility due to the linear dispersions near the band crossings [113, 77], giant magnetoresistance [113], and topologically protected surface states which are insensitive to backscattering and disorder [164].

The second category of material we will study, i.e. electrically controllable compounds with AFM magnetism, is highly promising for spintronics applications. Magnetic materials are natural choices for memory storage and sensing devices, since distinct magnetic states (e.g., all spins along $+z$ versus all spins along $-z$) can hold information analogously to classical bits. Traditionally, ferromagnets (FMs) have been viewed as the most attractive spintronics candidates, as their nonzero bulk magnetization allows for relatively straightforward reorienting of the magnetization using magnetic fields [228]. However, in the last decade there has been a shift of focus in spintronics towards AFMs due to several advantages over FMs. [60]. First, their vanishing bulk magnetization means that AFMs are insensitive to stray magnetic fields that can reorient magnetization in FM devices [201]. Secondly, the limiting rate of spin dynamics in AFMs (i.e. the rate at which the bulk magnetic moments can be reoriented) is several orders of magnitude higher than in FMs [153]. However, while the zero net magnetization of AFMs affords advantages, it is also problematic because it implies that AFMs are prohibitively difficult to purposefully manipulate using external magnetic fields. Much research, both experimental and theoretical, is devoted to circumventing this by finding and/or designing AFMs whose magnetization can be manipulated by electrical current [129]. These relativistic, current-induced mechanisms of spin torque can be highly efficient in manipulating AFMs, provided that the materials have the necessary crystal symmetries.

Theoretical and computational research on both TSMs and electrically switchable AFMs comes in two broad flavors. On the one hand, a great deal of invaluable and still ongoing work is devoted to the mathematical “ingredients” that lead to these categories of materials. This research, mostly based on tractable model Hamiltonians, explores, just to name a few examples: the constraints on topology and magnetism from group theory, the influence of mass terms on band energy inversions that can lead to protected band crossings, and the dynamical equations governing magnetization dynamics in the presence of current [145, 218, 128]. While this thesis touches on these more fundamental concepts, the bulk of our work is devoted to the understanding and realization of these phenomena in realistic materials. Specifically, we explore how nontrivial topology and controllable magnetism can emerge naturally, due to orbital overlap, spin-orbit coupling, and specific magnetic orders, or can be designed, for example by strain or elemental substitution. We also focus on materials where the properties of interest are easily accessible in practical applications (e.g., TSMs with the topological crossings near the Fermi energy where they will be relevant to transport properties in devices).

We mention here that with the exception of TiAsRh, a TSM material which we explore in Chapter 4, our materials of interest fall under two subcategories that are particularly promising for realizing functional TSM and magnetic features. These two categories are hexagonal oxides ($YVO_3$ and $YCrO_3$ in Chapter 6) and transition metal dichalcogenides (TMDs), with TMDs both in their pristine form ($NiTe_2$ in Chapter 5) and intercalated with magnetic ions between the TMD layers ($Fe_{1/3}NbS_2$ in Chapters 8 and 9). Our focus on hexagonal oxides and TMDs is primarily experimental in motivation. First, the synthesis of these materials is well established, both in bulk and thin-film form. Additionally, in particular for the oxides, there has been notable success in stabilizing the hexagonal structure even when it is not the ground state via epitaxial growth on a hexagonal substrate [62]. Moreover, both hexagonal oxides and TMDs (intercalated and non-intercalated) are highly tunable by external fields and chemical substitution. The hexagonal manganites $R\mathrm{MnO}_3$, $(R = \mathrm{Sc}, \mathrm{Y}, \mathrm{In}, \mathrm{Dy} - \mathrm{Lu})$ for example exhibit both ferroelectric (spontaneous polarization which can be switched by an electric field) and magnetic transitions at low temperatures, opening the possibility of controlling magnetic and electric properties by temperature, magnetic field, electric fields, or even strain [181]. Tuning of magnetism in particular can have significant effects on the band structure, and subsequent topological properties, as we will see in Chapter 6. In relation to the second material category, magnetic and topological properties of intercalated and non-intercalated TMDs can also be changed dramatically within the same material motif by substituting different transition metal ions in the TMD, or varying the concentration and/or species of the intercalant between the TMD layers. Overall, the tunability of the hexagonal oxides and TMDs give us a large phase space in which to search for and manipulate materials with TSM properties and/or switchable magnetism.

This thesis is structured as follows. After an introduction to density functional theory, maximally localized Wannier functions, and their relevant extensions in Chapter 2, in Chapter 3 we introduce the concepts, properties and varieties of topological semimetals in more detail. The next three chapters are focused on our studies of particular examples of TSMs.

In Chapter 4, we use a combination of DFT and Wannier function-based tight-binding to examine the electronic structure of a previously synthesized compound TiRhAs. We show that TiRhAs hosts a topological nodal line (a continuous loop of linear crossings in the Brillouin zone) nearly exactly at the Fermi level, whose band crossings are protected by a mirror plane. At the time of this study relatively few nodal line semimetals had been experimentally synthesized and verified, and TiRhAs is a particularly promising candidate due to having a Fermi surface free from other trivial bands, with the nodal line right at the Fermi level. Later ARPES measurements confirmed our findings [109].

In Chapter 5, in a collaboration with ARPES experimentalists, we study the candidate Dirac semimetal $NiTe_2$. Isostructural TMDs such as $PdTe_2$ and $PtSe_2$ have been shown both experimentally and through DFT calculations to host so-called “topological ladders”: a series of band crossings along the $k_z$ direction within the chalcogen p manifold of the TMD that arise due to $k_z$-dependent bonding-antibonding splitting [36]. Depending on the irreducible representations of the bands, the multiple crossings manifest either as bulk Dirac cones or parity-inverted band gaps hosting topological surface states. Unfortunately, these topological ladders occur far below the Fermi level for both $PdTe_2$ and $PtSe_2$. Our DFT calculations demonstrate enhanced hybridization between Ni d states and the Te p states forming the topological ladder as compared to the previously studied 1T TMDs with other transition metal elements. The increased d-p hybridization has the effect of raising the energy of the ladder without destroying the $k_z$-dependent band inversions within the chalcogen manifold. The hybridization in $NiTe_2$ is at a "sweet spot" such that a tilted bulk Dirac cone and a spin-polarized topological surface state appear almost exactly at the Fermi level, making their topological properties highly relevant in transport. Our findings suggest a generic mechanism for designing functional topological materials within this class of TMDs: modifying the transition metal element to tune the hybridization between the transition metal d and topological chalcogen p states.

In Chapter 6, in a fully first-principles study, we investigate the possibility of realizing TSMs in multiferroic materials, specifically, compounds isostructural to the multiferroic hexagonal manganite $YMnO_3$. Multiferroics are highly tunable by virtue of their multiple order parameters which can be controlled via electric and magnetic fields, strain, and temperature. A multiferroic compound with TSM features in a particular phase would provide an opportunity to switch from nontrivial to trivial topology by tuning of the ferroic order parameters. We find that by enforcing ferromagnetic (FM) order on the Mn ions, the band structure of $YMnO_3$ changes from insulating to metallic in the centrosymmetric, nonpolar phase. Tuning the Fermi level by substituting Mn for other 3d transition metals, we show that hexagonal $YCrO_3$ and $YVO_3$ are topological nodal line semimetals in the nonpolar $P6_3/mmc$ phase with FM magnetic order. By computing the phonon spectra in both nonpolar and polar hexagonal phases, we demonstrate that $YCrO_3$ and $YVO_3$ undergo a structural phase transition to the polar $P6_3cm$ space group, analogous to the ferroelectric transition in $YMnO_3$. In the polar phase both compounds become topologically trivial. Thus, provided that one can synthesize these materials in the $P6_3/mmc$ and $P6_3cm$ phases by epitaxial growth on a hexagonal substrate and stabilize FM order, $YCrO_3$ and $YMnO_3$ can be switched between TSM and trivial band structures by tuning temperature through the nonpolar-polar phase transition.

Chapters 7-9 we transition to electrically switchable AFMs. After some background information on relevant concepts and recent progress in the electric control of magnetic compounds in Chapter 7, we turn to our material of interest, the AFM $Fe_{1/3}NbS_2$. It was recently shown by Analytis et al. that the intercalated TMD $Fe_{1/3}NbS_2$ can be switched between states of high and low electrical resistance by applying orthogonal current pulses in the plane of the Fe layers ("in-plane") [148, 132]. The different resistance states are thought to be caused by current-induced repopulation of AFM domains, indicating that $Fe_{1/3}NbS_2$ is a promising spintronics candidate meriting further characterization.

In Chapter 8, in collaboration with other theorists, we calculate the isotropic spin exchange constants and magnetoanisotropy energy (MAE) of $Fe_{1/3}NbS_2$ in order to develop a model Hamiltonian to explain a half-magnetization plateau observed at a wide range of magnetic fields in $Fe_{1/3}NbS_2$ [69]. We find that the plateau arises due to a competition between strong interplanar (where planes of Fe atoms are stacked along the c axis) and intraplanar exchange of the Fe spins. This is in contrast to the intuitive assumption that an intercalated TMD will have quasi two-dimensional behavior and hence negligible out-of-plane spin exchange. The relative values of the spin interactions that are responsible for the magnetization plateau are also presumably connected to some of the unusual aspects of the electrical switching, such as the unusually low current density required, and the fact that the Fe spins are nearly perpendicular to the current pulses.

In Chapter 9, we explicitly investigate the magnetism and transport of $Fe_{1/3}NbS_2$ as it pertains to the current-induced electrical switching. We first calculate the relative energetics of two different experimentally proposed AFM ground states, corresponding to in-plane "stripe" and "zigzag" orderings of the Fe spins. Our DFT calculations with Hubbard U corrections indicate that these two AFM states are nearly degenerate, consistent with neutron studies indicating that the preferred ground state can switch between stripe and zigzag ordering for minuscule deviations in Fe concentration [197, 185, 214]. Secondly, the hypothesis that the resistance switching is caused by current-induced repopulating of magnetic domains relies on the assumption that the electric structure and corresponding in-plane resistance of $Fe_{1/3}NbS_2$ is anisotropic, which has yet to be confirmed by ARPES or other first-principles studies. Hence, we compute the in-plane electronic structure of $Fe_{1/3}NbS_2$ with both stripe and zigzag AFM order, and calculate the corresponding resistivity tensors using a constant relaxation time approximation within the Kubo linear-response formalism. We confirm the in-plane transport anisotropy for both stripe and zigzag order. Finally by comparing the directional anisotropy of our computed resistivity tensors to the signs of resistance changes in experiment, we provide new insight into the specifics of the current domain response, that is, which domains are stabilized for a given current pulse direction.

In Chapter 10, we provide a summary of the thesis and outlook for possible future directions.

# Chapter 2

# Computational methods: DFT, Wannier functions and some offshoots

## 2.1 Density Functional Theory: the basics

### The Many-Body Hamiltonian

The most general time-independent Schrödinger equation for an atomic solid composed of many electrons and many nuclei may be written in Hartree atomic units as [59]

$$\begin{aligned} H\Psi &= \left[\hat{T}_e + \hat{T}_n + \hat{V}_{en} + \hat{V}_{ee} + \hat{V}_{nn}\right]\Psi \\ &= \left[-\sum_i \frac{\nabla_i^2}{2} - \sum_I \frac{\nabla_I^2}{2M_I} - \sum_{i,I} \frac{Z_I}{|\mathbf{r}_i - \mathbf{R}_I|} + \frac{1}{2}\sum_{i\neq j} \frac{1}{|\mathbf{r}_i - \mathbf{r}_j|} + \frac{1}{2}\sum_{I\neq J} \frac{Z_i Z_J}{|\mathbf{R}_I - \mathbf{R}_j|}\right]\Psi = E_{tot}\Psi, \end{aligned} \tag{2.1}$$

where $\Psi(\mathbf{r}_1, \mathbf{r}_2 ... \mathbf{r}_N; \mathbf{R}_1, \mathbf{R}_2 ... \mathbf{R}_M)$ is the many-body wavefunction which is dependent on the coordinates $\mathbf{r}_i$ of all $N$ electrons and $\mathbf{R}_I$ of all $M$ nuclei in the material. The first two terms $\hat{T}_e$ and $\hat{T}_n$ in equation 2.1 give the kinetic energy of the electrons and nuclei respectively, $\hat{V}_{en}$ gives the Coulomb interaction between the negatively charged electrons and positively charged nuclei, and $\hat{V}_{ee}$ and $\hat{V}_{nn}$ give the Coulomb interactions between the electrons and between the nuclei respectively. $M_I$ and $Z_I$ refer to the masses and atomic numbers of individual nuclei.

Of course, given the number $3(N+M)$ of independent coordinates, solving equation 2.1 as it stands is impossible for more than a few degrees of freedom; to make any headway we must employ several approximations and assumptions. Before getting to some of the approximations unique to density functional theory, or DFT, we first use the Born-Oppenheimer approximation, a consequence of which being that the nuclear positions $\{\mathbf{R}\}$ are considered to be fixed in space, i.e. $M_I = \infty$. With the assumption that the nuclear positions can be treated as parameters, the nuclear kinetic energy $\hat{T}_n$ goes to zero and the nuclear-nuclear repulsion $\hat{V}_{nn}$ is simply a constant energy shift. Then the above Schrödinger equation can be written as

$$H\Psi = \left[\hat{T}_e + \hat{V}_{en} + \hat{V}_{ee}\right]\Psi = \left[-\sum_i \frac{\nabla_i^2}{2} + \sum_i V_n(\mathbf{r}_i) + \frac{1}{2}\sum_{i\neq j}\frac{1}{|\mathbf{r}_i - \mathbf{r}_j|}\right]\Psi = E\Psi, \qquad (2.2)$$

where now $\Psi(\mathbf{r}_1, \mathbf{r}_2 ... \mathbf{r}_N)$ is a function of the dynamical electronic coordinates only, with the nuclear coordinates treated as external parameters and

$$V_n(\mathbf{r}) = -\sum_I \frac{Z_I}{|\mathbf{r} - \mathbf{R}_i|} \qquad (2.3)$$

is the external Coulomb potential of the nuclei experienced by the electrons. Equation 2.2 is the fundamental "electronic structure" Hamiltonian for the electronic degrees of freedom in a material on which all subsequent approximations we discuss will be based.

## The Hohenberg-Kohn theorem, mean-field theory, and the Kohn-Sham equations

While the Born-Oppenheimer approximation allows us to to simplify the general solid-state Hamiltonian by neglecting the motion of the nuclei, contending with $3N \sim 10^{23}$ electronic degrees of freedom in equation 2.2 is still intractable. The most fundamental tenet of density functional theory (DFT), the Hohenberg-Kohn theorem [59, 75], dramatically simplifies the problem. The gist of the Hohenberg-Kohn theorem is that the total energy $E$ of the electronic many-body ground state (and we should emphasize that this is only true for the ground state, not excited states) is uniquely determined by the electronic density $n(\mathbf{r})$, where

$$n(\mathbf{r}) = \left\langle \Psi(\mathbf{r}_1 ... \mathbf{r}_N) \middle| \sum_i \delta(\mathbf{r} - \mathbf{r}_i) \middle| \Psi(\mathbf{r}_1 ... \mathbf{r}_N) \right\rangle = N \int d\mathbf{r}_2 .. d\mathbf{r}_N \Psi^*(\mathbf{r}, \mathbf{r}_2 ... \mathbf{r}_N) \Psi(\mathbf{r}, \mathbf{r}_2 ... \mathbf{r}_N). \qquad (2.4)$$

Note that by going from the wavefunction $\Psi(\mathbf{r}_1 ... \mathbf{r}_N)$ to the electronic density $n(\mathbf{r})$ the number of independent variables on which our ground state energy depends goes from $3N$ to 3. In proving that the ground state energy is determined by the ground-state electronic density alone, three initial facts are required which we state here (the last two are intuitive, and the first may be proven by *reductio ad absurdum* [75]).

1. In the ground state, the electronic density uniquely determines the external potential from the nuclei: $n(\mathbf{r}) \rightarrow V_n(\mathbf{r})$.

2. In any state, the external potential from the nuclei uniquely determines the many-body electron wavefunction: $V_n(\mathbf{r}) \rightarrow \Psi$.

3. In any state the total energy $E$ is a functional of the many-body wavefunction through $E = \langle\Psi|\hat{H}|\Psi\rangle$. Thus $\Psi \rightarrow E$.

These three facts together imply $n(\mathbf{r}) \rightarrow V_n(\mathbf{r}) \rightarrow \Psi \rightarrow E$, i.e. the ground state energy $E_{GS}$ is indeed uniquely a functional of the ground-state density, as the theory states. Mathematically, the Hohenberg-Kohn theorem may be written as

$$E_{GS} = \min_{n(\mathbf{r})} E\left[n(\mathbf{r})\right] = \int V_n(\mathbf{r}) n(\mathbf{r}) d\mathbf{r} + \langle \Psi\left[n\right] | \hat{T}_e + \hat{V}_{ee} | \Psi\left[n\right] \rangle , \tag{2.5}$$

where $\hat{V}_n$ is the external potential created by the nuclei defined in equation 2.3 and $\hat{T}_e$ and $\hat{V}_{ee}$ are the electronic kinetic and potential energies also defined earlier. Equation 2.5 states that the ground state energy of the many-body electronic Schrödinger equation is found by minimizing the functional $E\left[n\right]$ with respect to the density $n(\mathbf{r})$, which in turn also yields the true ground-state electronic density $n_0(\mathbf{r})$ related to the many-body wavefunction through equation 2.4. Thus, if we had a practical way to construct and evaluate the energy functional, our work in evaluating the ground-state properties of our material of interest would be basically done.

The fact that the 3-component electronic density, rather than the 3N-component electron wavefunction, is sufficient to determine the ground state energy of a solid, is a major simplification. However, the functional is unknown. To make progress, Kohn and Sham first wrote the exact functional in terms of the functional for a system of noninteracting electrons plus a correction term, the so-called exchange-correlation functional. Minimizing this functional with respect to a density expressed in terms of single-particle states leads to the "Kohn-Sham" equations [101, 59]. The Kohn-Sham approach is motivated by the goal of recasting the many-body Schrödinger equation in section 2.1 into the sum of kinetic and Coulomb energies of independent electrons, plus a term which accounts for deviations due to electron-electron interactions (i.e. correlation and exchange). The Kohn-Sham equations are an example of a "mean-field" approximation, in which we assume that each electron experiences an *average* potential created by the sum of contributions from all other electrons, as well as the nuclei [39, 59]. In fact, the Kohn-Sham approach represents a mapping of the fully interacting $N$ electron system onto a set of $N$ noninteracting, single-electron orbitals $\phi_i$ that yield the *true*, many-bodied electron density via $n(\mathbf{r}) = \sum_i |\phi_i(\mathbf{r})|^2$. Now the energy $E\left[n\right]$ in equation 2.5 may be rewritten in the following way:

$$E\left[n(\mathbf{r})\right] = \int V_n(\mathbf{r}) n(\mathbf{r}) d\mathbf{r} - \sum_i \int d\mathbf{r} \phi_i^*(\mathbf{r}) \frac{\nabla^2}{2} \phi_i(\mathbf{r}) + \frac{1}{2} \iint d\mathbf{r} d\mathbf{r}' \frac{n(\mathbf{r}) n(\mathbf{r}')}{|\mathbf{r} - \mathbf{r}'|} + E_{xc}\left[n(\mathbf{r})\right]. \tag{2.6}$$

Here, the first term is again the electronic energy contribution due to the external potential of the fixed nuclei. The second term is the kinetic energy of the noninteracting electrons, the third is the mean-field electron-electron Coulomb interaction, and the fourth term is the infamous "exchange-correlation" energy which accounts for contributions to the $\langle \Psi\left[n\right] | \hat{T}_e + \hat{V}_{ee} | \Psi\left[n\right] \rangle$ term in equation 2.5 which are not included in the independent electron approximation (terms two and three in equation 2.6). While equation 2.6 is formally exact, the specific form of $E_{xc}\left[n(\mathbf{r})\right]$ is unknown, and finding reasonable approximations to this exchange-correlation energy is the subject of much ongoing research.

In practice, to find the ground-state density $n_0(\mathbf{r})$ and corresponding ground state energy, we minimize the energy functional $E\left[n\right]$ by requiring $\frac{\delta E[n]}{\delta n}|_{n_0} = 0$. This yields a set of Euler-Lagrange equations for the single-particle fictitious orbitals $\phi_i(\mathbf{r})$ [39]:

$$\left[-\frac{\nabla^2}{2} + \hat{V}_n(\mathbf{r}) + \int d\mathbf{r}' \frac{n(\mathbf{r}')}{|\mathbf{r}-\mathbf{r}'|} + \frac{\delta E_{xc}\left[n\right]}{\delta n}\right]\phi_i(\mathbf{r}) = \left[-\frac{\nabla^2}{2} + \hat{V}_n(\mathbf{r}) + \hat{V}_{ee}(\mathbf{r}) + \hat{V}_{xc}(\mathbf{r})\right]\phi_i(\mathbf{r}) = \epsilon_i\phi_i(\mathbf{r}) \tag{2.7}$$

Note that the equations 2.7 are single-particle Hamiltonians for the orbitals $\{\phi_i(\mathbf{r})\}$ with an effective potential, $V_{eff} = V_n + V_{ee} + V_{xc}$. These are the so-called Kohn-Sham equations, and with them at last we have covered the basic components of a DFT calculation workflow. Figure 2.1 shows a schematic of the steps required to reach the most fundamental output of DFT, the ground-state energy. The fact that the exchange-correlation potential $\hat{V}_{xc}$ and the electron-electron potential $\hat{V}_{ee}$ depend on the density $n$, and the fact that the density depends on the single-particle Kohn-Sham orbitals $\phi_i$, together imply that the set of equations 2.7 must be solved self-consistently. We start with the external nuclear potential $V_n(\mathbf{r})$, which can be constructed from knowledge of the atomic species and crystallographic coordinates in the unit cell of a material. We then construct an ansatz for the the initial Kohn-Sham orbitals and from these we generate a starting density. From the starting guess for the density we construct the potentials $\hat{V}_{xc}$ and $\hat{V}_{ee}$. With these potentials plus the nuclear potential we then solve the set of eigenvalue equations , generating a *new* set of Kohn-Sham orbitals. With these Kohn-Sham-orbitals we construct a new density $n(\mathbf{r}) = \sum_i |\phi_i(\mathbf{r})|^2$. We take this new, improved density, construct new potentials, and iterate the steps self-consistently until the density generated from solving the Kohn-Sham equations is equal to our initial input density. Finally, having obtained the ground state electron density $n_0(\mathbf{r})$ we plug it back into the full many-bodied energy functional 2.6 to evaluate the ground state energy of our material. From derivatives of $E_{GS}$, many additional ground state properties such as polarizability, elastic constants, and Born charges can also be obtained from a DFT calculation [39].

## Exchange-Correlation functional

As mentioned in section 2.1, the exchange-correlation energy functional $E_{xc}\left[n(\mathbf{r})\right]$ is generally unknown and we must treat it with some approximations. The two most common approximations are the “Local Density Approximation” (LDA) [101] and the “Generalized Gradient Approximation” (GGA) [160]. In the LDA, $E_{xc}\left[n(\mathbf{r})\right]$ is given by

$$E_{xc}^{LDA} = \int d^3\mathbf{r} n(\mathbf{r})\epsilon_{xc}(n(\mathbf{r})), \tag{2.8}$$

where $\epsilon_{xc}(n\mathbf{r})$ is the exchange correlation energy per particle corresponding to that of a homogenous electron gas (HEG) of density $n(\mathbf{r})$ at point $\mathbf{r}$. Thus each infinitesimal volume element $d\mathbf{r}$ is associated with an idealized electron gas having a locally uniform density. The exchange energy (arising from the Pauli exclusion principle) for a HEG for given density

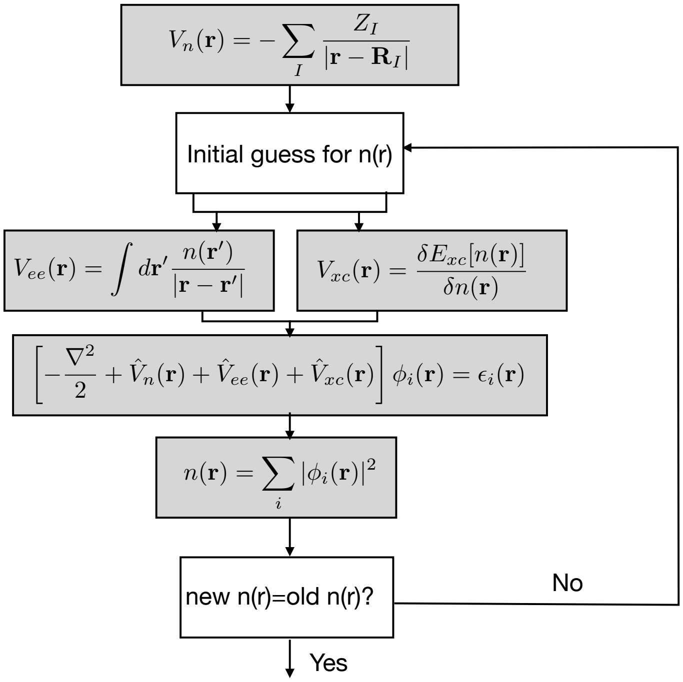

Figure 2.1: Basic workflow for a DFT calculation. Figure adopted from [59].

$n(\mathbf{r})$ has an exact solution, while the correlation energy for an HEG is generally obtained by solving the full many-bodied Schrödinger equation with stochastic methods [59].

The GGA approximation improves upon the LDA by accounting for local spatial variations in the electron density. In this approximation $E_{xc}$ is given by

$$E_{xc}^{GGA} = \int d^3\mathbf{r} f(n(\mathbf{r}), \nabla n(\mathbf{r})), \tag{2.9}$$

where the form of the function $f$ depends on the implementation of GGA used. Perhaps the most common GGA implementation was developed by Perdew, Burke, and Ernzerhof (PBE) [157], and we shall use this functional throughout the thesis.

Both LDA and GGA have inherent shortcomings; for example, LDA tends to underestimate lattice parameters by up to a few percent in a geometry optimization (overbind) whereas GGA tends to overestimate lattice parameters by up to a few percent (underbind) [43]. Moreover, numerical values for band gaps (and more importantly for this thesis, band inversions) can be severely underestimated (overestimated) with both functionals [199]; we note that the band gap is not a ground state property, and therefore good agreement with experiment is not expected. We will discuss some improvements on these methods such as LDA(GGA)+U and hybrid functionals, later in the chapter. However, the relative computational cheapness of LDA and GGA as well as their reasonable accuracy for many materials of interest make them broadly used in DFT research to this day.

### Basis functions and Pseudopotentials

When constructing the Kohn-Sham orbitals in a DFT calculation, a choice of basis is required. In this thesis, and in most modern DFT codes employing periodic boundary conditions, a plane-wave basis is used in which the Kohn-Sham orbital $i$ with crystal momentum $\mathbf{k}$ is expanded in the following manner:

$$\phi_{i,\mathbf{k}}(\mathbf{r}) = e^{i\mathbf{k}\cdot\mathbf{r}} \sum_{\mathbf{G}} C_{i,\mathbf{G}} e^{i\mathbf{G}\cdot\mathbf{r}}, \tag{2.10}$$

where $\mathbf{G}$ are the reciprocal lattice vectors and $C$ are the coefficients in the expansion. Note that equation 2.10 is in the Bloch form $\psi_{n\mathbf{k}}(\mathbf{r}) = e^{i\mathbf{k}\cdot\mathbf{r}} u_{n\mathbf{k}}(\mathbf{r})$, where $u_{n\mathbf{k}}(\mathbf{r})$ in a function with the periodicity of the crystal lattice. In practice the basis has to be truncated at some point due to computational limitations, and the cutoff wavevector $\mathbf{G}_{max}$ is usually specified by choosing a cutoff energy defined by $E_{cut} = \frac{\hbar^2 \mathbf{G}_{max}^2}{2m_e}$ where $m_e$ is the electron mass.

Another practical concern is the question of how to treat core electrons, which are chemically inert and irrelevant for many material properties. A common method is to use pseudopotentials, which lump the core electrons together with the nuclear potential $V_n(\mathbf{r})$, allowing us to solve the Kohn-Sham equations for the outer valence electrons only [236, 39]. This reduces computational expense significantly because the requirement that all electronic orbitals are orthogonal means that the tightly bound core electrons must have highly oscillatory wavefunctions, thus mandating a huge plane wave cutoff in equation 2.10 if we include these electrons explicitly. Computation time is also cut due to the fact that eliminating the core electrons reduces the number of Kohn-Sham equations we need to solve in our DFT calculation, and the computational time scales as $\sim N^3$ where $N$ is the number of electrons.

In practice, a pseudopotential for a specific atomic element is constructed by first solving the all-electron Kohn-Sham equations for that element to obtain Kohn-Sham orbitals and eigenvalues for the valence electrons with all electrons included. We then construct "pseudowavefunctions" by splicing the exact form of the valence electrons far away from the nucleus with a smooth, node-less function at distances close to the nucleus. We can then invert the Schrödinger equation for that pseudowavefunction to obtain a corresponding smooth pseudopotential that combines the exact nuclear potential with screening effects from the core electrons [39].

## 2.2 $d$ and $f$ electrons: capturing localization and strong correlations in DFT

### DFT+U

While the LDA and GGA (or specifically, PBE) functionals are excellent for describing a wide variety of systems, they can fail catastrophically for materials containing transition metal or rare-earth ions, which usually have unfilled $d$ and $f$ shells respectively. A well-known example is found in many of the transition metal oxides, which LDA predicts as metallic, although they are experimentally known to be insulators [45]. These and other failures are in part because LDA and PBE fail to take into account the orbital dependence of the Coulomb and exchange interactions, thereby over-delocalizing the unpaired $d$ and $f$ electrons [5]. Many different improvements on LDA (PBE) for the treatment of strongly correlated materials have been proposed and implemented within DFT, but the most computationally inexpensive is almost certainly the so-called LDA (PBE)+U method [7]. This formalism separates the electrons into two types; those in $s$ or $p$ orbitals which are relatively delocalized, and localized electrons in $d$ and $f$ shells. The former are treated in the normal LDA (PBE) formalism. For the $d$ (or $f$) electrons however, a repulsive Hubbard potential $E^{\mathrm{U}} = \frac{1}{2}U\sum_{i\neq j} l_i l_j$, where $l_i$ and $l_j$ are density matrices for the specific $d$ orbitals $i$ and $j$, is added. The modification to the LDA (PBE) energy functional $E^{LDA(PBE)}\left[n(\mathbf{r})\right]$ in equation 2.5 is then [114]

$$E^{LDA(PBE)+U}\left[n(\mathbf{r}), l\right] = E^{LDA(PBE)}\left[n(\mathbf{r})\right] + E^{U}\left[l\right] - E^{dc}\left[l\right], \tag{2.11}$$

where $n(\mathbf{r})$ is again the total electron density. $E^{dc}\left[l\right]$ is a term subtracted to partially mitigate double counting from the Coulomb energy of the $d$ or $f$ electrons as calculated within plain LDA (PBE).

In practical terms, $E^{U}$ and $E^{dc}$ are constructed using the ad hoc Hubbard U and Hund's exchange J parameters, the values of which are specified as input at the beginning of the LDA (PBE)+U calculation. The specific values, in units of energy, of U and J must be proposed on a case-by-case basis for each material of interest; sometimes, this can be done self-consistently within a linear response approach [38], or else by empirical matching of the DFT outputs to experimental data. The necessarily ad-hoc nature of LDA(PBE)+U is a downside to the method, and as will become abundantly clear in Chapters 8 and 9, there are some materials for which no single set of values for U and J can satisfactorily describe all properties of interest.

## Hybrid functionals

Hybrid functionals are in general a more robust way to treat strongly correlated $d$ and $f$ electrons than DFT+U. Rather than using the LDA or PBE approximations for the exchange part of the exchange-correlation functional $E_{xc}$, hybrids incorporate some amount of exact Hartree-Fock exchange, given by [39]

$$E_x^{HF} = -\frac{1}{2}\sum_{i\mathbf{k},j\mathbf{q}} \iint d\mathbf{r}d\mathbf{r}' \frac{\phi^*_{i\mathbf{k}}(\mathbf{r})\phi_{i\mathbf{k}}(\mathbf{r}')\phi^*_{j\mathbf{q}}(\mathbf{r})\phi_{j\mathbf{q}}(\mathbf{r}')}{|\mathbf{r}-\mathbf{r}'|}, \tag{2.12}$$

where the $\phi_{i\mathbf{k}}$ and $\phi_{j\mathbf{q}}$ are different Kohn-Sham orbitals, and the quantum numbers corresponding to their crystal momenta $\mathbf{k}$ and $\mathbf{q}$ are included. Correlation on the other hand is still treated in the LDA or PBE formalism. The most straightforward implementation of a

Hybrid functional is PBE0 [158], where the total exchange-correlation energy is given by

$$E_{xc}^{PBE0} = \frac{1}{4}E_x^{HF} + \frac{3}{4}E_x^{PBE} + E_c^{PBE}, \tag{2.13}$$

where $E_c^{PBE}$ is the correlation energy from standard PBE. However, the computational expense of the nonlocal Hartree-Fock calculation in PBE0 can be reduced, while still getting comparable results, by using a range-separated hybrid functional; variations of these are known as Heyd-Scuseria-Ernzerhof, or HSE functionals [73]. In HSE functionals, the Hartree-Fock treatment for a fraction of the exchange energy is applied *only* at short ranges, whereas 100% of the exchange energy at long ranges is treated with PBE or LDA. The range separation is controlled by a parameter $\mu$ that defines the short and long range portions of the Coulomb operator. The exchange energy within HSE is

$$E_{xc}^{HSE} = \frac{1}{4}E_x^{HF,SR}(\mu) + \frac{3}{4}E_x^{PBE,SR}(\mu) + E_x^{PBE,LR}(\mu) + E_c^{PBE}, \tag{2.14}$$

where SR and LR refer to short-range and long-range respectively. In spite of the computational speedup of HSE as compared to PBE0, for even moderately large systems HSE can still be prohibitively expensive. Thus, throughout this thesis we use PBE or PBE+U for the majority of our calculations, and use HSE calculations sparingly, as necessary.

## 2.3 Wannier Functions

### Basic idea

Bloch's theorem postulates that the one-electron eigenstates for an infinite periodic crystal can be written as $\phi_{n\mathbf{k}}(\mathbf{r}) = e^{i\mathbf{k}\cdot\mathbf{r}}u_{n\mathbf{k}}(\mathbf{r})$, where $u_{n\mathbf{k}}(\mathbf{r})$ is a function with the periodicity of the lattice and $\mathbf{k}$ is the crystal momentum with units of inverse length. Thus, crystals are naturally described in terms of "Bloch waves" $\phi_{n\mathbf{k}}(\mathbf{r})$ which are delocalized in real space and localized in reciprocal space. Plane-wave DFT calculations correspondingly cast the Kohn-Sham orbitals in the Bloch format (equation 2.10). However, there are many applications for which a basis localized in real space and delocalized in **k**-space is preferable to the Bloch form. Wannier functions, which are essentially Fourier transforms of Bloch functions, are a natural choice for such a basis within a DFT formalism [137, 138]. From a qualitative standpoint, WFs have many similarities with molecular orbitals and can thus provide insight into the details of chemical bonding for molecules or amorphous solids. More quantitatively, the modern theory of electric polarization, formulated by Vanderbilt et al. [98] recasts the electric polarization in an extended periodic solid in terms of either a Berry phase calculated in the Bloch basis, or equivalently and perhaps more intuitively, in terms of the positions of the WFs in the unit cell in a Wannier basis. Finally, and most relevantly to this thesis, WFs can serve as a very accurate tight-binding basis which can be used to transform back to reciprocal space and interpolate quantities on an extremely dense **k**-grid with massively reduced computational expense as compared to a plane-wave DFT calculation on an equivalent grid [138].

We briefly outline the basic concepts for constructing localized WFs starting from a DFT calculation; this procedure is implemented in the Wannier90 code [144] which interfaces with many popular DFT codes. In Dirac notation, a WF $|n\mathbf{R}\rangle$ localized in cell $\mathbf{R}$ and associated with band $n$ is defined as

$$|n\mathbf{R}\rangle = \frac{V}{(2\pi)^3}\int d\mathbf{k}e^{-i\mathbf{k}\cdot\mathbf{R}}\,|\phi_{n\mathbf{k}}\rangle\,, \tag{2.15}$$

where $V$ is the volume of the real-space primitive cell. The inverse equation defines the Bloch state, or Kohn-Sham orbital, in terms of WFs:

$$|\phi_{n\mathbf{k}}\rangle = \sum_{\mathbf{R}} e^{i\mathbf{k}\cdot\mathbf{R}}\,|n\mathbf{R}\rangle\,. \tag{2.16}$$

However, WFs are not unique due to a gauge freedom in the Bloch states which propagates nontrivially into the integral in equation 2.15. Concretely, in the case of a single Bloch state $|\phi_{n\mathbf{k}}\rangle$, the gauge freedom amounts to an arbitrary choice of phase that does not change any physical observables:

$$|\phi_{n\mathbf{k}}\rangle \to e^{i\theta_n(\mathbf{k})}\,|\phi_{n\mathbf{k}}\rangle\,, \tag{2.17}$$

where $\theta_n(\mathbf{k})$ is a real function of $\mathbf{k}$. If we now consider an isolated manifold of $N$ bands in reciprocal space (isolated here means that while there can be degeneracies among the $N$ bands at certain $\mathbf{k}$ points, this set is energetically separated from all other bands everywhere in the Brillouin zone), this gauge freedom generalizes to a unitary transformation that mixes the bands at a given $\mathbf{k}$ point:

$$|\phi_{n\mathbf{k}}\rangle \to \sum_{m=1}^{N} U_{mn}^{(\mathbf{k})}\,|\phi_{m\mathbf{k}}\rangle\,, \tag{2.18}$$

where $U^{(\mathbf{k})}$ is an $N \times N$ unitary matrix. The propagation of equation 2.18 to the definition of WFs leads to a set of $N$ generalized Wannier functions given by

$$|n\mathbf{R}\rangle = \frac{V}{(2\pi)^3}\int d\mathbf{k}e^{-i\mathbf{k}\cdot\mathbf{R}}\sum_{m=1}^{N} U_{mn}^{(\mathbf{k})}\,|\phi_{m\mathbf{k}}\rangle\,. \tag{2.19}$$

The shapes and spreads of the WFs depend on our choice for the unitary matrix $U^{(\mathbf{k})}$. The question then becomes how to choose $U^{(\mathbf{k})}$ such that the resulting WFs have the properties we desire. Because the motivation for using WFs over the Bloch eigenstates is usually the need for a localized basis set, the most common criterion is to choose the unitary matrix such that the spatial spread of the WFs is minimized. This is the approach developed by Marzari and Vanderbilt and taken within the Wannier90 code developed by Mostofi, Vanderbilt et al. and the resulting "Maximally localized Wannier Functions" or MLWFs are the most common choice in DFT applications. The spread of the manifold of $N$ WFs is defined as

$$\Omega = \sum_{n=1}^{N} \left[ \langle \mathbf{0}n | r^2 | \mathbf{0}n \rangle - \langle \mathbf{0}n | \mathbf{r} | \mathbf{0}n \rangle \right] = \sum_{n=1}^{N} \left[ \langle r^2 \rangle_n - \langle \mathbf{r} \rangle_n \right] , \tag{2.20}$$

where the $\mathbf{0}$th unit cell is chosen arbitrarily as the origin. MLWFs are constructed such that equation 2.20 is minimized. This is done by calculating the gradient of $\Omega$ with respect to infinitesimal changes in the unitary matrix, $U^{(\mathbf{k})} \rightarrow U^{(\mathbf{k})} + \delta U^{(\mathbf{k})}$. The gradient is then used to minimize the spread by a steepest-descent or conjugate-gradient algorithm. It can be shown [137] that the only ingredients required to calculate the gradient using finite differences are the overlaps of the cell-periodic parts of the Kohn-Sham Bloch orbitals:

$$M_{mn}^{\mathbf{k},\mathbf{b}} = \langle u_{m\mathbf{k}} | u_{n\mathbf{k}+\mathbf{b}} \rangle , \tag{2.21}$$

where $\mathbf{b}$ are vectors connecting the $\mathbf{k}$ point to its nearest neighbors in the reciprocal lattice. The one other quantity required in the construction of MLWFs is a set of initial guesses $|g_n\rangle$ for the final forms of the localized Wannier functions (generally, the best procedure is to select atomic orbitals which have significant weight in the Bloch bands of interest, e.g. copper $d$ states). The initial guesses are projected onto the $N$ Bloch states in the isolated manifold, as

$$A_{mn}^{(\mathbf{k})} = \langle \phi_{m\mathbf{k}} | g_n \rangle . \tag{2.22}$$

These projection matrices are then used to construct from the original Bloch orbitals a new reference set which should be closer to the ideal, generalized Bloch states (equation 2.18) that yield the MLWFs. These modified Bloch orbitals are the actual states which go into the overlaps in equation 2.21.

Thus, everything needed to generate MLWFs is contained in the output of a DFT calculation. In practice, the basic steps in the "Wannierization" process are the following:

1. Perform a self-consistent DFT calculation to generate a set of Bloch-like Kohn-Sham orbitals.

2. Choose a subset of $N$ isolated energy bands which we wish to wannierize; in general, these will be bands close to the Fermi level, which are the most relevant for material properties.

3. In Wannier90, specify initial guesses for the MLWFs; the original Kohn-Sham orbitals will be projected onto these localized states to generate a gauge-transformed set of Bloch states that will be the starting point for the minimization procedure.

4. Using the overlaps $M_{mn}^{(\mathbf{kb})}$ of neighboring Bloch states in the Brillouin zone, calculate the gradient of the spread $\Omega$ of the WFs with respect to changes in the unitary matrix in equations 2.18 and 2.19. Minimize $\Omega$ using the gradient to update the matrices $U^{(\mathbf{k})}$.

5. Once $\Omega$ is minimized, use the resulting unitary matrices to construct a manifold of $N$ maximally localized Wannier functions using equation 2.19.

We should mention that is possible to extend the formalism of MLWFs to the case where the bands of interest are not isolated, but instead become degenerate with other bands at higher or lower energies at points in reciprocal space. This is often the case for metallic or semimetallic materials on which this thesis primarily focuses. In this case one can use a "disentanglement" procedure developed by Souza, Marzari and Vanderbilt [180]. Very generally, the idea is to choose an energy window that encompasses at minimum the $N$ bands of interest and at some points in the Brillouin zone may contain some number $M > N$ bands. At each point $\mathbf{k}$ with more than $N$ bands, the optimal subspace of $N$ bands is extracted by a unitary mixing of all $M$ Bloch states at this $\mathbf{k}$ point. The "optimal subspace" is defined by minimization of the part of $\Omega$ which is gauge-invariant for a given subspace.

## Uses of WFs in this thesis: tight-binding, surface states, and transport tensors

Before concluding this chapter, we briefly discuss the main applications of MLWFs in this thesis. As mentioned in 2.3, MLWFs can serve as a localized basis from which to construct tight-binding Hamiltonians. Given the matrix elements of the Hamiltonian in the Wannier basis, which are given as output in the Wannier90 code,

$$H_{mn}(\mathbf{R}) = \langle \mathbf{0}m|\hat{H}|\mathbf{R}n\rangle \,, \tag{2.23}$$

where the notation for the Wannier functions is defined in the previous section, the tight-binding Hamiltonian in reciprocal space may be obtain via a computationally efficient Fourier transformation:

$$H_{mn}(\mathbf{k}) = \sum_{\mathbf{R}} e^{i\mathbf{k}\cdot\mathbf{R}} H_{mn}(\mathbf{R}). \tag{2.24}$$

An extremely useful extension is using MLWFs to construct "slab" tight-binding models where we are interested in looking at topological states localized at the material surface. In principle it is possible to generate a surface state band structure directly from a DFT calculation using a supercell with vacuum in one direction to model a surface; in fact, we use this direct method in Chapter 5. However, the supercell must be large enough to contain a bulk-like region in the middle of the supercell; otherwise, hybridization between the top and bottom surfaces will generally obscure topological surface states. The minimal acceptable supercell size is dependent on the material, and in some cases (as in TiAsRh which we describe in Chapter 4) this can be tens or even hundreds of primitive unit cells, which is computationally infeasible for a direct DFT calculation. Thus, a tight-binding calculation is sometimes the only way to go. We emphasize that in constructing a tight-binding Hamiltonian for a supercell with surfaces, we still use the primitive cell in the DFT calculation from which we generate the Hamiltonian matrix elements in the Wannier basis. The construction of a slab tight-binding Hamiltonian is completely analogous to the case of bulk, with the modification that the reciprocal lattice vector in the direction perpendicular to the surface is no longer a good quantum number (due to the periodicity of the crystal being broken in this direction). Instead, we can index the $S$ layers of the slab in real space to distinguish matrix elements for lattice vectors $\mathbf{R}$ that connect cells in different layers. Explicitly, the elements of the slab tight-binding Hamiltonian (of size $(N \times S) \times (N \times S)$ for $N$ Wannier functions in a primitive unit cell) may be written as [213]

$$H_{mn,ij}(\mathbf{k}_{\|}) = \sum_{\mathbf{R}=(\mathbf{R}_1,\mathbf{R}_2,(i-j)\mathbf{R}_3)} e^{i\mathbf{k}_{\|}\cdot\mathbf{R}} H_{mn}(\mathbf{R}). \tag{2.25}$$

Here, $\mathbf{k}_{\|}$ is the component of crystal momentum parallel to the surface (defined here as perpendicular to the $\mathbf{R}_3$ lattice vector), $i$ and $j$ refer to the layer indices and the lattice vector $\mathbf{R}$ is restricted to the subspace which connect cells in layers $i$ and $j$, and $m$ and $n$ as usual refer to the band indices of the WFs in the primitive cell.

Finally, we mention that formulas involving expectation values of the velocity operator, $\hat{v}$, which feature heavily in studies of transport, can be evaluated very naturally in the Wannier basis. This is because $\hat{v} = \left[\hat{H}, \hat{\mathbf{r}}\right]$ can be written using the Wannier basis Hamiltonian matrix elements as [231]

$$\hat{v}_{nm\mathbf{k}} = \frac{i}{\hbar} e^{i\mathbf{k}\cdot\mathbf{R}} (\mathbf{R} + \mathbf{r}_m - \mathbf{r}_n) H_{mn}(\mathbf{R}), \tag{2.26}$$

where $\mathbf{r}_m = \langle \mathbf{0}m|\mathbf{r}|\mathbf{0}m\rangle$ is the center of WF $m$, and the matrix elements $H_{mn}(\mathbf{R})$ are defined in equation 2.23. The Kubo linear response conductivity formula which we discuss in connection to the spintronics candidate $\mathrm{Fe}_{1/3}\mathrm{NbS}_2$ in Chapter 9 is evaluated by Fourier transforming to a dense $\mathbf{k}$-grid from a Wannier basis and constructing the velocity operator in this manner.

# Chapter 3

# Topological Semimetals

## 3.1 Some Background on Topological Materials and Topological Phase Transitions

### Introduction: the Quantum Hall state and Topological invariants

A significant portion of condensed matter physics from both a theoretical and experimental standpoint involves the exploration of distinct phases of matter. For most of the twentieth century, Landau theory, which describes phase transitions in terms of spontaneously broken symmetries, was thought to successfully characterize all possible cases. However, with the discovery of the Quantum Hall effect 40 years ago [99], scientists realized that two or more phases of matter could exhibit distinct observable properties while being described by identical structural symmetries [71, 80]. This led to the development of an entirely new formalism for phase transitions whereby the distinct phases are characterized by different values of mathematical invariants rather than different global symmetries; these invariants change when the phases cannot be connected by a smooth or adiabatic evolution of the Hamiltonian through tuning of some order parameter, implying that they are topologically distinct. The specific form of the topological invariant of interest depends on the material's symmetries and band structure (i.e, whether it is a semimetal or insulator), but very broadly, these invariants involve integrating properties of occupied Bloch states over the crystal Brillouin zone (BZ). While the papers in the following sections, as well as the remainder of this introductory chapter, focus on topological materials with three-dimensional semimetallic band structures (topological semimetals, or TSMs), following [71] we will use the example of the two dimensional insulating quantum hall state (QHS) to introduce topological phases, as it the most conceptually straightforward case.

Figures 3.1a-3.1c show a cartoon of the simplest insulating system, an atomic insulator: a structure of periodically arranged atoms with electrons bound to the atoms in closed shells. The translational invariance of the material implies that the energy eigenstates can be written as Bloch states $\psi(n, \mathbf{k}) = e^{i\mathbf{k}\cdot\mathbf{r}} |u_n(\mathbf{k})\rangle$, with $\mathbf{k}$ the crystal momentum, $n$ indexing the

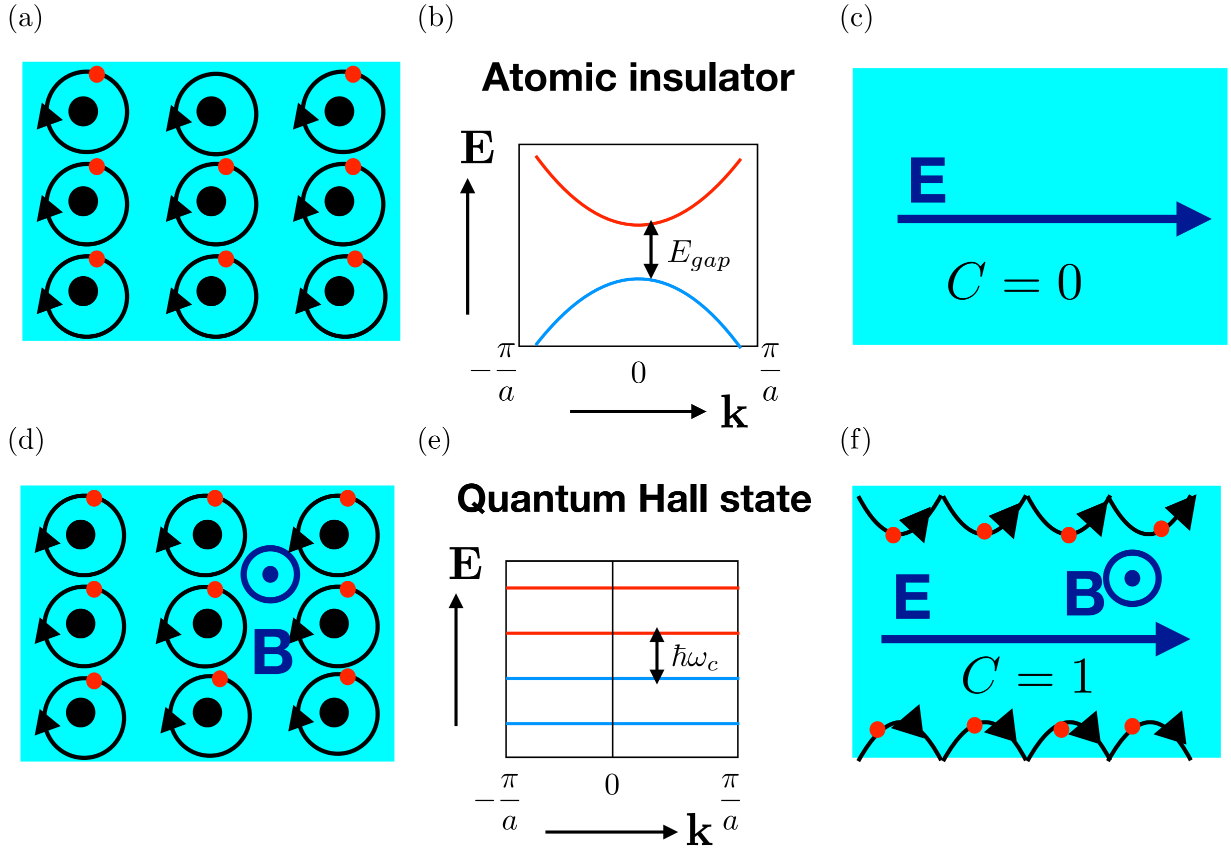

Figure 3.1: Atomic insulator (a)-(c) versus Quantum Hall State (QHS) (d)-(f). (a) Cartoon of atomic insulator. Large black circles indicate atomic nuclei, with electrons (red) orbiting in closed shells. (b) Trivial insulating bandstructure with occupied valence band in blue, unoccupied conduction band in red, and a finite energy gap $E_{gap}$. (c) Response of the boundary of a trivial insulator to an electric field. Like the bulk material, the boundary of a trivial insulator will also be insulating. (d) Quantum Hall State (QHS) with electrons in the two-dimensional bulk undergoing cyclotron orbits. (e) Band structure with Landau levels caused by perpendicular magnetic field B (in this cartoon, the **k** dispersion is neglected.) (f) In contrast to (c), a QHS has conducting, chiral electronic states at the edges of the material perpendicular to the applied electric field due to the nonzero Chern number $C$.

energy level, and $|u_n(\mathbf{k})\rangle$ a periodic function in the BZ. The eigenvalues $E_n(\mathbf{k})$ form the energy bands and in the case of the atomic insulator the occupied and unoccupied bands are separated by an energy gap at all points **k** in the BZ. The atomic insulator is topologically equivalent to vacuum.

The integer quantum hall state (QHS) (Figure 3.1d-3.1f), which manifests when electrons are confined to two dimensions in the presence of a strong perpendicular magnetic field, also has an insulating band structure with Landau levels separated by $\hbar\omega_c$ with $\omega_c$ the cyclotron frequency. In the presence of a periodic potential the Landau levels will disperse with crystal momentum $\mathbf{k}$, identically to the trivial insulator. However, unlike the trivial atomic insulator, the application of an electric field along one direction of the quantum hall state induces a transverse, quantized electrical current known as the hall conductivity:

$$\sigma_{xy} = Ne^2/h. \tag{3.1}$$

The fundamental distinction between the QHS and the trivial insulator lies in a topological invariant known as the Chern number, which can be expressed in terms of the Berry connection of the cell-periodic part of the Bloch wavefunctions, $|u_n(\mathbf{k})\rangle$. Given the Berry connection, defined as

$$A_n(\mathbf{k}) = i \langle u_{n\mathbf{k}}| \nabla_{\mathbf{k}} |u_{n\mathbf{k}}\rangle , \tag{3.2}$$

and Berry curvature, which is the wedge product of $A_n(\mathbf{k})$, which is the normal cross product in three dimensions and in two dimensions is simply $F_n = \partial_{k_x} A_n^{k_y} - \partial_{k_y} A_n^{k_x}$, the Chern invariant is the Berry curvature integrated over the two-dimensional BZ, summed over occupied bands [71, 63]:

$$C = \frac{1}{2\pi} \sum_{n,occ} \int d^2\mathbf{k} F_n. \tag{3.3}$$

For the case of a trivial insulator, $C = 0$, while $C = 1$ for the QHS. In spite of their qualitatively similar band structures, the different values of the Chern invariant imply highly distinct physical properties, perhaps the most striking of which is the existence in the QHS of conducting, chiral states localized on the edges of the material which are perpendicular to the Hall current, and are insensitive to disorder and backscattering [55] (Figure 3.1 (f)). Robust surface states occur in most topological materials as a consequence of the change of topological invariant in going from vacuum to bulk. This is simplest to visualize in the case of insulators. Imagine slowly tuning the Hamiltonian of a QHS material by changing the distance $y$ from an interface. As we mentioned previously, topologically distinct objects with different topological invariants cannot be connected without closing the energy gap. Thus, at the boundary between the QHS ($C = 1$) and vacuum ($C = 0$), where the Chern invariant changes value, there must exist low-energy electron states localized at the surface where the energy gap closes.

The QHS only exists under specific experimental conditions (i.e. two-dimensional system, externally applied magnetic field). However, following the discovery of the Integer Quantum Hall effect, the concept of topological invariants as descriptors for phases of matter has been extended to a broad variety of insulating materials. In addition to three-dimensional variants of the QHS with an applied magnetic field [100], seminal papers in the early 2000's revealed that, in both two and three dimensions, materials with time-reversal symmetry $\mathcal{T}$ can be characterized by a class of so-called $\mathcal{Z}_2$ invariants [94, 140]. Nontrivial $\mathcal{Z}_2$ insulators (also sometimes referred to as Quantum spin hall, or QSH insulators in the literature) can be thought of as a superposition of two QHS systems with effective magnetic fields in opposite directions; these effective magnetic fields are created by the the spin-orbit coupling of electrons in the material, where electrons with up and down spins generate opposite effective fields [71]. Both copies of the QHS state contribute a single chiral edge state. Due to the $\mathcal{T}$ symmetry these two edge states form Kramer's pairs with opposite spins and opposite crystal momenta $\mathbf{k}$ and $-\mathbf{k}$, meaning they are counter-propagating. It is notable that due to the spin-orbit coupling, the $\mathcal{Z}_2$ insulators have topological properties that are intrinsic to the material, and unlike the QHS do not require an external magnetic field to be realized.

## Extending topology to semimetals

While a topological classification for three-dimensional normal metals, which have two-dimensional Fermi surfaces, is still unclear, the concept of topologically nontrivial materials *has* been extended to include semimetals; these topological semimetals (TSMs) will be the focus of the following chapters. Semimetallic band structures have discrete band touchings where the highest occupied and lowest unoccupied bands are exactly degenerate, which may either occur at singular $\mathbf{k}$ points (as for Weyl and Dirac semimetals) or for one-dimensional loops in the BZ (nodal line semimetals). The existence of gapless materials with topological properties was first demonstrated theoretically in 2007 by Suichi Murakami [145]. Below, we repeat the main points of his paper and discuss the resulting topological Weyl semimetal (WSM) phase, as it is the historical and conceptual precedent for other TSM variants, such as the nodal line semimetal (NSLM) which we focus on later in this thesis.

Murakami studied the effect of varying a single parameter $m$ to induce the phase transition between a $\mathcal{T}$-symmetric, QSH state (discussed above), and a trivial insulator. Because the value of the $\mathcal{Z}_2$ invariant changes at the phase transition, the energy gap between occupied and unoccupied states must close for some crystal momentum $\mathbf{k}$. $\mathcal{T}$ symmetry implies that for any band $n$, $E_n(\mathbf{k}) = E_n(-\mathbf{k})$. Thus, if for some value of the parameter $m = m_0$ a band crossing occurs at $\mathbf{k}$, a crossing must also occur at $-\mathbf{k}$. For materials without inversion symmetry, these band crossings are separated in reciprocal space at generic BZ points $\pm k_0$. In two dimensions, this semimetallic band structure is a critical point which occurs for a single value of the parameter $m$; any infinitesimal deviation from $m = m_0$ will gap out the crossing points and drive the material to either the QSH or trivial insulating phase. The situation changes fundamentally when one considers three-dimensional systems. Specifically, for three-dimensional materials with $\mathcal{T}$ symmetry but no $\mathcal{I}$ symmetry, there is no longer a phase transition between the QSH and the trivial insulator at single value of $m$. Instead, there is a finite range of the parameter $m_1 < m < m_2$ for which the material's band structure remains gapless (see Figure 3.2a). The difference in nature of the phase transition in two and three dimensions can be seen simply from a codimension argument. For an arbitrary point $\mathbf{k}$, a band touching, up to an overall constant proportional to the identity matrix, can be minimally described by a $2 \times 2$ Hamiltonian,

$$\mathcal{H} = f_1(m, \mathbf{k})\sigma^x + f_2(m, \mathbf{k})\sigma^y + f_3(m, \mathbf{k})\sigma^z, \tag{3.4}$$

where $f_1$, $f_2$ and $f_3$ are functions of $(m, k_x, k_y)$ or $(m, k_x, k_y, k_z)$ in two and three dimensions respectively, and the $\sigma$ are the $x$, $y$ and $z$ Pauli matrices. The codimension of equation 3.4, namely the number of conditions required to enforce the eigenvalues to be degenerate, is three ($f_1 = f_2 = f_3 = 0$). In two dimensions this is equal to the number of independent variables ($m$ and the two components of $\mathbf{k}$), meaning that band crossings can occur at only a single point in the $(m, k_x, k_y)$ phase space. But in three dimensions, the codimension is one less than the number of independent parameters $(m, k_x, k_y, k_z)$, such that the possible solutions form a curve in the four-dimensional parameter space. This means that as $m$ is varied there is a range of $\mathbf{k}$ values at which band crossings exist at $k_0$ and $-k_0$. Thus, in three dimensions a semimetallic phase which is distinct from the insulating QSH or trivial phases emerges for a finite range of parameters. We will now see that this gapless phase (known as a Weyl semimetal, or WSM phase) is itself topologically nontrivial.

## Topological nature of the gapless state: the Weyl semimetal

Murakami showed that the gapless phase discussed above is topological in the sense that the pair of band touchings, or Weyl points, cannot be destroyed individually by tuning of the Hamiltonian, or introduction of disorder. While tuning the parameter $m$ causes the band crossings to move around in reciprocal space, they can only be created or annihilated in pairs, at the points $m = m_1$ and $m = m_2$ when they overlap in reciprocal space. The robustness of the Weyl points is due to the fact that each gapless point carries a topological invariant. The topological invariants for insulators which we have discussed thus far involve integrating properties of occupied Bloch states over the entire BZ. Because the manifold of occupied states is ill-defined at the band touching points in semimetals, at first glance the application of a topological description might seem untenable. However, this difficulty can be overcome by defining topological invariants along closed loops or surfaces in the BZ for which any gapless points are excluded [110]. In the case of the zero-dimensional Weyl points, the invariant associated with a single crossing is the integral of the Berry curvature flux through a gapped surface $S$ in the BZ which encloses the degeneracy, as depicted in Figure 3.2b:

$$C = \frac{1}{2\pi} \sum_{n,occ} \int_S (\nabla_{\mathbf{k}} \times A_n(\mathbf{k})) \cdot \mathbf{n} dS, \tag{3.5}$$

where $\mathbf{n}$ is a vector normal to $S$. Note that Equation 3.5 is just an extension to three dimensions of the Chern formula 3.3 for the insulating QHS. The Chern number for an individual Weyl point is quantized to ±1. In the case described here in which the QSH/WSM system has broken $\mathcal{I}$ symmetry but preserved $\mathcal{T}$, the transformation of the Berry curvature under $\mathcal{T}$ symmetry dictates that Weyl points at $\mathbf{k} = \pm k_0$ have the same sign of the Chern number, $C(k_0) = C(-k_0)$. However, the net Chern number, or Berry flux, in the three-dimensional BZ must be zero (this is evident by noting that if we expand the surface $S$ in equation 3.5 to encompass the entire BZ rather than a single band crossing, by periodicity this surface is equivalent to a point, and thus cannot have a net flux of Berry curvature [207].) Therefore in the gapless $m_1 < m < m_2$ region, in order to enforce zero net Berry flux in the BZ there must be an additional pair of Weyl points both with opposite Chern sign located at a different set of points $\mathbf{k} = \pm k_1$. This implies that the minimum number of Weyl points in a system with $\mathcal{T}$ symmetry (but no $\mathcal{I}$ symmetry) is four. At the end points $m_1$ and $m_2$ of the WSM phase, Weyl points with opposite Chern numbers meet in the BZ (at points $\mathbf{k} = \mathbf{G}/2 \pm k$, with $\mathbf{G}/2$ a time-reversal invariant BZ center or boundary, such that the Weyl points with identical Chern numbers still respect $\mathcal{T}$ symmetry) and are annihilated (Figure 3.2a).

The conceptual demonstration of the WSM phase by Murakami as well as the first experimentally and theoretically verified WSM materials such as TaAs, TaP, NbAs and NbP [124, 210] focused on nonmagnetic $\mathcal{T}$-symmetric compounds with broken inversion symmetry. We note here that the WSM phase can also occur in materials with intact inversion symmetry but broken $\mathcal{T}$ symmetry [207] (magnetic Heusler alloys are one verified example [206, 31]). In this case, $\mathcal{I}$ symmetry implies that $C(k_0) = -C(-k_0)$. Therefore for WSMs with $\mathcal{I}$ symmetry (but no $\mathcal{T}$ symmetry), the minimum number of Weyl points is two rather than four.

Finally, we point out that in addition to ensuring the robustness of the bulk band crossings provided they do not overlap in reciprocal space, the topological Chern numbers associated with individual Weyl points imply the existence of exotic surface states in the WSM phase, analogously to the surface states in topological insulating phases. The presence of surface states, and their functional form in the WSM phase, can be understood by the following argument [207]. Consider a single pair of Weyl points with Chern numbers $\pm 1$ on the $k_z$ axis of the BZ at $k_z = \pm k_0$. We define the gapped surface $S$ in equation 3.5 which encloses the Weyl point at $k_z = -k_0$ as the box formed by four two-dimensional side planes at $k_x = \pm\frac{\mathbf{g_1}}{2}$, $k_y = \pm\frac{\mathbf{g_2}}{2}$, a bottom plane at $k_z = -\frac{\mathbf{g_3}}{2}$, and a top plane at some $k_z$ value $-k_0 < k_z < k_0$ ($\mathbf{g}_{1,2,3}$ refer to the reciprocal lattice vectors in the $x$, $y$, and $z$ directions which define the boundaries of the BZ). Because the BZ is gapped everywhere except the location of the Weyl points, each of these two-dimensional planes has a well-defined Chern number. If we keep the locations of the five planes at the BZ boundaries constant and move the plane between the two Weyl points along the $k_z$ axis, the Chern number defined by $S$ must change from $C = 1$ for $-k_0 < k_z < k_0$ to $C = 0$ for $k_z > k_0$ (at which point the net Berry flux piercing $S$ is zero because the surface encloses both Weyl points). Therefore all two-dimensional planes at fixed $k_z$ between the Weyl points must have Chern number $C = 1$ (i.e. it is equivalent to a QHS insulator), and all planes below $k_z = -k_0$ and above $k_z = k_0$ must have $C = 0$. Each of these $C = 1$ planes at constant $k_z$ will have chiral edge states at $x$ and $y$ boundaries of the material. Going back to the three-dimensional WSM, this implies that there will be continuous topological edge states (or "Fermi arcs") on the side surfaces of the WSM which must begin at the projection of one Weyl point and terminate at the projection of a Weyl point of opposite Chern number (see Figure 3.2c). Note that because the projections of the Weyl points with opposite Chern numbers overlap on the $k_z = 0$ boundary, no such Fermi arcs are implied on surfaces perpendicular to the $z$ direction [202].

Before closing out this chapter with a discussion of practical applications of TSMs, we will briefly introduce two other TSMs which we discuss in more detail in the following chapters; the Dirac semimetal and the Nodal Line semimetal. While these TSMs differ in several ways from the Weyl semimetal, their bulk and surface properties can similarly be described and understood from the standpoint of topological invariants, and changes in these invariants as one moves about the Brillouin zone.

## 3.2 Beyond the Weyl semimetal: other TSMs

### Dirac Semimetals

In Section 3.1 we emphasized that WSMs must have either time-reversal symmetry $\mathcal{T}$ or inversion symmetry $\mathcal{I}$, but not both. It is natural to ask what happens when a material has both of these symmetries, and whether a semimetal phase with topological features can exist in this case. At the very least, Weyl-like points involving the crossing of a single valence and single conduction band are not possible in the presence of both $\mathcal{T}$ and $\mathcal{I}$ symmetry. This is clear by noting that in addition to reversing the direction of crystal momentum, $\mathcal{T}$ symmetry also flips an electron spin, implying that $E_n^{\uparrow}(\mathbf{k}) = E_n^{\downarrow}(-\mathbf{k})$. On the other hand, $\mathcal{I}$ symmetry reverses the direction of $\mathbf{k}$ but does not flip spin, i.e. $E_n^{\downarrow}(\mathbf{k}) = E_n^{\downarrow}(-\mathbf{k})$. These two conditions together imply $E_n^{\uparrow}(\mathbf{k}) = E_n^{\downarrow}(\mathbf{k})$; thus with $\mathcal{I}$ and $\mathcal{T}$ symmetry all bands are doubly spin degenerate at each $\mathbf{k}$ point. This also means that any crossing of bands at a single $\mathbf{k}$ point will necessarily be fourfold, rather than doubly degenerate as in the WSM. Furthermore, the coexistence of $\mathcal{I}$ and $\mathcal{T}$ symmetries forces the Berry curvature to vanish at every point in the BZ. Thus, unlike a singular Weyl point, a fourfold degenerate crossing in this case does *not* carry a topological invariant; in this sense, compounds with $\mathcal{I}$ and $\mathcal{T}$ symmetry that have fourfold-degenerate, zero-dimensional crossings are not as topologically robust as their WSM counterparts. Nevertheless, this TSM variant (known as a “Dirac semimetal”, or DSM) *can* be stabilized in three dimensions for a finite range of Hamiltonian tuning parameters, provided there exists an additional rotational symmetry that protects that bands from mixing and gapping out at the crossing [9]. Moreover, while the absence of finite Chern number for the fourfold crossings in a DSM means that surface Fermi arcs terminating at the band crossings are not guaranteed, for one of the two classes of DSM which we shall discuss in this section, we can define a nontrivial $\mathcal{Z}_2$ invariant on a gapped two-dimensional plane in the three-dimensional BZ. This invariant does imply the existence of topological surface states on the boundaries of the 2D plane, although they are not intimately connected to a topological nature of the Dirac points as is the case for Fermi arcs in the WSM phase [9].

There are two ways in which a stable DSM phase can arise in a material with $\mathcal{I}$, $\mathcal{T}$, and uniaxial rotation symmetries, which can be understood from considering the minimal Hamiltonian in three dimensions for a $4 \times 4$ band crossing [207, 218]:

$$H(\mathbf{k}) = \sum_{i,j=0}^{3} f_{ij}(k_x, k_y, k_z, m)\sigma_i\tau_j = \begin{pmatrix} h_{\uparrow\uparrow}(\mathbf{k}, m) & h_{\uparrow\downarrow}(\mathbf{k}, m) \\ h_{\downarrow\uparrow}(\mathbf{k}, m) & h_{\downarrow\downarrow}(\mathbf{k}, m), \end{pmatrix} \tag{3.6}$$

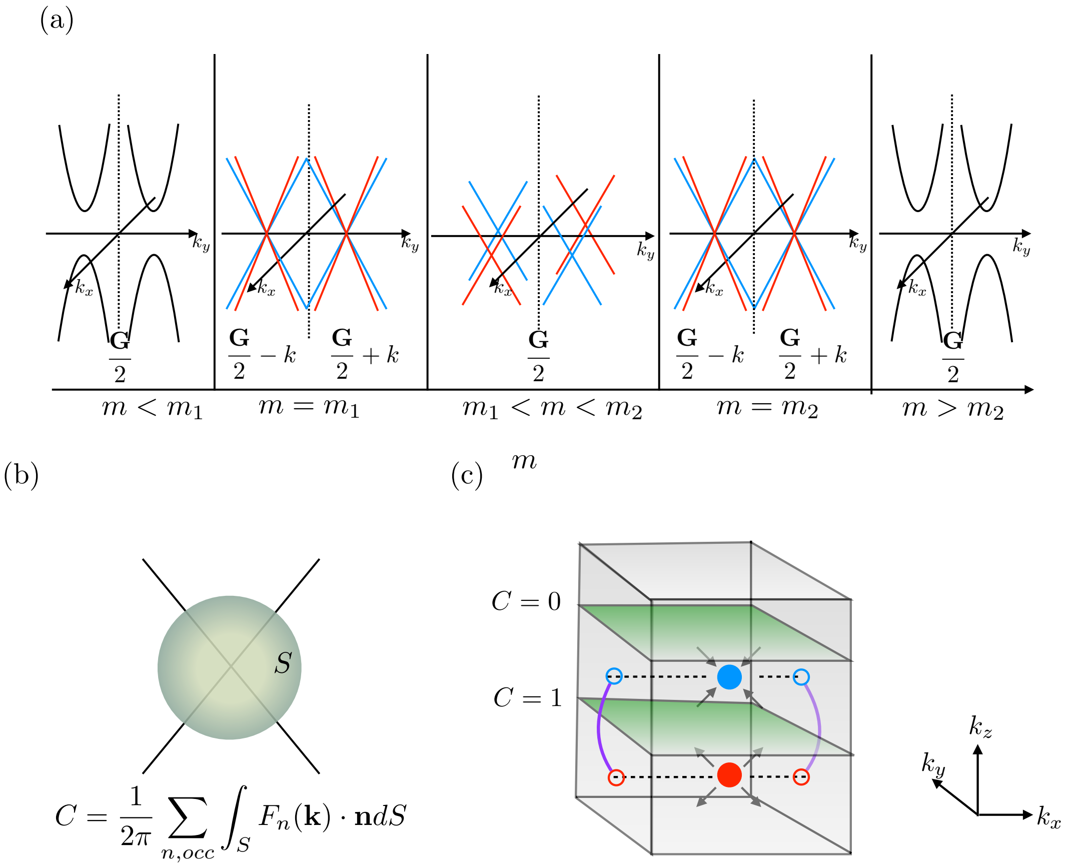

Figure 3.2: Weyl semimetal phase (WSM) in three dimensions with broken $\mathcal{I}$ symmetry (and intact $\mathcal{T}$ symmetry.) (a) Evolution from a topological insulating QSH state to a trivial insulator by tuning of some parameter $m$. Two pairs (each containing Weyl points with opposite sign Chern numbers) of gapless Weyl points are created/annihilated at $m = m_1$ and $m = m_2$. Between those $m$ values the Weyl points move apart in $\mathbf{k}$-space, with the $C = +1$ Weyl points (red) symmetrically displaced from the time-reversal invariant $\mathbf{G}/2$ point due to $\mathcal{T}$ symmetry, and the $C = -1$ Weyl points (blue) also symmetrically displaced. Adopted from [146]. (b) The Chern invariant $C$ of a single Weyl point is calculated by integrating the Berry curvature over a gapped surface $S$ in the BZ enclosing the degenerate point. (c) Cartoon of the Fermi surface arcs (purple lines) in WSMs that arise as a consequence of the nonzero Chern numbers associated with individual Weyl points. The red and blue represent a pair of bulk Weyl points displaced along $k_z$ with Chern numbers ±1 respectively (arrows denote the direction of Berry curvature flux in each case). The Fermi arcs begin and end at the projections of the bulk Weyl points onto the surface of interest (note that while the cartoon depicts Fermi arcs on the $x$ surfaces of the material, analogous Fermi arcs would be expected on the $y$ boundaries). Figure reproduced from [207].

where $\sigma_{1,2,3}$ and $\tau_{1,2,3}$ are Pauli matrices denoting spin and orbital degrees of freedom, respectively, and $\sigma_0$ and $\tau_0$ are $2 \times 2$ identity matrices. While the presence of $\mathcal{T}$ and $\mathcal{I}$ symmetries constrains several of the $f_{ij}$ in equation 3.6 to be zero, these two symmetries only reduce the codimension of the above equation to five, greater than the number of independent variables ($(k_x, k_y, k_z, m) = 4$); thus, in general it is not possible to tune the four parameters to realize a band crossing. However, if the material also has a rotational symmetry $C_n$, (n-fold rotation about a principle axis), $[C_n, H(\mathbf{k})] = 0$ for $\mathbf{k}$ along that rotational axis (from now on we take the axis to lie along $k_z$ without loss of generality). Therefore, if we restrict ourselves to $\mathbf{k}$ values on the $k_z$ axis (such that $k_x = k_y = 0$), the Hamiltonian 3.6 can be further constrained by using a basis in which $C_n$ and $H(k_z)$ are both diagonal. Specifically, it can be shown [218] that the Hamiltonian now takes the form

$$H = f_0(k_z, m)\sigma_0\tau_0 + f_1(k_z, m)\Gamma, \tag{3.7}$$

where $\Gamma$ can either be $\sigma_0\tau_3$ or $\sigma_3\tau_3$. The codimension of equation 3.7 is now one, whereas the number of independent variables is two ($k_z$ and the mass term $m$). Thus, analogously to the stable WSM phase described in section 3.1, we expect a finite range of values of $m$ for which we have semimetallic DSM crossings located on the $k_z$ axis.

The two distinct classes of DSM phases mentioned above depend on whether $f_1(k_z, m)$ in equation 3.7 is an even or odd function of $k_z$. This in turn is dictated by the matrix representation of inversion symmetry $\mathcal{I}$ in the space group in question. In the case of symmorphic space groups (space groups for which all symmetries, apart from lattice translations, leave at least one common point fixed), $\mathcal{I}$ takes on a diagonal representation $\mathcal{I} = \tau_0$ or $\mathcal{I} = \tau_3$ (depending on whether the orbitals in question have same or opposite parities). For non-symmorphic space groups (space groups which contain either screw axes or glide planes, operations that combine point group symmetries with a fractional lattice translation), the matrix representation of $\mathcal{I}$ is off-diagonal, i.e. $\mathcal{I} = \tau_1$. “Class I” DSMs occur in symmorphic space groups where $f_1(k_z, m)$ is even, meaning that to leading order $f_1 \sim m + \frac{1}{2}ck_z^2$. Since $f_1(k_z, m)$ is proportional to the energy gap between the two pairs of degenerate bands in equation 3.7, a necessary condition to have fourfold degenerate crossings is a band inversion (reversal of energy ordering), which can be achieved if $mc < 0$; for $mc > 0$ the pair of doubly degenerate bands is gapped at all $k_z$ and the material is a trivial insulator. Once the band inversion is achieved at some critical value of $m = m_1$, a pair of Dirac points will locate symmetrically about the $k_z$ axis at $k_z = \pm\sqrt{\frac{2m}{|c|}}$. These fourfold crossings are protected from mixing and reentering an insulating state provided they have different rotational eigenvalues under the $C_n$ operation. As the parameter $m$ is varied, the Dirac points will move along the $k_z$ axis but will not disappear so long as the band inversion condition is maintained. Generally, at some higher value $m = m_2$, two or more band inversions will occur simultaneously at different high-symmetry points and this tends to drive the material into an insulating state again [207] (see Figure 3.3a). Class I DSMs are the only experimentally verified DSMs to date, with $Na_3Bi$ and $Cd_3As_2$ perhaps the best known examples [118, 117]. This type of DSM, as we mentioned before, can in general host topological surface states on the boundaries parallel to the rotation symmetry axis provided the gapped two-dimensional plane $k_z = 0$ has a nontrivial $\mathcal{Z}_2$ invariant. However, these surface states are not intrinsically connected to topological invariants of the individual bulk Dirac points as was the case for WSMs, and indeed, are not required to terminate at the surface projections of the Dirac crossings.

"Class II" DSMs occur in the situation where $f_1(k_z, m)$ is an odd function of $k_z$, which is the case in space groups with nonsymmorphic symmetries. $f_1(k_z, m) = -f_1(-k_z, m)$ implies that $f_1$ must vanish at the center and end points ($k_z = 0$ and $k_z = \pi$) of the BZ along the rotational axis, due to the periodicity of the BZ. Therefore, in contrast to class I DSMs where a pair of Dirac points locate symmetrically from the BZ center along $k_z$, in class II DSMs a *single* Dirac point locates at the center or boundary of the BZ along the rotational axis. Furthermore, because $f_1(k_z, m) \sim ak_z$ to leading order in this case, the stability of the Dirac point is independent of the tuning parameter $m$ and will be robust as long as the crystalline space group symmetries are not broken [218] (see Figure 3.3b). Although this "symmetry-enforced" class of DSMs is in some ways more robust than the class I DSMs, and has been proposed theoretically in several classes of compounds such as $BiO_2$ as well as distorted spinels [223, 182], these compounds have yet to be experimentally synthesized. Moreover, class II DSMs do not have a topological invariant associated with them, and do not in general support surface states. The two classes of DSMs and their evolution as a function of tuning parameter $m$ are shown in Figure 3.3.

## Nodal Line Semimetals

Because we will discuss nodal line semimetals, or NLSMs, in some detail in two of the following chapters, we will give only a brief, high-level overview here. Whereas the Dirac and Weyl semimetals described previously consist of band crossings at discrete points in the BZ, NLSMs in three dimensional materials have band crossings that form closed loops in reciprocal space (see Figure 3.4). NLSMs may be grouped into three broad categories based on the symmetries which protect the one-dimensional loops of crossings: NLSMS protected by a mirror symmetry, NLSMs protected by the combination of inversion and time reversal symmetry, and NLSMs with strong spin orbit coupling protected by inversion, time-reversal, and a nonsymmorphic screw axis symmetry [46, 47]. We should emphasize that in the first two categories, the NLSMs are only stable when spin-orbit coupling (SOC), is neglected. Briefly, this is because SOC mixes orbital and spin degrees of freedom, and thus fundamentally changes the form of space group symmetry operators. This can cause bands whose crossings were protected without SOC by having different symmetry eigenvalues to hybridize and gap out due to having the same symmetry eigenvalues with the inclusion of SOC (The effect of SOC on NLSMs in the first two categories will be discussed further in Chapters 4 and 6). Thus, the first two mechanisms of protection for nodal lines are only relevant in materials with elements light enough such that SOC is negligible.

Type A NLSMs are protected in the absence of SOC by a mirror reflection symmetry, $\mathcal{M}$ which acts in real space as $(x, y, z) \rightarrow (x, y, -z)$ and in reciprocal space as $(k_x, k_y, k_z) \rightarrow$

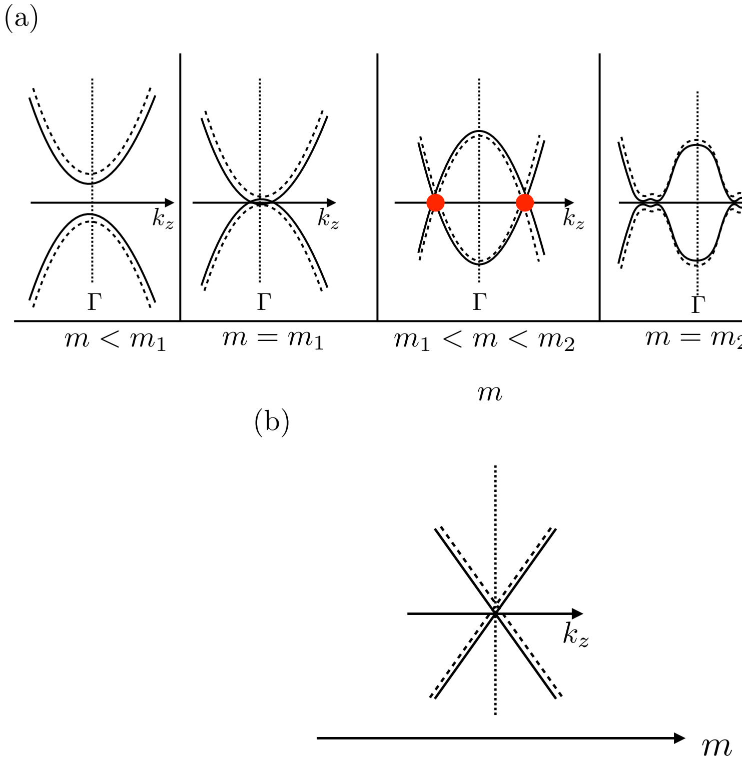

Figure 3.3: Dirac semimetal phase (DSM) In both (a) and (b) the solid and dashed lines refer pairs of bands which are doubly degenerate at all $\mathbf{k}$ due to the combination of time-reversal and inversion symmetries. While the bands are slightly separated for visual clarity, in reality they are completely degenerate. (a) Class I DSM. With $\mathcal{I}$, $\mathcal{T}$ and a uniaxial rotation symmetry $C_n$, a pair of fourfold degenerate Dirac points emerge along the rotation axis $k_z$. The pair of Dirac points is robust for a range of tuning parameter $m_1 < m < m_2$. At the critical point $m_1$ a single band inversion occurs, creating the symmetrically located pair of Dirac points. At $m = m_2$ the crossings gap out due to additional band inversions which tend to modify the rotation eigenvalues of the crossing bands, allowing hybridization. (b) Class II DSM. A single Dirac point locates at the center or boundary of the BZ on the rotational symmetry axis, and is robust for all values of the mass term $m$. This “symmetry-enforced” class of DSM retains the fourfold Dirac point as long as no symmetries in the corresponding nonsymmorphic space group are broken.

$(k_x, k_y, -k_z)$ for the example of a mirror plane perpendicular to the $z$ axis. Because the Hamiltonian $H(\mathbf{k})$ is invariant under $\mathcal{M}$ on the $k_z = 0$ and $k_z = \pi$ planes, the energy bands may be labeled by the eigenvalues of $\mathcal{M}$, meaning that as long as the mirror eigenvalues of the crossing bands are not the same, the bands are prevented from hybridizing and the crossing is protected. This can be represented quantitatively by a topological invariant equal to the difference in occupied bands with a given $\mathcal{M}$ eigenvalue, say $m = +1$, at two points on the inside and outside of the nodal line [30] (see Figure 3.4a):

$$\eta = N_{m=+1}^{k=k_1} - N_{m=+1}^{k=k_2}, \tag{3.8}$$

where we have picked $k_1$ and $k_2$ as arbitrary points on the mirror-invariant plane on the outside and inside respectively of the nodal line. Recall that we since we are assuming that the energy spectrum is gapped everywhere except the one-dimensional nodal line, the manifold of occupied states at $k_1$ and $k_2$ is well defined, as well as the subset $N_{m=+1}$ with a specific mirror eigenvalue. In the case that $\eta \neq 0$, the crossing is between bands of opposite mirror eigenvalues and the nodal line is protected provided the mirror symmetry is not broken.

The second category of NLSM is protected by a combination of inversion and time-reversal symmetries $\mathcal{I}$ and $\mathcal{T}$, in the absence of spin-orbit coupling (when SOC is strong, the NLSM will normally evolve into either a topological insulator or DSM [96].) The protection of a nodal line with $\mathcal{I}$ and $\mathcal{T}$ symmetries and no SOC is apparent from a codimension argument similar to those outlined in previous sections [82]. When SOC is absent, the time-reversal symmetry $\mathcal{T}$ acts simply as a complex conjugation operator. In this case it can be shown that the minimal Hamiltonian for a two-band crossing $H(\mathbf{k}) = f_1(m, \mathbf{k})\sigma_x + f_2(m, \mathbf{k})\sigma_y + f_3(m, \mathbf{k})\sigma_z$ is real-valued, $H_{nm}(\mathbf{k}) = H_{mn}(\mathbf{k})$. This means that $f_2(\mathbf{k}) = 0$ and the codimension of the Hamiltonian is two. This is two less than the number of independent variables ($(m, k_x, k_y, k_z) = 4$) as opposed to one less as in the arguments above with WSMs and DSMs. Thus, assuming the parameter $m$ is tuned to some value $m_0$ such that there is a band inversion, the set of points $(k_x, k_y, k_z)$ that yield degenerate eigenvalues (band crossings) form a one-dimensional line, rather than zero-dimensional points, in reciprocal space. Unless there is an additional mirror plane symmetry, the topological invariant $\eta$ defined above cannot be applied to this class of NSLM. However, a $\mathcal{Z}_2$ invariant can be defined for NSLMs with $\mathcal{I}$, $\mathcal{T}$ and no SOC as the integral of Berry connection $A_n(\mathbf{k})$(equation 3.2) around a closed loop $L$ encircling the nodal line [96, 47] (see Figure 3.4b):

$$\phi = \sum_{n,occ} \oint_L A_n(\mathbf{k}) \cdot dk. \tag{3.9}$$

$\mathcal{I}$ and $\mathcal{T}$ symmetries quantize $\phi$ to be either 0 or $\pi$. If $\phi = \pi$, the loop $L$ cannot be shrunk to a point (since an infinitesimally small loop must necessarily have zero Berry phase), and therefore must enclose a protected degeneracy (i.e. the nodal line).

The final class of NSLMs is unique in that the nodal lines are not gapped out by SOC. With both $\mathcal{I}$ and $\mathcal{T}$ symmetries, when spin degrees of freedom and/or SOC are included all bands are doubly degenerate (for the reasons outlined in the section on DSMs). Thus, the crossings of valence and conduction bands making up the nodal line are fourfold degenerate and made up of two crossing "doublet" bands. These fourfold crossings are robust if the material has an additional nonsymmorphic symmetry, specifically a twofold screw symmetry $\mathcal{S}_z$ (twofold rotation followed by half a lattice translation along the rotation axis, where again we have chosen the $z$ axis for concreteness). This is because the product of screw axis with inversion symmetry generates a new symmetry operator $\mathcal{M}' = \mathcal{I} \cdot \mathcal{S}_z$ that is equivalent to a mirror plane shifted by half a lattice vector from $k_z = 0$ for the normal mirror symmetry $\mathcal{M}$ described earlier to $k_z = \pi$ in this case. On the $k_z = \pi$ plane we can now label the four bands in a nodal line by their $\mathcal{M}'$ eigenvalues. Crucially, for this shifted mirror symmetry the mirror eigenvalues of the bands in a given doublet are the same. Thus, if a doubly degenerate conduction band whose subbands have $\mathcal{M}'$ eigenvalues $+m'$ crosses with a doubly degenerate valence band whose subbands have mirror eigenvalues $-m'$, the two doublets form a symmetry-protected fourfold degenerate nodal line. This is in contrast to the normal mirror symmetry $\mathcal{M}$ on the $k_z = 0$ plane, for which the subbands related by $\mathcal{I} \cdot \mathcal{T}$ have opposite mirror eigenvalues; in this case, a subband in the conduction doublet will mix with a subband having the same mirror eigenvalue in the valence band, leading to an anticrossing or gapping out of the nodal line [47, 46] (see 3.4c). These NLSMs can be classified by a topological invariant very similar to the $\eta$ defined in equation 3.8 for NSLMs with a mirror plane symmetry but no SOC, i.e. the difference in number of occupied states with a certain eigenvalue of $\mathcal{M}'$ inside and outside the NL [46].

Finally, we mention that all classes of bulk NSLMs described above host an exotic form of surface state known as a "drumhead" state: a two-dimensional, usually dispersionless band which terminates on the surface projection of the bulk nodal line and can locate either inside or outside the area subtended by the nodal line [30, 96, 82, 46] (see Figure 3.4d). The nature of this drumhead state is also topological in origin and specifically can be inferred from a one-dimensional variant of the Berry phase defined in equation 3.9 [30]. We will discuss these unique surface states further in the following chapters.

## 3.3 Technical applications of TSMs

This thesis focuses on the design and characterization of "functional" TSM materials (and later, functional spintronic materials). Thus, in this introductory chapter it seems relevant to mention, at least in passing, some of the technical applications and fundamental physics questions that can be realized by functional TSMs whose topological features are easily accessible. Specific examples are too numerous to list so we will just give a few broad concepts.

First, the linear dispersion of energy bands in the proximity of the band crossings in WSMs, DSMs and NSLMs implies ultrahigh carrier mobility in these TSMs, making them highly desirable for efficient, dissipationless electronic devices [77, 169]. Connected to the high carrier mobility is usually an extremely large magnetoresistance (change in resistance with application of a magnetic field), that can be leveraged for magnetic sensing applications

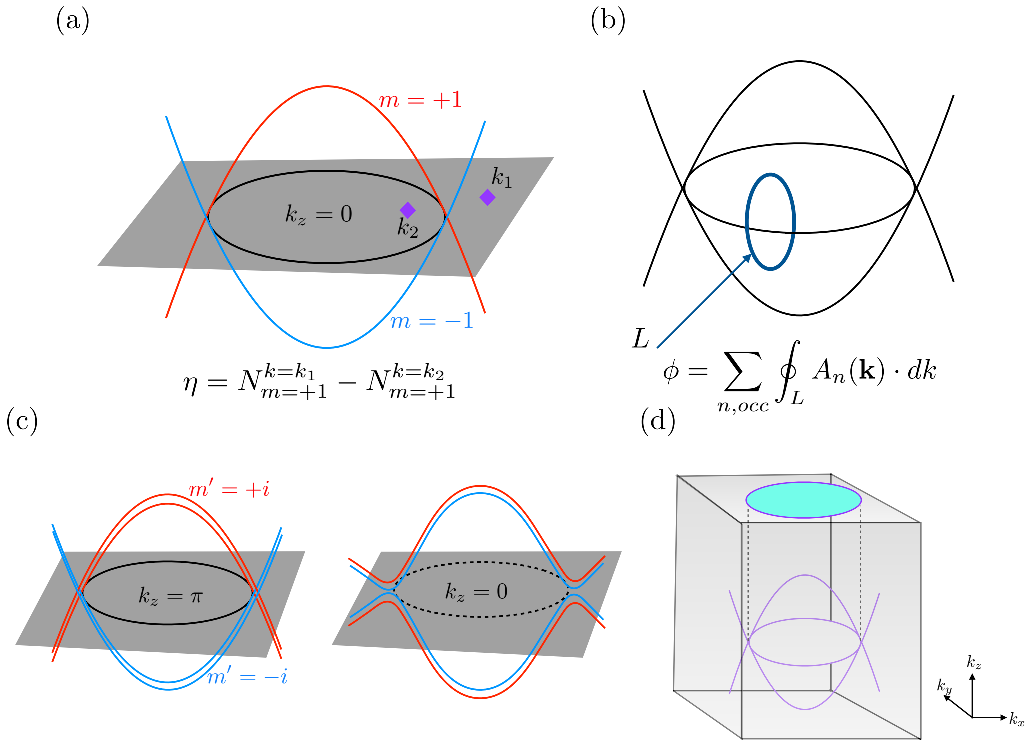

Figure 3.4: Categories of nodal lines semimetals (NSLM) based on the mechanism of protection. (a) NLSM protected by a mirror plane symmetry, where bands with opposite mirror eigenvalues $m$ cross in a mirror-invariant plane of the BZ. (b) NSLM protected by inversion and time-reversal symmetry in the absence of SOC. The Berry connection integrating around a closed loop $L$ encircling the nodal line is a topological invariant. (c) Fourfold degenerate nodal line with SOC protected by $\mathcal{I}$, $\mathcal{T}$ and a two-fold screw axis $\mathcal{S}_z$. On the $k_z = \pi$ plane, the subbands in a single doublet have the same eigenvalues of the composite mirror symmetry $\mathcal{M}' = \mathcal{I} \cdot \mathcal{S}_z$, and their crossing with another doublet is protected (left). On the $k_z = 0$ plane (right), subbands in a single doublet have opposite $\mathcal{M}'$ eigenvalues, leading to an anticrossing when they meet bands of like eigenvalue in the other doublet. In this case an NSLM does not occur. (d) Two-dimensional "Drumhead" surface state (colored turquoise), which terminates on the projection of the nodal line on the $k_z$ surface

[113, 77, 169].

A second possible application of TSMs is in optoelectronics. The linear dispersions in TSMs imply that they can absorb photons of arbitrarily long wavelength, making them useful in devices such such as infrared photodetectors [169]. While in TSMs with symmetrical dispersion (i.e., the slopes of the linearly crossing bands are identical), the net photocurrent generated will be zero, this can be circumvented by using DSMs or WSMs with a "tilted" dispersion, in which the slopes of the crossing bands are asymmetric [169, 28] (The DSM $NiTe_2$ which we discuss in chapter 4 is an example of such a "Type II" asymmetric Dirac system).

In the last few years there has also been a surge of interest in using TSMs in catalytic chemistry [169, 164]. High carrier mobilities, intrinsic to the TSMs, are important for efficient charge separation and diffusion, and the robust surface states in TSMs can reduce surface contamination, one of the limiting factors in catalytic processes. As a proof of principle in a study by Rajamathi et al., several known WSMs (NbP, TaP, NbAs, and TaAs) were tested for dye-sensitized hydrogen evolution reaction (HER), a catalytic process in which solar light is absorbed to produce hydrogen from water. All four compounds were found to have strong activity for HER. Moreover, whereas a topologically trivial transition metal dichalcogenide (TMD) compound $TaS_2$ was inactive for HER, the WSM $MoTe_2$ with similar metallicity and Gibbs free energy for hydrogen absorption showed significant HER activity [164], strongly suggesting that topology has a strong influence on catalytic activity at least for this particular reaction.

In connection to the second half of this thesis, in which we discuss a magnetic material with promising spintronics applications, we mention here that there is both a fundamental and applied interested in finding *magnetic* TSM materials whose topological features can be manipulated by using the material's spin degrees of freedom [176, 177]. Because magnetic order affects electronic structure, magnetism acts a natural order parameter by which one can tune the band structure of a material between a certain TSM phase and another TSM variant, or an insulating phase. This was demonstrated theoretically by Smejkal et al. in the case of the antiferromagnetic compound CuMnAs, which evolves from a topological DSM to a trivial semiconductor depending on the direction of the magnetization (or Néel vector) [176]. We discuss the connection between magnetism and topological order further in Chapter 6.

Finally, on a more fundamental note, because two of the next three chapters focus on NSLMs, we mention a couple properties of NSLMs in particular. First, the unique dimensionality of the Fermi surface (one-dimensional as opposed to zero-dimensional for WSMs and DSMs) means that NSLMs may exhibit effects from long-range Coulomb interactions due to reduced screening [85]. Secondly, the flat "drumhead" surface states provide an exciting platform for the study of exotic correlation physics, due the high localization of the surface state, and may even provide a route for high-temperature superconductivity because of the flat band's high density of states [30, 102].

## 3.4 Conclusion

In this chapter we have introduced the concept of characterizing phases of matter by their topological invariants rather than by the Landau formalism of broken symmetries. We have applied this idea to materials with semimetallic band structures and have described three cases of TSMs, or semimetals with topologically protected bulk and surface states (Weyl semimetals, Dirac semimetals, and nodal line semimetals). Finally, we have given a broad overview of some important applications which can be realized using TSMs. However, in order for the unique features of the TSMs to be efficiently leveraged in any application, the topological band structures should fulfill a subset of criteria including proximity of the band crossings to the Fermi energy, lack of trivial bands at nearby energies, and general tunability. The following chapters will focus on three material examples in which we have characterized functional TSMs and explored methods and parameters (e.g. elemental substitution, manipulation of magnetic order) by which these criteria can be realized.

# Chapter 4

# Prediction of TiRhAs as a Dirac nodal line semimetal via first-principles calculations

The material was previously published as

- Sophie F. Weber, Ru Chen, Qiman Yan, and Jeffrey B. Neaton, *Prediction of* TiRhAs *as a Dirac nodal line semimetal via first-principles calculations*, Physical Review B **96**, 235145 (2017).

## 4.1 Introduction

A recent development in the field of condensed matter physics is the discovery of topological semimetals (TSMs) [208, 145]. These materials have robust, symmetry-protected crossings in reciprocal space, and can be characterized by topological invariants, analogous to the topological insulators (TIs). Three types of TSMs which have been studied in detail both theoretically and experimentally are [208] Weyl semimetals, hosting pairs of massless twofold degenerate nodal points with opposite chirality in the three-dimensional (3D) Brillouin zone (BZ) [216, 124, 203, 210]; Dirac semimetals, with fourfold degenerate nodal points consisting of overlapping Weyl points [117, 118, 205]; and Dirac nodal line semimetals (DNLs), in which the valence and conduction bands touch in a closed loop in momentum space [76, 18, 150, 224]. All three categories are expected to display unusual and intriguing properties, such as ultrahigh mobility, giant magnetoresistance, chiral anomalies, and surface states [113, 156].

DNLs are unique from other types of TSMs by virtue of having a one-dimensional Fermi surface, in contrast to the zero-dimensional Fermi surfaces of Weyl and Dirac semimetals. This implies that the density of states (DOS) of low-energy bulk excitations is quadratic in $|E - E_f|$, where $E_f$ is the Fermi energy, rather than linear [18]. The larger DOS means that interaction-induced instabilities which are predicted for Weyl semimetals can be even more pronounced in DNLs [19]. The one-dimensional nature of the Fermi surface also suggests that such compounds may exhibit effects from long-range Coulumb interactions due to reduced screening [86]. Finally, the topological surface states of DNLs, which take the form of a two-dimensional "drumhead" terminating on the projection of the nodal line onto the surface BZ, have been suggested to provide a platform for exotic physics arising from electronic correlations [30].

In spite of their numerous desirable properties, less than ten DNL compounds have been identified or verified experimentally thus far [27, 76]. This might seem surprising given the fact that there are many different crystalline symmetries that that can stabilize a DNL. But a challenge to experimental realization is that the majority of these protecting mechanisms are only robust when spin-orbit coupling (SOC) is ignored [46]; the nodal line degeneracies are often lifted to a significant degree by SOC unless an additional nonsymmorphic symmetry, such as a screw axis, is present [47, 33]. Another experimental difficulty for DNL compounds, including those synthesized thus far is that there are often trivial bulk bands near the Fermi level coexisting and interfering with the nontrivial nodal line, making a definitive experimental study of the topological properties challenging [150].

Here, we use first-principles calculations to predict that TiRhAs, which has been synthesized in the past [166] but whose electronic properties have thus far remained unexamined, is a DNL semimetal with a nodal line around the Fermi energy which lies in the $k_x = 0$ plane, pinned to the plane by a mirror symmetry. Our study of TiRhAs is motivated by several factors. First, its nonsymmorphic space group possesses several of the symmetry elements known to protect nodal lines. Second, the effect of SOC, given the elements involved, is likely small, and the lifting of degeneracy is expected to be nearly negligible. Lastly, because TiRhAs has an even number of electrons per unit cell, the Kohn-Luttinger theorem suggests

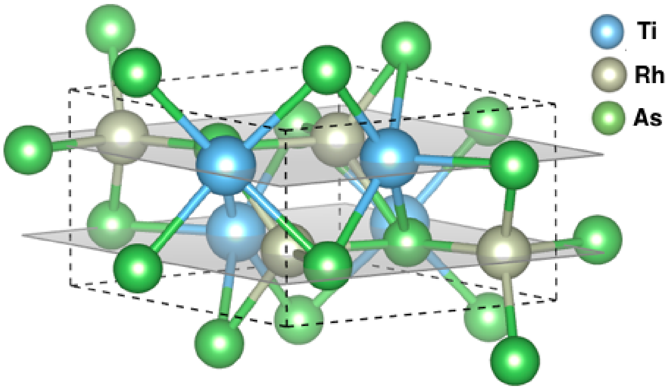

Figure 4.1: Orthorhombic crystal structure of TiRhAs, with space group *Pmnb*. The primitive cell consists of two mirror planes perpendicular to (100), each with two Ti atoms (blue), two As atoms (green), and two Rh atoms (gray).

any DNL might be fixed near the Fermi energy [123, 203], which is desirable for further experimental study and for applications.

## 4.2 Crystal structure and methodology

Prior experimental work has shown that TiRhAs crystallizes in an orthorhombic lattice with the nonsymmorphic centrosymmetric space group *Pmnb* [62] [166]. The primitive cell is shown in Figure 9.1. It is composed of two layers with six atoms each in the $(\frac{1}{4}, y, z)$ and $(\frac{3}{4}, y, z)$ planes. Each Ti atom is five-fold coordinated by As in the shape of "distorted" edge-sharing square pyramids; the Rh atoms are tetragonally-coordinated by As.

For our first-principles density functional theory (DFT) calculations on TiRhAs, we use the Vienna *ab initio* simulation package (VASP) [103]with generalized gradient approximation (GGA) using the Perdew-Burke-Ernzerhof (PBE) functional [157] and projector augmented-wave method (PAW) [21]. The PAW-PBE pseudopotentials of Ti, Rh and As treat $3d^2 4s^2$, $4d^8 5s^1$ and $4s^2 4p^3$ electrons as valence states. We employ an energy cutoff of 300 eV for our plane wave basis set and a Monkhorst-Pack **k**-point mesh of $8 \times 6 \times 6$. Brillouin zone integrations are performed with a Gaussian broadening of 0.05 eV during all calculations citeElsasser1994. These parameters lead to total energies converged to within a few meV. We fully relax the lattice parameters starting from the experimental values. Our GGA lattice constants agree with the experimental results to within 1% (see Table 6.1). We use the optimized lattice parameters for all band structure calculations. For calculations with SOC, we include SOC self-consistently [189].

Table 4.1: Comparison between experimental lattice parameters and Wyckoff positions, and values obtained after full optimization with DFT-PBE.

| | Experiment[166] | DFT-PBE |
|---|---|---|
| $a$ (Å) | 3.816 | 3.841 |
| $b$ (Å) | 6.334 | 6.366 |
| $c$ (Å) | 7.388 | 7.434 |
| Rh (4c) y | 0.855 | 0.857 |
| Rh (4c) z | 0.064 | 0.063 |
| Ti (4c) y | 0.972 | 0.968 |
| Ti (4c) z | 0.684 | 0.682 |
| As (4c) y | 0.243 | 0.252 |
| As (4c) z | 0.122 | 0.122 |

## 4.3 Band structure and symmetries

The GGA band structure of TiRhAs without SOC is plotted in Figure 4.2a. The band crossings along the high symmetry lines $Y - \Gamma$ and $\Gamma - Z$ indicate the presence of a nodal line in the $k_x = 0$ plane encircling $\Gamma$. From an analysis of the site and angular momentum-projected band character, we find that the bands near the crossings are a mixture of Rh $4d$ and Ti $3d$ states. Because GGA is known to overestimate band inversion[199], we also compute bulk band structures using the hybrid density functional HSE06 [73]. The HSE06 result reproduces the DNL and yields an even cleaner Fermi surface than GGA, as the lone trivial band at $\Gamma$ is pushed down relative to $E_f$ to lower energies (see Appendix 4.7).

The DNL in TiRhAs is protected by two different symmetries: (a) the combination of inversion and time reversal symmetries $\mathcal{P}$ and $\mathcal{T}$ in the absence of SOC, and (b) a mirror plane at $x = \frac{a}{4}$. The protection of DNLs by $\mathcal{P}$ and $\mathcal{T}$, provided that SOC is ignored, has been discussed extensively in the literature [30, 96, 47, 224, 209, 208, 82]. Here we briefly motivate why the generic solution for a band crossing in such a system is a closed nodal line (rather than discrete crossings) using a codimension argument [82]. The Bloch Hamiltonian $\mathcal{H}(\mathbf{k})$ for a spinless system near a generic band crossing may always be written as a linear combination of the identity and the three Pauli matrices, with $\mathbf{k}$-dependent coefficients. The combination of $\mathcal{P}$ and $\mathcal{T}$ allow us to choose a gauge for the cell-periodic part $u_{n\mathbf{k}}(r)$ of the Bloch eigenfunctions in which $u^*_{n\mathbf{k}}(r) = u_{n\mathbf{k}}(-r)$. From this fact it trivially follows that $\mathcal{H}(\mathbf{k})$ is real-valued. Consequently we can always express $\mathcal{H}(\mathbf{k})$ in terms of only two of the three Pauli matrices, giving our band crossing a codimension of two. Since this is one less than the number of independent variables ($k_x$,$k_y$,$k_z$), the generic solution $E(\mathbf{k})$ is a line node, which will always be stable in the presence of $\mathcal{P}$ and $\mathcal{T}$.

We now discuss the consequences of the mirror symmetry $\mathcal{R}_x$ in the absence of SOC. The explicit form of the operator in real space is

$$\mathcal{R}_x : (x, y, z) \to (-x + \frac{a}{2}, y, z). \tag{4.1}$$

It is clear from equation 4.1 that $\mathcal{R}_x^2 = +1$. Thus the eigenvalues of $\mathcal{R}_x$ in the absence of SOC are $\pm 1$. Moreover, the action of $\mathcal{R}_x$ in reciprocal space is

$$\mathcal{R}_x : (k_x, k_y, k_z) \to (-k_x, k_y, k_z). \tag{4.2}$$

Therefore, all Bloch functions $\psi_{n\mathbf{k}}(\mathbf{r}) = e^{i\mathbf{k}\cdot\mathbf{r}} u_{n\mathbf{k}}(\mathbf{r})$ in the $k_x = 0$ plane are invariant under $\mathcal{R}_x$, meaning that the bands in this plane may be labeled by the mirror eigenvalues $\pm 1$. Bands with the same mirror eigenvalue can hybridize, leading to a band gap. However, bands with opposite eigenvalues are symmetry-forbidden from mixing and thus their crossing is protected. We check the $\mathcal{R}_x$ eigenvalues of the valence and conduction bands along $Y - \Gamma - Z$ using wavefunctions obtained with the all-electron WIEN2k code [20] and confirm that the crossing bands have opposite eigenvalues, as shown in Figure 4.2a (details of our WIEN2k calculations appear in the Supplementary Material). It should be noted that even if the mirror symmetry is broken in TiRhAs, the DNL will still be protected as long as $\mathcal{P}$ and $\mathcal{T}$ symmetries persist; it will merely be unpinned from the $k_x = 0$ plane.

The self-consistent inclusion of SOC opens a small gap (Figure 4.6). The DFT-PBE-SOC gap varies depending on position along the DNL from less than 1 meV to a maximum of 40 meV. SOC gaps the nodal line by coupling spin and spatial degrees of freedom. Thus, $\mathcal{R}_x$ not only maps $x$ to $\frac{1}{2} - x$, but also maps $s_{y,z}$ to $-s_{y,z}$, i.e, the effect of $\mathcal{R}_x$ on spin space is to perform a $\pi$ rotation about the $\hat{x}$ axis (The difference in the effect of $\mathcal{R}_x$ on real space and spin space is due to the fact that spin is a pseudovector). Now, with SOC included, squaring $\mathcal{R}_x$ amounts to a $2\pi$ rotation in spin space which gives a minus sign for a spin-$\frac{1}{2}$ system, meaning that the eigenvalues of $\mathcal{R}_x$ become $\pm i$. Thus, each band with eigenvalue $\pm 1$ in the non-SOC system becomes doubly degenerate with mirror eigenvalues $\pm i$ in the SOC system. Conduction and valence bands with the same eigenvalues can now hybridize, leading to an anticrossing (Figure 4.6). We wish to emphasize that while absence of SOC is necessary to keep conduction and valence bands completely degenerate along the DNL, TiRhAs maintains its nontrivial $\mathbb{Z}_2$ indices even with SOC[96].

Finally, we check the DFT-PBE band structure upon several isovalent substitutions for TiRhAs, specifically TiCoAs, TiRhP and ZrRhAs. We start with the optimized lattice parameters of TiRhAs and relax these substituted structures within the *Pmnb* space group. The resulting lattice parameters in all three cases deviate from the starting values by 0.4Å at most. The band structures are qualitatively identical to TiRhAs; in particular, they all have a DNL in the $k_x = 0$ plane. This implies that as long as the valence electron count is preserved, partial or full isovalent substitution may be attempted in order to reduce or enhance the effect of SOC.

## 4.4 $\mathbf{k} \cdot \mathbf{p}$ analysis of band velocities

A detailed analysis of band velocities at various points along the DNL (where the band velocity $v_{n\mathbf{k}}$ is given by $\frac{1}{\hbar}\frac{\partial E_{n\mathbf{k}}}{\partial \mathbf{k}}$ at the crossing point of interest), is crucial for understanding

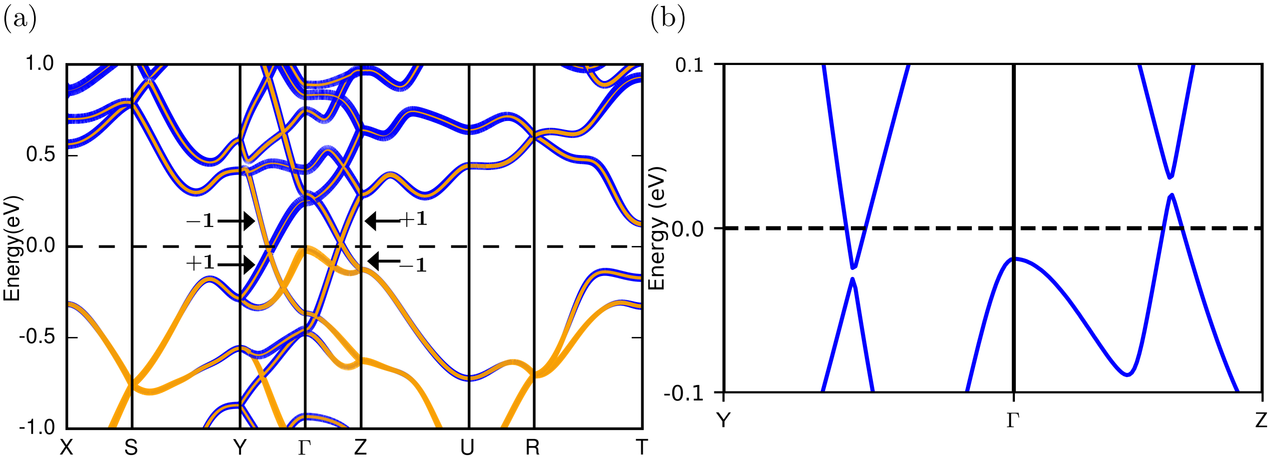

Figure 4.2: (a)DFT-PBE band structure without SOC. The projection of the bands onto Ti $d$ orbitals is shown in blue, and the projection onto Rh $d$ orbitals is shown in orange. The widths of the lines are proportional to the values. The mirror eigenvalues ±1 of the crossing bands are also indicated. (b)DFT-PBE band structure with SOC included, indicating that SOC opens a small gap due to hybridization of bands with like mirror eigenvalues.

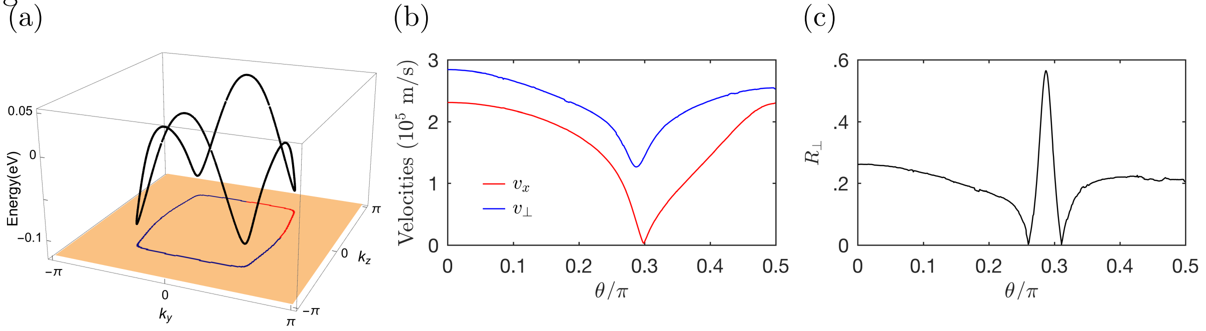

Figure 4.3: (a) DFT-PBE calculations of the DNL in TiRhAs in the $k_x = 0$ plane, with the irreducible quadrant highlighted in red. (b) $v_\perp$ and $v_x$ as a function of $\theta$. (c) Ratio of tilting magnitude to isotropic velocity, $R_\perp$, along the $v_\perp$ direction as a function of $\theta$.

transport experiments. We employ a $\mathbf{k}\cdot\mathbf{p}$ analysis to ascertain the symmetry constraints in TiRhAs that determine the $\mathbf{k}$-dependent band velocities along the nodal line. The generators of the space group $Pmnb$ are two mutually perpendicular two-fold screw axes and inversion $\mathcal{P}$. Since TiAsRh is nonmagnetic, $\mathcal{T}$ is also a symmetry as discussed above. The Bloch Dirac Hamiltonian (without SOC) may be expanded around any point $\mathbf{k}$ on the DNL as

$$\mathcal{H}(\mathbf{k}+\delta\mathbf{k}) = E(\mathbf{k}) + h^i_\mu(\mathbf{k})\sigma^\mu\delta k_i + \mathcal{O}(\delta\mathbf{k}^2), \tag{4.3}$$

where $\delta\mathbf{k} = (\delta k_x, \delta k_y, \delta k_z)$ is the deviation from a point $\mathbf{k}$ in the Brillouin zone, $\sigma^\mu$ are the Pauli matrices with $\mu \in 0, 1, 2, 3$ and $i \in x, y, z$ and $h^i_\mu(\mathbf{k})$ are real, $\mathbf{k}$-dependent coefficients.

We now restrict our discussion to the $k_x = 0$ plane in which the DNL lies. For a generic point on this plane the only remaining space group symmetry is the mirror symmetry $\mathcal{R}_x$. The product of inversion and time reversal, $\mathcal{PT}$, is also a symmetry. If we choose the two crossing bands with $+1$ and $-1$ $\mathcal{R}_x$ eigenvalues as pseudospin up and down, respectively, the symmetries for the nodal line may be expressed as

$$\mathcal{R}_x = \sigma^3; \mathcal{PT} = \sigma^0 K, \tag{4.4}$$

where $K$ denotes complex conjugation. These symmetries place constraints on the allowed $h^i_\mu(\mathbf{k})$;

$$\mathcal{R}_x \mathcal{H}(k_x, k_y, k_z)\mathcal{R}_x^{-1} = \mathcal{H}(-k_x, k_y, k_z) \tag{4.5}$$

and

$$(\mathcal{PT})\mathcal{H}(k_x, k_y, k_z)(\mathcal{PT})^{-1} = \mathcal{H}(k_x, k_y, k_z). \tag{4.6}$$

It follows from Equations 4.5 and 4.6 that the only nonzero $h^i_\mu(\mathbf{k})$ values are $h_0^{y,z}(\mathbf{k})$, $h_3^{y,z}(\mathbf{k})$, and $h_1^x(\mathbf{k})$. The band dispersion at each point $\mathbf{k}$ on the nodal line can then be expressed as

$$\delta E_{\mathbf{k}+\delta\mathbf{k}} \approx h_0^y(\mathbf{k})\delta k_y + h_0^z(\mathbf{k})\delta k_z \pm \sqrt{(h_3^y(\mathbf{k})\delta k_y + h_3^z(\mathbf{k})\delta k_z)^2 + (h_1^x(\mathbf{k})\delta k_x)^2}, \tag{4.7}$$

where $\delta E_{\mathbf{k}+\delta\mathbf{k}} = E_{\mathbf{k}+\delta\mathbf{k}} - E_{\mathbf{k}}$.

We fit Equation 4.7 to our DFT calculations at each point on the nodal line in the irreducible quadrant of the BZ. The coefficients outside the square root, $h_0^y(\mathbf{k})$ and $h_0^z(\mathbf{k})$, are symmetry-allowed "tilting" terms which characterize the tilting of the Dirac cone along $k_y$ and $k_z$ respectively [179, 29, 195]. The terms inside the square root can be written as $\sum_{i,j=1}^{3} \mathcal{A}_{ij}\delta k_i \delta k_j$ where $\mathcal{A}_{ij}$ is a real symmetric matrix. The square root of the eigenvalues of $\mathcal{A}$ correspond to the principle components of $v_{n\mathbf{k}}$ when the tilt terms are neglected, i.e the splitting of the Dirac cone; they are $(0, \sqrt{(h_3^y(\mathbf{k}))^2 + (h_3^z(\mathbf{k}))^2}, h_1^x(\mathbf{k})) \propto (v_\parallel(\mathbf{k}), v_\perp(\mathbf{k}), v_x(\mathbf{k}))$, where $v_\parallel$ is tangential to the DNL, $v_\perp$ is perpendicular to the DNL in the $k_x = 0$ plane, and $v_x$ is along $k_x$. The zero $v_\parallel$ corresponds to the "soft" direction where the dispersion scales at least as $\mathcal{O}(\delta\mathbf{k}^2)$. We parametrize points along the DNL by the polar angle $\theta = \tan^{-1} k_z/k_y$, and plot $v_\perp$ and $v_x$ as a function of $\theta$ in Figure 4.3b. As shown, our computed DFT-PBE $v_\perp$ is between $1.2 - 2.8 \times 10^5$ m/s, on the same order of magnitude as reported values for $\mathrm{Na_3Bi}$ and $\mathrm{Cd_3As_2}$ [118, 113]. $v_x$ is computed to be smaller at all $\theta$ and more anisotropic, between $3 \times 10^3$ and $2.3 \times 10^5$ m/s.

From an experimental perspective, while both tilt and relative magnitudes of the velocities given by $\mathcal{A}$ affect directional dependence of conductance in transport experiments, tilt also has an effect on the Fano factor (the ratio of shot noise to current) [195]; thus, quantitative characterization is important. The relative degree of tilting at the point $\mathbf{k}$ on the DNL in the direction $(\delta k_x, \delta k_y, \delta k_z)$ is given by the ratio of the magnitude of the tilting to the magnitude of the "isotropic" velocity, which for TiRhAs is

$$R = \frac{|h_0^y(\mathbf{k})\delta k_y + h_0^z(\mathbf{k})\delta k_z|}{|(h_3^y(\mathbf{k})\delta k_y + h_3^z(\mathbf{k})\delta k_z)^2 + (h_1^x(\mathbf{k})\delta k_x)^2|}. \tag{4.8}$$

Values greater than 1 indicate a switch in the sign of the the dispersion, analogous to the the type-II Weyl semimetals [179]. For concreteness, we choose the direction $(0, h_3^y(\mathbf{k})/h_3^z(\mathbf{k}), 1)$ parallel to $v_\perp$ and plot $R_\perp$ as a function of $\theta$ in Figure 4.3c. We see that amount of tilting along $v_\perp$ varies greatly, ranging from nearly 0 to .56 at $\frac{\theta}{\pi} \approx 0.3$, at the same point where $v_\perp$ has a prominent dip.

## $\mathbb{Z}_2$ invariant

In order to confirm the topological nature of TiRhAs and its robustness, we calculate $\mathbb{Z}_2$ invariants analogous to those used to characterize three-dimensional topological insulators (TIs) for systems with inversion symmetry as formulated by Fu and Kane[55]. The authors showed that in a compound with $\mathcal{P}$ and $\mathcal{T}$ symmetries (and SOC which drives the topological gapping), the topological invariants $(\nu_0; \nu_1\nu_2\nu_3)$ can be computed via the parity eigenvalues $\epsilon_n$ of the occupied Bloch states at the eight time-reversal invariant momenta (TRIM) in the 3D BZ, defined by $\Gamma_i = (n_1\mathbf{b}_1 + n_2\mathbf{b}_2 + n_3\mathbf{b}_3)/2$, where $n_j = 0, 1$ and the $\mathbf{b}$ denote the primitive reciprocal lattice vectors. Defining $\epsilon_i = \prod_{n_{occ}} \epsilon_n(\Gamma_i)$, i.e. the product of the parity eigenvalues of all occupied bands at the TRIM point $\Gamma_i$, the "strong" topological index $\nu_0$ is given by

$$(-1)^{\nu_0} = \prod_{i=1}^{8} \epsilon_i, \tag{4.9}$$

where the product is over the eight TRIM points. The "weak" indices $\nu_{1,2,3}$ are given by products of four $\epsilon_i$ which lie in the same plane:

$$(-1)^{\nu_{1,2,3}} = \prod_{n_i=1; n_{j\neq i}=0,1} \epsilon_{i=n_1n_2n_3}. \tag{4.10}$$

$\nu_0 = 1$ indicates that the TI is topologically nontrivial. One can imagine slowly turning off the SOC, thereby closing the bulk gap. At the critical point between a topological and trivial insulator, the gap closes and a DNL forms, hosting the same topological indices as the TI. Moreover, Kim et al. [96] showed that one can determine the number of DNLs intersecting any of the six invariant surfaces $S_{abcd}$ bounded by the four TRIM $a, b, c$ and $d$ by multiplying the $\epsilon_i$ at those four points:

$$(-1)^{N(S_{abcd})} = \epsilon_a\epsilon_b\epsilon_c\epsilon_d. \tag{4.11}$$

If the product is $-1$, $N(S_{abcd}) = 1$ and an odd number of DNLs must pierce $S_{abcd}$. For the trivial case $N(S_{abcd}) = 0$ an even (including zero) number of DNLs pierce the surface.

Using wavefunctions calculated with WIEN2k, we determine the parity eigenvalues at the eight TRIM in TiRhAs (a table is given in the supplementary material). The only TRIM point with $\epsilon_i = -1$ is $\Gamma$. Thus from Equations 4.9 and 4.10 we see that the topological indices for TiRhAs are $(\nu_0; \nu_1\nu_2\nu_3) = (1; 000)$, and that TiRhAs is topologically robust. Additionally, the parities imply that the three invariant surfaces containing $\Gamma$, namely $k_x = 0$, $k_y = 0$, and $k_z = 0$, are intersected by an odd number of DNLs, whereas the surfaces on the edge of

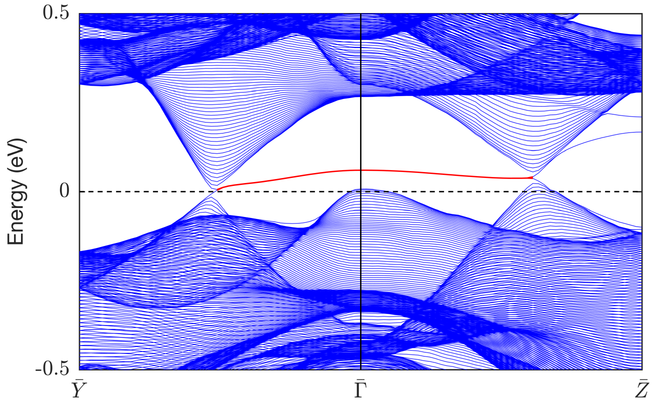

Figure 4.4: DFT-PBE tight-binding band structure (without SOC) for the (100) surface plotted along the $\bar{Y} - \bar{\Gamma} - \bar{Z}$ direction, showing surface states (colored red) in the projected interior of the DNL.

the BZ are intersected by an even number of DNLs. This is completely consistent with our finding of the single DNL lying in the $k_x = 0$ plane surrounding $\Gamma$.

## 4.5 Topological surface states

Topologically robust nodal lines are predicted to host nearly flat, two dimensional drumhead surface states [30]. To study the surface states in TiRhAs we construct a tight-binding model from our DFT-PBE calculations using maximally localized Wannier functions (MLWFs) [137, 143] as our basis states. We use 40 MLWFs derived from Ti $d$ and Rh $d$ bands around the Fermi level using a disentanglement procedure implemented in the open-source code Wannier90. [180] Our model for a 100 unit cell thick slab in the [100] direction is plotted for the (100) surface in Figure 4.4. Large slabs are required to recover the bulk DNL in our calculations. Since our tight-binding model has two identical surfaces we see two completely degenerate surface states in the interior of the projected nodal line. The states have a slight dispersion due to the particle-hole asymmetry [224].

We also construct a tight-binding model for the case where SOC is included. Because the effect of SOC is very slight in TiRhAs, the qualitative band structure is very similar to Figure 4.4. However, since SOC introduces a continuous gap in the DNL the surface spectrum evolves from a nearly flat, drumhead state to a very shallow Dirac cone characteristic of TIs (see Appendix 4.8).

## 4.6 Conclusion

In summary we have performed extensive first-principles calculations on the previously synthesized compound TiRhAs and identify it as a new Dirac nodal line semimetal. The nodal

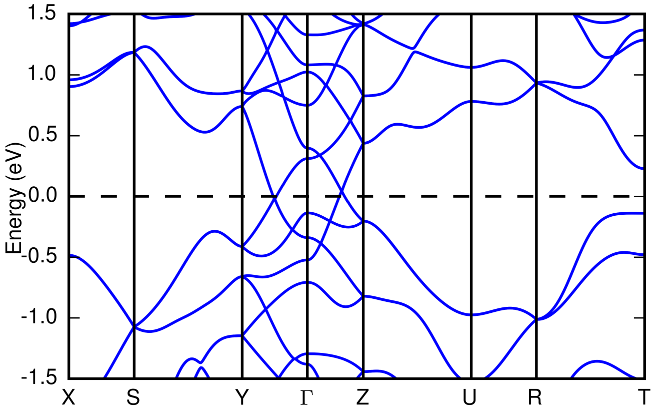

Figure 4.5: TiRhAs band structure computed using the HSE06 hybrid functional method.

line is topologically protected by both reflection symmetry and composite inversion and time-reversal symmetry; hence TiRhAs is particularly robust to local crystalline defects. We have performed a $\mathbf{k} \cdot \mathbf{p}$ analysis to determine the magnitude and tilting of band velocities along the DNL. We have calculated the $\mathbb{Z}_2$ invariants and have confirmed the presence of drumhead surface states. Moreover, the Fermi surface in TiRhAs is remarkably clean, and although SOC introduces gaps in the DNL, the effect is small. We therefore believe that further experimental studies on this compound should yield results consistent with our calculations.

## 4.7 Appendix I: HSE06 band structures

As mentioned in the main text, GGA is expected to overestimate the inversion of conduction and valence bands necessary for a nodal line compound [199]. To confirm our prediction of TiRhAs as a DNL system we repeat our bulk calculations using the hybrid density functional HSE06, which uses a fraction of screened Hartree-Fock (HF) exchange to correct for self-energy errors inherent in GGA [73]. Our energy cutoff and reciprocal grid are identical to our GGA parameters (300 eV and $8 \times 6 \times 6$ respectively). The result is shown in Figure 4.5, confirming that the DNL persists and is not a false positive of the GGA functional. HSE06 yields an even more attractive result than GGA in terms of experimental implications. While the GGA band structure is overall free from trivial bands near the Fermi surface, there is one band located at Γ which is almost exactly at $E_f$. Such a feature is potentially problematic because it makes experimental probing and manipulation of the DNL itself difficult, an issue explicitly mentioned for the recent example of synthesized $PbTaSe_2$ [150]. However, we see in Figure 6.9 that the HSE06 functional pushes this band down away from the DNL, suggesting that experimental studies of the topological properties in TiAsRh should be relatively straightforward to implement and interpret.

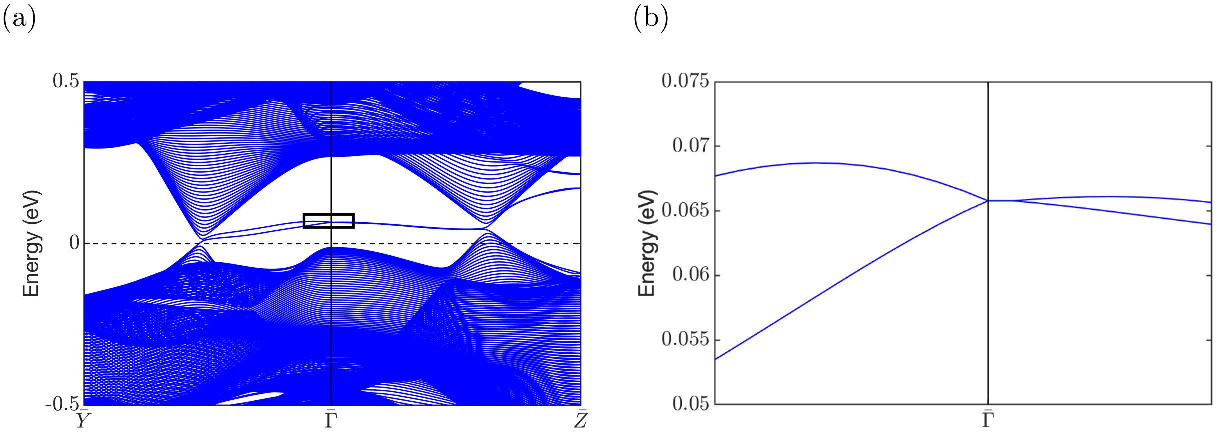

Figure 4.6: (a)DFT-PBE-SOC tight-binding band structure for the (100) surface plotted along the $\bar{Y}-\bar{\Gamma}-\bar{Z}$ direction. Note that the flat, drumhead states on the two surfaces shown in the main text without SOC have evolved into a shallow Dirac cone, characteristic of a TI. (b) Zoomed-in plot of the portion of (a) bordered by the rectangle.

## 4.8 Appendix II: Surface states with SOC

With the inclusion of SOC, the DNL in TiRhAs develops a continuous gap. The compound with SOC has topological indices $(\nu_0;\nu_1,\nu_2\nu_3) = (1;000)$, equivalent to those for the DNL compound with no SOC. To study the effect of SOC on the surface spectrum we construct a tight-binding model from DFT-PBE-SOC calculations, again using MLWFs as our basis states. The band structure along the $\bar{Y}-\bar{\Gamma}-\bar{Z}$ direction is plotted in Figure 4.6a. Overall the band structure is nearly identical to the case with no SOC as in Figure 4 of the main text. This is not surprising given that the gap induced by SOC is very small. However, the key difference is that the nearly flat, completely degenerate drumhead states on the two surfaces of the DNL compound without SOC have evolved into an extremely shallow Dirac cone at $\Gamma$, characteristic of a topological insulator (TI) with band inversion at $\Gamma$ [232]. The two branches of the cone from $\bar{\Gamma}-\bar{Z}$ are very nearly degenerate; we provide a zoomed-in plot around $\Gamma$ in Figure 4.6b. The surface state does not cross the Fermi level, unlike the general case for a TI, merely because the DNL without SOC is not pinned to the Fermi energy, and thus the gap, upon inclusion of SOC, does not cut through the Fermi level everywhere in the BZ.

# Chapter 5

# Fermi-crossing Type-II Dirac fermions and topological surface states in $\mathrm{NiTe_2}$

The material was previously published as

- Saumya Mukherjee, SungWon Jung, Sophie F. Weber et al., *Fermi-crossing Type-II Dirac fermions and topological surface states in* $\mathrm{NiTe_2}$, Scientific Reports **10**, 12957 (2020).

ARPES experiments were performed by collaborators using methods described in Section 9.2 in this chapter.

## 5.1 Introduction

Topologically protected electronic states hold great promise for the development of next-generation electronic and spintronic devices [147, 141, 26]. For topological insulators (TI), such as the well-known case of Bi2Se3 [71], the carriers associated with the topologically-protected surface states have the unique properties of spin-momentum locking and suppression of backscattering, making the surfaces of such TIs highly attractive platform for spin-transport applications. In the case of topological semimetals, topologically protected crossings occur in the bulk band structure, leading to the formation of bulk Dirac points. In the vicinity of these points, the electronic bands cross linearly, opening up the potential for carriers with ultrahigh-mobility, such as are found in $Cd_3As_2$ [149].

The class of transition metal dichalcogenides (TMDs), already well-known for hosting an array of correlated electronic phenomena, has recently been identified as a materials system which also hosts topologically-protected states [37, 12, 81, 217, 36, 135]. Density functional theory (DFT) calculations for a wide range of compounds predict a set of bulk Dirac points and band inversions (associated with topological surface states, TSS), as the chalcogen orbital symmetries combined with a natural hierarchy of energy scales ensure that these states exist rather generically. However, the energies at which they occur is not guaranteed by any physical constraint, and many are predicted to exist in the unoccupied states, where they are hard to verify experimentally. On the other hand, topological states below the Fermi level ($E_F$) can be readily verified and scrutinized by angular resolved photoemission spectroscopy (ARPES) and spin-ARPES. When these states lie at high binding energies however, they do not affect the transport properties, limiting any potential applications.

Given that TMDs are being increasingly incorporated into device structures [191, 188, 16, 163, 234, 35], it is highly desirable to identify a candidate material whose transport properties might be predominantly derived from topologically protected states. An intriguing candidate in this regard is $NiTe_2$. Recent transport measurements have confirmed a substantial magnetoresistance effect, the response becoming large and linear in magnetic field, a characteristic feature of topological semimetals [215]. The Berry phase of the observed quantum oscillations is close to $\pi$, often interpreted as a signature of the contribution of a topologically non-trivial state. Moreover, DFT calculations have suggested that one of the bulk Dirac points of $NiTe_2$ may indeed lie much closer to the Fermi level than in other members of the family where the equivalent states are much further away and thus less relevant to transport (or superconductivity) [37]. These calculations strongly motivate an experimental survey of the electronic structure of $NiTe_2$ using ARPES.

In this chapter, we demonstrate with a combination of ARPES and comprehensive DFT calculations that the band structure of $NiTe_2$ shows the formation of type-II Dirac fermions near the Fermi level and a set of spin polarised topological surface states. A Fermi surface consisting of electron pockets associated with type-II Dirac fermions and topological surface states is predicted. The band crossing leading to type-II Dirac fermions is dominated by Te p-orbitals, consistent with the mechanism of band inversion from the chalcogen p-orbital manifold shown in other TMDs [37, 12]. Our ARPES study shows the formation of electron pockets hosting Dirac carriers at the Fermi level. Topological surface states observed through ARPES agree well with our DFT calculations. One of the surface states is found to intersect the Fermi level, forming electron pockets. The measured Fermi surface map matches well with our calculations and the observation of electron pockets implies finite contribution of Dirac and surface carriers to the transport properties.

## 5.2 Methods

### ARPES measurements

High quality single crystals of NiTe$_2$ were grown by chemical vapour transport as discussed elsewhere [215]. We used the high-resolution vacuum ultraviolet (VUV) ARPES branch of I05 beam line at Diamond Light Source, UK [58]. The samples were cleaved at 10 K, in ultra-high vacuum chamber of I05. Linear horizontal and vertical polarization of photon at energies between $h\nu = 20$ and 120 eV is used. The inner potential $V_0 = 16$ eV of NiTe$_2$ is determined from the $k_z$ dispersion from photon-energy-dependent ARPES studies using a free electron final state model. We want to point out that the final state induced matrix element effect can lead to suppression of the spectral intensity. This might give an impression of asymmetric spectra in the experimental data.

### First principle calculations

Our calculations were performed within density functional theory (DFT) with room-temperature lattice parameters (details on lattice parameters is discussed elsewhere [215]. We employ the Vienna ab-initio simulation package (VASP) [103] with generalized gradient approximation (GGA) using the Perdew-Burke-Ernzerhof (PBE) functional [157] and projector augmented-wave (PAW) method [21]. We treat 3p, 3d, and 4s, and 5s and 5p electrons as valence for Ni and Te, respectively. We use an energy cut off of 550 eV for our plane-wave basis set, with a Γ-centred k-point mesh of 14x14x14 for the primitive unit cell. For surface state features, we perform full self-consistent DFT calculations using a Te-terminated supercell with a slab of ten primitive unit cells of NiTe$_2$ stacked along the [001] direction, with 15 Å of vacuum. We conducted calculations with U-parameter related to Ni-d orbitals and found that the best agreement with experimental data occurs at U = 0. Here, we do not show DFT calculations using GGA + U $\neq$ 0, since they fail to improve the agreement with the experimental data.

## 5.3 Results and discussion

In what follows, we adopt the tight-binding-based analysis introduced in Refs [37, 12] for understanding the band structure of NiTe$_2$, which is distinct from previously known cases of isovalent and isostructural transition-metal dichalcogenides TMX$_2$ (TM = Pd, Pt; X = Te, Se). Our tight-binding model incorporates two chalcogen sites (Fig 5.1a), and captures the manner in which the chalcogenide p orbital manifold develops into dispersive bands which generically possess topological characteristics: bulk Dirac points, inverted band gaps (IBGs), and topologically protected surface states (TSS).

In $\mathrm{NiTe_2}$, the triply degenerate energy levels of the Te $\mathrm{p_{x,y,z}}$-orbitals split into $\mathrm{p_z}$ (upper-state) and $\mathrm{p_{x,y}}$ (lower-state) manifolds due to crystal-field splitting (CFS) (Fig. 5.1c). Additionally, spin-orbit coupling (SOC) causes the $\mathrm{p_{x,y}}$ orbitals to split into singlets ($R_{4'}$ and $R_{5,6}$ levels) and modifies the energetic separation between $\mathrm{p_z}$ and $\mathrm{p_{x,y}}$. The $\mathrm{p_z}$ orbital transforms according to the irreducible representation (IREP) $R_4$ [12]. The two Te sites in the unit cell imply that the p-orbitals are split into bonding (B) and antibonding (AB) levels at the $\mathbf{\Gamma}$ ($\mathbf{k} = (0,0,0)$) and the $\mathbf{A}$ ($\mathbf{k} = (0,0,\pi/c)$)-points of the Brillouin zone [12, 36]. Symmetry wise, the p-bands associated with B and AB levels at $\mathbf{\Gamma}$ and $\mathbf{A}$ points transform as the IREPs of the double space groups $\bar{\mathbf{\Gamma}}_8$ ($\bar{\mathbf{A}}_8$), $\bar{\mathbf{\Gamma}}_4\bar{\mathbf{\Gamma}}_5$ ($\bar{\mathbf{A}}_4\bar{\mathbf{A}}_5$) and $\bar{\mathbf{\Gamma}}_9$ ($\bar{\mathbf{A}}_9$) [11, 10]. Because of the phase introduced, the B-AB splitting of the $\mathrm{p_z}$-states decreases from the $\mathbf{\Gamma}$ to the $\mathbf{A}$ point [188]. This induces strong $k_z$ dispersion and a large bandwidth for $\mathrm{p_z}$-derived bands as compared to planar $\mathrm{p_{x,y}}$ orbitals. For TMDs, the approximation of $\mathrm{p_z}$-derived bands having larger bandwidth is valid considering the expected large inter-layer-hopping ($t_3$, $t_4$ in Fig. 5.1a) along the c-axis for $\mathrm{p_z}$ states as compared to the $\mathrm{p_{x,y}}$ states.

When the bandwidth of $\mathrm{p_z}$-derived states become greater than the combination of CFS and SOC, a crossing between the $\mathrm{p_z}$ and$\mathrm{p_{x/y}}$ states occurs as a function of $k_z$, resulting in band inversion. The states formed due to the B-AB splitting of p-orbitals pick up even (+) or odd (-) parity since the Te-atom sites at the $\mathbf{\Gamma}$ and $\mathbf{A}$ points are located across the crystal inversion point. Therefore, $k_z$-dispersion of a single orbital (p) manifold leads to band parity inversion. Fig. 1c, shows the symmetry correspondence between IREPs of the double group at the $\mathbf{\Gamma}$ and $\mathbf{A}$ point, and along the $\Delta$ symmetry line for all the $\mathbf{k} = (0,0,k_z)$ points with $0 < k_z < \pi/c$. A crossing between $R_{4'}$ (±) and $R_4$ (∓) causes hybridization as seen from the identical IREP, $\bar{\Delta}_6$ , for these two levels along the $\Delta$ point. This leads to a parity inverted band gap (IBG) (See Fig. 5.1c). In addition, the opposite parity of $R_{4'}$ (±) and $R_4$ (∓) suggests that the IBG will have a $\mathcal{Z}_2$ topological order and are capable of hosting topological surface states [12]. On the other hand, $R_4$ (±) and $R_{5,6}$ (±) have different symmetry properties along the $\Delta$ line, as they transform differently under 3-fold rotation. This allows band crossing between and and leads to the formation of the bulk Dirac points (BDPs) along the $k_z$ direction (valid for $0 < k_z < \pi/c$). The location of the BDP in k-space is determined by the band width of $R_4$ (±)-derived bands and the strength of CFS.

The discussion above is based on symmetry, yielding a generic and phenomenological viewpoint. To obtain a more quantitative prediction of the location of the expected bulk Dirac points and IBGs, we turn to ab-initio DFT calculations. Our calculated band structure showing band dispersion and the orbital character of bands is shown in Fig. 5.2a. The density of states (DoS) confirms that the bands close to the Fermi level, $E_F$, are dominated by Te p-orbitals. Ni d-orbital derived bands appear away from the Fermi level at $E - E_F \sim -2$ eV (Fig. 5.2b). The $\mathrm{p_{x/y}}$ bands show significantly stronger dispersion along the in-plane high symmetry directions $\mathbf{\Gamma}(\mathbf{A})$-$\mathbf{M}$ ($\mathbf{L}$) and $\mathbf{\Gamma}(\mathbf{A})$-$\mathbf{K}$ ($\mathbf{H}$), compared to the out-of-plane $\mathbf{\Gamma}$-$\mathbf{A}$ direction. However, consistent with the tight-binding analysis, the $\mathrm{p_z}$ bands have a large dispersion along **Γ**-**A** with wide band width and cross the $\mathrm{p_{x/y}}$ bands as a function of $k_z$.

Our DFT calculations indicate several important differences between $\mathrm{NiTe_2}$ and the other $\mathrm{TMX_2}$ compounds. Weakly dispersive bands of predominantly d-character are found at $E - E_F \sim -2$ eV (Fig. 5.2a, c). The location of these bands is almost 1.5 eV closer to the Fermi level compared to $\mathrm{PdTe_2}$, a significant difference on replacing Pd with Ni. In addition, at K close to the Fermi level ($E - E_F \sim 0$ to $-250$ meV), the electron pockets are predominantly formed by bands derived from d-orbitals.

The large shift of TM-derived bands towards the Fermi level in $\mathrm{NiTe_2}$ increases the hybridization between Ni-d and the Te-p bands. For example, the crossing of Te $\mathrm{p_z}$ and $\mathrm{p_{x,y}}$ bands occurs near the **A** point around $E - E_F \sim -1$ eV, but the $\mathrm{p_z}$ bands in this energy range show a significant hybridization with Ni d-orbitals, unlike in other $\mathrm{TMX_2}$ compounds. However, this hybridization does not disrupt the universal mechanism of formation of the inverted band gaps, Dirac fermions and topological surface states in $\mathrm{TMX_2}$. A type-I bulk Dirac point (BDP-I) appears at $E - E_F \sim 1.5$ eV, which is followed by a type-II protected bulk Dirac point (BDP-II) at $E - E_F \sim 76$ meV and $k_z = 0.36c^*$ ($c^* = 2\pi/c$). The bands forming the BDP-II are labelled as 1 and 2 (Fig. 5.2d). These bands cross $E_F$ and form electron pockets. This type-II Dirac fermion has been found in other $\mathrm{TMX_2}$; however, the proximity of BDP-II to the Fermi level is unique to $\mathrm{NiTe_2}$ [37, 12, 81, 217, 36, 215]. In $\mathrm{NiTe_2}$, the location of BDP-II in momentum space is slightly closer to **A**-point than $\mathrm{PtTe_2}$ ($k_z = 0.346c^*$) but further away from **A** than in $\mathrm{PdTe_2}$ ($k_z = 0.40c^*$) [12, 217, 36, 48]. This implies that the strength of CFS and bandwidth of $R_4$ (±) derived bands is intermediate between $\mathrm{PtTe_2}$ and $\mathrm{PdTe_2}$. From the calculated band structure we found that close to BDP-II, the $\mathrm{p_z}$ derived bands form inverted band gap IBG-I at $E - E_F \sim -0.65$ eV (smaller gap $\sim 200$ meV), which is accompanied by IBG-II at $E - E_F \sim -1.5$ eV (larger gap $\sim 1$ eV). We want to point out that the inverted band gaps (IBGs) at the **A**-point have inverted parity, implying the existence of topological states.

With these predictions in hand, we now turn to the experimental measurements of the bulk and surface electronic structure of $\mathrm{NiTe_2}$. First, we focus on tracking the BDP-II and surface states along **Γ**-**A** using photon-energy-dependent ARPES and measure the occupied states below the Fermi level (Fig. 2e). The band features are broadened due to the finite $k_z$ resolution of photoemission but the states are in good agreement with calculated bulk bands. Both IBGs, near Fermi level ($E - E_F \sim -0.65$ eV) and away from it ($E - E_F \sim -1.5$ eV) are found. The BDP-II lying above the Fermi level is not accessible by ARPES, but the bands 1 and 2 forming the BDP-II are observed at the **A**-point ($k_z = \pi/c$). Interestingly, a non-dispersive two-dimensional band is found at $E - E_F \sim -1.35$ eV close to **A**-point which does not match any calculated bulk band (marked in Fig. 5.2e).

To better understand the band structure, we compared the experimental and calculated in-plane band dispersion along **A**-**L** and **A**-**H** in Fig. 5.3. The bulk bands show good agreement with bulk DFT calculations (Fig. 5.3a, b, d, e). Our DFT slab calculations (see Methods for details) show a set of surface states which match well with the experimental data (Fig. 5.3 c,f). The non-dispersive feature at $E - E_F \sim -1.35$ eV is reproduced as one of the surface states by the slab calculations. We assign the surface state as TSS2. At the **A**-point, TSS2 forms sharp and intense bands. This feature threads through the IBG-II and connects the time-reversal invariant momentum (TRIM) points (here **A**,**L**, **H**). TSS2 represents a topological non-trivial band but lies far away from the Fermi level.

Slightly closer to the Fermi level, our DFT calculations show a topological surface state at $E - E_F \sim -0.65$ eV within the band gap IBG-I. This is named as TSS1 and lies within the manifold of bulk bands. TSS1 experiences strong interaction with the bulk states and is classified as a surface resonance state. In ARPES spectra, we observe weak spectral intensity of TSS1 at **A**, which matches well with the calculations (Fig. 5.3 a, c). However, the mixing of TSS1 with bulk bands makes it difficult to resolve.

At the Fermi level, a surface state is visible in our DFT surface band structure along **A**-**L** (Fig. 5.3c). This is assigned as TSS0, which shows a large spin splitting of around 120 meV and lies between $E - E_F \sim 0$ to $-200$ meV. TSS0 is not present along **A**-**H** (Fig. 3f). Experimentally, TSS0 is found between **A** and **L** with in-plane momentum $k_\parallel \sim 0.5$ (Å)$^{-1}$. TSS0 is formed from two parabolic-like upper (labelled as $\epsilon$) and lower ($\gamma$) branches which intersect $E_F$ and form electron pockets (see Fig. 5.4a).

The $k_z$ -dependence of the electronic states spanning over a wide photon energy range ($h\nu = 20 - 120$ eV) shows that TSS0 is non-dispersive along **Γ**-**A** (Fig. 5.4b). This confirms that TSS0 is two-dimensional. The vicinity of TSS0 to $E_F$ in $\mathrm{NiTe_2}$ makes it unique compared to other surface states and implies finite contribution of topological surface carriers to the non-trivial transport properties. All topological surface states found previously in other $\mathrm{TMX_2}$ are also found in $\mathrm{NiTe_2}$ [37, 12, 81, 217, 36], but notably TSS0 is absent in $\mathrm{PtSe_2}$.

To complete our studies, we map the Fermi surface of $\mathrm{NiTe_2}$ using photon energy tuned to the **A**-point ($h\nu = 23$ eV) (Fig. 5.4c). It is found that the Fermi surface is formed by TSS0 and the bulk bands crossing the Fermi level. The $\epsilon$ and $\gamma$ bands of TSS0 are identified. These bands form electron pockets at the Fermi level. The pockets formed by $\epsilon$ are more circular than the pockets of the $\gamma$ band. Identical to $\mathrm{PdTe_2}$, these bands form arc-like features and imply small projected bulk band gaps. At the **A**-point, band 2 forms an electron pocket (labelled as $\alpha$) and the projected bulk bands form a hexagonal shape. We show that the calculated bulk Fermi surface agrees well with the experimental data (see Inset of Fig. 5.4c).

To identify the topological character of the surface states, the associated spin texture is calculated as shown in Fig. 4d, e. In our description, the x- and y-axis are along **A**-**L** and **A**-**H**, respectively. TSS2 has a chiral spin texture in the x-y plane with finite $\langle S_x \rangle$ and $\langle S_y \rangle$ components. Negligible $\langle S_z \rangle$ component is found. The strong interaction with bulk bands for TSS1 limits the estimation of spin polarization, and we do not include polarization for TSS1. The electron pockets formed by TSS0 along **L**-**A**-**L** (indicated in Fig. 5.4c) are well separated from the bulk and hence it is possible to resolve spin texture here. We find that TSS0 has non-zero spin component solely along the y-direction $\langle S_y \rangle$, which is normal to the **A**-**L** direction. The branches of TSS0, $\epsilon$ and $\gamma$, show opposite spin polarization. We want to point out that the spin-split branches of the surface state TSS0 close to the Fermi level are connected to the conduction band and the valence band separately, which highlights the topological non-trivial character [17]. For completeness, we include spin polarization for TSS0 along the entire and paths, but note that the only location where the surface character has not significantly hybridized with bulk is at the electron pockets, so calculated spin texture at all other locations does not accurately represent surface state spin texture of TSS0.

## 5.4 Conclusion

We have shown that $\mathrm{NiTe}_2$ exhibits topological surface states and bulk type-II Dirac points, which are derived solely from the Te 5p orbitals, consistent with the generic band inversion mechanism for transition metal dichalcogenides. However, the choice of Ni as the transition metal leads to 3d states significantly closer to the Fermi level compared with (Pd, Pt)(Se, Te)2, allowing additional d-p hybridizations which tune the bulk Dirac point very close to $E_F$. The band dispersions away from this BDP-II, which form the alpha electron pocket, thus have a topologically non-trivial character, likely to explain the non-trivial Berry phase of a small electron-like pocket observed in transport studies [215]. We have also shown that $\mathrm{NiTe}_2$ harbours a unique topological surface state, TSS0, with one of the largest spin-splitting of up to 120 meV reported for any Fermi-crossing surface state of a transition metal dichalcogenide. For future studies, an exciting approach would be to exfoliate individual monolayers or grow very thin films of $\mathrm{NiTe}_2$, with a significantly increased contribution of these topological surface carriers to the transport properties. Thus both the surface and bulk electronic structures of this material are candidates for engineering novel spintronics devices underpinned by a robust and generic topological mechanism.

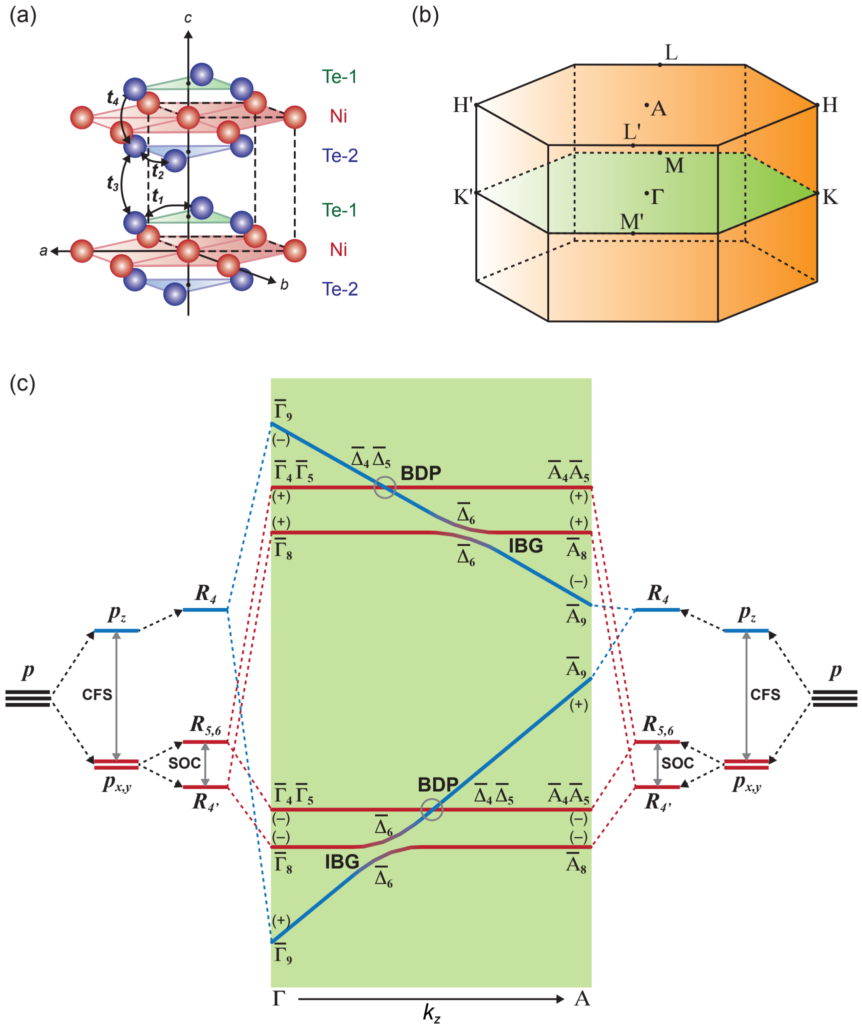

Figure 5.1: (a) Crystal structure of 1T-NiTe$_2$ (space group: $P-3m1$), composed of hexagonal basal planes (ab-planes) of Ni-atom (red sphere) coordinated to the Ni-atom at the centre and triangular layers with inequivalent Te atomic site (blue sphere) above (Te -1) and below (Te -2) the basal plane along the (001)-direction [18]. The hopping parameters between 2-site Te p-orbitals are categorized as intra-layer hopping ($t_1 = t_2$), interlayer hopping ($t_3$) within the unit cell and between two unit cells (t4). (b) Brillouin zone. (c) Hierarchy of p-orbital derived energy levels at $\mathbf{\Gamma}$ and $\mathbf{A}$-point showing the inverted band gaps (IBG), Dirac points (BDP: circled) and topological states. The symmetry of the states are labelled with IREPs ($\mathbf{\Gamma}_i$, $\mathbf{A}_j$, $\mathbf{\Delta}_k$) and parity (+/-). Inspired from Ref. [12, 36]. Figure made using Adobe Illustrator [1].

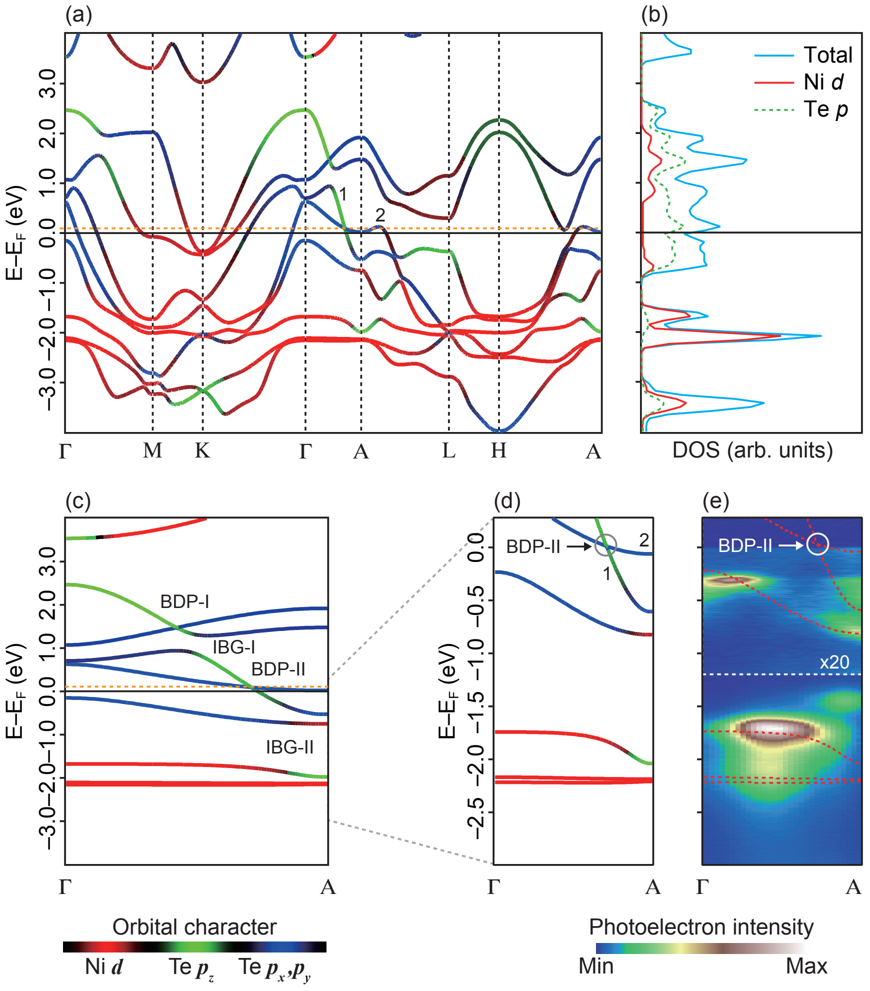

Figure 5.2: (a) Electronic DFT bulk band structures with orbital character of bands. Type-II Dirac fermion formed by crossing of band 1 and 2 near Fermi level. (b) Density of states (DoS) showing dominant contribution of Te p-bands at the Fermi Level compared to Ni d-bands. Above Fermi level, the DoS spectra is scaled up by factor of 2. (c) Band dispersion along the **Γ**-**A** direction with inverted band gaps (IBG) and bulk Dirac points (BDP) marked, (d) and (e) Zoomed-in dispersion and measured photon-energy dispersion with linear horizontal polarization along the **Γ**-**A** direction. A non-dispersive feature is marked with an arrow, which does not match with bulk DFT calculation. Figures made using Igor [151] and Adobe Illustrator [1].

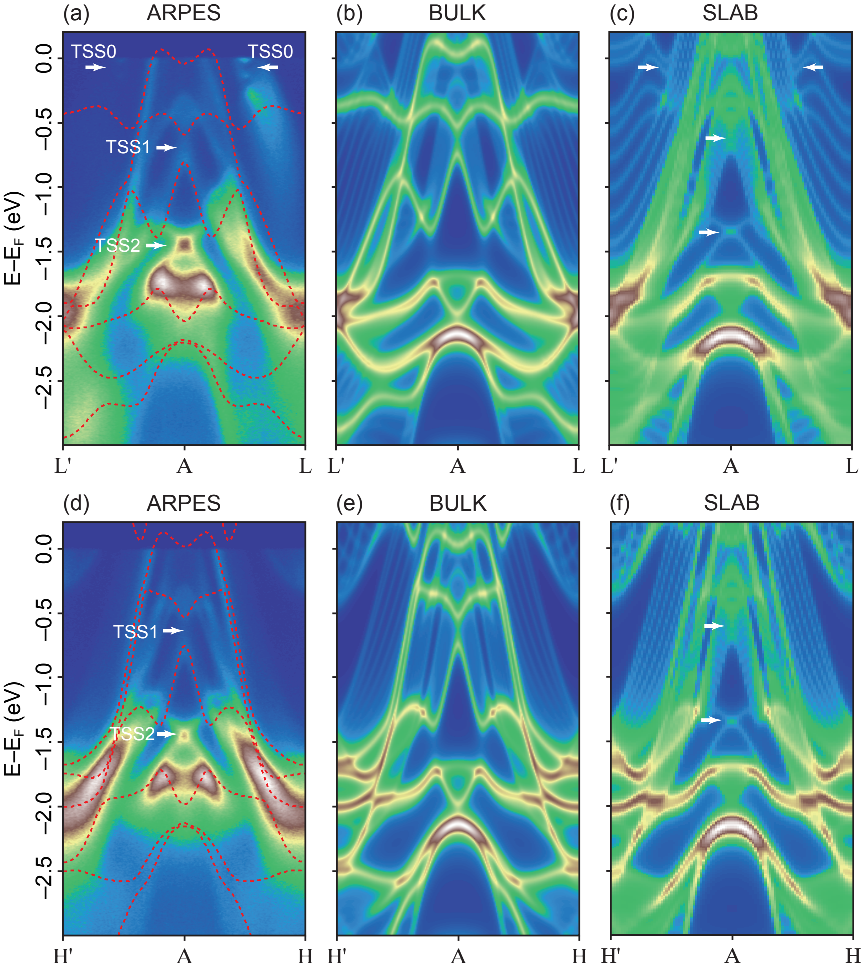

Figure 5.3: Spectral band dispersion along in-plane **L′-A-L** (a-c) and **H′-A-H** (d-e) direction, probed with photon energy $h\nu = 99$ eV (a) experimental ARPES data with linear horizontal polarization, supercell calculation integrated along $k_z$ with (b) bulk DFT and (c) slab surface. Arrows mark the position of the topological surface states (TSS). The overlaid dotted red lines in (a, d) represent the calculated bulk DFT bands. Figures made using Igor [151] and Adobe Illustrator [1].

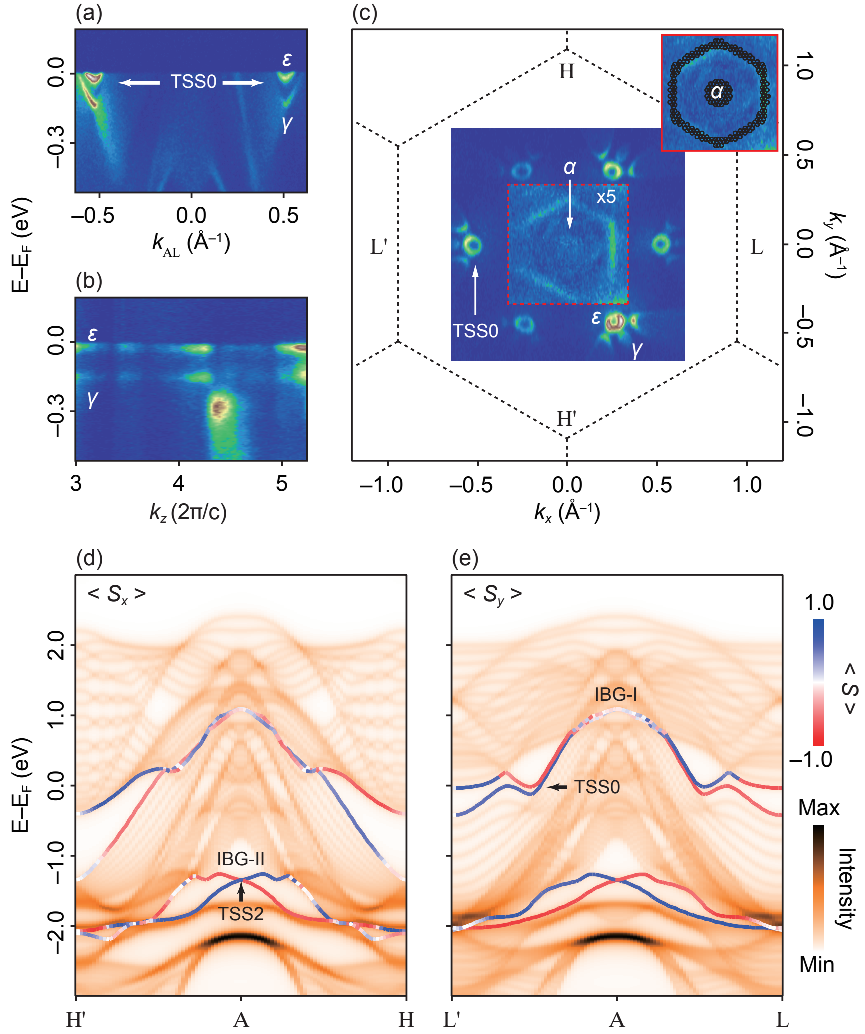

Figure 5.4: (a) In-plane dispersion of TSS0 forming electron pockets labelled as $\epsilon$ and $\gamma$ and (b) the non-dispersive behaviour of TSS0 surface state close to the Fermi level in the photon-energy dependence. (c) Fermi surface measured with horizontal polarization of light and photon energy, $h\nu = 23$ eV, which corresponds to the **A**-plane. The region under the red dotted box is magnified by a factor of 5 to show the electron pockets $\alpha$ (Band 2), $\epsilon$ and $\gamma$ (TSS0) and the bulk bands. (Inset: calculated bulk Fermi surface consisting of the circular $\alpha$ electron pocket and bands forming hexagonal contour, in good agreement with measured data). (d) and (e) Slab calculation with projected spin components of the topological surface states. TSS2 shows finite $\langle S_x \rangle$ and $\langle S_y \rangle$ components normal to **H′-A-H** and **L′-A-L** direction, respectively. TSS0 has finite spin component $\langle S_y \rangle$ normal to **L′-A-L** (note that TSS0 is hybridized with bulk in all other regions of the plots, so no further conclusions about surface state spin texture can be made). Figures made using Igor [151] and Adobe Illustrator [1].

# Chapter 6

# Topological semimetal features in the multiferroic hexagonal manganites

The material was previously published as

- Sophie F. Weber, Sinéad M. Griffin, and Jeffrey B. Neaton, *Topological semimetal features in the multiferroic hexagonal manganites*, Physical Review Materials **3**, 064206 (2019).

## 6.1 Introduction

Since their discovery in 1963[15], the hexagonal manganites ($R\mathrm{MnO}_3$, $R = \mathrm{Sc}, \mathrm{Y}, \mathrm{In}, \mathrm{Dy}-\mathrm{Lu}$) have attracted great interest by virtue of their combined magnetic and ferroelectric order. The hexagonal manganites undergo an improper ferroelectric transition from a centrosymmetric $P6_3/mmc$ [194] phase to the polar $P6_3cm$ [185] structure ($P\bar{3}c1$ for $\mathrm{InMnO}_3$[78]) at around 1000K; they develop a noncollinear antiferromagnetic ground state at much lower temperatures (for example in $\mathrm{YMnO}_3$, magnetic ordering sets in around  80K[84]). Multiferroic materials such as the hexagonal manganites are interesting for both basic research and for technology due to the possibility for controlling multiple order parameters (via, for example, temperature, magnetic field, or strain) within a single material[181].

Another class of systems of current interest are topological materials, which include, more recently, topological semimetals (TSMs)[208, 145]. TSMs exhibit band crossings protected by crystalline and other symmetries. The nodes in TSMs can be either zero-dimensional, as in the case of Dirac and Weyl semimetals[216, 124, 203, 210, 117, 118, 205], or they can form a closed one-dimensional ring, which occurs for nodal line (NL) semimetals[76, 19, 18, 150, 224]. As a consequence of their nontrivial topological character, these three broad categories of TSMs host a wide variety of exotic phenomena including ultrahigh mobility, the chiral anomaly, giant magnetoresistance, and unusual surface states, such as Fermi arcs in Weyl semimetals and two-dimensional 'drumhead' states in NLs[112, 156].

The remarkable properties of TSMs and multiferroic materials have sparked interest in compounds that combine the two properties, i.e. multiferroic systems that are also TSMs in either their high-symmetry nonpolar or low-symmetry polar phases[193, 111, 225]. Such compounds can potentially be switched between topological and trivial electronic structure by application of an external field or by tuning temperature through the ferroelectric transition, and they also provide an excellent platform for studying the interplay between the topology, ferroelectricity, and magnetism.

There are several arguments for investigating the hexagonal manganite structure as a possible platform for combining multiferroic and TSM properties. First, the synthesis of hexagonal manganites is well-developed both in bulk and in ultrathin epitaxial film form. For example, $R\mathrm{MnO}_3$-type compounds that have an orthorhombic ground state have been grown in the metastable hexagonal structure, primarily via epitaxial stabilization on a hexagonal lattice[62]. Second, hexagonal manganites are known to exhibit real-space topological defects in their ferroelectric $P6_3cm$ state, which manifest as adjacent domains of opposite polarization directions, with the vortex phase remaining in the nonpolar $P6_3/mmc$ space group at low temperature[79]. Such nontrivial real-space topology existing concomitantly with reciprocal-space topological order, i.e the TSM phase, would provide an unprecedented opportunity to explore the interaction between such types of topology.

While the prototypical hexagonal manganite $\mathrm{YMnO}_3$ is insulating in both polar and nonpolar phases with its ground state antiferromagnetic (AFM) order, the band structure can be significantly altered by stabilizing ferromagnetic (FM) order. FM order can be achieved, for example, by application of a magnetic field, or by substituting other transition metal

(TM) ions for $Mn^{3+}$ to alter the balance in the competition between in-plane noncollinear AFM order and slight out-of-plane canting which has been observed in the hexagonal manganites[178].

In this work, we undertake a first-principles study of the electronic band structure and its topology in compounds isostructural to $YMnO_3$ with FM ordering. Specifically, in addition to $YMnO_3$, we investigate four other compounds in which the $Mn^{3+}$ cation has been substituted with $V^{3+}$, $Cr^{3+}$, $Fe^{3+}$ and $Co^{3+}$ in order to shift the Fermi level systematically. We predict that nonpolar hexagonal manganites $YVO_3$ and $YCrO_3$ have band crossings very close to the Fermi level, and in fact feature topological nodal lines in the $k_z = 0$ plane that are protected by a mirror symmetry. We also predict that they should undergo a ferroelectric (FE) $P6_3/mmc \rightarrow P6_3cm$ transition characteristic of the traditional $R\mathrm{MnO}_3$ compounds. Stabilizing this set of compounds in the hexagonal structure should hence provide new opportunities for studying the interaction between topological and multiferroic order.

## 6.2 Methodology

For our first-principles density functional theory (DFT) calculations, we employ the Vienna *ab intitio* simulation package (VASP)[103] with generalized gradient approximation (GGA) using the Perdew-Burke-Ernzerhof (PBE) functional[157] and projector augmented-wave (PAW) method[21]. We treat $4s, 4p, 5s$ and $4d$, and $2s$ and $2p$ electrons explicitly as valence for Y and O, respectively. For the five transition metals V-Co, we include $3p$ as well as the valence $d$ and $s$ electrons. To account for the localized nature of the $d$ electrons in the transition metal cations, we add a Hubbard U correction (GGA+U)[159]. We apply the rotationally invariant version of GGA+U by Dudarev et al.[45], and for ease of comparison we choose a $U$ of 3 eV for all elements, a value consistent with previous literature[107] (see supplementary material for further discussion of our GGA+U calculations). We use an energy cutoff of 800 eV for our plane wave basis set, with a Gamma-centered **k**-point mesh of $16 \times 16 \times 6$ for the 10-atom nonpolar unit cell and $8 \times 8 \times 6$ for the 30-atom polar unit cell. Starting from the structures in the Materials Project database[89], we relax lattice parameters and internal coordinates for all structures until forces on the atoms are less than 0.001 eV/Å. We use collinear spin-polarized calculations to account for the finite magnetic moments of the transition metal (TM) ions. We do not include spin-orbit coupling (SOC) unless explicitly stated. When relevant, we approximate the noncollinear AFM order inherent to the hexagonal manganites[51] with a collinear G-type AFM ordering (GAFM), consisting of a two up, one down (one up, two down) pattern in a given 30-atom supercell for the upper (lower) basal plane[235] (see Figure 6.1b). Finally, for all topological analysis we use a tight-binding model constructed from our DFT-GGA+U calculations using maximally localized Wannier functions (MLWFs)[137, 143] as our basis states. For the surface state plots and surface polarization calculation we use the WannierTools software[213] which takes the tight-binding model as input. Finally, to assess dynamical stability of the $YXO_3$ compounds in their hexagonal form, we perform first-principles phonon calculations. The details of the computations as well as the results are described in Appendix 6.8.

## 6.3 Nonpolar $P6_3/mmc$ Crystal Structure and Energetics

To begin, we focus on the centrosymmetric, nonpolar crystal structure of the hexagonal manganites in the $P6_3/mmc$ space group. This $YXO_3$ ($X = V, Cr, Mn, Fe$ and Co) structure is shown in Figure 6.1a ($YCrO_3$ is chosen as the example). The primitive cell consists of two TM atoms, two yttrium atoms, and six oxygen atoms. The TM ions $X^{3+}$ are five-fold coordinated by oxygen $O^{2-}$, forming trigonal bipyramids, and they lie in the $z = \frac{1}{4}$ and $z = \frac{3}{4}$ planes. The yttrium $Y^{3+}$ ions are sandwiched between, in the $z = 0$ and $z = \frac{1}{2}$ planes.

While all of our subsequent calculations are performed assuming FM order, we also perform relaxations using the GAFM configuration in order to examine the relative energies of the two magnetic states. We note that at the high temperatures for which the nonpolar $P6_3/mmc$ space group is naturally favored over the polar $P6_3cm$ space group, the structure is paramagnetic. However, it may be possible to stabilize the nonpolar structure at low temperatures, for example by alloying or introducing defects[65]. The results of our calculations for both orderings are given in Table 6.1. To date, the only crystal in Table 6.1 which has been synthesized in bulk $P6_3/mmc$ structure is $YMnO_3$, with reported lattice parameters $a = 3.61$ Å and $c = 11.39$ Å[122]. Comparing this to our relaxed FM GGA+U results of $a = 3.617$ Å and $c = 11.366$ Å suggests that our GGA+U calculations will be good predictors of experimental lattice constants of the other four compounds.

We also report energy differences between FM and GAFM orderings in Table 6.1. These values may be viewed as a guide since the frustrated collinear GAFM order is an approximation to that of noncollinear AFM. Nonetheless, comparison with collinear GAFM should be useful for predicting the relative ease of stabilizing the FM state in these compounds, for example by application of a magnetic or electric field[121]. Specifically, FM ordering becomes more stable relative to GAFM the further to the left we move on the periodic table, so achieving FM order should be most feasible in the $V^{3+}$ and $Cr^{3+}$ compounds. Note that when GAFM is enforced, for X = Cr-Co the relaxed O-X-O bond angle between apical and in-plane oxygen atoms differs by less than 0.5° from the ideal 90°. However, in the case of $YVO_3$ the enforced magnetic frustration results in non-uniform magnetic moments on the inequivalent V atoms, leading to a large and unrealistic distortion of the bond angles by as much as 15°. Including SOC and allowing $YVO_3$ to relax to the noncollinear AFM should remove this artifact, but to be consistent with the other compounds in Table 6.1 we include our results for the collinear GAFM structure; the parameters and energetics for $YVO_3$ with this enforced magnetic order relative to the other four compounds should be interpreted with appropriate caution.

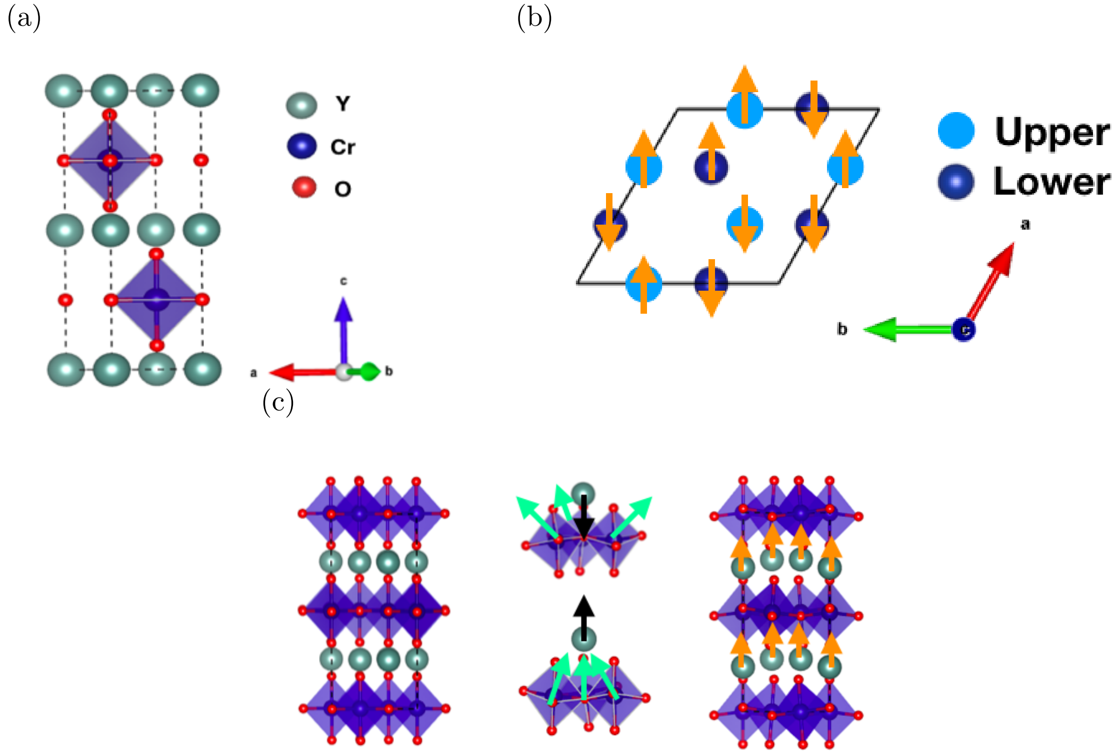

Figure 6.1: (a) Primitive cell for nonpolar hexagonal $YCrO_3$, with centrosymmetric space group $P6_3/mmc$ [194]. The primitive cell consists of two Y atoms (green), two Cr atoms (blue), and six O atoms (red) (the structures of all other compounds studied in this paper are qualitatively identical). (b) Depiction of the GAFM in-plane magnetic ordering which we use as a collinear approximation to the true noncollinear antiferromagnetism in the hexagonal manganites. Note that the 10-atom $P6_3/mmc$ primitive cell is tripled to accommodate this ordering. (c) Depiction of the nonpolar-to-polar structural transition in the hexagonal manganites. Left panel: Nonpolar centrosymmetric space group $P6_3/mmc$ (primitive cell tripled for easier comparison to polar phase). Middle panel: Action of the unstable $q = (1/3, 1/3, 0)$ $K_3$ phonon on the $XO_5$ trigonal bipyramids. Outward trimerization pulls the $Y$ ions downwards (top), whereas inward trimerization forces the $Y$ ions upwards (bottom). Right panel: Polar $P6_3cm$ space group. The $K_3$ phonon couples to a secondary order parameter, the zone-centered $\Gamma_2^-$ mode (upward arrows), which further shifts the $Y$ ions in the $\hat{z}$ direction and causes net polarization in the unit cell.

Table 6.1: Lattice constants (for the primitive 10-atom unit cell), energy per formula unit (f.u) for FM and collinear GAFM ordering, and $\Delta E = E_{FM} - E_{GAFM}$ for $YXO_3$ in the $P6_3/mmc$ space group after full optimization with GGA+U. As mentioned in the main text, the inherent frustration of the GAFM ordering on a triangular lattice has a strong effect on the bond angles of $YVO_3$. We include the relaxed GAFM result for completeness but with the caveat that the distortion may be unphysical.

| | $YVO_3$ | $YCrO_3$ | $YMnO_3$ | $YFeO_3$ | $YCoO_3$ |
|---|---|---|---|---|---|
| FM | | | | | |
| $a$ (Å) | 3.496 | 3.510 | 3.617 | 3.566 | 3.640 |
| $c$ (Å) | 12.382 | 12.041 | 11.366 | 11.762 | 11.193 |
| E/f.u (eV) | −42.366 | −42.242 | −42.188 | −40.223 | −37.218 |
| GAFM | | | | | |
| $a$ (Å) | 3.561* | 3.525 | 3.609 | 3.548 | 3.608 |
| $c$ (Å) | 11.912 | 12.010 | 11.359 | 11.798 | 11.272 |
| E/f.u (eV) | −42.341 | −42.062 | −42.182 | −40.407 | −37.512 |
| $\Delta E$ (eV) | −0.025 | −0.180 | −0.006 | +0.184 | +0.294 |

## 6.4 Semimetal Features in Ferromagnetic Band Structures

In Figure 6.2 we present the GGA+U band structures for the $P6_3/mmc$ $YXO_3$ compounds in the FM configuration in the absence of SOC (see supplementary material for GAFM band structures). Because they dominate the states near the Fermi level, we focus on the spin up bands and plot their orbital-projected character. (The spin down bands are included with dashed black lines and without orbital projection.) The spin up bands near the Fermi level are composed almost exclusively of transition metal X $d$ states and O $p$ states. Going from left to right across the $3d$ elements, we observe a simultaneous upwards shift of the Fermi level and a lowering in energy of the X $d$ states toward the O $p$ states, leading to greatest hybridization for $YFeO_3$. In $YVO_3$ and $YCrO_3$, the uppermost $d$ states have started to invert energies with the lower states of mixed $d$ and $p$ character; in particular, for both we compute a band inversion centered at the $K$ point $(\frac{1}{3}, \frac{1}{3}, 0)$ with linear nodes to the left and right, boxed in red (upon further inspection the apparent inversion at $H$ is actually an anticrossing). For $YVO_3$, the crossings at $K$ are about 80 meV above Fermi level, whereas for $YCrO_3$ they are about 300 meV below.

We note that GGA+U Kohn-Sham eigenvalues can only approximate single-particle excitations and band structure. Therefore it is reasonable to question whether for GGA+U, and specifically for $U = 3$ eV, our approach to computing the band structure near the Fermi energy, specifically the band inversions responsible for the nodes in $YVO_3$ and $YCrO_3$, will be predictive. Based on prior calculations for similar oxide systems with V and Cr in the same $3^+$ oxidation state, a $U$ of 3 eV can lead to band structures that nearly reproduce

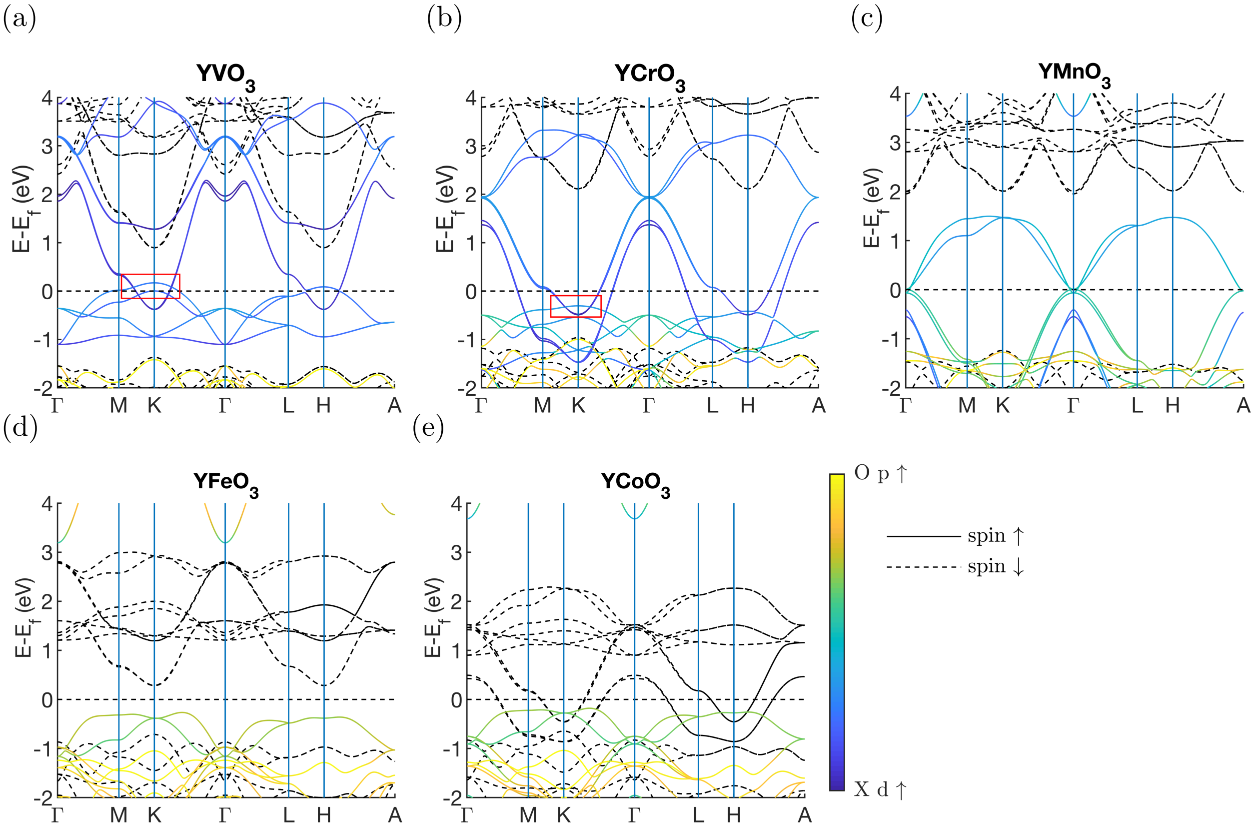

Figure 6.2: Orbital-projected DFT-GGA+U ($U = 3$ eV) band structures for spin up bands in the ferromagnetic $P6_3/mmc$ YXO$_3$ compounds (X = V − Co), with spin down bands included without projections. The bands near the Fermi energy are composed of X $d$ states (where X is the relevant transition metal ion) and O $p$ states, with negligible Y character. Color scale varies from dark blue for purely X $d$ character to yellow for purely O $p$ character. The Fermi level is marked by the dashed black line. Panels (a)-(e) correspond to YVO$_3$, YCrO$_3$, YMnO$_3$, YFeO$_3$, and YCoO$_3$, respectively.

experimental gaps (see Appendix 6.9 for a detailed discussion). Thus, we have reason to expect our $U = 3$ eV calculations will be qualitatively accurate for the band inversions near the Fermi energy.

We now further analyze the band structure and topology of YVO$_3$ and YCrO$_3$. Orbital decompositions of the inverted bands reveals that the conduction bands are composed of mostly V/Cr $d_{xz}$ and $d_{yz}$ states whereas the valence bands are $d_{xy}$ and $d_{x^2-y^2}$ states. Plotting only these projections, it is clear that at $K$ the bands cross with no mixing whereas at the $(\frac{1}{3}, \frac{1}{3}, \frac{1}{2})$ $H$ point they hybridize, exchange character, and very slightly gap out (see Figures 6.3a and 6.3b). In both cases we find that the non-gapped crossings in fact form nodal lines (NLs) lying in the $k_z = 0$ plane, centered at $K$ and $K'$ (see Figure 6.3c).

The mirror plane symmetry $\mathcal{M}_z$ centered at $z = \frac{1}{4}$ is responsible for the protection of the

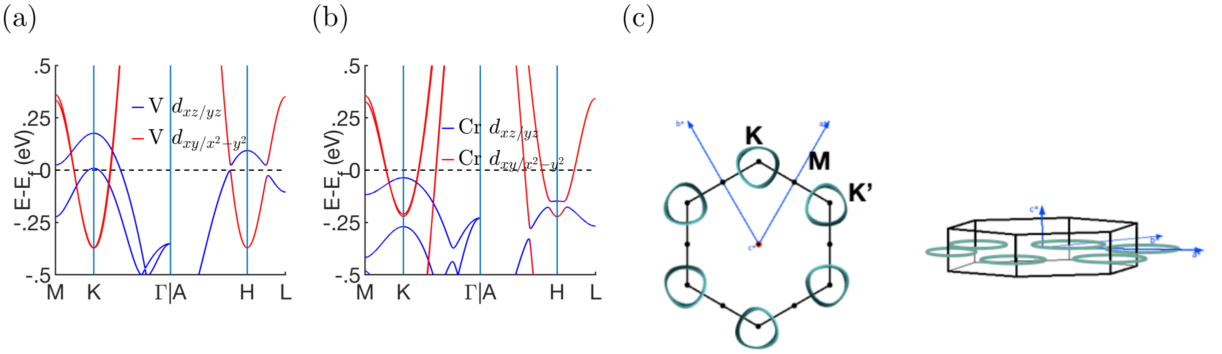

Figure 6.3: Analysis of band crossings in Figure 6.2. (a) and (b) show zoomed-in band structures of $YVO_3$ and $YCrO_3$ respectively about the $K$ and $H$ points, with the orbital character decomposed into planar ($d_{xy}/d_{x^2-y^2}$) and z-oriented ($d_{xz}/d_{yz}$) d states. (c) Isoenergy contours (specifically for $E = -0.38$ eV for $YCrO_3$) in the hexagonal 3D Brillouin zone.

NLs. (Note that with FM ordering and no SOC the magnetic space group is identical to the crystal space group $P6_3/mmc$). The action of $\mathcal{M}_z$ in reciprocal space is

$$\mathcal{M}_z : (k_x, k_y, k_z) \to (k_x, k_y, -k_z). \tag{6.1}$$

Thus $k_z = 0$ and $k_z = \frac{\pi}{c}$ planes are invariant under $\mathcal{M}_z$ and can be labeled by its eigenvalues, which are $\pm 1$ in the absence of SOC. If two bands with opposite mirror eigenvalues cross on one of these planes due to a band inversion, their crossing is symmetry-protected and they form a closed loop of Dirac nodes. This is the case for $K$ in the $k_z = 0$ plane. However, if the bands have the same eigenvalues they will mix and gap out[47], which occurs on the $k_z = \frac{\pi}{c}$ plane where $H$ lies. In the supplementary material we construct an explicit tight-binding model to calculate the $\mathcal{M}_z$ eigenvalues throughout the Brillouin zone and thus verify our observations.

Let us now consider what happens when we include spin-orbit coupling (SOC). With SOC, spin and orbital degrees of freedom are coupled and symmetry operators act on both Hilbert spaces simultaneously. Notably for us, a mirror plane symmetry becomes the combination of (a) a reflection of the spatial coordinates about the mirror plane, and (b) a $\pi$ rotation of the spin coordinates about the axis perpendicular to the mirror plane[210]. Thus, depending on the spatial orientation of the spins, a mirror plane symmetry may either be broken or preserved when SOC is taken into account. For our nonpolar hexagonal manganites, let us first examine the case where the spin orientation is along the [001] axis. In this example, the magnetic point group symmetry is reduced from $D_{6h}$ in the collinear case to $C_{6h}$. In $C_{6h}$, the total mirror symmetry is still preserved, since rotating the spins $180^o$ about the $z$ axis leaves them invariant; thus, the NL should still be protected in the $k_z = 0$ plane in this case. The only difference from the non-SOC case is the functional form of $\mathcal{M}_z$ due to the requirement that the operator must now be antiunitary, such that spin up (down) bands

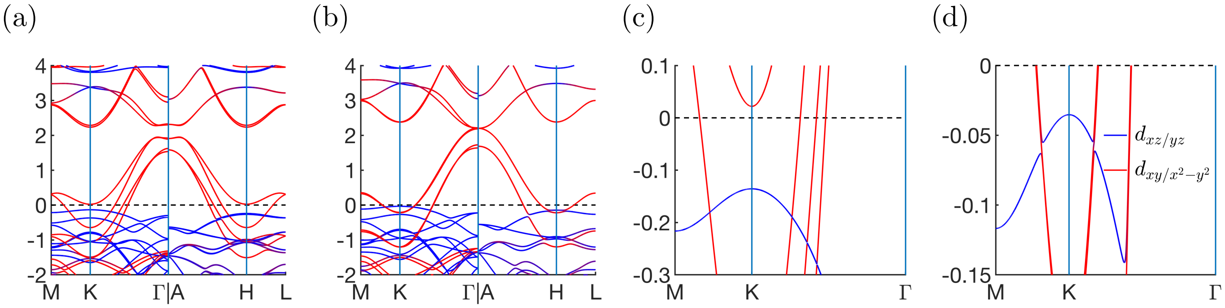

Figure 6.4: DFT-GGA+U band structures with SOC, using $YCrO_3$ as the example. Planar $d_{xy/x^2-y^2}$ character is plotted in red, while $d_{xz/yz}$ states are plotted in dark blue. (a) and (b) show full band structures with SOC included and spin quantization along the [001] and [100] directions respectively. (c) and (d) show the zoomed-in portions of (a) and (b) around the $K$ where the topological NLs are centered in the collinear spin case. In (c) the NL crossings are still robust with the [001] spin orientation, whereas a very small gap forms between one of the conduction bands and the valence band in (d) with [100] spin orientation, with the second conduction band passing through the gap.

pick up a factor of $+i$ $(-i)$ when acted on by $\mathcal{M}_z$ (we include a tight-binding model which incorporates SOC in addition to the collinear tight-binding models in our supplementary material). Taking the example of $YCrO_3$, we plot the band structure with SOC for [001] oriented spins in Figures 6.4a and 6.4c and as expected the crossings are still robust.

If we choose, on the other hand, to orient the spins such that they have a component perpendicular to the [001] axis, say in the [100] direction (the band structure with [100] oriented spins is plotted in Figures 6.4b and 6.4d), the magnetic point group is reduced to $C_{2h}$. Now the action of the mirror operator will still leave the orbital coordinates in the $k_z = 0$ plane unchanged, but it will send a spin with components $(s_x, s_y, s_z) = (1, 0, 0)$ to $(s_x, s_y, s_z) = (-1, 0, 0)$. Hence the mirror plane is no longer a symmetry of the crystal and generically the crossing bands can hybridize and gap out the NL. This is demonstrated in Figure 6.4d. From the orbital projection onto $d_{xy/x^2-y^2}$ and $d_{xz/yz}$ states one can clearly see the hybridization and gap between the valence band and one of the two near-degenerate conduction bands (the second conduction band passes through the gap).

Although magnetization along any axis other than [001] will break the mirror symmetry protecting the nodal line, it is possible for discrete points along high-symmetry directions to remain ungapped. Specifically, in cases of inversion-symmetric NL systems such as $YVO_3$ and $YCrO_3$, if the spins are orientated along an axis $\hat{n}$ in the $a-b$ plane with a two-fold rotational symmetry $C_2^n$, the points on the NL which intersect this axis are protected from hybridizing, and a pair of Weyl points can remain even though the rest of the NL becomes gapped[90, 210]. For the point group $D_{6h}$ there are six such axes: $C_2^{[100]}$, $C_2^{[010]}$, $C_2^{[110]}$, $C_2^{[1\bar{1}0]}$, $C_2^{[210]}$ and $C_2^{[120]}$. Thus, for the example in Figures 6.4b/6.4d in which the spins are oriented along [100], the $C_2^{[100]}$ rotational symmetry remains unbroken and we expect that Weyl points will remain along [100], while the rest of the line is gapped out, as seen along the $M-K-\Gamma$

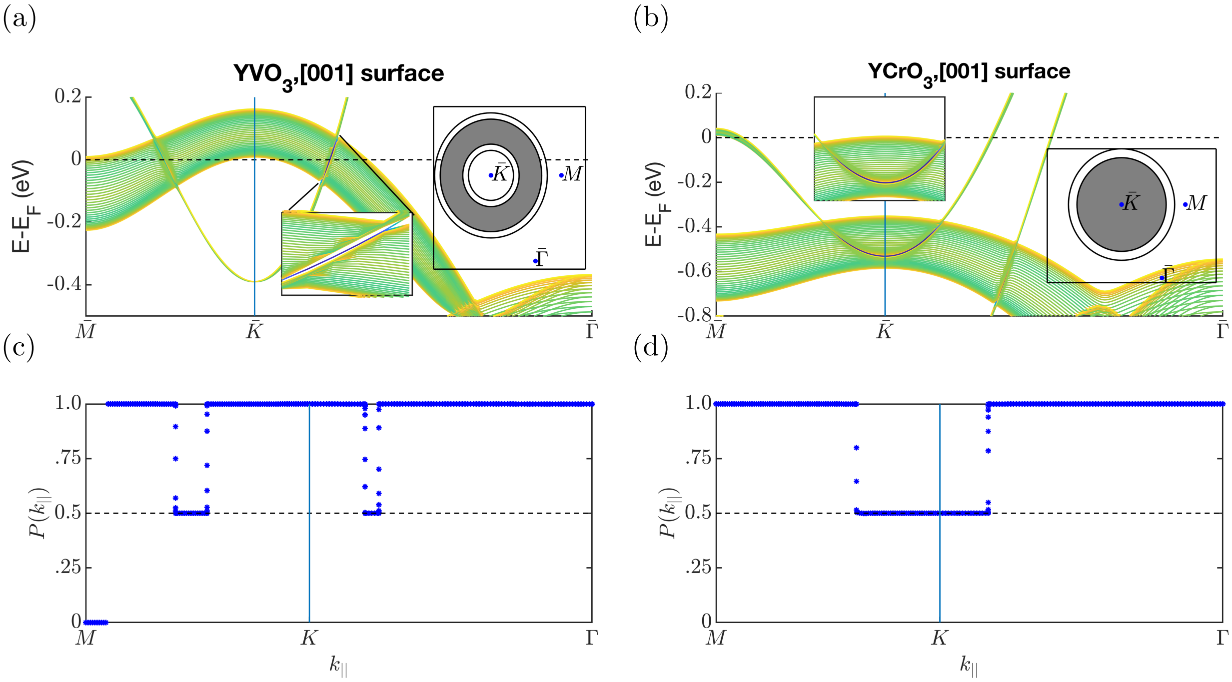

Figure 6.5: Projected band structures for the [001] surface in (a) YVO$_3$ and (b) YCrO$_3$ from slab geometries (see text). Color is proportional to weight of projection onto the outermost layers of the slab, with blue being highest weight. The discernible surface state is magnified in one inset for both cases. The insets with the shaded circles are cartoons depicting the boundaries of the NL pairs projected onto the [001] surface, with the region where surface states appear shaded in grey. Figures (c) and (d) show the [001] surface polarization charge $P(k_{||})$ for YVO$_3$ and YCrO$_3$ respectively along the same high-symmetry path as (a) and (b). Note that $P(k_{||})$ jumps to a nonzero value at the same momenta where the surface states are visible.

path in Figure 6.4d. Unfortunately, the existence of two nearly degenerate conduction bands makes detection of the Weyl points difficult.

Finally, we note that the magnetic anisotropy energy $E_{[001]} - E_{[100]}$ is very small ([100] oriented spin is lower in energy than [001] by 1.5 meV/f.u), implying that it should be feasible to switch between a robust and gapped nodal line within the nonpolar $P6_3/mmc$ space group by varying the direction of an external magnetic field.

## 6.5 Surface States

A hallmark feature of topological NLs is their two-dimensional "drumhead" surface states[30]. These surface states must terminate at the surface projection of the nodal line and they may lie either outside or inside the area subtended by the NL. Using our maximally localized Wannier functions (MLWFs), we construct a tight-binding slab model with 20 unit cells in the [001] direction. The 2D projected band structures on the [001] surface for $YVO_3$ and $YCrO_3$ are shown in Figures 6.5a and 6.5b, respectively. At the the $K$ point, the top valence band of $YCrO_3$ and top two valence bands of $YVO_3$ invert with the bottom two conduction bands which are very nearly degenerate for both compounds. Thus, one (two) pair(s) of NLs are actually projected onto on the [001] surface in the case of $YCrO_3$ and $YVO_3$, respectively, as depicted schematically in the figure insets. While in principle there is a single surface drumhead state associated with each bulk NL[19], the projected bulk from the multiple NLs interferes with the surface states, making detection difficult. However, by projecting the tight-binding wave functions onto the outermost cells in the slab we can make out a single surface state (dark blue) which has not hybridized with bulk. It is sandwiched between the pair of NLs in $YCrO_3$, whereas in $YVO_3$ it is visible only in the region between the two NL pairs (the corresponding regions are shaded in grey for the top-view cartoons of the [001] surface in Figures 6.5a and 6.5b).

We can infer physical meaning from the observable surface states by calculating a series of one-dimensional Berry phases at fixed momenta $\mathbf{k}_{\|}$ parallel to the the [001] surface, where the one-dimensional Berry phase $\theta$ at $\mathbf{k}_{\|} = (k_x, k_y)$ is defined by

$$\theta(\mathbf{k}_{\|}) = -i \sum_{E_n < E_F} \int_{-\pi}^{\pi} \langle u_n(\mathbf{k}) | \, \partial_{k_z} \, | u_n(\mathbf{k}) \rangle \, dk_z, \tag{6.2}$$

where $|u_n(\mathbf{k})\rangle$ is the cell-periodic part of the Bloch eigenstate $\psi_{\mathbf{k}}(r) = e^{i\mathbf{k}\cdot\mathbf{r}} u_{n,k}(r)$, and the sum over $n$ is over occupied states. It has been shown in previous work[198] that $\phi(\mathbf{k}_{\|})$ is related to the bound charge on a surface perpendicular to $\mathbf{k}_{\|}$. To be more explicit, the amount of surface polarization charge $P(k_{\|})$ at (provided the band structure is gapped at $\mathbf{k}_{\|}$) is given by

$$P(k_{\|}) = \frac{e}{2\pi} \theta(\mathbf{k}_{\|}), \tag{6.3}$$

modulo $e$, where $e$ is the electron charge. For the case of an NL semimetal, we can divide the $\mathbf{k}_{\|}$ into distinct regions of the surface Brillouin zone, with the [001] projections of the NLs acting as region borders. For $\mathcal{M}_z$ symmetric systems such as $YVO_3$ and $YCrO_3$, $\theta(\mathbf{k}_{\|})$ is quantized to either 0 or $\pi$ (and hence $P(k_{\|})$ is quantized to 0 or $\frac{1}{2}$) [30]. The NL boundaries are the only momenta at which $P(k_{\|})$ can switch values, since all gapped $\mathbf{k}_{\|}$ within a given boundary are topological indistinct. In fact, the $\mathbf{k}_{\|}$ at which the surface polarization charge becomes nonzero are exactly the momenta at which we expect the drumhead surface states to appear[30, 18, 74]. Using the hybrid Wannier charge center (WCC) method[19] we calculate $P(k_{\|})$ for momenta in the $k_z = 0$ plane along the $M - K - \Gamma$ path for $YVO_3$ and $YCrO_3$ in Figures 6.5c and 6.5d respectively. As we expect, the surface polarization is zero except at the momenta where we see the surface states, at which point it jumps to $\frac{1}{2}$.

## 6.6 Ferroelectric Instabilities of the $P6_3cm$ Structure

The topological NLs near the Fermi level occur in the high-symmetry $P6_3/mmc$ space group due to the combination of band inversion at $K$ and the $\mathcal{R}_z$ mirror symmetry. However, as mentioned previously the hexagonal manganites $\text{RMnO}_3$ are known to undergo a ferroelectric (FE) transition to the nonpolar $P6_3cm$ space group as the temperature is lowered[119]. Here we verify that the $\text{YXO}_3$ (X = V-Co) compounds in their metastable hexagonal structure also have a lower-energy $P6_3cm$ phase connected to the $P6_3/mmc$ topological semimetal phase through unstable phonon modes.

We first compute the energy per formula unit of the FM $P6_3cm$ polar structures and compare with our previously calculated energies for the FM $P6_3/mmc$ nonpolar structures. The GGA+U $\Delta E = E_{polar} - E_{nonpolar}$ is given in Table 6.2. For all five compounds the polar phase is lower in energy. Next, we decompose the atomic displacements involved in the distortion from the nonpolar to the polar phase into symmetry-adapted phonon modes using the AMPLIMODES software[155, 161] provided by the Bilbao Crystallographic Server. The primary structural order parameter responsible for the $P6_3/mmc \rightarrow P6_3cm$ transition in hexagonal manganites is the unit-cell tripling $K_3$ phonon mode at $q = (\frac{1}{3}, \frac{1}{3}, 0)$[119, 49]. As temperature is lowered this phonon can condense, leading to trimerizing tilts of the $\text{XO}_5$ trigonal bipyramids and a subsequent shifting either up or down of the Y ions, as shown in the middle panel of Figure 6.1c. At this point the $P6_3/mmc \rightarrow P6_3cm$ transition has already occurred, but there is no *net* polarization in the unit cell. The spontaneous polarization is caused by the coupling to $K_3$ of the zone-centered $\Gamma_2^-$ mode at $q = (0, 0, 0)$. $\Gamma_2^-$ causes an additional uniform shift of the Y ions in the $\hat{z}$ direction, resulting in non-zero polarization[64] (right panel of Figure 6.1c). Based on the relative amplitudes of the modes (given in Å) in the $P6_3cm$ structures relative to the parent $P6_3/mmc$ structures in Table 6.2, we can conclude that the FE transitions in the $\text{YXO}_3$ compounds of interest also exhibit the $K_3$ mode as their primary order parameter, with the distortion caused by the $\Gamma_2^-$ mode significantly smaller. Moreover, the $K_3$ distortion amplitudes are all modest in magnitude, roughly 1 Å, implying that the FE transition is realistic for these systems.

Finally, we briefly examine the band structures for the fully relaxed $P6_3cm$ compounds in Figure 6.6. In addition to the loss of inversion symmetry in the nonpolar-to-polar transition, the $\mathcal{R}_z$ symmetry protecting the NLs in the $P6_3/mmc$ space group is no longer a symmetry for $P6_3cm$. Thus, the topological NLs in $P6_3cm$ $\text{YVO}_3$ and $\text{YCrO}_3$ are necessarily absent. According to our band structure calculations, $\text{YCrO}_3$ becomes a trivial metal. $\text{YVO}_3$ on the other hand develops a 1 eV direct gap in Figure 6.6a. Since this would allow a tuning between a topological semimetal state and a trivial insulator by changing temperature, $\text{YVO}_3$ seems to be the most promising of the $\text{YXO}_3$ candidates for future studies.

Table 6.2: $\Delta E = E_{polar} - E_{nonpolar}$ and amplitudes of $K_3$ and $\Gamma_2^-$ modes of the polar $P6_3cm$ structure with respect to $P6_3/mmc$ parent structure. Note that all calculations here are with FM ordering.

| | $YVO_3$ | $YCrO_3$ | $YMnO_3$ | $YFeO_3$ | $YCoO_3$ |
|---|---|---|---|---|---|
| $\Delta E$ (eV) | $-0.354$ | $-0.075$ | $-0.100$ | $-0.103$ | $-0.358$ |
| $K_3$ (Å) | 1.056 | 0.958 | 0.971 | 1.030 | 1.026 |
| $\Gamma_2^-$ (Å) | 0.402 | 0.158 | 0.183 | 0.199 | 0.218 |

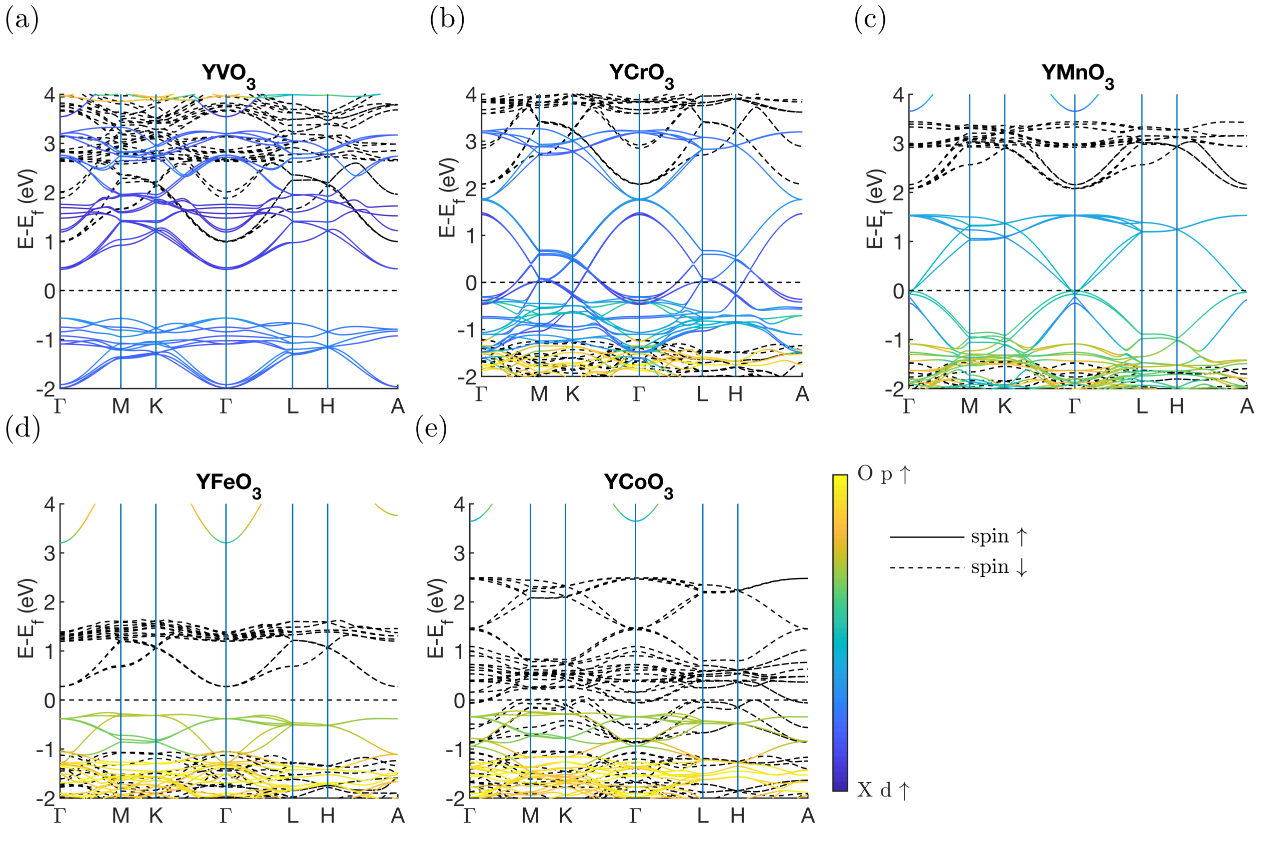

Figure 6.6: DFT-GGA+U band structures for the FM $YXO_3$ compounds (X=V-Co) in the polar $P6_3cm$ space group . For comparison to Figure 6.2, the spin-up bands are again projected onto the relevant atomic orbitals and the spin-down bands are plotted in dashed black. Panels (a)-(e) correspond to $YVO_3$, $YCrO_3$, $YMnO_3$, $YFeO_3$, and $YCoO_3$, respectively.

## 6.7 Conclusion

In summary we have performed extensive first-principles calculations on five $YXO_3$ (X=V-Co) compounds isostructural to the hexagonal manganite $YMnO_3$. We find that with FM ordering the nonpolar $P6_3/mmc$ phase hosts topologically nontrivial nodal lines near the Fermi level for $YVO_3$ and $YCrO_3$. The NLs are formed by a band inversion and protected by a mirror plane symmetry. We show that the $YXO_3$ compounds are also ferroelectric, undergoing a structural transition to polar $P6_3cm$ upon lowering of temperature. Finally, $YVO_3$ becomes insulating in the polar phase, suggesting the possibility of switching from a TSM to an insulating state concomitantly with the FE transition. In realizing these structures, FM magnetic order must be stabilized in the nonpolar space group; in principle this could be done via application of a magnetic, electric, or even strain field[50]. Although all compounds except $YMnO_3$ naturally crystallize in an orthorhombic structure, rather than the hexagonal phase studied here[41, 126, 139, 196], it is possible to synthesize a metastable structure by epitaxial growth on a hexagonal substrate. In fact, this has already been done successfully for the case of $YFeO_3$[2]. Thus, our studies provide motivation for future experimental work stabilizing the hexagonal FM phases, thereby providing a new opportunity for examining the interplay of multiferroicity and topology.

## 6.8 Appendix I: Phonon Dispersions for Nonpolar and Polar phases

In order to analyze the dynamical stability of both polar and nonpolar hexagonal $YVO_3$ and $YCrO_3$, we perform detailed phonon spectra calculations for $YCrO_3$. We do not repeat the calculations for $YVO_3$; however, given the similar ionic radii of V and Cr ($\sim 0.75$ Å), we expect the results to be analogous. Our phonon spectra are computed using the finite displacement method as implemented in the Phonopy software[192]. We construct $3 \times 3 \times 1$ and $2 \times 2 \times 1$ supercells for the nonpolar $P6_3/mmc$ and polar $P6_3cm$ structures respectively. With these supercells we use Phonopy to make the symmetry-inequivalent displacements necessary to build the matrix of interatomic force constants. The dynamical matrix at a given wavevector $\mathbf{q}$ is calculated from the force constants and diagonalized along the high-symmetry lines in Figure 6.7 to get phonon frequencies (given in THz).

Let us first examine the phonon dispersion for the nonpolar $P6_3/mmc$ space group, for which we see the topological NLs. As shown in Figure 6.7a, all phonons are stable except for a single mode which becomes imaginary in frequency with a maximum instability at the $K$ point. A symmetry analysis reveals that this is a $K_3$ phonon. Hence, the phonon spectra for $P6_3/mmc$ $YCrO_3$ is precisely what we would hope: that is, the nonpolar phase has an unstable $K_3$ phonon which at the unit cell tripling wavevector $\mathbf{q} = (1/3, 1/3, 0)$ mediates the ferroelectric $P6_3/mmc \to P6_3cm$ transition upon lowering of temperature.

The phonon dispersion for the low temperature $P6_3cm$ structure of $YCrO_3$ is shown in Figure 6.7b. As hoped for, all phonon modes in the polar compound are positive-definite,

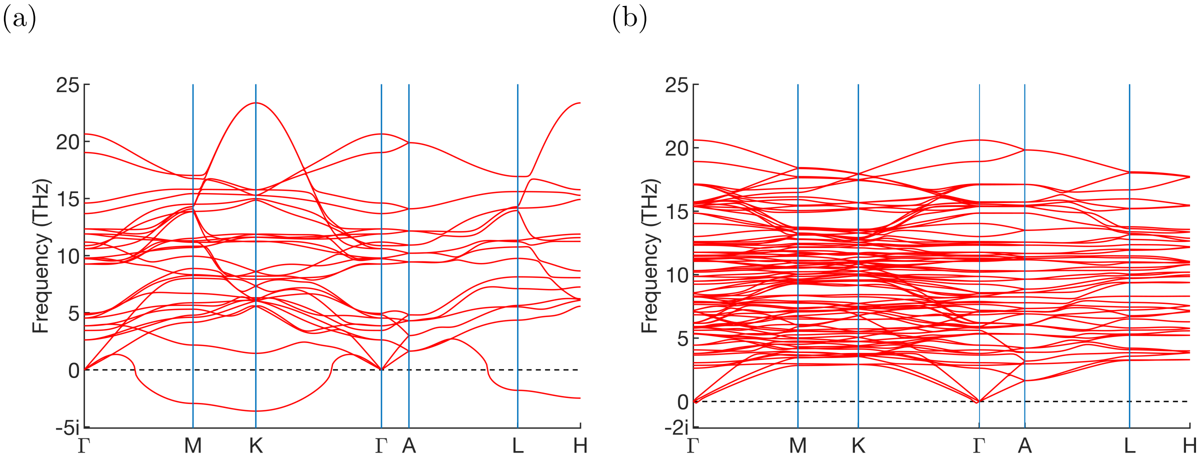

Figure 6.7: Phonon dispersions for $YCrO_3$ in the (a) nonpolar $P6_3/mmc$ and (b) polar $P6_3cm$ phases respectively.

meaning that the structure is dynamically stable. This strongly implies that the synthesis of $YCrO_3$ and $YVO_3$ in the hexagonal structure, via epitaxial growth, will be feasible.

## 6.9 Appendix II: Discussion and Comparison of GGA+U and HSE06 band structures

Although GGAs such as PBE are computationally inexpensive and often yield results comparable to experiment for structural and other ground-state properties, Kohn-Sham eigenvalues computed with GGAs are well known to systematically underestimate experimental band gaps (and hence overestimate band inversion) due to spurious self-interaction errors and an inaccurate description of exchange and correlation effects necessary to capture charged excitation energies quantitatively[194, 67]. Thus interpreting predicted band structures from GGA or GGA+U calculations must be done with care. Band gap underestimation can be more severe in compounds containing elements with localized, unpaired d and f electrons[67], which is precisely the case for the TM ions in our $YXO_3$ ($X = V - Co$) compounds. Higher-order methods for computing band structures from DFT input, such as dynamical mean-field theory (DMFT) and the GW method, are computationally expensive, and results for complex systems can depend on the DFT starting point; DMFT and GW calculations for systems as complex as these are studies in their own right. Hybrid functionals, which mix a fraction of Hartree-Fock exchange with that of traditional GGA approximations, can approximate self-energy corrections and improve GGA Kohn-Sham band structures relative to photoemission experiments[194, 107]. A more approximate but computationally-inexpensive correction to DFT band structures (and total energies) is the GGA+U approach[4, 45], which we use throughout the analysis in the main text. GGA+U reduces the spurious GGA delocalization of the d electrons by adding an on-site Coulomb repulsion term to the total energy. The primary drawback of GGA+U is that the choice of value for the Hubbard U parameter is ad hoc and, in principle, system and environment-dependent; U is often chosen empirically by comparison to measured oxidation energies[204] or measured band gaps[67]. Since photoemission spectroscopy data for hexagonal $YVO_3$ and $YCrO_3$ are not yet available, it is reasonable to ask whether our choice of $U = 3$ eV can be expected to predict an experimentally-observable band structure, i.e whether the band inversion leading to the topological NLs predicted by our GGA+U calculations is accurate.

Although $YVO_3$ and $YCrO_3$ have yet to be synthesized in the hexagonal $P6_3/mmc$ and $P6_3cm$ space groups, experimental band gap data is available for the stoichiometrically equivalent compounds in the related orthorhombic $Pnma$ structure. Thus, a value of $U$ which yields a GGA+U band structure with the correct (or near-correct) experimental band gap for the $Pnma$ phase could also be expected to be predictive for band gaps and/or band inversions for the hypothetical hexagonal phase. Taking the experimental lattice parameters for $Pnma$ $YVO_3$ and $YCrO_3$ and enforcing the GAFM magnetic ordering found in experiment, we calculate the GGA+U band structures with $U = 3$ eV; the results are shown in figure 6.8. For $YVO_3$ in Figure 6.8a, the resultant 1.6 eV direct band gap matches experiment nearly perfectly, whereas for $YCrO_3$ in Figure 6.8b the 2.9 eV GGA+U gap underestimates the experimental direct gap by 0.3 eV.[196, 95, 105] Thus while our choice of $U$ in the main text may be slightly lower than the ideal value for Cr, the discrepancy is likely to be small; and moreover we find that a $U$ of 4 eV for $Pnma$ $YCrO_3$ (Figure 6.8c) results in a slightly overestimated 3.3 eV band gap, whereas this value of $U$ for the hexagonal $P6_3/mmc$ space group still results in a band inversion (Figure 6.8d). While the band inversion at this point is very small, about 0.1eV, we find this band inversion can be increased by moderate biaxial compression in the a-b plane.

Finally for comparison, we repeat our band structure calculations for the nonpolar $P6_3/mmc$ $YVO_3$ and YCrO3 with FM magnetic ordering (neglecting SOC) using the hybrid density functional HSE06, a standard hybrid functional implemented in VASP.[73] HSE06 mixes GGA exchange with a fraction, 1/4, of Hartree-Fock exact-exchange at short range, where “short range” is defined by a range-separation parameter $\mu$; at longer range, the exchange becomes that of the GGA. This is often written as

$$E_{XC}^{HSE} = \frac{1}{4}E_X^{SR}(\mu) + \frac{3}{4}E_X^{GGA,SR}(\mu) + E_X^{GGA,LR}(\mu) + E_C^{GGA}, \tag{6.4}$$

where SR and LR denote short-range and long-range parts respectively, of the electron-electron interactions, $E_X$ refers to the exchange energy, and $E_C$ refers to the correlation energy. For our calculations $\mu$ is fixed to the standard value of 0.2. The HSE06 band structures are plotted in Figure 6.9, with the GGA+U with $U = 3$ eV band structures from the main manuscript included for comparison. For both $YVO_3$ and $YCrO_3$, HSE06 removes the band inversion necessary for the topological NLs and opens up an appreciable gap. This is to be expected: HSE06 can overestimate experimental band gaps by more than 1 eV in some cases, and for transition metal oxides the overestimates are particularly extreme[42]. In the present case, for $YVO_3$ and $YCrO_3$, there is reason to believe that HSE

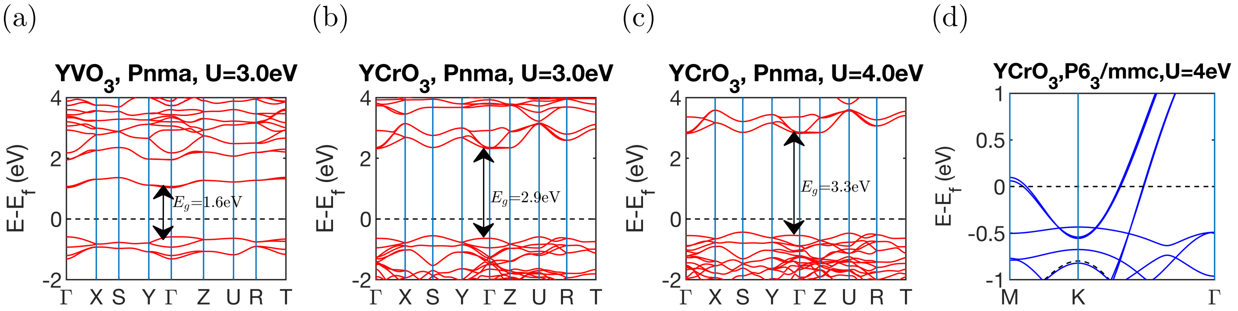

Figure 6.8: GGA+U calculations for $YVO_3$ and $YCrO_3$ in the orthorhombic $Pnma$ structure with experimental GAFM ordering. (a) and (b) use a $U$ of 3 eV for $YVO_3$ and $YCrO_3$ respectively, which is the value we use in our calculations for the hexagonal phases in the main text. Experimental band gaps are 1.6 and 3.3 eV respectively, so for $YVO_3$ the choice of $U$ exactly reproduces the experimental gap. (c) shows the GGA structure for $Pnma$ $YCrO_3$ using a $U$ of 4 eV, which overestimates the experimental band gap by 0.1 eV. (d) shows the nonpolar $P6_3/cmm$ band structure of $YCrO_3$ using $U = 4$ eV. The band inversion necessary for the NL is still present, implying that while $U = 3$eV may be slightly too low for the case of $YCrO_3$, the qualitative band structure should be accurate.

is spuriously removing the band inversion. Firstly, HSE has been found to overestimate the experimental band gap of the transition metal oxides $V_2O_3$ and $Cr_2O_3$ by 1.14 eV and 1.0 eV respectively[88, 67]. Since $V_2O_3/Cr_2O_3$ have the same 3+ oxidation states for V and Cr as $YVO_3$ and $YCrO_3$, HSE calculations for the latter compounds are very likely to yield a similarly large band gap overestimation. Secondly, we find that a $U$ of 5 eV is necessary to reproduce the 0.65 eV gap opened up by HSE06 in $YVO_3$. For $YCrO_3$, $U = 5$ eV is still too small to remove the band inversion at $K$. To our knowledge, few if any GGA+U studies in the literature use a $U$ larger than 3.5 eV (4 eV) for V (Cr)[67, 196, 168, 165, 204] where these values have been obtained either from empirical fitting to experimental data or from constrained DFT calculations[7]. Thus, it would appear that HSE will lead to unrealistic gaps and band inversion.

In conclusion, while future calculations using an ab initial dynamical mean-field theory[57] or the GW approach[72] would be desirable for a more quantitative analysis, there is good evidence that our calculations of topological NLs in nonpolar hexagonal $YVO_3$ and $YCrO_3$ are predictive.

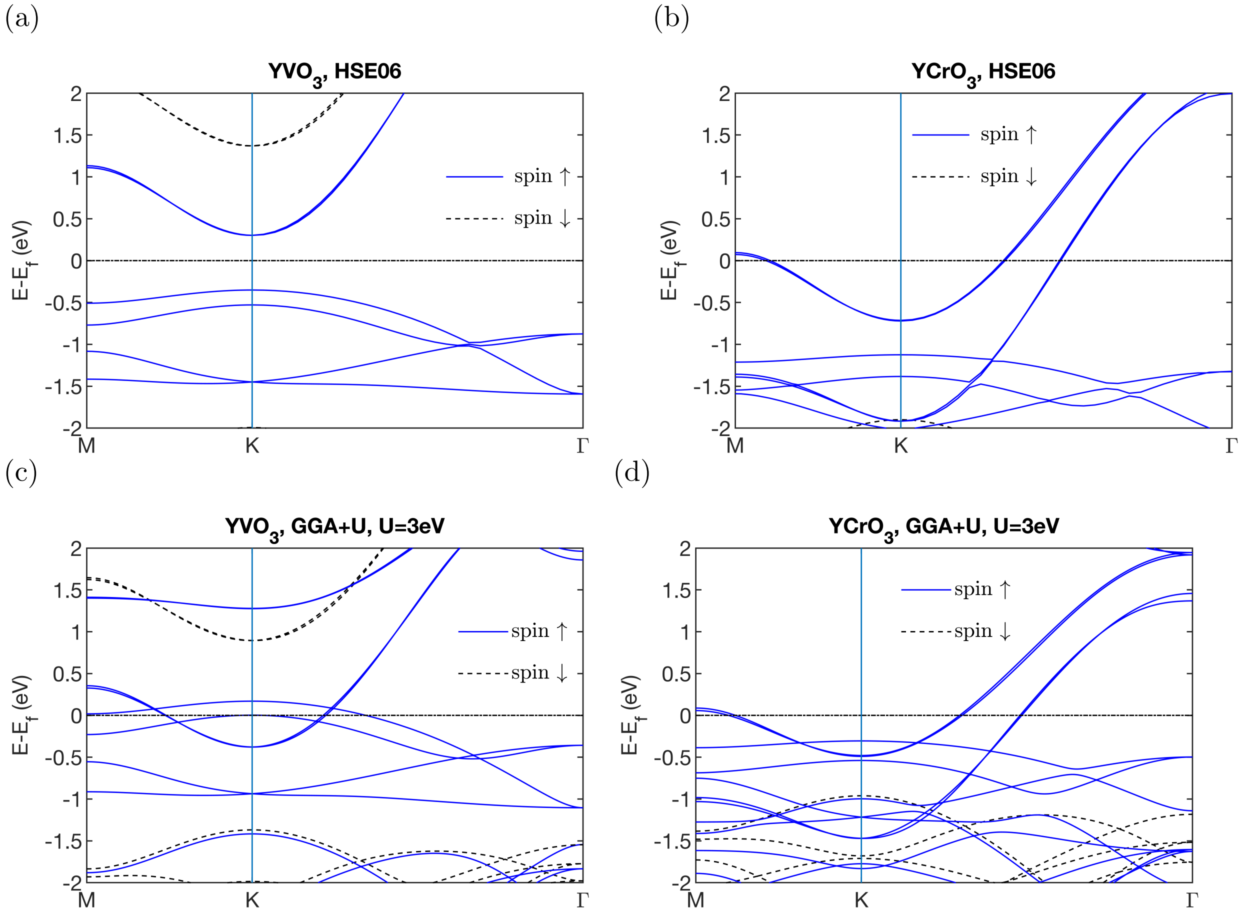

Figure 6.9: HSE06 band structure plots for (a) $YVO_3$ and (b) $YCrO_3$ in the $P6_3/mmc$ space group. Note that HSE06 overestimates the band gaps and consequently loses the band inversion creating the topological NLs at $K$ with the GGA+U calculations in the text ((c) and (d)).

# Chapter 7

# Antiferromagnets in spintronics applications: concepts and status

## 7.1 Spintronics: some background and motivation

Spintronics ("spin electronics") is a field of research which has emerged and subsequently exploded in the last three decades. The underlying concept is the use of an electron's spin degree of freedom rather than, or in addition to, its charge degree of freedom, to encode, write, and transfer information in electronic devices [212, 60, 129].

The use of ordered spin states to record information dates back much earlier than modern spintronics. Indeed, the earliest use of a magnetized material to store information was in 1898 with the invention of the magnetic wire recorder to record sound [129, 173]. Related technologies such as magnetic hard-drives and magnetic core memory soon followed [173]. However, these 19th and 20th century technologies rely on the use of external magnetic fields to "write" or orient the spins in the magnetic compound used for storage. The main disadvantage of this technique is the poor scalability. In general, the smaller the magnetic "bit" (where the bits in a device are defined by magnetic domains of different orientations), the larger the external magnetic field required to stabilize the bit in the presence of thermal fluctuations. The current needed to generate the magnetic Oersted fields traditionally used to manipulate magnetic bits scales linearly with the strength of the external field [25]. Thus, the miniaturization and general tailoring of magnetism-based devices becomes untenable due to the huge current amplitudes required for the writing fields.

A primary focus in current spintronics research is to exploit spin-dependent transport phenomena in order to use electrical current, rather than magnetic fields, to manipulate the spin degrees of freedom in a material. This is achieved through the so-called "s-d exchange", which we will describe quantitatively later. Qualitatively, s-d exchange occurs when an electric current induces a nonzero magnetic polarization in itinerant conduction, or "s" electrons. These spin-polarized electrons create an effective magnetic field, which analogously to the traditional external fields described above, can reorient the localized magnetic moments (generally composed of localized, d orbital electrons) through a spin exchange term in the Hamiltonian [60]. Crucially, in contrast to external magnetic fields, the effective magnetic field from the polarized conduction electrons scales linearly with applied current *density* rather than absolute current. This means that the current needed to reorient or "switch" localized magnetic order scales decreases proportionally to the cross-sectional area of the magnetic bits [25]. Thus, by using s-d exchange rather than externally applied magnetic fields, spintronics-based devices at nanoscale size become feasible [32].

A comprehensive overview of the field of spintronics is beyond the scope of this thesis. Moreover, in our studies on the antiferromagnetic spintronics candidate $\mathrm{Fe_{1/3}NbS_2}$ in Chapters 8 and 9, we focus primarily on magnetic properties and electronic structure which may have consequences for spintronics applications, rather than the theoretical details of the actual spin-transport phenomena. Thus, in this introductory chapter we introduce just a few key concepts in spintronics, (in particular, spintronics using antiferromagnets) to put recent interest in $\mathrm{Fe_{1/3}NbS_2}$ in perspective.

## 7.2 Spin transfer torque

Spin-transfer torque (STT) is a nonrelativistic spin-transport phenomenon discovered independently by Slonczewski and Berger in 1996 [175, 14], which was first realized in ferromagnets (FMs), but as we will see later, can also be leveraged in antiferromagnets (AFMs). Before the discovery in the last decade of spin-orbit torque [129], which can be viewed as STT's relativistic analog, STT formed the conceptual basis of most spintronics applications. Since many aspects of the phenomenon are directly transferable to spin-orbit torque, we will spend some time introducing STT, although spin-orbit torque is the effect relevant for $\mathrm{Fe_{1/3}NbS_2}$.

The experimental setup required to generate STT is illustrated in Figure 7.1a. An electrical current passes through a thick "fixed" layer of FM material ("FM I") with magnetic moments on the localized "d" electrons oriented along $\hat{\mathbf{S}}_1$. After exiting FM I and entering a nonmagnetic "spacer", the conduction electrons will have acquired a net spin polarization along $\hat{\mathbf{e}}_1 = \hat{\mathbf{S}}_1/\left|\hat{\mathbf{S}}_1\right|$. Provided that the thickness of the nonmagnetic spacer is smaller than the spin diffusion length, the conductions electrons will still be primarily polarized along $\hat{\mathbf{S}}_1$ when they impinge on a second "free" FM layer ("FM II") with magnetic moments along $\hat{\mathbf{S}}_2 \neq \hat{\mathbf{S}}_1$. These polarized conduction electrons generate an effective magnetic field $\hat{\mathbf{B}}_{sd}$, given by [60]

$$\hat{\mathbf{B}}_{sd} = -J_{sd}\frac{\delta\hat{\mathbf{m}}}{M_s}, \tag{7.1}$$

where $J_{sd}$ is the exchange integral between s and d electrons, $\delta\hat{\mathbf{m}} = \hat{\mathbf{m}} - \hat{\mathbf{m}}_{eq}$ is the current-induced nonequilibrium spin polarization of the s conduction electrons, and $M_s$ is the saturated magnetic moment of a lattice site in FM II. Note from equation 7.1 that it is the deviation $\delta\hat{\mathbf{m}}$ from the equilibrium conduction spin polarization $\hat{\mathbf{m}}_{eq}$ that explicitly generates the STT, but since $\hat{\mathbf{m}}_{eq}$ in the absence of current is in most cases zero, in this chapter we generally assume $\delta\hat{\mathbf{m}} = \hat{\mathbf{m}}$ for ease of notation. The localized magnetic moments in FM II then couple to this effective magnetic field via the s-d exchange mentioned above:

$$H_{sd} = -J_{sd}\frac{\hat{\mathbf{m}}}{M_s} \cdot \hat{\mathbf{M}} = \hat{\mathbf{B}}_{sd} \cdot \hat{\mathbf{M}}, \tag{7.2}$$

where $\hat{\mathbf{M}}$ is the magnetization of FM II. Through this exchange term, the polarized conduction electrons exert a torque $\hat{\mathbf{T}} = \hat{\mathbf{M}} \times \hat{\mathbf{B}}_{sd}$ on the localized moments in FM II and by transfer of angular momentum, can induce the moments $\hat{\mathbf{M}}$ to rotate from their original direction $\hat{\mathbf{e}}_2$ to point towards the effective magnetic field along $\hat{\mathbf{e}}_1$. Overall, if we combine the torque due to $\hat{\mathbf{B}}_{sd}$ with torque from the effective magnetic field $\hat{\mathbf{B}}_{eff}$ of FM II (which has contributions from crystalline anisotropy, magneto-dipole fields, demagnetization fields, and other material effects), the steady-state equation of motion for the magnetization of the localized moments in FM II can be shown to be [175, 128, 60]

$$\frac{d\hat{\mathbf{M}}}{dt} = -\gamma\hat{\mathbf{M}} \times \hat{\mathbf{B}}_{eff} + \eta\hat{\mathbf{M}} \times \frac{d\hat{\mathbf{M}}}{dt} + \frac{J_{sd}}{\hbar}\hat{\mathbf{M}} \times \hat{\mathbf{m}}, \tag{7.3}$$

where $\gamma$ is the gyromagnetic ratio. The first term in equation 7.3 is the instantaneous torque on a localized moment due to the effective magnetic field in FM II in the absence of current, the third term is the STT due to the current of polarized conduction electrons, and the second term arises due to frictional damping of $\mathbf{M}$ with $\eta$ the so-called "Gilbert damping constant". The dynamics of the localized moments in FM II are then a combination of energy-conserving precession of $\mathbf{M}$ about the fields $\mathbf{B}_{eff}$ and $\mathbf{B}_{sd}$, and dissipative damping due to the second term as well as alignment of $\mathbf{M}$ along the effective fields due to angular momentum exchange with the polarized conduction electrons. We note that the strength and direction of $\hat{\mathbf{B}}_{eff}$ with respect to $\hat{\mathbf{B}}_{sd}$ are important in determining the experimental thresholds for which the desired alignment or "switching" of $\hat{\mathbf{M}}$ dominates over precession [175]. However, the details of $\hat{\mathbf{B}}_{eff}$ are not relevant for our broad discussions of STT and related spintronic mechanisms, so we will neglect this term for the remainder of the chapter.

Before moving on to the closely related phenomenon of spin-orbit torque, we mention that in general, the STT $\hat{\mathbf{T}}_{ST} = \frac{J_{sd}}{\hbar}\hat{\mathbf{M}} \times \mathbf{m}$ can be either "fieldlike" or "antidamping" depending on the relative time scales of the conduction electron spin lifetime (i.e., the time before the spin polarization acquired from FMI decoheres) compared to the precession period of the free ferromagnet FM II [92]. In the case that the conduction spin lifetime is short compared to the equilibrium FMII dynamics, the polarization of the carrier electrons is independent of the localized magnetization $\hat{\mathbf{M}}$ in FM II. Thus, the nonequilibrium conduction electron polarization $\hat{\mathbf{m}}$ in FM II remains along the initial axis of polarization acquired in FM I, $\hat{\mathbf{m}} \sim \hat{\mathbf{S}}_1$. This means the effective magnetic field defined in equation 7.1 is directly proportional to the polarization $\hat{\mathbf{S}}_1$ of the conduction electrons impinging on FM II, and the resulting torque is "fieldlike" in that it is equivalent to the torque generated by an external

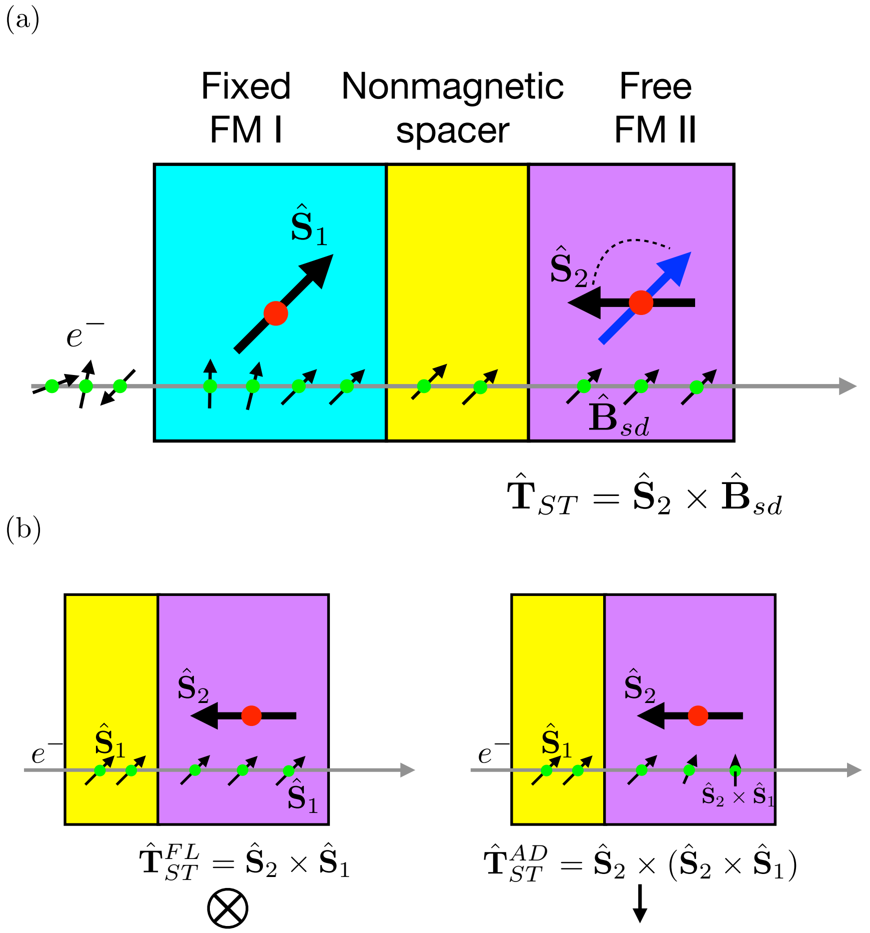

Figure 7.1: Experimental setup and mechanism of spin-transfer torque (STT) in ferromagnets (a) Electrical current (grey arrow) with initially non-spin polarized electrons (small arrows) passes through FMI, with magnetization along $\hat{\mathbf{S}}_1$ (large black arrow). When the conduction electrons exit FM I and enter a nonmagnetic spacer they will have acquired a polarization along $\hat{\mathbf{S}}_1$ which they maintain when they enter FM II with magnetization along $\hat{\mathbf{S}}_2$. The polarized spin current acts as an effective magnetic field $\hat{\mathbf{B}}_{sd}$ that exerts a torque on the magnetization in FMII and can cause the localized spins to rotate and align along $\hat{\mathbf{B}}_{sd}$ (large blue arrow) via transfer of angular momentum from the conduction to localized electrons. (b) Fieldlike (FL) versus antidamping (AD) STT (left and right respectively). If the spin lifetime of the conduction electrons is short compared to the movement of localized moments in FM II, the conduction electrons will remain polarized along $\hat{\mathbf{S}}_1$ and the effective field $\hat{\mathbf{B}}_{sd}$ is in this direction (FL). If the spin lifetime of the conduction electrons is long compared to that of the localized moments in FM II, the polarization of the conduction electrons becomes dependent on the direction of magnetization, and effective magnetic field will be proportional to $\hat{\mathbf{S}}_2 \times \hat{\mathbf{S}}_1$ (AD).

magnetic field along $\hat{\mathbf{e}}_1$:

$$\hat{\mathbf{T}}_{ST}^{FL} \sim \hat{\mathbf{M}} \times \hat{\mathbf{S}}_1. \tag{7.4}$$

Conversely, if the conduction spin lifetime is long compared to the dynamics of the localized moments in FM II, the polarized conduction electrons will precess around $\hat{\mathbf{M}}$. In this case, the carrier polarization is modified to $\hat{\mathbf{m}} \sim \hat{\mathbf{M}} \times \hat{\mathbf{S}}_1$ This "antidamping" component of the STT is given by

$$\mathbf{T}_{ST}^{AD} = \hat{\mathbf{M}} \times (\hat{\mathbf{M}} \times \hat{\mathbf{S}}_1). \tag{7.5}$$

The directions of $\mathbf{T}_{ST}^{FL}$ and $\mathbf{T}_{ST}^{AD}$ are shown in Figure 7.1b. Spin-orbit torque, which we discuss next, can also be antidamping or fieldlike, with the nature of the torque dependent primarily on the symmetries of the magnetic space group, rather than the conduction electron spin lifetime. We will also see that for AFMs in particular, only one of the two torque components is usually useful for reorienting the magnetization in a given AFM material.

## 7.3 Relativistic analog of STT: spin-orbit torque

Spin-orbit torque (SOT) is in most respects nearly identical to STT. It is a spin-transport phenomenon that involves the reorientation of localized spins in a magnetic material due to an effective field generated by spin-polarized conduction electrons from a current. The crucial difference between SOT and STT is the mechanism by which the conduction electrons become polarized. Whereas the polarization in STT requires passing the current through a reference FM polarizer (FM I in the above discussion), through the SOT mechanism the conduction electrons become polarized in the material of interest (FM II) in the presence of current via relativistic spin-orbit coupling [128]. Thus, spintronic devices leveraging SOT can have a single self-referencing magnetic component, rather than needing an additional FM material to polarize the conduction electrons as is the case for devices using STT, making SOT an inherently more robust mechanism.

We briefly outline the principle of SOT, again focusing first on FM materials for simplicity. Our discussion closely follows references [128] and [129]. Consider the one-particle Hamiltonian for an "s" conduction electron with the s-d exchange described in section 7.2, and an additional spin-orbit coupling term:

$$\hat{H} = -\frac{\hat{\mathbf{p}}^2}{2m} - J_{sd}\hat{\mathbf{M}} \cdot \hat{\sigma} + \hat{H}_{SOC}, \tag{7.6}$$

$$\hat{H}_{SOC} = \frac{\hbar}{2mc^2}(\nabla\hat{V} \times \hat{\mathbf{p}}) \cdot \hat{\sigma}, \tag{7.7}$$

where $m$ is the conduction electron's effective mass, $\hat{\mathbf{M}}$ is again the magnetization of the FM material, $J_{sd}$ the exchange integral between s and d electrons, $c$ is the velocity of light, and $\hat{\mathbf{p}}$ is the electron's momentum. $\hat{\sigma}$ is the operator of Pauli spin matrices for a single conduction ("s") electron. In the spin-orbit coupling (SOC) term defined in equation 7.7, $\nabla\hat{V}$ is the effective electric field seen by the conduction electron. The SOC-inducing potential

$\hat{V}$ can have different forms depending on the crystal symmetries and material details. From Equations 7.6 and 7.7, we can then use Ehrenfest's theorem ($\frac{d\hat{\mathbf{A}}}{dt} = \frac{1}{i\hbar}\langle \left[\hat{\mathbf{A}}, \hat{H}\right]\rangle + \langle \frac{\partial \hat{\mathbf{A}}}{\partial t}\rangle$ for an operator $\hat{\mathbf{A}}$) to obtain the coupled equations for the localized magnetization $\hat{\mathbf{M}}$ and the conduction spin polarization density $\hat{\mathbf{m}} = \langle \sigma \rangle$ (where $\langle\rangle$ denotes quantum mechanical averaging over occupied conduction electron states).

$$\frac{d\hat{\mathbf{m}}}{dt} = \frac{J_{sd}}{\hbar}\hat{\mathbf{m}} \times \hat{\mathbf{M}} + \frac{1}{2mc^2}\left\langle (\nabla \hat{V} \times \hat{\mathbf{p}}) \times \hat{\sigma} \right\rangle, \tag{7.8}$$

$$\frac{d\hat{\mathbf{M}}}{dt} = \frac{J_{sd}}{\hbar}\hat{\mathbf{M}} \times \hat{\mathbf{m}}. \tag{7.9}$$

If we assume steady-state for the conduction electron spin polarization $d\hat{\mathbf{m}}/dt = 0$ in equation 7.8, we can substitute the result into equation 7.9 to obtain the SOT:

$$\frac{d\hat{\mathbf{M}}}{dt} = \mathbf{T}_{SO} = \frac{J_{sd}}{\hbar}\hat{\mathbf{M}} \times \hat{\mathbf{m}} = \frac{1}{2mc^2}\left\langle (\nabla \hat{V} \times \hat{\mathbf{p}}) \times \hat{\sigma} \right\rangle. \tag{7.10}$$

Note that equation 7.9 is equivalent to the STT part (third term) of equation 7.3. The difference is that for the case of SOT, we can see explicitly from equation 7.10 that the non-equilibrium conduction spin polarization $\hat{\mathbf{m}}$ comes from the spin-orbit interaction of the conduction electrons in the material, rather than an external FM polarizer.

It is important to emphasize that in equilibrium the net conduction spin polarization density $\hat{\mathbf{m}}$ is generally zero, and so too is the SOT. For a nonzero SOT, both the spin orbit coupling *and* an applied current to generate a nonzero $\hat{\mathbf{m}}$ are necessary. As a concrete example, let us consider a Rashba-type spin-orbit interaction due to broken inversion symmetry at an interface, in which $\hat{H}_{SOC} = \alpha_R(\hat{\mathbf{z}} \times \hat{\mathbf{p}}) \cdot \hat{\sigma}$. Here, $\hat{\mathbf{z}}$ is perpendicular to the interface and $\alpha_R$ is the Rashba coupling constant. In this case, equation 7.10 becomes

$$\hat{\mathbf{T}}_{SO} = \frac{\alpha}{\hbar}\left\langle (\hat{\mathbf{z}} \times \hat{\mathbf{p}}) \times \hat{\sigma} \right\rangle. \tag{7.11}$$

Figure 7.2b shows the Fermi surface for conduction electrons in the $\hat{\mathbf{k}}_x$-$\hat{\mathbf{k}}_y$ plane with Rashba spin-orbit coupling, where the conduction spins tend to align along $(\hat{\mathbf{k}} \times \hat{\mathbf{z}})$ (recall that the wavevector $\hat{\mathbf{k}}$ is proportional to $\hat{\mathbf{p}}$). In the absence of current, $\langle \hat{\mathbf{k}} \rangle = 0$, so the net spin polarization density is zero. However, in the presence of current (Figure 7.2c), the Fermi surface shifts in reciprocal space along the direction of the current (taken to be $\hat{\mathbf{x}}$ in this case) such that $\langle \hat{\mathbf{k}} \rangle \neq 0$. As a result of the nonequilibrium redistribution of the conduction Fermi surface by the current, the conduction electrons acquire a net spin polarization, $\hat{\mathbf{m}} \sim \hat{\mathbf{z}} \times \hat{\mathbf{J}}$ where $\hat{\mathbf{J}}$ is the direction of the current. In this case, equation 7.11 yields a nonzero torque $\hat{\mathbf{T}}_{SO}$ which can reorient the localized magnetization $\hat{\mathbf{M}}$ analogously to the STT. Note that spin-polarized conduction electrons generated by the current in the SOT mechanism are in general spatially localized, e.g. near the inversion-breaking interface (Figure 7.2a). This is relevant in discussion of spintronics for AFMs, which we discuss next.

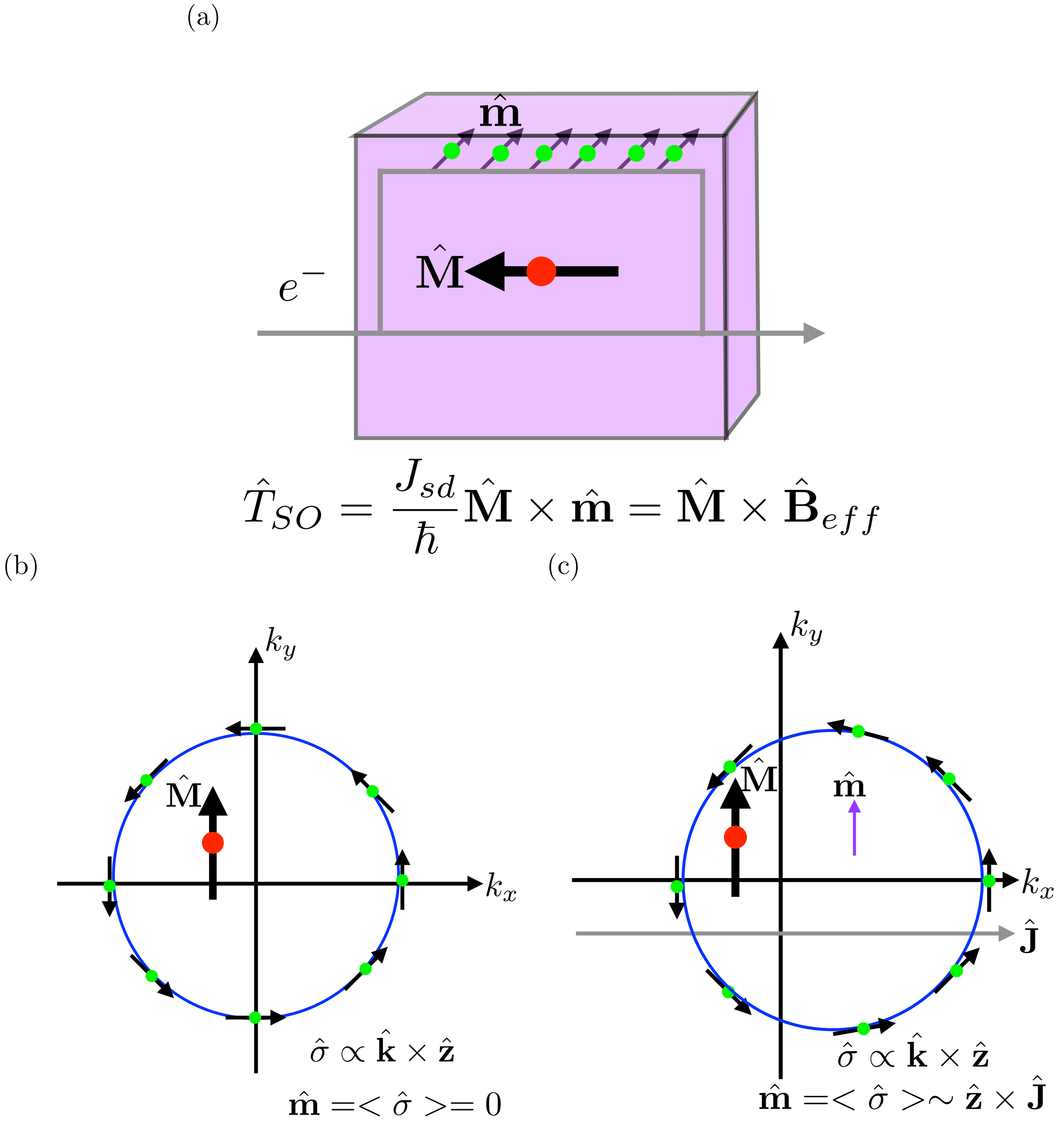

Figure 7.2: Spin-orbit torque (SOT). (a) depiction of SOT mechanism. A non-spin polarized electrical current is applied directly to an FM material with magnetization $\hat{\mathbf{M}}$, and via spin-orbit coupling of the conduction electrons in the FM, these electrons acquire a nonzero spin polarization density $\hat{\mathbf{m}}$ that can exert a torque on the localized moments. (b) Equilibrium Fermi surface cross section (blue circle) for conduction electrons with a Rashba-type spin orbit coupling in the absence of current. While the individual electrons have polarization dictated by the Rashba coupling, because the Fermi surface is centered at $\mathbf{k} = 0$ the polarizations cancel and the spin polarization density $\hat{\mathbf{m}} = 0$. (c) Fermi surface in the presence of current $\hat{\mathbf{J}} \parallel \hat{\mathbf{x}}$. The distribution of electrons at the Fermi surface shifts in the $+\hat{\mathbf{k}}_x$ direction and as a result there is a net conduction spin polarization density along $\hat{\mathbf{y}}$.

## 7.4 AFMs as spintronics materials: some attractive features

Until recently, AFMs were not regarded as useful for spintronics devices. Because the oppositely pointed magnetic sublattices on an AFM add to zero bulk magnetization, the traditional method of spin reorientation using external magnetic fields as described in Section 7.1 is prohibitively challenging. However, following the discovery of electrical current-based methods of magnetization control in FMs such as STT and SOT, and the realization that these mechanisms can also be leveraged in AFMs with certain symmetries, focus in the spintronics community has shifted to AFMs due to several inherent advantages over FMs. The first advantage stems from the same feature that makes AFMs difficult to manipulate with external magnetic fields, namely, their vanishing net magnetization. A hidden benefit of this insensitivity to magnetic fields is that data encoded in the magnetization state of AFM-based devices is less likely to be accidentally erased by perturbing stray fields in the lab than the states in FM-based devices [60].

A second advantage of AFMs is that their characteristic frequencies (corresponding to the rate at which the AFM can be switched between different magnetization states) is several orders of magnitude higher than the limiting frequencies in FMs. This can be understood by considering the energy scales involved in rotating AFM versus FM magnetization. For FMs, the resonance frequency is simply proportional to $\hat{\mathbf{H}}_A$: $\omega_{FM} \sim \mathbf{H}_A$, where $\hat{\mathbf{H}}_A$ is the effective anisotropy field (the energy difference between states with spins oriented along different crystallographic axes) [97]. On the other hand, due to the large energy cost for adjacent spins in AFMs to partially align, the rate of rotation for the Néel vector, defined as the difference $\hat{\mathbf{L}} = \hat{\mathbf{M}}_a - \hat{\mathbf{M}}_b$ of the magnetizations on sublattices $a$ and $b$, is enhanced by the effective exchange field $\hat{\mathbf{H}}_{ex}$ between the sublattices: $\omega_{AFM} \sim \sqrt{\mathbf{H}_A \mathbf{H}_{ex}}$ [153]. Typical anisotropy fields in crystals are less than 1 Tesla, whereas $\mathbf{H}_{ex}$ is generally $\sim 100$ Tesla. This implies that, provided we can effectively rotate the Néel vector using SOT, AFM-based spintronics devices have a limiting speed of data encoding that is two orders of magnitude faster than in devices using FM materials [97].

Before concluding this section, we mention that for both FMs and AFMs, in addition to mechanisms such as SOT which, via rotation of the magnetism, dictate or "write" the magnetization state, some method of distinguishing different states is also necessary for any practical application. The most intuitive method of distinction is simply a magnetization measurement to determine the orientation of the internal magnetic field. However, such a detection scheme with an AFM is complicated by the AFM's zero bulk magnetization. In principle, the bit-like nature of different FM states (e.g., spins along $\hat{\mathbf{x}}$ versus spins along $\hat{\mathbf{y}}$) can be naturally extended to collinear AFMs by considering different orientations of the Néel vector, (see Figure 7.3b). However, while states "0" and "1" are clearly distinguishable by magnetization measurements in the case of an FM (Figure 7.3a), the analogous states for an AFM cannot be distinguished due to the lack of bulk magnetization (Figure 7.3b). Happily, this can also be circumvented by an electrically-based readout mechanism that leverages

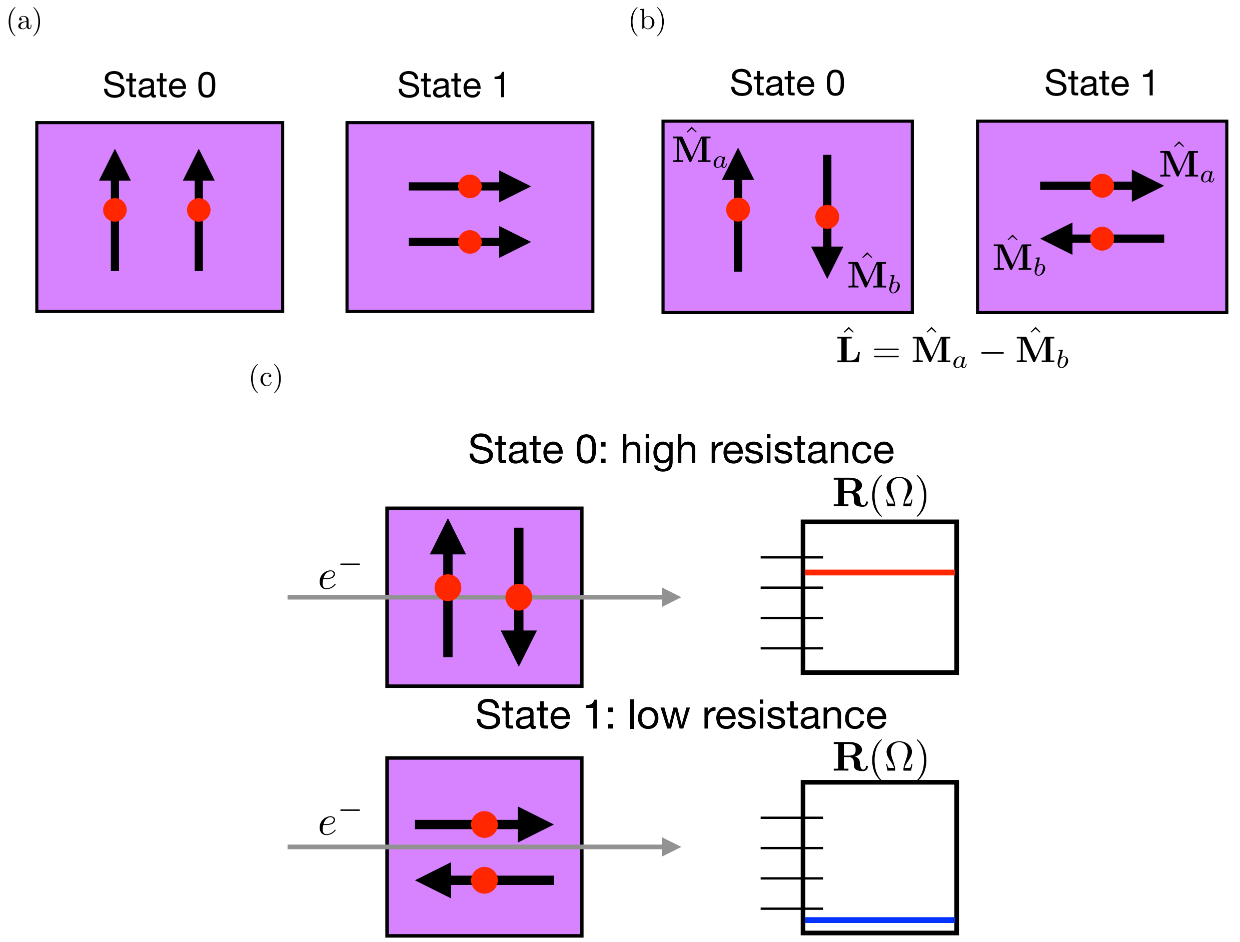

Figure 7.3: Magnetization states in FMs versus AFMs, and the concept of anisotropic magnetoresistance (AMR). (a) Different magnetization states corresponding to bits in an FM-based device are distinguished by relative orientations of the magnetization $\hat{\mathbf{M}}$, for example along $\hat{\mathbf{y}}$ versus $\hat{\mathbf{x}}$. (b) Different magnetization states corresponding to bits in an AFM-based device are distinguished by relative orientations of the Néel vector $\hat{\mathbf{L}} = \hat{\mathbf{M}}_a - \hat{\mathbf{M}}_b$ which is the difference between the magnetization on sublattices $a$ and $b$. (c) Readout of magnetic states. Detection of different orientations of magnetization in FMs (AFMs) can be accomplished by detecting changes in resistance depending on the relative orientation of the current and the magnetic moment (Néel vector). An AFM is depicted here.

anisotropic magnetoresistance (AMR) [92]. Qualitatively, AMR is simply the concept that, due to spin-dependent electron scattering, the electrical resistance of a magnetic material is dependent on the relative angle between the probe current and the magnetic moments. Crucially for our purposes, AMR is an *even* function of the magnetic moment [92, 201], meaning it is present in both FMs and AFMs. Thus, we can detect different magnetic states in an AFM indirectly by detecting changes in the electrical resistivity along a given sample direction (Figure 7.3c). This is the concept on which the experiments for $\mathrm{Fe}_{1/3}\mathrm{NbS}_2$ described in Chapter 9 are based.

## 7.5 Extension of SOT to AFMs

We now describe the extension of SOT to collinear AFMs, and the additional requirements on the symmetry of the SOT for efficient manipulation of the Néel vector. In our description of SOT for the simpler case of FMs in Section 7.3, we stated that the mechanism works by spin-orbit coupling-mediated polarization of the conduction electrons in the presence of a current. These polarized conduction electrons then create an effective magnetic field which can reorient the localized magnetization. However, in the case of AFMs, if the effective magnetic field is uniform in direction throughout the material, the SOT mechanism is no more efficient than an external magnetic field in manipulating the Néel vector. This is because, just as the exchange energy cost $\sim \mathbf{H}_{ex}$ for partial alignment of sublattices in AFMs implies ultrafast spin dynamics, it also implies that the critical field needed to reorient magnetization in an AFM scales with the inter-sublattice exchange, whereas this enhancement is absent in FMs [97]. However, unlike an external magnetic field, the fields generated by the polarized conduction electrons in SOT can be modified in the presence of crystal symmetries such that the SOT-mediated control of AFM magnetism is tractable. As mentioned in Section 7.3, the spin-polarized conductions generated through SOT are spatially localized. Thus, for the case of a collinear AFM with sublattice magnetizations $\hat{\mathbf{M}}_a = -\hat{\mathbf{M}}_b$, in principle the local effective magnetic fields $\hat{\mathbf{m}}_a$ and $\hat{\mathbf{m}}_b$ in the vicinity of sublattices $a$ and $b$ can be different. In particular, for SOT to effectively reorient the Néel vector, the local effective fields on each sublattice (and subsequently, the local torques) MUST be staggered with the sublattice, i.e. have opposite signs [228]. In this case, where $\hat{\mathbf{m}}_a = -\hat{\mathbf{m}}_b$, the localized spins on the the sublattices can maintain their AFM alignment as they rotate [190].

Keeping in mind this requirement of staggered local polarizations for efficient SOT in AFMs, we can easily generalize the formalism of SOT to apply to AFMs. Now rather than considering the torque on the total bulk magnetization $\hat{\mathbf{M}}$, we instead consider the local torque on sublattice $a$ (or analogously, sublattice $b$):

$$\hat{\mathbf{T}}^a_{SO} = \frac{J_{sd}}{\hbar}\hat{\mathbf{M}}_a \times \hat{\mathbf{m}}_a, \tag{7.12}$$

where again $J_{sd}$ is the exchange integral between s and d electrons, $\hat{\mathbf{M}}_a$ is the magnetization on sublattice $a$, and $\hat{\mathbf{m}}_a$ is the current-induced spin polarization of the s conduction electrons in the vicinity of sublattice $a$. Note that equation 7.12 is identical to equation 7.10 except that it describes *local* SOT on a single sublattice.

Finally, we discuss the symmetries in AFMs which can lead to staggered effective fields on the sublattice. Recall that in general, STT and and SOT can have two parts: a so-called "fieldlike" component and an "antidamping" component. If we again consider just the SOT on a given AFM sublattice $a$, the total SOT can be written as

$$\hat{\mathbf{T}}^a_{SO} = \hat{\mathbf{T}}^a_{SO,FL} + \hat{\mathbf{T}}^a_{SO,AD} \sim \hat{\mathbf{M}}_a \times \hat{\eta}_a + \hat{\mathbf{M}}_a \times (\hat{\mathbf{M}}_a \times \hat{\eta}_a), \tag{7.13}$$

where $\hat{\eta}_a$ is a vector local to sublattice $a$ which is independent of the sublattice magnetization $\hat{\mathbf{M}}_a$ [129]. For the case of STT, $\hat{\eta}_a = \hat{\eta}_b$ is simply the initial conduction electron polarization $\hat{\mathbf{S}}_1$ acquired from the FM polarizer. In the case of SOT, $\hat{\eta}_a$ roughly corresponds to the initial polarization of the conduction electrons near sublattice $a$ the instant a current is introduced, rather than the steady-state polarization density $\hat{\mathbf{m}}_a$ which is proportional to the effective magnetic field that induces SOT. Indeed, by comparing Equation 7.12 to Equation 7.13, we see that for fieldlike SOT,

$$\hat{\mathbf{m}}_a = \hat{\eta}_a, \tag{7.14}$$

and for antidamping SOT,

$$\hat{\mathbf{m}}_a = \hat{\mathbf{M}}_a \times \hat{\eta}_a. \tag{7.15}$$

We see that in the case of FL SOT, the effective magnetic field is (trivially) an even function of the sublattice magnetization, whereas for AD SOT the effective field is an odd function of $\hat{\mathbf{M}}_a$. From a symmetry standpoint, this means that the effective field for FL SOT is even under time-reversal, whereas the effective field for AD SOT is time-reversal odd [228, 129].

To understand the implications of this on the magnetic space group restrictions for efficient SOT in AFMs, it is useful to go to a linear-response type formalism. If we assume a local current-induced spin polarization $\mathbf{m}_a$, we can define a tensor $\chi_a$ such that $\hat{\mathbf{m}}_a = \chi_a \mathbf{E}$ with $\mathbf{E}$ the electric field parallel to the applied current. The components of $\chi_a^{ij}$ are then proportional to the nonequilibrium spin polarization in the $ith$ direction induced by a current in the $jth$ direction. Because, as we saw above, the SOT has components which are odd and even under time-reversal, we can also divide $\chi_a$ into components which are even and odd under time-reversal, corresponding to the fieldlike and antidamping components of SOT respectively. The group symmetries $\mathcal{D}$ of the magnetic space group restrict the form of $\chi_a$ by requiring that the tensor components transform in the following way:

$$\chi_{a'}^{even} = \det(\mathbf{D})\mathbf{D}\chi_a^{even}\mathbf{D}^{-1}, \tag{7.16}$$

$$\chi_{a'}^{odd} = \pm\det(\mathbf{D})\mathbf{D}\chi_a^{odd}\mathbf{D}^{-1}, \tag{7.17}$$

where a' is the sublattice to which sublattice $a$ transforms under symmetry operation $\mathbf{D}$, $\chi_a^{even}$ $\chi_a^{odd}$ are the parts of $\chi_a$ which are even and odd under time reversal respectively, and the + (−) in equation 7.17 is for group symmetry operations that do not (do) contain time reversal. Now in order for the SOT-induced effective magnetic field to be staggered with the sublattice magnetization $\hat{\mathbf{M}}_a = -\hat{\mathbf{M}}_b$, either $\chi_a^{even}$ or $\chi_a^{odd}$ must transform under equations 7.16 and 7.17 such that

$$\chi_a^{even/odd} = -\chi_b^{even/odd}, \tag{7.18}$$

where $\chi_b$ is the SOT tensor projected onto sublattice b with opposite magnetization of sublattice a. The part of the tensor (even or odd) which generates efficient torque to manipulate an AFM depends on what symmetries transform sublattice a to sublattice b [228]. For the examples of electrically switchable AFMs CuMnAs and $Mn_2Au$ which are well documented in the literature [201, 23], the sublattices are connected by inversion symmetry, implying that $\chi_a^{even}$ is the tensor component, corresponding to the fieldlike SOT, which generates the staggered field. On the other hand, in $Fe_{1/3}NbS_2$, the sublattices in a single Fe plane are related by a translation accompanied by time inversion. This means that the odd component of the SOT tensor has a staggered form. Thus it is likely the antidamping component of SOT which generates the efficient control of AFM domains in $Fe_{1/3}NbS_2$ which we discuss in Chapter 9.

## 7.6 A few complications in $Fe_{1/3}NbS_2$

Before wrapping up this chapter, we mention some thorny issues with our compound of interest, $Fe_{1/3}NbS_2$, which make direct application of the concepts in this chapter difficult. The theory of SOT in collinear AFMs as outlined in this chapter applies quite straightforwardly to the two previously mentioned compounds CuMnAs and $MnAu_2$, the only experimentally verified electrically switchable bulk AFMs prior to $Fe_{1/3}NbS_2$. For example, CuMnAs is a tetragonal collinear AFM whose spins are oriented in the $\hat{\mathbf{a}}$-$\hat{\mathbf{b}}$/$\hat{\mathbf{x}}$-$\hat{\mathbf{y}}$ plane, with four energetically equivalent AFM domains distinguished by the Néel vector pointing along $\pm\hat{\mathbf{x}}$ and $\pm\hat{\mathbf{y}}$. As mentioned in Section 7.5, for CuMnAs the efficient component of the SOT-induced effective field $\hat{\mathbf{B}}_a \propto \hat{\mathbf{m}}_a$ is the time-reversal even, or fieldlike component. The symmetry-constrained form of $\chi_a^{even}$ for CuMnAs is

$$\chi_a^{even} = \begin{pmatrix} 0 & \chi_{xy} & 0 \\ \chi_{yx} & 0 & \chi_{yz} \\ 0 & \chi_{zy} & 0 \end{pmatrix}, \tag{7.19}$$

and $\chi_b^{even} = -\chi_a^{even}$. This implies that a current along $\hat{\mathbf{x}}$ ($\hat{\mathbf{y}}$) generates SOT-induced fields along $\pm\hat{\mathbf{y}}$ ($\pm\hat{\mathbf{x}}$) for sublattice $a$ and $b$ respectively (see Figure 7.4a). Thus, a current in the $\hat{\mathbf{a}}$-$\hat{\mathbf{b}}$ plane in CuMnAs will tend to increase the fraction of AFM domains whose Néel vectors are oriented perpendicular to the current, as is observed experimentally [201].

For the experiments by Analytis et al. performed in references [148] and [132], the experimental setup is exactly the same. Current pulses are applied in the $\hat{\mathbf{a}}$-$\hat{\mathbf{b}}$/$\hat{\mathbf{x}}$-$\hat{\mathbf{y}}$ plane of the sample, and depending on the direction of the current, the measured electrical resistance switches between high and low states, which are hypothesized to occur due to an SOT-induced repopulation of AFM domains. In fact, for the magnetic space group corresponding

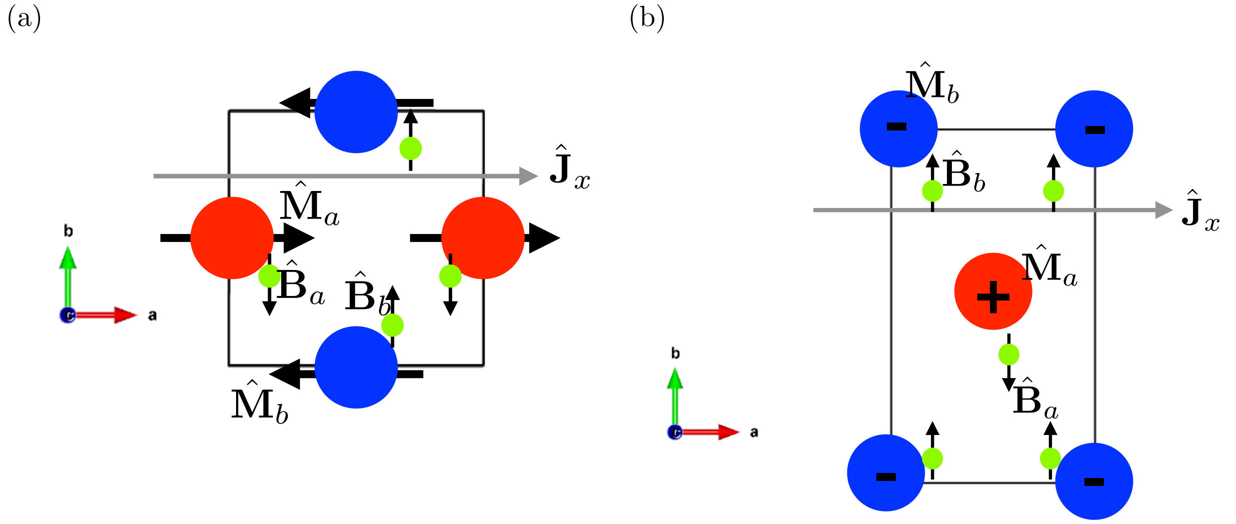

Figure 7.4: SOT in CuMnAs compared to $Fe_{1/3}NbS_2$. (a) CuMnAs (with only the magnetic Mn sublattices shown), depicting a domain with the Néel vector oriented along $\hat{\mathbf{x}}$. A current along $\hat{\mathbf{x}}$ induces local effective fields in the $\pm\mathbf{y}$ directions for the two Mn sublattices, thereby causing the Néel vector to reorient perpendicular to the current. (b) $Fe_{1/3}NbS_2$ (with only the magnetic Fe sublattices in one Fe layer shown) with the stripe AFM ordering described in Chapter 9. Although the direction of the effective fields is identical to CuMnAs for in-plane current pulses, because the Néel vector in $Fe_{1/3}NbS_2$ domains is oriented along $\hat{\mathbf{c}}$ (out of the page), the SOT is unlikely to cause a redistribution of the domains unless there is a slight in-plane canting.

to stripe AFM order, discussed in detail in Chapter 9, the symmetry-allowed form of the efficient SOT is equivalent to that of CuMnAs given in equation 7.19 (with the only difference being that for $Fe_{1/3}NbS_2$, this is the antidamping, time-reversal odd SOT-induced field). However, a puzzle which has yet to be fully solved is that, based on published neutron scattering studies to date of $Fe_{1/3}NbS_2$ [197, 185], the Néel vector appears to lie fully along the $\hat{\mathbf{c}}/\hat{\mathbf{z}}$ axis (Figure 7.4b). Three AFM domains are distinguished by rotations of the in-plane AFM ordering by $2\pi/3$ about the $\hat{\mathbf{c}}$ axis, but for all domains the Néel vector remains along $\hat{\mathbf{c}}$ [116]. Thus, it is unclear how the SOT-induced effective fields, which are oriented in the $\hat{\mathbf{a}}$-$\hat{\mathbf{b}}$ plane for currents applied in that same plane, could couple to the $\hat{\mathbf{c}}$-directed Néel vector and cause a reorientation of the domains. Perhaps the most plausible explanation is that there is a slight canting of the Néel vector in $Fe_{1/3}NbS_2$ towards the $\hat{\mathbf{a}}$-$\hat{\mathbf{b}}$ plane, and it is this in-plane component with couples to the SOT-induced fields and causes a redistribution of AFM domains [148, 132]. There is some evidence of a slight in-plane canting in $Fe_{1/3}NbS_2$ based on more recent, unpublished neutron scattering studies by Wu and Birgeneau [214], but the details are as yet inconclusive.

An additional complication for $Fe_{1/3}NbS_2$ is that there is some evidence that the SOT mechanism itself is completely novel; specifically, that conduction electron spin polarization is induced by a disordered spin glass which appears to coexist with the ordered AFM magnetism when the Fe concentration deviates from the stoichiometric $\frac{1}{3}$ concentration [132]. One compelling piece of evidence for this is that the AMR-based changes in electrical resistance are greatly enhanced for off-stoichiometry samples (both for $x < 1/3$ and $x > 1/3$) compared to the pristine $x = 1/3$ case (which we focus on in our DFT studies) where there is no experimental indication of a coexisting spin glass. If the spin glass is responsible for the current-induced conduction spin polarization, then determination of the symmetry-allowed form of the SOT based on the magnetic space group of the AFM as described in Section 7.5 is not possible. This is part of our motivation in Chapter 9 for making inferences about the effects of the SOT on the AFM domains in $Fe_{1/3}NbS_2$ through DFT-based calculations of the AMR rather than symmetry analysis.

## 7.7 Conclusion

In this chapter we have given a very brief introduction to the concept of spintronics, in particular, spintronics based on electrical control of AFM materials. We have attempted to justify the interest in AFMs based on the appeal of their ultrafast spin dynamics and insensitivity to data-erasing fields. We have also outlined the basic theories of SOT and AMR-based readout as they apply to FMs and AFMs, with the caveat that there are some added subtleties in our material of interest. We now turn to our detailed DFT studies of one particularly promising electrically switchable AFM, $Fe_{1/3}NbS_2$.

# Chapter 8

# Half-magnetization plateau and the origin of threefold symmetry breaking in an electrically switchable triangular antiferromagnet

The material was previously published as

- Shannon C. Haley, Sophie F. Weber et al., *Half-magnetization plateau and the origin of threefold symmetry breaking in an electrically switchable triangular antiferromagnet*, Physical Review Research **2**, 043020 (2020).

## 8.1 Introduction

The electrical manipulation of antiferromagnetic (AFM) spin textures has the potential to effect transformative technological change [93]. Exotic magnets with complex interactions are of special interest in this field, because they are likely to leverage novel mechanisms for their manipulation, possibly allowing ultra low-power or ultra-fast functionality. Diagnosing the relative magnitude of these interactions gives a direct insight into these mechanisms. The existence of magnetization plateaus at fractions of saturation, when a material is subjected to large external magnetic fields, is a powerful tool to this end [187].

In this work we study magnetization plateaus in the antiferromagnet $Fe_{1/3}NbS_2$, a magnetically intercalated transition metal dichalcogenide which has recently been found to exhibit reversible, electrically-stimulated switching between stable magnetic states [148]. This behavior has been seen with considerably lower energy requirements in $Fe_{1/3}NbS_2$ as compared to the other systems [148], raising the question of whether the mechanism differs significantly [227, 200]. At the center of this question is the nature of the magnetic ground state, which has been challenging to determine because collinear and non-collinear order are energetically close and the true ground state depends strongly on the magneto-crystalline anisotropy [133]. The nature of the underlying ordering in $Fe_{1/3}NbS_2$ has been studied by both neutron scattering [197, 185] of magnetic order and optical linear birefringence microscopy [116], which probes nematic structure in the electrical conductivity. Both measurements — electric and magnetic — find indications of three-fold symmetry breaking in the ground state, whose origin is unclear.

We report here a hitherto unobserved plateau in the field-induced magnetization at half of the saturation value. Such a plateau has been discussed theoretically, [170, 221] in triangular lattice antiferromagnets, appearing whenever there is a significant next nearest neighbor magnetic coupling [222]. As compared to plateaus occurring at one-third saturation magnetization [154, 186, 211, 226, 68, 184, 3], experimental realizations of a half-magnetization plateau on a triangular lattice are relatively rare [40, 211]. The implication from theory is that the same interactions that generate the plateau are also responsible for a threefold symmetry breaking stripe phase in the ground state, for both quantum and classical models. The half-magnetization plateau found in $Fe_{1/3}NbS_2$ thus gives a clear clues regarding the microscopic mechanism for the electrically switchable antiferromagnetic ground state.

## 8.2 Results

$Fe_{1/3}NbS_2$ is a layered material with space group $P6_322$ **No. 182** whose magnetism arises from the iron which sits between layers of $NbS_2$ (Fig. 8.1 (a)). These magnetic atoms form triangular lattices in each layer, with adjacent layers staggered with respect to one another (Fig. 8.1 (b)). Charge from the iron atoms is transferred to the $NbS_2$ conduction band, leaving them in a 2+ ionized state, with four unpaired localized electrons per atom [61, 183]. The macroscopic behavior of the material in low field is antiferromagnetic (AFM). The

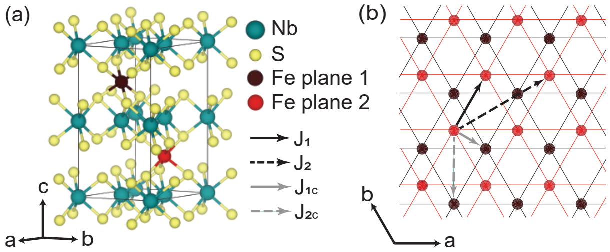

Figure 8.1: (a) The crystal structure of $Fe_{1/3}NbS_2$. Iron atoms sit between layers of $NbS_2$, aligned with the niobium atoms above and below. (b) Looking along the $c$-axis, the iron atoms in a given layer form a triangular lattice. These triangular lattices are shifted from layer to layer. Arrows indicate in-plane and out-of-plane first and second nearest neighbors, labeled by their relevant exchange constants.

samples discussed in this study were grown via chemical vapor transport, as described in Ref. [44]. Using EDX and ICP, the ratio of Fe:Nb was found to be 0.330:1.

Measurements of the magnetic susceptibility as a function of temperature in low applied fields show AFM behavior below a transition near 45K (Fig. 8.2 (a)). Fitting to the paramagnetic regime, the Curie-Weiss law yields an estimate of 5 $\mu_B$/Fe for the effective moment of the material, a quantity which is slightly higher than the expected moment at saturation. This is in agreement with the values found in the literature, which predominantly range from 4.3-5 $\mu_B$/Fe[61, 87, 106, 8, 152], although there is one report as high as 6.3 $\mu_B$/Fe [53]. Heat capacity measurements resolve two clear transitions at zero field (Fig. 8.2 (b)). With the application of field, these transitions move apart from each other in temperature. The lower temperature transition has a further splitting at higher fields, indicating the presence of an additional intermediate phase.

High field measurements further elucidate the nature of the phase transitions. Measurements at 0.6K and 20K of the magnetization as a function of applied field are shown in Fig. 8.3 (a). The full set of measurements, taken at temperatures ranging from 0.6K to 50K, and the phase boundaries determined in part from these measurements are shown in Fig. 8.4. These measurements were performed on a stack of about 30 co-aligned crystals, which were roughly 1mm in diameter and had an average thickness of 0.1mm.

There are three dominant phases at low temperature evident in the data: (I) the zero field phase characterized by a small magnetic moment, (II) the ‘plateau’ phase characterized by a nearly constant magnetic moment centered around half the estimated saturation moment, and (III) a high field phase which approaches the fully saturated moment. The final phase gets pushed above 60T at the lowest temperatures. An intermediate phase bridging the zero field and plateau phase has only a weak feature in the magnetization.

The experimental phase diagram, Fig. 8.4, shows a non-monotonic dependence of the ordering temperature on applied field. This can be explained by the impact of an applied field on a reduced dimensional system [171]; as the field increases, both the order parameter and these fluctuations are suppressed. The latter effect increases in the transition temperature

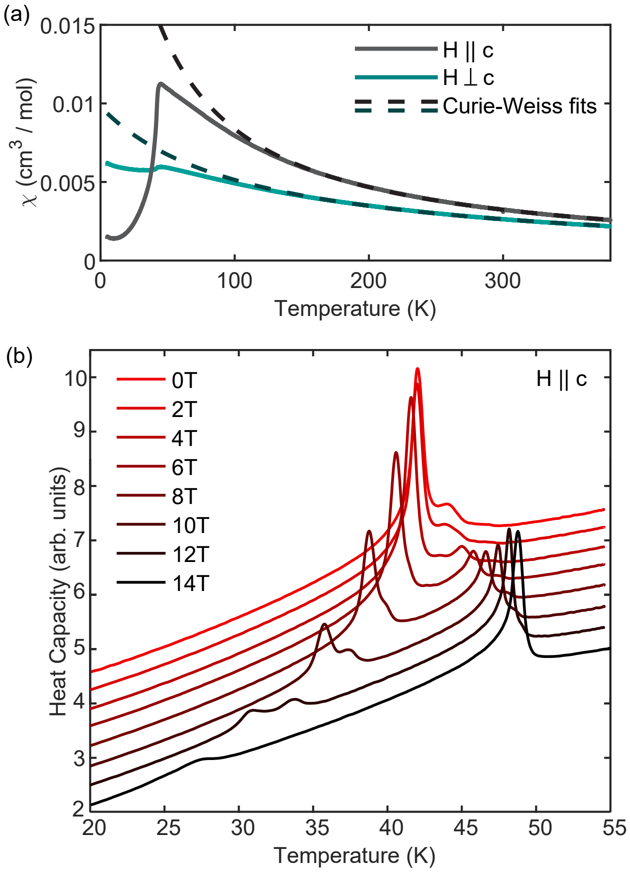

Figure 8.2: (a) Curie-Weiss fits of both out of plane ($H \parallel c$) and in plane ($H \perp c$) susceptibility. (b) Heat capacity measurements show two transitions, which split with the application of field parallel to the c-axis. Curves are offset to enhance visibility.

in low field, and the former brings down the transition temperature at higher fields. We also observe a second ordered phase, which is destroyed in that low field regime.

These measurements were confirmed in stacks and individual single crystals in pulsed and DC magnetic fields. The latter was used to scale the former, because only relative changes could be recorded in our pulsed-field measurements. In addition, data on other compositions with $x = 0.339$ suggest changes in stoichiometry do not affect the field-dependent ground state, though they can shift the phase boundaries.

To understand the physical mechanism responsible for the magnetization plateaus (Fig. 8.3(a)), we study a minimal model motivated by our density functional theory (DFT) calculations, discussed below. In addition to the single-ion anisotropy $D$, we find that a model with nearest neighbor (NN) and next nearest neighbor (NNN) exchange couplings within a single Fe plane, as well as NN and NNN couplings between adjacent planes, is sufficient to accurately reproduce the ab-initio energies of various magnetic states. We restrict our attention to the Fe atoms and their localized $d$ states, which form a lattice of $S = 2$ spins, and consider a short-range Hamiltonian

$$\begin{aligned}\widehat{H} = E_0 + 2J_1 \sum_{\langle i,j \rangle} \mathbf{S}_i \cdot \mathbf{S}_j + 2J_2 \sum_{\langle\langle i,j \rangle\rangle} \mathbf{S}_i \cdot \mathbf{S}_j \\ + 2J_{1c} \sum_{\langle i_c,j_c \rangle} \mathbf{S}_i \cdot \mathbf{S}_j + 2J_{2c} \sum_{\langle\langle i_c,j_c \rangle\rangle} \mathbf{S}_i \cdot \mathbf{S}_j - \sum_i D \left( \widehat{S}_i^z \right)^2 ,\end{aligned} \tag{8.1}$$

where $J_1$ and $J_2$ are the NN and NNN exchange couplings within a single Fe plane, $J_{1c}$ and $J_{2c}$ are the NN and NNN couplings between adjacent planes and $D$ is the magnetoanisotropy of Fe spins. $E_0$ encompasses any non-magnetic contributions to the total energy. The exchange coupling sums are over all unique bonds. In a large neighborhood of relevant exchange coupling values, this model has three distinct phases at zero temperature as the magnetic field is varied. (1) An "AFM stripe" phase at low field with a magnetic unit cell of 4 Fe spins, with 2 pointing up along $+c$ and 2 along $-c$ in a stripe configuration. (2) A half-magnetization plateau at intermediate field with a magnetic unit cell of 8 Fe spins, with three up spins and one down spin per layer (denoted UUUD). (3) A saturated phase at high field with a magnetic unit cell of 2 Fe spins which are all pinned to point up, parallel to $\mathbf{H}$. These configurations are shown in Fig. 8.3 (c). The phases are consistent with two close antecedents of this Hamiltonian, discussed in Refs. [170, 221]

Due to the spins being large ($S = 2$), we perform a classical analysis of Eq. 8.1. We search for the ground state of Eq. 8.1 using many different sized trial unit cells. While a fully 3D classical Monte-Carlo simulations would be more exhaustive, the present analysis is sufficient because high-field measurements of the nuclear magnetic resonance suggest that the plateau has a relatively simple spin texture. We find that the magnetic unit cell for the ground state is always small over a very broad range of parameters $J$, $D$, and $h$, with no more than 8 Fe atoms. Intuitively, this small unit cell is consistent with the short-ranged nature of the dominant interactions.

The classical analysis shows there is a large range of couplings $(J_1, J_2, J_{1c}, J_{2c})$ which produce the three phases observed as a function of magnetic field when $D > 0$ is large. The key observation is that, for $J_1 > 0$ and $J_2/J_1 << 1$, there is a large region in the $(J_{1c}, J_{2c})$ parameter space that approximately reproduces the magnetization curves - the "stripy" AFM, UUUD, and UUUU are the only three ground states for a wide range of $J_{1c}/J_1 > -1$ and $J_{2c}/J_1 < 0$. In fact, the only 1/2-magnetization plateau without a UUUD structure between the two layers occurs for only a small region of parameter space. We may conclude that Eq. 8.1 qualitatively reproduces the observed transitions in the magnetization even without precise estimates for the coupling parameters.

We now quantitatively predict the critical magnetic fields for the transitions from the model Eq. 8.1. For large $D > 0$, the transition from the stripe phase to the plateau phase occurs when $h = 4(J_1 + J_{1c} + J_2)$ and the transition from the plateau phase to the saturated phase occurs when $h = 12(J_1 + J_{1c} + J_2)$. Quantitative analysis requires estimates of the parameters $(J_1, J_2, J_{1c}, J_{2c}, D)$, which we now ascertain through a combination of experimental and numerical means. Following Ref. [91], we can relate the magneto-crystalline anisotropy

| $D$ | $J_1$ | $J_2$ | $J_{1c}$ | $J_{2c}$ |
|---|---|---|---|---|
| 1.09 | 0.76 | -0.006 | 0.39 | -0.22 |

Table 8.1: PBE+U ($U = 0.3$ eV) values of magneto-crystalline anisotropy $D$ and NN and NNN interplanar and intraplanar couplings in Eq. 8.1. Units are meV per Fe atom. With the conventions used in Eq. 8.1 positive values for $J$ represent AFM couplings, negative values are FM, and a positive value of $D$ implies an easy-axis along c for the anisotropy.

$D$ to the in- and out-of-plane Curie-Weiss temperatures, which are found from the fits in Fig. 8.2(a) to be -110 K and -26 K, respectively; this analysis yields $D \sim 1$ meV. While Ref. [61] gives slightly lower Curie-Weiss temperatures (-135 K and -40 K), these values give a virtually unchanged estimate of $D$, which is proportional to their difference.

Our DFT calculations, performed with the Perdew-Burke-Ernzerhof (PBE) functional [157] and Hubbard U corrections [159], corroborate this picture. We note that the calculated $D$, being a highly local property, is sensitive to the Hubbard $U$ used to approximately treat the localized Fe $d$ electrons. This sensitivity has been documented for several Fe-based compounds in previous literature [219, 24]. However, the experimental estimate of $D$ allows us to choose a $U$ value that yields a similar anisotropy, and with which to compute the exchange constants in the minimal model. Using a Hubbard $U$ of 0.3 eV in our PBE+U calculations at experimental lattice parameters, we obtain $D = 1.09$ meV, with the easy axis along $c$, in very good agreement with experiment. Using six inequivalent magnetic collinear configurations with Fe spins along the $c$ axis, we solve an overdetermined system of equations to determine the unknown couplings $J$. The values of all $J$ as well as $D$ are given in Table 9.2.

As an experimental check, the Curie-Weiss temperatures can be related to the sum of the coupling constants corresponding to all of a given Fe atom's interactions, giving an estimate $\sum_i J_i = 6(J_1 + J_2 + J_{1c} + J_{2c}) \sim 1.1$ meV (assuming all couplings beyond nearest and next-nearest neighbors are negligible), where the factor of 6 arises because each atom has six nearest and next nearest neighbors. This is somewhat in tension with our PBE+U results, which from Tb. 9.2 gives $6(J_1 + J_2 + J_{1c} + J_{2c}) \sim 5.4$ meV. Despite the fairly large overestimate, our PBE+U calculations, with $U = 0.3$ eV so that $D \sim 1$ meV, notably yield reliable *relative* values of exchange constants consistent with the estimates based on our experiments. Our choice of $U$ also predicts an AFM stripy phase to have the lowest energy of all collinear magnetic configurations examined, in line with the results of our classical model and neutron data [185]. Moreover, the tendency for DFT+U to overestimate exchange constants at small or near-zero values of U is well documented [108, 120, 136], while capturing their relative values well. Following previous work [115] we uniformly scale $J_1$,$J_2$, $J_{1c}$ and $J_{2c}$ so that $6(J_1 + J_2 + \cdots) = 1.1$ meV, in line with our Curie-Weiss data, and closely agreeing with the data in Ref. [61], whose fitted temperatures predict a slightly higher $\sum_i J_i \sim 1.3$ meV.

Taking the scaled parameters $(J_1, J_2, J_{1c}, J_{2c}, D) = (0.15, -0.0012, 0.077, -0.044, 1.09)$ meV, we can semi-quantitatively reproduce the magnetization curve. We estimate the $g$-

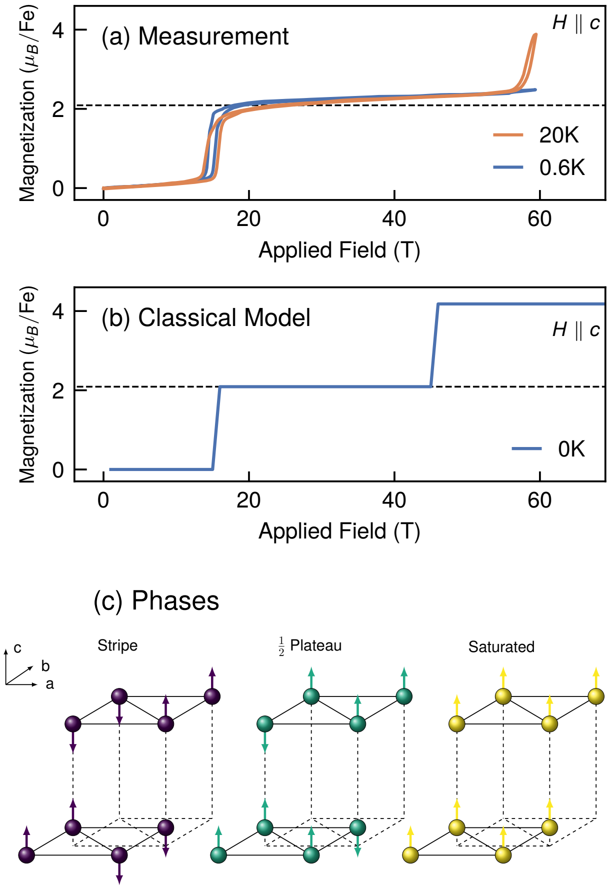

.pdf

Figure 8.3: (a) Magnetization response of $\mathrm{Fe_{1/3}NbS_2}$ to an out-of-plane pulsed field. (Data from a 25T pulse is used below 15T for the 0.6K curve.) At 0.6K, the magnetization shows two flat plateaus at 0 and 1/2 of the saturated magnetization (dashed line). At 20K a further transition, likely to a fully saturated state, is observed near 60T. (b) Magnetization response of the model, Eq. 8.1, computed classically. Three plateaus are clearly visible: a stripy AFM phase, a UUUD phase, and a saturated PM phase. (c) Cartoons of the spin configurations in the eight site unit cell.

factor as $g = 2.09 = g_{\mathrm{Fe}}$ [172]. This yields estimated critical fields of 15T and 45T, as shown in Fig. 8.3. With no fitting to the experimental magnetization in Fig. 8.3, we already have found remarkable agreement between theory and experiment. Fine-tuning the $J$ values within the range of error of the Curie-Weiss data moves the transition fields into even better agreement.

The UUUD phase responsible for the half-magnetization plateau is stable at the classical level over a wide range of applied fields. The model Eq. (8.1) qualitatively reproduces the critical field strengths and quantitatively captures the magnitude of the magnetization. However, it fails to describe some of the fine features of the measurements, such as the small,

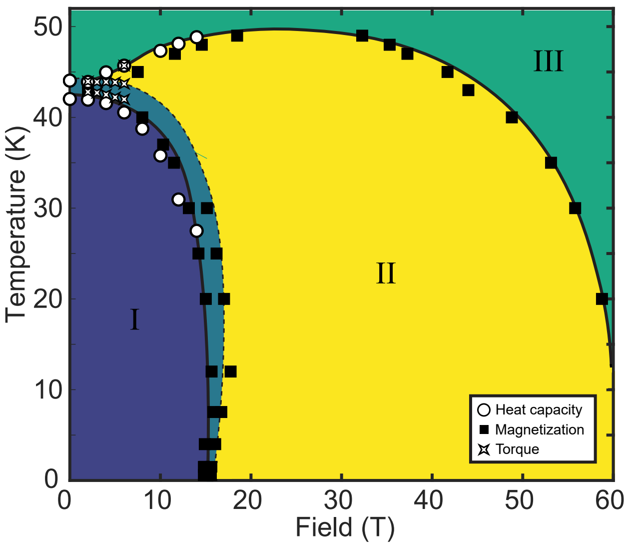

Figure 8.4: Experimental phase diagram of $Fe_{1/3}NbS_2$, as a function of temperature and field applied along the c-axis. Calculations suggest that region I is a stripe phase while region II (the plateau) is UUUD. The origin of the intermediate phase bridging the stripe and UUUD phase is not known. Phase boundaries were determined by torque magnetometry, heat capacity and pulsed field magnetization measurements. Phase boundary lines are a guide to the eye.

positive slope of the magnetization within plateaus and the intermediate phase detected by measurements between the plateau and stripy order. The symmetry constraints of the switching reported in Ref. [148] also indicate an in-plane component to the moment at zero field which is not accounted for in this model. To capture the remaining fine features of $Fe_{1/3}NbS_2$ would require a more sophisticated 3D model with vastly more parameters and temperature effects, similar to [133, 170]. Nevertheless, as a minimal model that only includes a subset of the degrees of freedom, the model is highly consistent with measurements and seems to have identified the dominant interactions responsible for the magnetization response of $Fe_{1/3}NbS_2$.

The applicability of the lattice model suggests that $Fe_{1/3}NbS_2$ is proximate to many other phases, some of which are possibly similar to supersolid phases discussed by Seabra and Shannon [170]. One of these may describe the boundary phase dividing stripy and plateau orders in Fig. 8.4. Preliminary data appears to be consistent with an UUD phase, though more data is required to confirm this.

The agreement of the experimentally observed magnetization with a classical model suggests that the magnetic behavior, while originating from many competing interactions, involves conventional magnetic phases. This model could be further confirmed by inelastic neutron scattering. The existence of an UUUD half-magnetization plateau had previously been studied as a result of strong next-nearest neighbor interactions within the triangular-lattice plane; we have determined that it is not limited to that case, as we see its emergence from strong interplanar interactions. The determination of these interactions and of the abnormally strong single-ion anisotropy has a large impact on the zero-field ground state of this material; the three-fold symmetry breaking seen in optical measurements [116], for example, originates from a magnetic order driven by a large ratio of $J_{1c}/J_1 \sim 1/2$, likely stripy in nature with a significant $c$-axis component. It is interesting to consider the implications for the electrical switching of the spin texture of this material. In the typical mechanism, an in-plane Néel vector can be naturally rotated by the angular momentum imparted by an in-plane spin polarized current. In contrast, $\mathrm{Fe}_{1/3}\mathrm{NbS}_2$ has a Néel vector that is predominantly pointed out-of-plane, so that a different kind of mechanism to transfer angular momentum is likely to be active. The present work suggests that this leverages both strong inter- and intra-planar exchange interactions.

# Chapter 9

# Origins of anisotropic transport in electrically switchable antiferromagnet $Fe_{1/3}NbS_2$

## 9.1 Introduction

Due to the bit-like nature of electronic spins, magnetic materials are natural candidates for storage and sensing devices. In particular, the scaling advantages of electrical current over magnetic fields makes spintronic materials whose magnetism can be controlled by current especially desirable [129]. The underlying mechanism for current-induced magnetic switching is generally thought to be spin-orbit torque; the applied electric current, in a manner dictated by crystal symmetries, induces a polarization in conduction electrons, thereby creating an effective magnetic field [127, 128, 13, 56, 174, 228]. This effective field imparts a torque on the localized magnetic moments, enabling them to switch to different orientations.

There has been growing interest in electrically induced switching in antiferromagnetic (AFM) compounds. AFMs have been reported to switch (via a rotation of the Néel vector) at THz rates by electrical current compared to a nominal $\sim$ GHz limit for ferromagnets [153]. Moreover, their vanishing bulk magnetization makes them insensitive to stray magnetic fields, enhancing their stability for memory storage relative to ferromagnets (FMs). In spite of their appeal, there are just a few reports of AFM materials which can be electronically manipulated; until very recently the only known examples in single crystal form were the collinear AFMs CuMnAs and $Mn_2Au$ [201, 23].(Additionally, current-driven manipulation of AFMs has also been confirmed in heterostructure devices [142, 34]).

Recently, an electrically switchable AFM was discovered among the magnetically intercalated transition metal dichalcogenides (TMDs), layered compounds in which the magnetic ions are intercalated between the layers. These materials have received attention in the past due to their high tunability; by simply varying the intercalated element, concentration of the intercalant, or base TMD, a wide variety of magnetic and electric ground states are induced

[54, 197]. Transport experiments by Nair et al. [148] demonstrated that one particular case, $Fe_{1/3}NbS_2$, can be switched between states of high and low resistance by applying orthogonal current pulses. The switching occurs below the Néel temperature of 49 K, indicating that the magnetic order is relevant to the changes in resistance.

However, the origin of the high and low resistance states has yet to be clarified. It has been hypothesized, based on the results of optical polarimetry measurements, that the resistance change is associated with a current-induced repopulation of three AFM domains [148, 116], analogously to the current-induced switching observed in CuMnAs [66]. Little et al. [116] point out that this could occur in theory even if the Néel vector of $Fe_{1/3}$NbS2 is fully out of plane. If domain repopulation leads to changes in resistance along a given direction, this will necessarily be reflected in the anisotropy of the electronic structure and transport for a single domain.

In what follows, we perform density functional theory (DFT) calculations of the electronic structure and the nature of the magnetic order in $Fe_{1/3}NbS_2$. We find an AFM ground state, and two nearly degenerate in-plane magnetic orderings corresponding to previously reported “stripe” and “zigzag” AFM states. We find that the Fermi surfaces for stripe and zigzag order are both anisotropic in the $k_x$-$k_y$ plane, though the in-plane anisotropy is larger for stripe order. Using our DFT electronic structure and a constant relaxation time approximation within the Kubo linear response formalism, we find that with stripe order the resistivity along the [120] crystallographic axis is roughly twice as large as along the orthogonal [100] direction. On the other hand, the resistivity along [100]/ $\hat{x}$ is larger than [120]/$\hat{y}$, and the relative anisotropy is reduced for zigzag order. Our computed resistivity tensors for stripe and zigzag order, combined with the experimental switching data, suggest that for both magnetic states a current pulse depopulates the AFM domain whose principle axis is parallel to the current and increases the populations of the other domains. Our calculations support the domain repopulation hypothesis and provide insight into the specific current-domain dynamics in $Fe_{1/3}NbS_2$.

## 9.2 Methods

For our first-principles density functional theory (DFT) calculations on $Fe_{1/3}NbS_2$, we employ the Vienna *ab intitio* simulation package (VASP) [103] with generalized gradient approximation (GGA) using the Perdew-Burke-Ernzerhof (PBE) functional [157] and projector augmented-wave (PAW) method [21]. For all DFT calculations we include spin orbit coupling (SOC), and treat it self-consistently. We take 3d and 4s; 4p, 4d, and 5s; and 3s and 3p electrons explicitly as valence for Fe, Nb, and S, respectively. We use an energy cutoff of 650 eV for our plane wave basis set. For our **k**-point grid we use a Γ-centered mesh of $12 \times 7 \times 6$ for the $1 \times \sqrt{3} \times 1$ orthorhombic supercell consistent with stripe order, and a $6 \times 7 \times 6$ mesh for the $2 \times \sqrt{3} \times 1$ supercell consistent with zigzag AFM order. We use the tetrahedron method [22] for Brillouin zone integrations. These parameters lead to total energy convergence of $< 1$ meV/Fe ion. We use the experimental lattice constants of $a = 5.76$ Å and $c = 12.20$

Å, and experimental atomic coordinates [197], having checked that relaxation changes parameters and atomic positions negligibly. For calculations of two-dimensional fermi surfaces and velocities, we use Wannier interpolation as implemented in the post-processing utility postw90 for Wannier90 [137, 143, 220]. We use 208 and 416 bands for stripe and zigzag order respectively in our Wannierizations. We select Fe d, Nb $d_{z^2}$, and S p orbitals as our localized projections. Cross sections of the Fermi surfaces and Fermi velocities are evaluated on a $k_x \times k_y \times k_z$ grid of $251 \times 251 \times 1$. Fermi surface cross sections shown in the the Supplement without band velocities were generated using WannierTools [213]. The evaluation of the Kubo formula for conductivity is performed using the Wannier-linear-response code [230]. The code calculates linear response properties within the Kubo formalism based on DFT-parameterized tight-binding Hamiltonians, taking the overlap of Wannier functions as input. We use a converged k-grid of $400 \times 400 \times 400$ for evaluation of the conductivities.

To approximately account for the localized nature of the Fe d electrons we add a Hubbard U correction[6], and we select the rotationally invariant implementation by Dudarev et al. [45]. We note here that our quantitative results for energetics, Fermi surface cross sections, and transport tensors are highly sensitive to the specific value of Hubbard U chosen. This is because U is an ad-hoc parameter that acts explicitly on the Fe d states, which have a very large weight near the Fermi energy in $Fe_{1/3}NbS_2$; therefore, small changes in U have a disproportionate effect on bands in the relevant energy window for transport properties. Given the limitations of PBE+U with a single choice of the U parameter, to gain confidence in consistent qualitative features in transport anisotropy we perform and describe PBE+U calculations using two different U values in the main text. We first use PBE+U with $U = 0.3$, eV following previous work, which results in a magnetoanisotropy energy (MAE) consistent with experiment [70]. However, as we noted in reference [70], $U = 0.3$ eV overestimates Heisenberg exchange constants as compared to experiment by several orders of magnitude. This motivates our consideration of a larger value $U = 0.9$ eV for comparison, which results in smaller (though still overestimated) Heisenberg exchange constants due to increased localization, and also gives the correct sign for the MAE (easy axis along c) while the magnitude of the MAE is overestimated. We note here that, as shown in the Supplement, even if we use a much larger $U = 4$ eV which gives an incorrect sign for the MAE, the qualitative trends for transport with both zigzag and stripe magnetism are identical to those presented here using $U = 0.3$ eV and $U = 0.9$ eV, giving us further confidence in the robustness of our results. We refer the reader to Appendix 9.8 for further details and discussion.

## 9.3 Crystal Structure

$Fe_{1/3}NbS_2$ is a layered compound with Fe intercalated between 2H-type TMD $NbS_2$ layers[54]. The primitive non-magnetic unit cell is depicted in Figure 9.1. The Nb atoms are surrounded by the S atoms in a trigonal prismatic coordination. $Fe_{1/3}NbS_2$ takes up the space group $P6_322$ [182]. The Fe atoms are sandwiched between the $NbS_2$ layers at relative

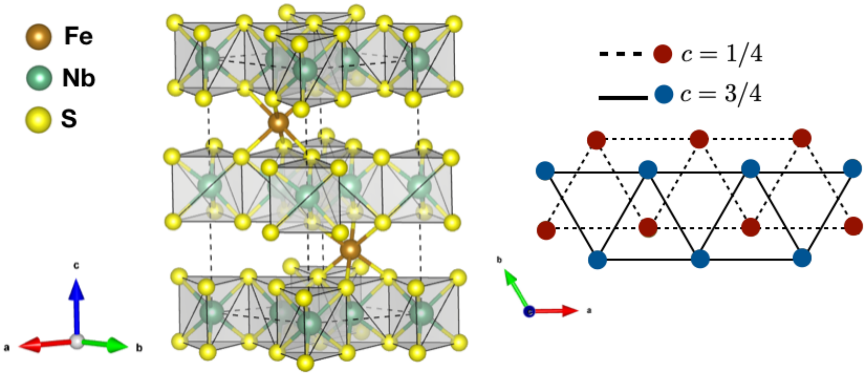

Figure 9.1: Left: hexagonal crystal structure of $Fe_{1/3}NbS_2$, with space group $P6_322$.The primitive cell contains two Fe atoms sandwiched between the layers of $NbS_2$ at $c = 1/4$ and $c = 3/4$. Right: c-oriented view of the two Fe layers with ions in layer $c = 1/4$ and $c = 3/4$ colored red and blue respectively.

coordinates $(1/3, 2/3, 1/4)$ and $(2/3, 1/3, 3/4)$ (Wyckoff position 2d). There are two different Fe layers stacked along c, with each layer forming a triangular lattice in the a-b plane (note that the a-b plane is what we refer to as "in-plane" in what follows).

## 9.4 Magnetic Order

The magnetic ground state of $Fe_{1/3}NbS_2$ is known to be AFM below about 50K [54], but the nature of the AFM order is highly sensitive to small changes in Fe concentration. Seminal work more than 40 years ago [197] indicated that for $Fe_xNbS_2$ with $x = 0.323$, an in-plane"zigzag" AFM order of the Fe spins, with the Néel vector oriented out of plane along [001] and the spins along one in-plane Fe bond direction alternating between up and down and between"up up" and "down down" along the other two bond directions (Figure 9.2b). However, another neutron scattering study by Suzuki et al. [185] with $x = 0.297$ found evidence for a stripe AFM ground state, with rows of spins along one Fe bond direction alternating between all up and all down (Figure 9.2a).

We perform DFT calculations for both experimentally proposed collinear magnetic orderings, with the Néel vector taken along c, corresponding to magnetic space groups $P_C2_12_12_1$ (stripe) [185] and $P_c2_12_12$ (zigzag)[197] (see figure 9.2). In what follows, we will refer to them as a-stripe and a-zigzag respectively, with the "a" indicating that adjacent planes of Fe ions are AFM coupled. From our PBE+U calculations, these two magnetic orders are nearly degenerate; the energy differences between the magnetic states are 0.9 and 2.5 meV per Fe atom for U = 0.3 and U = 0.9 eV, respectively. Additionally, the slightly preferred ground state switches from a-stripe for U = 0.3 eV to a-zigzag for U = 0.9 eV.

The near-degeneracy of a-stripe and a-zigzag phases can be understood quantitatively from a Heisenberg Hamiltonian which we discussed in reference [70] for PBE+U calculations with U = 0.3 eV. We will mention it again here and discuss the exchange constants in the case of both U = 0.3 eV and U = 0.9 eV. Neglecting antisymmetric spin exchange which could lead to slight deviations from fully collinear order, magnetic contributions to the energy of $Fe_{1/3}NbS_2$ can be described approximately by the following Heisenberg Hamiltonian for the Fe lattice:

$$H = E_0 + \sum_{\langle ij \rangle} J_1 S^2 + \sum_{\langle\langle ij \rangle\rangle} J_2 S^2 + \sum_{\langle ij \rangle_c} J_{1c} S^2 + \sum_{\langle\langle ij \rangle\rangle_c} J_{2c} S^2 + \sum_{\langle\langle\langle ij \rangle\rangle\rangle_c} J_{3c} S^2 - \sum_i D (S_i^z)^2, \quad (9.1)$$

where $S = 2$ is the spin value of $Fe^{2+}$, one, two and three pairs of brackets distinguish Heisenberg exchange constants between equidistant nearest, next-nearest and third-nearest neighbors respectively, and the $c$ subscript refers to interplanar, rather than in-plane couplings. The last term is the magnetoanisotropy energy (MAE) which, while relevant to our studies in reference [70], we can neglect in our discussion here as both a-stripe and a-zigzag phases have their Néel vectors fully along [001]. $E_0$ encompasses nonmagnetic contributions to the energy. Note that we neglected the third nearest neighbor exchange $J_{3c}$ in reference [70] as it did not qualitatively alter our conclusions. To obtain the five coupling constants plus $E_0$ we fit our DFT total energies for six inequivalent collinear magnetic configurations, which include the a-stripe and a-zigzag phases, to Equation 9.1 for each U value studied.

We find for both sets of PBE+U calculations that the in-plane and interplanar nearest neighbor exchange constants $J_1$ and $J_{1c}$ are antiferromagnetic ($J > 0$) and significantly larger in magnitude than the other three exchange constants $J_2$, $J_{2c}$ and $J_{3c}$ which are all ferromagnetic ($J < 0$). We note that this is also qualitatively consistent with a previous DFT study of the exchange constants in $Fe_{1/3}NbS_2$ with no Hubbard U correction (U = 0 eV)[134]. Focusing on the experimentally relevant a-stripe and a-zigzag phases, the difference in energy between a-stripe and a-zigzag phase using the above equation is given by

$$E_{a-stripe} - E_{a-zigzag} = 4J_{2c}S^2 - 4J_2 S^2 - 8J_{3c}S^2, \quad (9.2)$$

where again, the interplanar $J_{2c}$, $J_{3c}$ and in-plane $J_2$ are all FM ($J < 0$). We see then that the condition for the a-stripe phase to be favored is $|J_{2c}| > |J_2| + 2|J_{3c}|$, whereas the a-zigzag is energetically favored when $|J_{2c}| < |J_2| + 2|J_{3c}|$. Thus, the switching in our PBE+U calculations between a-stripe and a-zigzag phase ground states as a function of U is caused by a shift in calculated relative values of three very small exchange constants (a table with all Heisenberg exchange constants in equation 9.1 for both U values is provided in the Supplement). Specifically, while the magnitudes of most of the exchange constants using U = 0.9 eV shrink fairly uniformly relative to those calculated with U = 0.3 eV (as expected due to increased electron localization with larger U), the in-plane next-nearest neighbor exchange constant $J_2$ becomes larger with the greater U value. This is likely

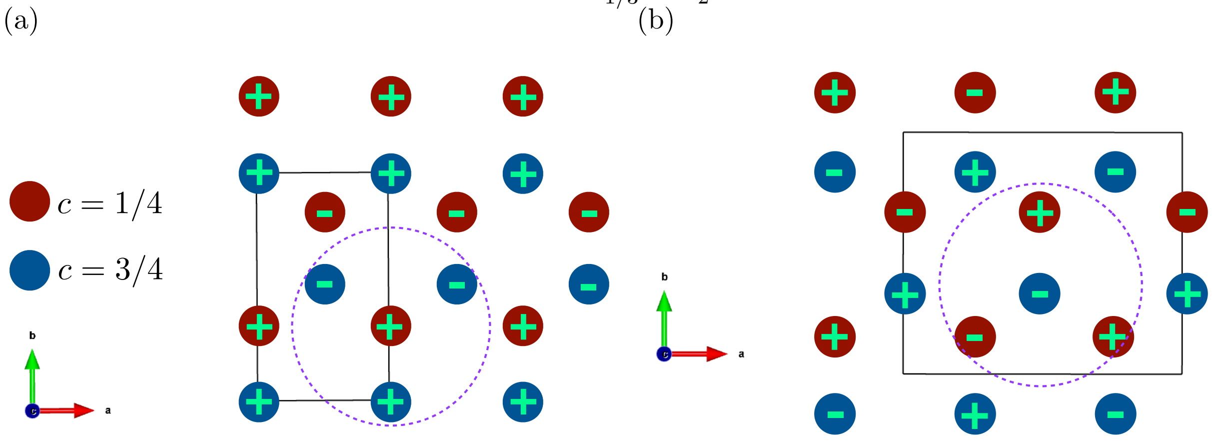

Figure 9.2: Experimentally proposed magnetic orderings, (a) $P_C2_12_12_1$ (a-stripe); (b) $P_c2_12_12$ (a-zigzag), with only Fe spins shown. In our DFT calculations the Néel vector is purely out of plane; + and − symbols refer to up and down spins respectively. Magnetic supercells are outlined in black. The orthohexagonal supercell for stripe order in terms of the primitive hexagonal lattice vectors a and c is a $\times \sqrt{3}$a $\times$ c and the supercell for zigzag order is 2a $\times \sqrt{3}$a $\times$ c. Dashed purple circles show the three interplanar nearest neighbors for a given ion, which determine whether the planes are "FM" coupled or "AFM" coupled; the coupling is AFM in both cases.

due the enhanced hybridization between Nb d and Fe d states in the $k_z = 0$ plane for PBE+U with U = 0.9 eV compared to U = 0.3 eV. Because the magnetism in $Fe_{1/3}NbS_2$ and other magnetically intercalated TMDs is thought to be RKKY-mediated[54], enhanced hybridization between Fe and Nb states in the $k_z = 0$ plane is consistent with larger long-range in-plane couplings.

Direct conclusions regarding the magnetic ground state of $Fe_{1/3}NbS_2$ for intercalations slightly below or above $x = \frac{1}{3}$ cannot be made from our PBE+U calculations using this stoichiometric intercalation. Nevertheless, our PBE+U result of competing ground states at $x = \frac{1}{3}$ is consistent with the experimental sensitivity of the magnetic ground states to minuscule intercalation changes. Moreover, the change in our computed exchange constants, and consequently in the magnetic ground state, for small changes in the U parameter are consistent with the unpublished neutron scattering report[214] suggesting that a-stripe and a-zigzag phases may coexist at $x = \frac{1}{3}$. If the experimental ground state at $x = \frac{1}{3}$ is in fact a superposition of a-stripe and a-zigzag phases, the changes in magnetic energetics as a function of U could reflect the fact that this compound is incompletely described by single set of Heisenberg exchange constants. In any case, the experimental relevance of the a-stripe and a-zigzag phases, in addition to our PBE+U findings that they are energetically competitive, motivate us to study the transport anisotropy of both magnetic orders in what follows.

## 9.5 Fermi Surface Cross Sections

We now examine cross sections of the Fermi surfaces (FSs) for a-stripe and a-zigzag order computed with our two sets of PBE+U calculations. We focus on electronic structure parallel to the $k_x$-$k_y$ plane, relevant to the switching experiments. We plot Fermi contours in the $k_z = 0$ plane of the Brillouin zone (BZ); cuts of the $k_x$-$k_y$ FS at other values of $k_z$ are given in the Supplement. We focus first on the a-stripe FS, depicted in Figures 9.3a-9.3b and 9.3e-9.3f for both U = 0.3 and U = 0.9 eV respectively. We consider the two U values for the reasons discussed in Section 9.2. For both choices of U, the a-stripe FS results from relatively flat bands extending along the entire $k_y$ direction of the BZ ($k_x$ is parallel to the [100] crystallographic direction in real space, and $k_y$ parallel to [120]; we use the hexagonal notation of the primitive cell for crystallographic directions through the text.) We gain a more explicit picture of the corresponding anisotropy in carrier transport by examining the in-plane components of the band velocities. Figures 9.3a and 9.3e are color-coded according to $v_x(k_0) = \frac{1}{\hbar}\frac{\partial E}{\partial k_x}|_{\mathbf{k}=k_0,E=E_F}$, where $x$ is along [100], $E_F$ is the Fermi energy, and $k_0$ is a point in the $k_x$-$k_y$ plane. Figures 9.3b and 9.3f are colored by $v_y$, whose magnitude is greatly reduced compared to $v_x$. This suggests that, for the stripe phase, the conductance $\sigma_{xx}$ along the $x$ direction of the sample (parallel to the magnetic stripes in real space) will be higher than $\sigma_{yy}$ (perpendicular to the stripes ); and equivalently, the resistance $R_{xx} < R_{yy}$ for a-stripe order.

While still anisotropic, the a-zigzag FS cuts, depicted in Figures 9.3c-9.3d and 9.3g-9.3h for U = 0.3 and U = 0.9 eV, are more symmetric as compared to a-stripe. This is also evident from examining the band velocities. For PBE+U with U = 0.3 the $v_x$ and $v_y$ components at $E_F$ appear isotropic (Figures 9.3c and 9.3d), likely a coincidental result due to this choice of U. The a-zigzag weight of $v_y$ relative to $v_x$ increases significantly for U = 0.9 eV (Figures 9.3g and 9.3h). This implies that that the transport anisotropy in a-zigzag, at least for U = 0.9 eV, switches compared to stripe (i.e. for a-zigzag, $\sigma_{xx} < \sigma_{yy}$ and $R_{xx} > R_{yy}$). We point out that the large qualitative changes in the FS cross section for a-zigzag order in going from U = 0.3 to U = 0.9 eV as compared to a-stripe order are presumably linked to the large number of low-dispersion bands near the Fermi level for a-zigzag which are highly sensitive to small changes in U.

## 9.6 Resistivity Tensor and Switching

In order to understand the specific current-domain response implied by the FS anisotropies above, we can compute the resistivity tensor for mono-domain $\mathrm{Fe}_{1/3}\mathrm{NbS}_2$ with input from our DFT calculations within the Kubo linear response formalism [125]. Within this formalism, using the eigenstate representation, the static conductivity tensor $\sigma$ in the zero-temperature

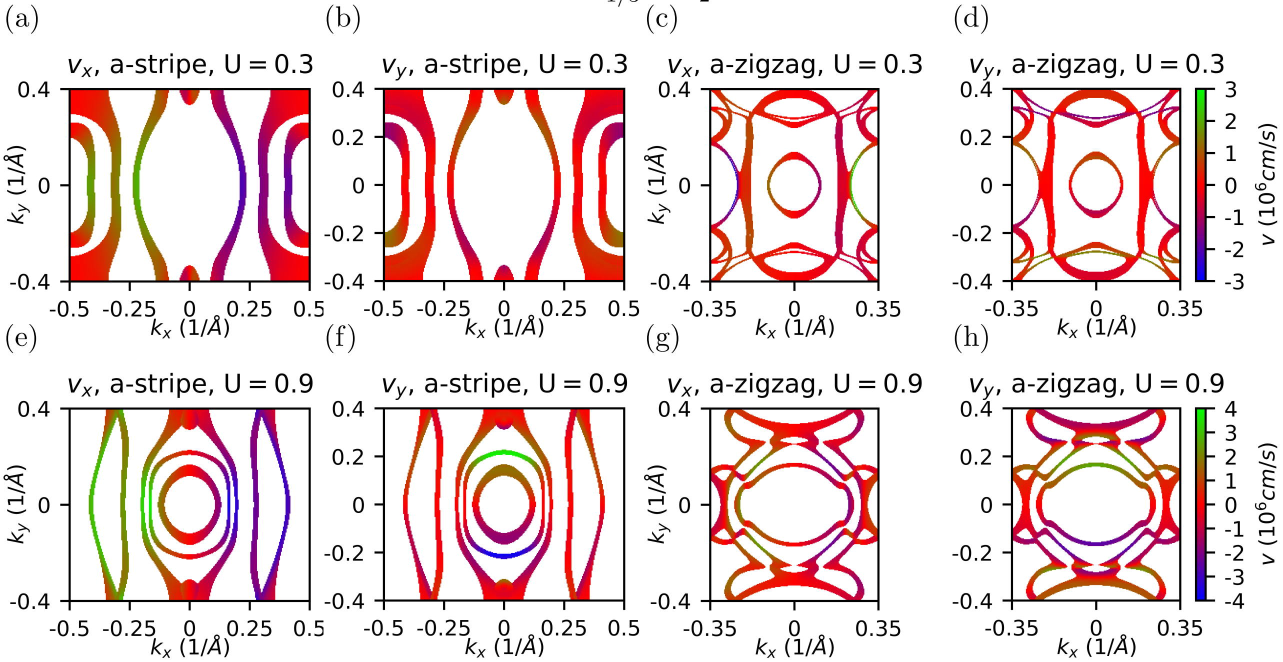

Figure 9.3: Electronic structure in the $k_z = 0$ plane of $\mathrm{Fe_{1/3}NbS_2}$, with a finite broadening for aesthetic purposes of 10 meV for a-stripe order with U = 0.3 ((a)-(b)) and U = 0.9 eV ((e)-(f)), and 2 and 5 meV for a-zigzag order with U = 0.3 ((c)-(d)) and U = 0.9 eV ((g)-(h)) respectively. The plots are colored by either the x or y component of band velocity, as indicated by the title.

limit may be written as [52, 231]

$$\sigma_{ij} = -\frac{e\hbar}{\pi} \sum_{\mathbf{k},n,m} [\Gamma^2 \operatorname{Re}(\langle n\mathbf{k}| \hat{v}_i |m\mathbf{k}\rangle \langle m\mathbf{k}| \hat{v}_j |n\mathbf{k}\rangle)]$$
$$([(E_F - \epsilon_{n\mathbf{k}})^2 + \Gamma^2][(E_F - \epsilon_{m\mathbf{k}})^2 + \Gamma^2])^{-1}, \quad (9.3)$$

with $\epsilon_{n\mathbf{k}}$ the eigenenergy of the corresponding eigenstate $|n\mathbf{k}\rangle$ and $\hat{v}_i$ the velocity operator in the *ith* direction. The indices $n$ and $m$ run over all bands (occupied and unoccupied). We use a constant band broadening $\Gamma$, where $\Gamma = \frac{\hbar}{2\tau}$ is inversely proportional to the electron relaxation time $\tau$, assuming $\tau$ is band and **k**-independent, sufficient for our purposes. The Bloch eigenstates, eigenvalues, and velocity operators in Eq. 9.3 are constructed using Wannier functions obtained from our PBE+U calculations, and Equation 9.3 is evaluated using the Wannier Linear Response software [229]. In general, the linear-response conductivity can also contain a term which is odd under time reversal, whereas Equation 9.3 is even under this operation [231]. However, both a-stripe and a-zigzag magnetism possess time reversal symmetry plus a translation according to their magnetic space groups, such that the part of the conductivity which is odd under time reversal is necessarily zero, leaving us with only Equation 9.3 to evaluate.

Apart from the approximations inherent in our conductivity tensors computed using Equation 9.3, additional deviations from experimental results may come from our use of the pristine $x = \frac{1}{3}$ Fe concentration in all PBE+U calculations, as the recent transport and switching experiments [148, 132] were performed on $\mathrm{Fe_xNbS_2}$ samples with a range of Fe concentrations $x \sim 0.31 - 0.35$. Although NMR data suggests that a spin-glass coexists with the AFM order above and below $x = \frac{1}{3}$, and may well be the underlying mechanism for the efficient switching of the ordered magnetic domains [132], we expect that the electronic structure and transport anisotropy of the stripe and zigzag phases, which we focus on in this paper, will not differ significantly between slightly off-stoichiometry structures and the $x = \frac{1}{3}$ structure we use in our DFT calculations. Moreover, the NMR measurements, as well as contemporary neutron experiments [214], find evidence for a slight in-plane magnetic moment in contrast to the earlier neutron studies [197, 185]. However, given the strong magnetic anisotropy which favors spins to point along the c axis in $\mathrm{Fe_{1/3}NbS_2}$ [54, 70], we expect our focus on calculations of transport properties with collinear magnetic order along c to be an acceptable simplification.

Having obtained conductivity tensors within the constant relaxation time approximation, the resistance R is then the resistivity $\rho = \sigma^{-1}$ multiplied by the ratio of device length to cross-sectional area ($\sim 3.7 \times 10^{-4}$ cm)$^{-1}$[148]. In order to meaningfully compare the anisotropy of the resistance tensors with different magnetic orders and U values, we treat Γ as a parameter and adjust it for each U and magnetic order such that the $R_{xx}$ component of the tensor (corresponding to the resistance along the [100] direction) is roughly equivalent to the experimentally measured resistance of $\mathrm{Fe_{1/3}NbS_2}$ samples, between 0.25-0.3 Ω[131]. Since the samples associated with these values are not mono-domain [148], this measured value does not, strictly speaking, correspond to the $R_{xx}$ of a single domain crystal, but we use it nonetheless to normalize the computed resistance tensors.

The results of our calculations appear in Table 9.1. The transport anisotropy we compute from our PBE+U calculations, which we define quantitatively as $A = \frac{R_{yy}}{R_{xx}}$, is consistent with the calculated band velocities in Figure 9.3. For a-stripe ordering, $R_{yy}$ along [120] is higher than $R_{xx}$ along [100] by roughly a factor of 2, for both U values considered. With a-zigzag ordering however, $R_{yy}$ becomes smaller than $R_{xx}$ ($A < 1$). For both sets of PBE+U calculations, the transport anisotropy for a-zigzag is significantly reduced compared with stripe ordering. Indeed, for U = 0.3 eV the transport anisotropy is nearly unity for zigzag ordering.

Having obtained approximate resistivity tensors for mono-domain $\mathrm{Fe_{1/3}NbS_2}$ with a-stripe and a-zigzag ordering based on our PBE+U calculations, we can infer the current-domain response by comparing with experiment. In the following discussion we use our PBE+U results with U = 0.9 eV. In Figure 9.4a we show the a-b plane of the $\mathrm{Fe_{1/3}NbS_2}$ crystal overlaid with the directions of applied currents and measured resistances for the experiments in references [148] and [132]. In these experiments, DC pulses, $\mathbf{J}_1^{write}$ and $\mathbf{J}_2^{write}$, were applied in succession along the $-k_y/[1\bar{2}0]$ and $k_x/[100]$ crystallographic directions. The low-frequency AC current $\mathbf{J}^{probe}$ used to measure the sample resistance after each writing pulse was applied at an angle of 45° with respect to DC pulses. The transverse resistance

Table 9.1: In-plane transport anisotropy computed for $Fe_{1/3}NbS_2$, defined as $A = \frac{R_{yy}}{R_{xx}}$ with x along [100], for a-zigzag and a-stripe phases for both U values used in our PBE+U calculations. Absolute values of $R_{xx}$ and the values of $\Gamma$ used in Equation 9.3 are provided as well.

| | $U = 0.3$ eV | | $U = 0.9$ eV | |
|---|---|---|---|---|
| | a-stripe | a-zigzag | a-stripe | a-zigzag |
| $\Gamma$ (meV) | 10 | 5 | 30 | 10 |
| $R_{xx}$ ($\Omega$) | 0.26 | 0.28 | 0.28 | 0.25 |
| $A$ | 2.15 | 0.97 | 2.00 | 0.77 |

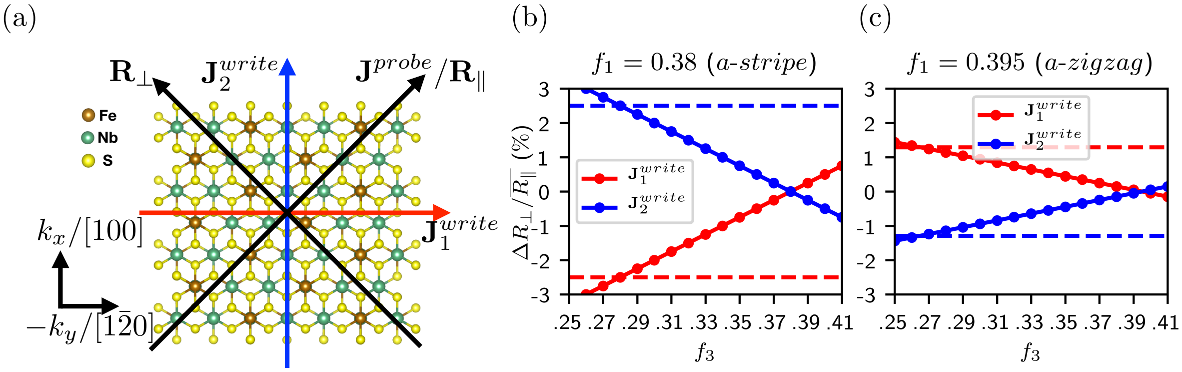

Figure 9.4: Electrical switching. (a) $Fe_{1/3}NbS_2$ crystal structure overlaid with directions of applied currents and measured resistance in experiment. In the experiment, orthogonal pulses applied along the red and blue arrows switch $Fe_{1/3}NbS_2$ between two states with different domain populations, detected by changes in the transverse resistance $\mathbf{R}_\perp$. (b)-(c) Calculated $\frac{\Delta \mathbf{R}_\perp}{\mathbf{R}_\parallel}$ based on equations 9.4 (red) and 9.5 (blue) as a function of $f_3$ for a fixed initial value of $f_1$. $f_1$ ($f_3$) can be viewed as the resulting fractional population of the domain with principle axis along [100] after $\mathbf{J}_1^{write}$ ($\mathbf{J}_2^{write}$). (b) corresponds to a-stripe phase, (c) corresponds to a-zigzag phase. Dashed lines (same color coding as the PBE+U-derived points) indicate the value of $f_3$ where the calculated $\frac{\Delta \mathbf{R}_\perp}{\mathbf{R}_\parallel}$ agrees with the experimental data in reference Maniv2021 for Fe intercalations likely corresponding to a-stripe and a-zigzag order.

$\mathbf{R}_\perp$ was read out along the contact which is orthogonal to $\mathbf{J}^{probe}$. Note that this is equal to the $\mathbf{R}_{xy}$ component of the resistance tensor with $x$ axis along $\mathbf{J}^{probe}$; we obtain this tensor by a rotation of our computed resistance matrix with $x$ axis along [100][233] (see Appendix 9.9 for details). The experimental changes in $\mathbf{R}_\perp$, normalized by the longitudinal resistance $\mathbf{R}_\parallel$ along $\mathbf{J}^{probe}$, are shown in reference [132] to be $\sim 2.5\%$ and $\sim 1.3\%$ (when normalized to the same DC pulse current density) for Fe intercalations corresponding to $x = 0.31$ and $x = 0.35$ respectively; the smaller intercalation was used in reference [148] as well. In addition to the reduction in magnitude of $\frac{\Delta \mathbf{R}_\perp}{\mathbf{R}_\parallel}$ going from the under-intercalated to over-intercalated sample, the sign of resistance change also switches; specifically, for $x = 0.31$ a pulse along $\mathbf{J}_1^{write}$ causes a decrease in $\mathbf{R}_\perp$ whereas for $x = 0.35$, $\Delta\mathbf{R}_\perp$ is positive after a pulse along $\mathbf{J}_1^{write}$. In interpreting the experimental results, we assume that $x = 0.31$ and $x = 0.35$ correspond to a-stripe and a-zigzag order respectively, as implied by neutron measurements (in addition to the results by Van Laar and Suzuki[197, 185], a recent more systematic analysis of Fe concentration specifically indicates a stripe ground state for $x \leq \frac{1}{3}$ and a zigzag AFM ground state for $x \geq \frac{1}{3}$[214].) We note also that both zigzag and stripe magnetic space groups are consistent with the three-fold AFM domain structure observed by Little et al. (where the zigzags/stripe directions for each domain are related by 120° rotations about c[116].)

With these assumptions of the experimental magnetic order, we can explore the implications of our computed resistance tensors for domain repopulation with a-stripe and a-zigzag magnetism. We assume the total transverse resistance after each $\mathbf{J}_1^{write}$ or $\mathbf{J}_2^{write}$ pulse is proportional to the sum of resistances of the three domains, weighted by their fractional areas $f$, analogously to previous studies of domain-based anisotropic magnetoresistance[104]. Then, we have

$$[1\bar{2}0]/\mathbf{J}_1^{write} \rightarrow \mathbf{R}_\perp^{\mathbf{J}_1^{write}} = f_1\mathbf{R}_\perp^{[100]} + f_2(\mathbf{R}_\perp^{[010]} + \mathbf{R}_\perp^{[\bar{1}\bar{1}0]}); \tag{9.4}$$

and

$$[100]/\mathbf{J}_2^{write} \rightarrow \mathbf{R}_\perp^{\mathbf{J}_2^{write}} = f_3\mathbf{R}_\perp^{[100]} + f_4(\mathbf{R}_\perp^{[010]} + \mathbf{R}_\perp^{[\bar{1}\bar{1}0]}), \tag{9.5}$$

where $\mathbf{R}_\perp^{[010]}$ for example is the transverse resistance for a single domain with principle axis along [010]. $f_1$ and $f_2$ are fractional domain populations after a $\mathbf{J}_1^{write}$ pulse, $f_3$ and $f_4$ result from a $\mathbf{J}_2^{write}$ pulse, and we set $f_2 = (1-f_1)/2$ and $f_4 = (1-f_3)/2$ in equations 9.4 and 9.5 to ensure the fractions add to unity. We assume in each case that $f([010]) = f([\bar{1}\bar{1}0])$ because both writing pulses bisect these two axes; the resistance tensors for the three domains are connected by rotations of $2\pi/3$. The $\mathbf{R}_\perp$ values in equations 9.4 and 9.5 are obtained from the off-diagonal components of these tensors.

We can calculate the relative fractional domain changes required to reproduce the experimental switching amplitudes for the pulses, defined as

$$\frac{\Delta\mathbf{R}_\perp^{\mathbf{J}_1^{write}/\mathbf{J}_2^{write}}}{\bar{\mathbf{R}}_\parallel} = \frac{\mathbf{R}_\perp^{\mathbf{J}_1^{write}/\mathbf{J}_2^{write}} - \bar{\mathbf{R}}_\perp}{\bar{\mathbf{R}}_\parallel}, \tag{9.6}$$

where

$$\bar{\mathbf{R}}_\perp = (\mathbf{R}_\perp^{\mathbf{J}_1^{write}} + \mathbf{R}_\perp^{\mathbf{J}_2^{write}})/2; \bar{\mathbf{R}}_\parallel = (\mathbf{R}_\parallel^{\mathbf{J}_1^{write}} + \mathbf{R}_\parallel^{\mathbf{J}_2^{write}})/2 \tag{9.7}$$

are the averages of the two resistances. We do this by selecting constant values of $f_1$ (fraction of [100] domain after $\mathbf{J}_1^{write}$) and plotting $\frac{\Delta\mathbf{R}_\perp}{\bar{\mathbf{R}}_\parallel}$ for both $\mathbf{J}_1^{write}$ and $\mathbf{J}_2^{write}$ as a function of $f_3$ (fraction of [100] domain after $\mathbf{J}_2^{write}$). Note that $\Delta\mathbf{R}_\perp^{\mathbf{J}_1^{write}}/\bar{\mathbf{R}}_\parallel$ and $\Delta\mathbf{R}_\perp^{\mathbf{J}_2^{write}}/\bar{\mathbf{R}}_\parallel$ are each dependent on both $f_1$ and $f_3$ through $\bar{\mathbf{R}}_\perp$ and $\bar{\mathbf{R}}_\parallel$ defined in equation 9.7. Results based on our PBE+U (with U = 0.9 eV) calculations are shown in Figures 9.4b and 9.4c. In both plots we have selected $f_1$ such that the values of $f_1$ and $f_3$ which yield the experimental resistance changes are symmetrically displaced about $f = \frac{1}{3}$, which is the equilibrium fraction we would expect for all three domains in the absence of external current. We emphasize however that for a given magnetic order, the qualitative results are identical regardless of the value of $f_1$, i.e. the sign and magnitude of the fractional change $f_1 - f_3$ of domain [100] between the the pulses remains constant. The dashed lines correspond to the experimental percent values for the intercalation corresponding to the same magnetic order. We see that, as a consequence of the crossover in the computed anisotropy from $A > 1$ for a-stripe to $A < 1$ for a-zigzag, the current-domain response for both magnetic structures is the same assuming the experimental data with opposite $\mathbf{\Delta R}_{\perp}$ signs indeed corresponds to the two proposed magnetic orders. Specifically, to replicate the correct sign of switching from experiment, for *both* a-stripe and a-zigzag order, $f_1 - f_3 > 0$. This means that the $\mathbf{J}_1^{write}$ pulse along $[1\bar{2}0]$ causes a fractional increase in the orthogonal [100] domain, whereas the $\mathbf{J}_2^{write}$ pulse parallel to [100] destabilizes the [100] domain and increases the fraction of domains alongs [010] and $[\bar{1}\bar{1}0]$. Moreover, we can see that experimental reduction in switching amplitude for a-zigzag order compared to a-stripe is consistent with the reduced in-plane anisotropy we find for a-zigzag order in our PBE+U calculations. Indeed, using our U = 0.9 eV PBE+U results, the computed fractional changes from the equilibrium distribution $\frac{1}{3} : \frac{1}{3} : \frac{1}{3}$ required to match the corresponding experimental resistance changes are very close, $f_1 = 0.38$ for a-stripe and $f_1 = 0.395$ for a-zigzag, as one would expect for a given current density.

## 9.7 Discussion and Conclusion

We have used DFT calculations to understand the magnetism and origins of the electrical switching observed in $Fe_{1/3}NbS_2$. Our PBE+U calculations indicate that the experimentally proposed a-stripe and a-zigzag magnetic phases are nearly degenerate, consistent with neutron data[197, 185, 214] indicating that the ground state switches for small changes in Fe concentration. We find that the in-plane Fermi surface and corresponding transport for a-stripe order is anisotropic, with $R_{yy} > R_{xx}$, for all values of U used in our PBE+U calculations. The FS and transport for a-zigzag order is also anisotropic but the degree of anisotropy is reduced relative to stripe, and the quantitative results are highly sensitive to small changes in the Hubbard U used. Our findings suggest that there are two important factors leading to the particularly high anisotropy in electronic structure and transport for stripe order in $Fe_{1/3}NbS_2$. Firstly, the reduction of six-fold symmetry in the high-temperature paramagnetic phase to two-fold symmetry due to the in-plane stripe magnetic order is consistent with the high anisotropy of the FS. Isostructural $Co_{1/3}NbS_2$, also believed to have a stripe ground state, has been reported to have an anisotropic FS with quasi-flat bands much like $Fe_{1/3}NbS_2$ from prior DFT calculations[162]. With a-zigzag ordering however, the anisotropy in electronic structure and transport for $Fe_{1/3}NbS_2$, while still present, is significantly reduced in spite of an identical reduction to two-fold rotational symmetry due to the magnetic order.

This suggests that the magnetic interactions between nearest Fe neighbors may play an even larger role than rotational symmetry reduction in determining the degree of anisotropy in transport.

Our calculations also reveal that, for both a-zigzag and a-stripe magnetic order, a pulse along a given direction should disfavor domains whose principle axes (and stripes/zigzags) are parallel to the pulse, and increase the populations of the other two domains. This directional dependence has implications for the microscopic details of the mechanism responsible for the current-induced domain repopulation. Further studies are required to understand the origins of the current-domain coupling which leads to domains parallel to the current pulse being disfavored, and whether this is consistent with the spin glass-mediated spin-orbit torque mechanism proposed in reference [132].

To be more concrete, we explicitly mention two possible future experimental outcomes for which our computed current-domain response will be informative. First, if further neutron scattering studies show unambiguously that the Fe spins in $Fe_{1/3}NbS_2$ have zero in-plane component, the origin of current-induced switching must differ from traditional spin-orbit torque mechanisms, including the spin-glass mediated case proposed in reference [132]. This is because the in-plane directionality of the spin-orbit torque in the experimental geometry could not result in a switching between domains with the Néel vector fully along [001] for all three domains. In this situation, knowledge of the directionality of domain stabilization could inform the search for a novel switching mechanism. Alternatively, further studies expanding on reference [132] may definitively establish the direction in which polarized electrons in the coexisting spin glass are rotating a small in-plane component of the Néel vector in the ordered a-stripe and a-zigzag phases studied in this manuscript (i.e., away from or toward the current). This information, combined with our finding that a current pulse destabilizes domains with principle axes parallel to the pulse, will indicate the likely direction of the in-plane Néel vector component for a given domain. To be specific, if the current is found to rotate the in-plane component of the Néel vector away from the current pulse, our current-domain response findings indicate that the in-plane component is along the direction of the domain principle axis (parallel to the stripes or zigzags). However, if the current tends to align the in-plane Néel vector component parallel to the pulse, this suggests that the small in-plane moment is perpendicular to the direction of the domain principle axis. Overall, our transport and electronic structure calculations support repopulation of magnetic domains being the underlying cause of electrical switching in $Fe_{1/3}NbS_2$, and provide a platform for future studies.

## 9.8 Appendix I: Commentary on PBE+U Treatment

As mentioned in the main manuscript, to approximately account for the localized nature of the $d$ electrons in $Fe^{2+}$, we add a Hubbard U correction (GGA+U)[6], and we select the rotationally invariant version of GGA+U by Dudarev et al.[45] Magnetic properties such as magnetic moment, ground state order, and magnetoanisotropy energy (MAE) can be extremely sensitive to the choice of Hubbard U; this is particularly well documented in the case of Fe-based compounds[219, 24]. Thus, it is crucial to rationalize our selection of U values. Perhaps the most consistent experimental finding across all studies of $Fe_{1/3}NbS_2$ is a very large MAE, with the easy axis of Fe spins lying along the $c$ ([001]) axis of the hexagonal unit cell[54, 185, 70]. Hence, in a recent study on $Fe_{1/3}NbS_2$[70], we chose U to recover the best experimental estimate of the MAE. From comparing Curie-Weiss temperatures with magnetic fields along [001] and [100], a quantitative estimate of the anisotropy $D = 1 \pm 0.2$ meV per Fe atom was established[70]. Note that $D$ is the so-called anisotropy constant defined through the MAE contribution to total energy:

$$E_{MAE} = -D \sum_i (S_z^i)^2, \tag{9.8}$$

where the sum is over all Fe spins in the unit cell. $E_{MAE}$ and $D$ can be calculated within DFT simply by comparing self-consistent total energies in the case of all $Fe^{2+}$ spins aligned along the a([100]) axis and along the c ([001]) axis:

$$D = \frac{E_{[100]} - E_{[001]}}{2S^2}, \tag{9.9}$$

where we use $S = 2$ for the $Fe^{2+}$ spins. The factor of two accounts for the two Fe atoms in the primitive unit cell. The PBE+U value of $D$ as a function of U is shown in Figure 9.5. We find that for values greater than $U = 2$ eV, PBE+U incorrectly predicts a negative MAE, implying an easy axis in-plane, along a, rather than c. Below $U = 2$ eV, $D$ changes non-monotically with U, increasing rapidly to large positive values (easy axis along c) before decreasing again below $U \sim 1.3$ eV. We find that a very small $U = 0.3$ eV gives $D = 1.09$ meV/Fe, in good agreement with experiment.

However, in examining the Fermi surface and transport anisotropy using $U = 0.3$ eV in the present study, we found negligible anisotropy for a-zigzag magnetic ordering, implying that a domain repopulation would have no effect on the sample resistance for zigzag ordering. The large contribution of Fe d states at the Fermi level for $Fe_{1/3}NbS_2$ (see Section **??**) makes the Fermi surface and transport extremely sensitive to small changes in U; thus we hypothesize that the isotropic transport with a-zigzag ordering for $U = 0.3$ eV is coincidental. We therefore repeated our calculations with $U = 0.9$ eV, with which the MAE as computed by PBE+U is overestimated (D = 11.95 meV/Fe), but has the correct sign. As shown in the main manuscript, the transport for a-zigzag order becomes much more anisotropic than with $U = 0.3$ eV, with $A = \frac{R_{yy}}{R_{xx}} = 0.77$. We note that, with a-zigzag order (a) although nearly isotropic, $R_{yy} < R_{xx}$ with $U = 0.3$ eV for reasonable values of $\Gamma$ used in the constant relaxation time approximation; and (b) a calculation with $U = 4$ eV (see later in Supplement), not included in the main manuscript, also yields $R_{yy} < R_{xx}$ with $A = 0.74$. Thus, we are quite confident of the qualitative finding $R_{yy} < R_{xx}$, even though the reduced magnitude of anisotropy makes it less unambiguous than our results for a-stripe.

Finally we explored whether the near-isotropic transport for a-zigzag at U = 0.3 eV might

Table 9.2: Calculated intraplane nearest neighbor spin exchange $\mathbf{J}_1$, in meV/Fe atom, and anisotropy $A = \frac{R_{yy}}{R_{xx}}$ with a-stripe and a-zigzag magnetic order for the two U values used for our PBE+U calculations in the main text, as well results with artificially expanded lattice parameters. The values of $\Gamma$ used in the Kubo linear response conductivity calculation and the resulting $R_{xx}$ (along [100]) are included as well.

| | U = 0.3 eV, experimental lat. | U = 0.9 eV | U = 0.3 eV, 1.05 lat |
|---|---|---|---|
| $\mathbf{J}_1$ (meV/Fe) | 0.76 | 0.57 | 0.11 |
| $A$, a-stripe | 2.15 | 2.0 | 1.88 |
| $\Gamma$ (meV) | 10 | 30 | 10 |
| $R_{xx}$ ($\Omega$) | 0.26 | 0.28 | 0.31 |
| $A$, a-zig | 0.97 | 0.77 | 0.96 |
| $\Gamma$ (meV) | 5 | 10 | 5 |
| $R_{xx}$ ($\Omega$) | 0.28 | 0.25 | 0.26 |

be connected to the overestimation of nearest-neighbor Heisenberg spin exchange parameters at this U value, as we reported in reference [70]. While the magnitude of MAE and *relative* values of different Heisenberg exchange parameters computed with U = 0.3 eV led to good agreement with experiment in reference [70], the magnitudes of our coupling parameters were overestimated by roughly a factor of 5. This was part of our motivation in this study for examining another U value larger than 0.3 eV, rather than smaller, as increased electron localization from the higher U is expected to lead to smaller orbital overlap, and hence smaller Heisenberg exchange parameters [115]. The nearest neighbor in-plane spin exchange parameter $\mathbf{J}_1$, as calculated with PBE+U for U = 0.9 eV, is reduced by nearly 25% as shown in Table 9.2, as expected. To test whether the changes in quantitative anisotropy were directly caused by the decrease in $\mathbf{J}_1$ rather than other effects influenced by U values, we repeated the transport and magnetic studies for U = 0.3 eV using a crystal structure with all three lattice constants expanded by 5% from the experimental values, to artificially decrease the exchange constants while keeping the U value constant. However, as shown in Table 9.2, while $\mathbf{J}_1$ decreases dramatically, much more so than when using U = 0.9 eV, compared to the calculations with experimental lattice constants, the anisotropy for a-zigzag order remains nearly constant (a-stripe anisotropy on the other hand does decrease). Thus, it seems that subtle changes in the electronic structure from the specific choice of U, which are independent of the Heisenberg exchange parameters, are responsible for the highly sensitive transport properties.

## 9.9 Appendix II: Rotation of coordinate system to determine conductivity of magnetic domains

The Kubo conductivity matrix $\sigma$ discussed in the main text is a second-order tensor with components $\sigma_{ij}$ referring to the conductance measured in the *jth* direction given an applied

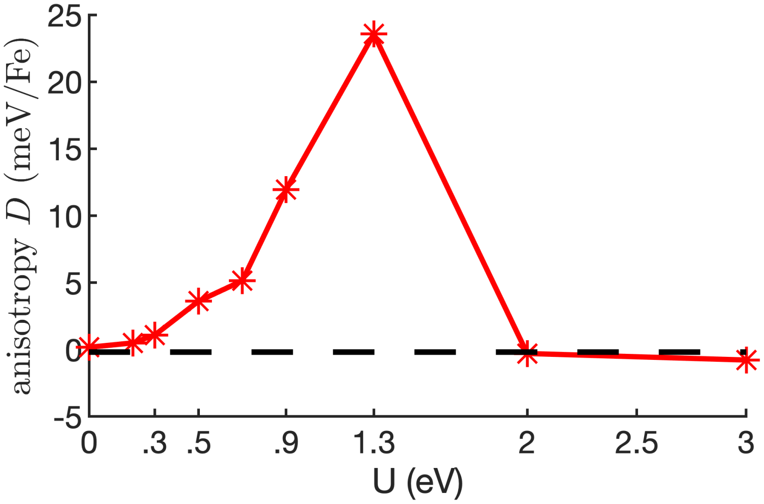

Figure 9.5: Magnetoanisotropy constant D as a function of effective Hubbard U for $\mathrm{Fe}_{1/3}\mathrm{NbS}_2$. Positive values indicate an easy axis along c, whereas negative values indicate an easy plane (spanned by a and b). $U = 0.3$ eV gives the best agreement with experiment, with $D = +1.09$ meV/Fe.

electric current in the *ith* direction. The magnetic space groups of the a-stripe order and a-zigzag order in $\mathrm{Fe}_{1/3}\mathrm{NbS}_2$ (specifically, $P_C2_12_12_1$ and $P_c2_12_12$ respectively) dictate the symmetry-allowed form of the tensor. With our coordinate system defined as having $x$ along the [100] direction (along the magnetic stripes/zigzags), and $y$ along the [120] direction in terms of the hexagonal lattice vectors, this form for both space groups is

$$\sigma = \begin{pmatrix} \sigma_{xx} & 0 & 0 \\ 0 & \sigma_{yy} & 0 \\ 0 & 0 & \sigma_{zz} \end{pmatrix}, \tag{9.10}$$

with all off-diagonal elements constrained to 0. This is consistent with our numerically calculated tensor for mono-domain $\mathrm{Fe}_{1/3}\mathrm{NbS}_2$. The resistivity tensor $\rho = \sigma^{-1}$ in this coordinate system has the same form:

$$\rho = \begin{pmatrix} \frac{1}{\sigma_{xx}} & 0 & 0 \\ 0 & \frac{1}{\sigma_{yy}} & 0 \\ 0 & 0 & \frac{1}{\sigma_{zz}} \end{pmatrix}. \tag{9.11}$$

Recall however, that for the device geometry used to write and read magnetization changes in $\mathrm{Fe}_{1/3}\mathrm{NbS}_2$, the current $\mathbf{J}^{probe}$ used to measure resistivity is applied at an angle of 45° with respect to the [100] crystalline axis. Thus, to model the actual transport measurements for the [100] oriented domain, we need to rotate the coordinate system of our resistivity tensor so that the $x$ axis is along $\mathbf{J}^{probe}$:

$$\rho^{[100]}_{measured} = \mathbf{R}_{\pi/4} \times \rho_0 \times \mathbf{R}^{-1}_{\pi/4}, \tag{9.12}$$

where $\rho^{[100]}_{measured}$ is the resistivity tensor for the [100] domain with $x$ axis along $\mathbf{J}^{probe}$, $\rho_0$ is our original ab-initio resistivity tensor with $x$ axis along [100], and

$$\mathbf{R}_{\pi/4} = \begin{pmatrix} \frac{1}{\sqrt{2}} & \frac{-1}{\sqrt{2}} & 0 \\ \frac{1}{\sqrt{2}} & \frac{1}{\sqrt{2}} & 0 \\ 0 & 0 & 1 \end{pmatrix} \tag{9.13}$$

is the matrix which rotates the coordinate system about the $z$/[001] axis by an angle of 45°. $\mathbf{R}_\perp$ in the main text (assuming a single domain along [100]) is then just the $(xy)$ component of $\rho^{[100]}_{measured}$ (which is no longer 0 in the rotated coordinate system). Following the same procedure, to obtain the resistivity tensor with $x$ along $\mathbf{J}^{probe}$ for the domains along [010] and $[\bar{1}\bar{1}0]$ we rotate $\rho^{[100]}_{measured}$ by an additional $2\pi/3$ and $4\pi/3$ respectively:

$$\rho^{[010]}_{measured} = \mathbf{R}_{2\pi/3} \times \rho^{[100]}_{measured} \times \mathbf{R}^{-1}_{2\pi/3}; \tag{9.14}$$

$$\rho^{[\bar{1}\bar{1}0]}_{measured} = \mathbf{R}_{4\pi/3} \times \rho^{[100]}_{measured} \times \mathbf{R}^{-1}_{4\pi/3}, \tag{9.15}$$

where $\mathbf{R}_{2\pi/3}$ and $\mathbf{R}_{4\pi/3}$ are again rotation matrices.

It should be noted that in the above methodology, we are implicitly assuming that the observed anisotropic magnetoresistance (AMR) in $\mathrm{Fe}_{1/3}\mathrm{NbS}_2$ is dominated by noncrystalline contributions [167]; that is, the transport signal is dependent only on the absolute angle subtended by the current and the direction of the magnetic stripes.

# Chapter 10

# Outlook

In this thesis, we have used DFT calculations to characterize properties which could be leveraged for technological applications in several topological semimetals and an electrically switchable AFM. We have also examined ways in which we can tune the ground state material properties to bring them closer to our desired functionalities. In Chapter 5 for example, we show that substitution of the transition metal ion in TMDs with topological ladders can bring the topological features closer to the Fermi level. In Chapter 6, we enforce metastable ferromagnetic order in hexagonal manganites to change the electronic structure from trivially insulating to topological and semimetallic. Our studies in Chapter 9 of transport anisotropy in $Fe_{1/3}NbS_2$ suggest that the contrast in resistance states induced by electrical switching of antiferromagnetic domains can be enhanced or decreased depending on the underlying AFM order (i.e. whether $Fe_{1/3}NbS_2$ is in the "stripe" or "zigzag" AFM phase). Our studies provide improved insight on the properties and tunability of TSMs and electrically switchable AFMs within the versatile material motifs of hexagonal oxides and TMDs. They also motivate questions for continued work in this subspace of functional materials. We will mention just a few here.

In our first-principles investigation of TSM features in hexagonal manganites in Chapter 6, we point out that while our findings of nontrivial topology in such tunable systems is highly promising for practical applications, many challenges must be overcome to experimentally realize the metastable structures studied in our DFT calculations. $YCrO_3$ and $YVO_3$ both have an orthorhombic space group as their ground state, but as discussed in reference [2] for the case of $YFeO_3$, it is possible to stabilize the hexagonal structure via epitaxial strain. A DFT-based total energy mapping for the orthorhombic versus hexagonal phases of $YCrO_3$ and $YVO_3$ as a function of strain would be invaluable in determining the feasibility of epitaxial stabilization for these particular compounds. Additionally, TSM features in hexagonal $YCrO_3$ and $YVO_3$ occur in the centrosymmetric $P6_3/mmc$ space group which is normally energetically favorable only at high temperatures where the magnetism is disordered; thus, in order to stabilize the FM magnetic order which induces the TSM band structures, some method of stabilizing the $P6_3/mmc$ phase at low temperatures is likely necessary. Griffin et al. found in reference [65] that for the hexagonal manganite $InMnO_3$, Ga alloying on the

Mn site favored the centrosymmetric $P6_3/mmc$ phase at low temperatures. This provides motivation for further studies of the stability of $P6_3/mmc$ relative to the polar $P6_3cm$ phase of $YCrO_3$ and $YVO_3$ upon alloying, and whether the TSM band structures remain robust with this alloying.

While our studies of electrically switchable AFMs focus on the single intercalated TMD $Fe_{1/3}NbS_2$, the high tunability of magnetically intercalated TMDs via intercalant species, intercalant concentration and TMD base suggests that other compounds in this space might also be promising for spintronics applications. To this end, DFT characterizations of the ground state magnetic order, electronic structure, and symmetry-dictated form of the spin-orbit torque for other magnetically intercalated TMDs would be instructive. For Fe-intercalated $NbS_2$, as mentioned in Chapters 8 and 9, our DFT calculations thus far only use the stoichiometric $x = \frac{1}{3}$ concentration of Fe, whereas experimental characterizations of the electrical switching suggest that a disordered spin-glass background at concentrations slightly above and below $\frac{1}{3}$ enhances the efficiency of the SOT [132]. While computationally challenging due to the large supercells required to mimic the concentrations, more comprehensive DFT studies of the magnetic order and transport anisotropy of $Fe_{1/3+\delta}NbS_2$ for small $\delta$ would provide further insight into the experimental observations.

Finally, we mention that there has been some recent experimental evidence that the topological Dirac semimetal $NiTe_2$ which we characterize in Chapter 5 may become superconducting when doped with Re on the Ni site [130]. The coexistence of TSM features and superconductivity holds great promise in the application of topological quantum computation in particular. We are currently performing DFT calculations to investigate the effect of Re substitution on the electronic structure of $Ni_{(1-x)}Re_xTe_2$, in particular, whether Fermi surface reconstruction that could facilitate the superconductivity appears to occur.

# Bibliography

[1] *Adobe inc.: Adobe Illustrator.* (Visited on 01/05/2020).

[2] Suk Jin Ahn et al. “Artificially imposed hexagonal ferroelectricity in canted antiferromagnetic YFeO3epitaxial thin films”. In: *Materials Chemistry and Physics* 138.2-3 (2013), pp. 929–936. ISSN: 02540584. DOI: 10.1016/j.matchemphys.2012.12.086.

[3] Jason Alicea, Andrey V Chubukov, and Oleg A Starykh. “Quantum Stabilization of the 1/3-Magnetization Plateau in Cs2CuBr4”. In: *Phys. Rev. Lett.* 102.13 (2009), p. 137201. DOI: 10.1103/PhysRevLett.102.137201. URL: https://link.aps.org/doi/10.1103/PhysRevLett.102.137201.

[4] V.I. Anisimov et al. “Spin Bags, Polarons, and Impurity Potentials in La_2-xSr_xCuO_4 from First Principles”. In: *Physical Review Letters* 68.3 (1992), pp. 345–348. ISSN: 00319007. DOI: 10.1103/PhysRevLett.68.345.

[5] Vladimir I. Anisimov, F. Aryasetiawan, and A. I. Lichtenstein. “First-principles calculations of the electronic structure and spectra of strongly correlated systems: The LDA + U method”. In: *Journal of Physics Condensed Matter* 9.4 (1997), pp. 767–808. ISSN: 09538984. DOI: 10.1088/0953-8984/9/4/002.

[6] Vladimir I. Anisimov, F. Aryasetiawan, and A. I. Lichtenstein. “First-principles calculations of the electronic structure and spectra of strongly correlated systems: The LDA + U method”. In: *Journal of Physics Condensed Matter* 9.4 (1997), pp. 767–808. ISSN: 09538984. DOI: 10.1088/0953-8984/9/4/002.

[7] Vladimir I. Anisimov, Jan Zaanen, and Ole K. Andersen. “Band theory and Mott insulators: Hubbard U instead of Stoner I”. In: *Physical Review B* 44.3 (1991), pp. 943–954. ISSN: 01631829. DOI: 10.1103/PhysRevB.44.943. arXiv: 0603670 [cond-mat].

[8] K Anzenhofer et al. “The crystal structure and magnetic susceptibilities of MnNb3S6, FeNb3S6, CoNb3S6 and NiNb3S6”. In: *Journal of Physics and Chemistry of Solids* 31.5 (1970), pp. 1057–1067.

[9] N. P. Armitage, E. J. Mele, and Ashvin Vishwanath. “Weyl and Dirac semimetals in three-dimensional solids”. In: *Reviews of Modern Physics* 90.1 (2018), p. 015001. ISSN: 0034-6861. DOI: 10.1103/RevModPhys.90.015001. arXiv: 1705.01111. URL: https://link.aps.org/doi/10.1103/RevModPhys.90.015001.

[10] Mois I. Aroyo et al. “Bilbao Crystallographic Server. II. Representations of crystallographic point groups and space groups”. In: *Acta Crystallographica Section A: Foundations of Crystallography* 62.2 (2006), pp. 115–128. ISSN: 01087673. DOI: `10.1107/S0108767305040286`.

[11] Mois Ilia Aroyo et al. “Bilbao Crystallographic Server: I. Databases and crystallographic computing programs”. In: *Zeitschrift fur Kristallographie* 221.1 (2006), pp. 15–27. ISSN: 00442968. DOI: `10.1524/zkri.2006.221.1.15`.

[12] M. S. Bahramy et al. “Ubiquitous formation of bulk Dirac cones and topological surface states from a single orbital manifold in transition-metal dichalcogenides”. In: *Nature Materials* 17.1 (2018), pp. 21–27. ISSN: 14764660. DOI: `10.1038/NMAT5031`. arXiv: `1702.08177`.

[13] V. V. Bel’kov and S. D. Ganichev. “Magneto-gyrotropic effects in semiconductor quantum wells”. In: *Semiconductor Science and Technology* 23.11 (2008). ISSN: 02681242. DOI: `10.1088/0268-1242/23/11/114003`. arXiv: `0803.0949`.

[14] L Berger. “Emission of spin waves by a magnetic multilayer traverse by a current”. In: *Physical Review B* 54.13 (1996), pp. 9353–9358.

[15] C R Bertaut, E. F., Forrat, F., Fang. “No Title”. In: *Acad. Sci., Paris, C. R.* 256 (1963), p. 1958.

[16] Ganesh R. Bhimanapati et al. “Recent Advances in Two-Dimensional Materials beyond Graphene”. In: *ACS Nano* 9.12 (2015), pp. 11509–11539. ISSN: 1936086X. DOI: `10.1021/acsnano.5b05556`.

[17] G. Bian, T. Miller, and T. C. Chiang. “Passage from spin-polarized surface states to unpolarized quantum well states in topologically nontrivial Sb films”. In: *Physical Review Letters* 107.3 (2011), pp. 1–4. ISSN: 00319007. DOI: `10.1103/PhysRevLett.107.036802`.

[18] Guang Bian et al. “Drumhead surface states and topological nodal-line fermions in TlTaSe2”. In: *Physical Review B* 93.12 (2016), pp. 2–7. ISSN: 24699969. DOI: `10.1103/PhysRevB.93.121113`. arXiv: `1508.07521`.

[19] Guang Bian et al. “Topological nodal-line fermions in spin-orbit metal PbTaSe2”. In: *Nature Communications* 7 (2016), pp. 1–8. ISSN: 20411723. DOI: `10.1038/ncomms10556`.

[20] P. Blaha et al. *Wien2k, An Augmented Plane Wave + Local Orbitals Program for Calculating Crystal Properties*. 2001.

[21] P. E. Blöchl. “Projector augmented-wave method”. In: *Physical Review B* 50.24 (1994), pp. 17953–17979. ISSN: 01631829. DOI: `10.1103/PhysRevB.50.17953`. arXiv: `arXiv:1408.4701v2`.

[22] P E Blöchl, O. Jepsen, and Ole K Andersen. “Improved tetrahedron”. In: *Physical Review B* 49.23 (1994), pp. 16223–16233.

[23] S. Yu Bodnar et al. “Writing and reading antiferromagnetic Mn2Au by Neél spin-orbit torques and large anisotropic magnetoresistance”. In: *Nature Communications* 9.1 (2018), pp. 1–7. ISSN: 20411723. DOI: 10.1038/s41467-017-02780-x. arXiv: 1706.02482.

[24] Eric Bousquet and Nicola Spaldin. “J dependence in the LSDA+U treatment of non-collinear magnets”. In: *Physical Review B - Condensed Matter and Materials Physics* 82.22 (2010), pp. 1–4. ISSN: 10980121. DOI: 10.1103/PhysRevB.82.220402.

[25] Arne Brataas, Andrew D. Kent, and Hideo Ohno. “Current-induced torques in magnetic materials”. In: *Nature Materials* 11.5 (2012), pp. 372–381. ISSN: 14764660. DOI: 10.1038/nmat3311.

[26] G. Brumfiel. “Topological Insulators: star material”. In: *Nature* 466 (2010), pp. 310–311.

[27] A. A. Burkov, M. D. Hook, and Leon Balents. “Topological nodal semimetals”. In: *Physical Review B - Condensed Matter and Materials Physics* 84.23 (2011), pp. 1–14. ISSN: 10980121. DOI: 10.1103/PhysRevB.84.235126. arXiv: 1110.1089.

[28] Ching Kit Chan et al. “Photocurrents in Weyl semimetals”. In: *Physical Review B* 95.4 (2017), pp. 1–5. ISSN: 24699969. DOI: 10.1103/PhysRevB.95.041104. arXiv: 1607.07839.

[29] Ching Kit Chan et al. “Type-II Weyl cone transitions in driven semimetals”. In: *Physical Review B* 94.12 (2016), pp. 1–5. ISSN: 24699969. DOI: 10.1103/PhysRevB.94.121106. arXiv: 1605.05696.

[30] Y. H. Chan et al. “Ca3 P2 and other topological semimetals with line nodes and drumhead surface states”. In: *Physical Review B* 93.20 (2016), pp. 1–16. ISSN: 24699969. DOI: 10.1103/PhysRevB.93.205132. arXiv: 1510.02759.

[31] Guoqing Chang et al. “Room-temperature magnetic topological Weyl fermion and nodal line semimetal states in half-metallic Heusler Co2 TiX (X=Si, Ge, or Sn)”. In: *Scientific Reports* 6.June (2016), pp. 1–9. ISSN: 20452322. DOI: 10.1038/srep38839.

[32] Claude Chappert, Albert Fert, and Frederic Nguyen Van Dau. “The emergence of spin electronics in data storage”. In: *Nature Materials* 6.11 (2007), pp. 813–823. ISSN: 1476-1122. arXiv: 1003.4058. URL: http://www.nature.com/articles/nmat2024{\%}0Ahttps://www.nature.com/articles/nmat2024.

[33] C. Chen et al. “Dirac line nodes and effect of spin-orbit coupling in the nonsymmorphic critical semimetals MSiS (M=Hf, Zr)”. In: *Physical Review B* 95.12 (2017), pp. 1–7. ISSN: 24699969. DOI: 10.1103/PhysRevB.95.125126. arXiv: 1701.06888.

[34] X. Z. Chen et al. “Antidamping-Torque-Induced Switching in Biaxial Antiferromagnetic Insulators”. In: *Physical Review Letters* 120.20 (2018), pp. 1–6. ISSN: 10797114. DOI: 10.1103/PhysRevLett.120.207204. arXiv: 1804.05462.

[35] Wonbong Choi et al. "Recent development of two-dimensional transition metal dichalcogenides and their applications". In: *Materials Today* 20.3 (2017), pp. 116–130. ISSN: 18734103. DOI: 10.1016/j.mattod.2016.10.002.

[36] O J Clark et al. "A general route to form topologically-protected surface and bulk Dirac fermions along high-symmetry lines". In: *Electronic Structure* 1.1 (2019), p. 014002. ISSN: 2516-1075. DOI: 10.1088/2516-1075/ab09b7. arXiv: 1902.09211.

[37] O. J. Clark et al. "Fermiology and Superconductivity of Topological Surface States in PdTe2". In: *Physical Review Letters* 120.15 (2018), pp. 1–7. ISSN: 10797114. DOI: 10.1103/PhysRevLett.120.156401. arXiv: 1712.04184.

[38] Matteo Cococcioni and Stefane De Gironcoli. "Linear response approach to the calculation of the effective interaction parameters in the LDA+U method". In: *Physical Review B - Condensed Matter and Materials Physics* 71.3 (2005), pp. 1–16. ISSN: 10980121. DOI: 10.1103/PhysRevB.71.035105. arXiv: 0405160 [cond-mat].

[39] Marvin L. Cohen and Steven G. Louie. *Fundamentals of Condensed Matter Physics*. Cambridge University Press, 2016.

[40] A I Coldea et al. "Cascade of field-induced magnetic transitions in a frustrated antiferromagnetic metal". In: *Physical Review B* 90.2 (2014), p. 20401. DOI: 10.1103/PhysRevB.90.020401. URL: https://link.aps.org/doi/10.1103/PhysRevB.90.020401.

[41] Fast Track Communication. "Observation of local non-centrosymmetry in weakly biferroic YCrO 3". In: *Journal of Physics: Condensed Matter* 19.10 (2007). DOI: 10.1088/0953-8984/19/10/102202.

[42] John E. Coulter, Efstratios Manousakis, and Adam Gali. "Limitations of the hybrid functional approach to electronic structure of transition metal oxides". In: *Physical Review B - Condensed Matter and Materials Physics* 88.4 (2013), pp. 1–5. ISSN: 10980121. DOI: 10.1103/PhysRevB.88.041107. arXiv: 1306.4948.

[43] Gabor Csonka et al. "Assessing the performance of recent density functionals for bulk solids". In: *Physical Review B* 79 (2009), p. 155107.

[44] Spencer Doyle et al. *Tunable Giant Exchange Bias in an Intercalated Transition Metal Dichalcogenide*. 2019. arXiv: 1904.05872 [cond-mat.str-el].

[45] S. Dudarev and G. Botton. "Electron-energy-loss spectra and the structural stability of nickel oxide: An LSDA+U study". In: *Physical Review B - Condensed Matter and Materials Physics* 57.3 (1998), pp. 1505–1509. ISSN: 1550235X. DOI: 10.1103/PhysRevB.57.1505. arXiv: 0927-0256(96)00008 [10.1016].

[46] Chen Fang et al. "Topological nodal line semimetals". In: *Chinese Physics B* 25.11 (2016), p. 117106. ISSN: 1674-1056. DOI: 10.1088/1674-1056/25/11/117106. arXiv: 1609.05414. URL: http://arxiv.org/abs/1609.05414{\%}5Cnhttp://stacks.iop.org/1674-1056/25/i=11/a=117106?key=crossref.57a2f50b0edfd44e59f2d0c8bb1d928c.

[47] Chen Fang et al. "Topological nodal line semimetals with and without spin-orbital coupling". In: *Physical Review B - Condensed Matter and Materials Physics* 92.8 (2015), pp. 1–7. ISSN: 1550235X. DOI: 10.1103/PhysRevB.92.081201. arXiv: 1506.03449.

[48] Fucong Fei et al. "Nontrivial Berry phase and type-II Dirac transport in the layered material PdT e2". In: *Physical Review B* 96.4 (2017), pp. 1–7. ISSN: 24699969. DOI: 10.1103/PhysRevB.96.041201.

[49] Craig J. Fennie and Karin M. Rabe. "Ferroelectric transition in YMnO3 from first principles". In: *Physical Review B - Condensed Matter and Materials Physics* 72.10 (2005), pp. 1–4. ISSN: 10980121. DOI: 10.1103/PhysRevB.72.100103. arXiv: 0504542 [cond-mat].

[50] Craig J. Fennie and Karin M. Rabe. "Magnetic and electric phase control in epitaxial EuTiO3 from first principles". In: *Physical Review Letters* 97.26 (2006), pp. 1–4. ISSN: 00319007. DOI: 10.1103/PhysRevLett.97.267602. arXiv: 0606664v2 [arXiv:cond-mat].

[51] Alessio Filippetti and Nicola A Hill. "First principles study of structural, electronic and magnetic interplay in ferroelectromagnetic yttrium manganite". In: *Journal of Magnetism and Magnetic Materials* 236.1 (2001), pp. 176–189. ISSN: 11781661. DOI: 10.1007/s40271-017-0264-6.

[52] Frank Freimuth, Stefan Blügel, and Yuriy Mokrousov. "Spin-orbit torques in Co/Pt(111) and Mn/W(001) magnetic bilayers from first principles". In: *Physical Review B - Condensed Matter and Materials Physics* 90.17 (2014), pp. 1–10. ISSN: 1550235X. DOI: 10.1103/PhysRevB.90.174423. arXiv: 1305.4873.

[53] R H Friend, A R Beal, and A D Yoffe. "Electrical and magnetic properties of some first row transition metal intercalates of niobium disulphide". In: *The Philosophical Magazine: A Journal of Theoretical Experimental and Applied Physics* 35.5 (1977), pp. 1269–1287. DOI: 10.1080/14786437708232952.

[54] R. H. Friend, A. R. Beal, and A. D. Yoffe. "Electrical and magnetic properties of some first row transition metal intercalates of niobium disulphide". In: *Philosophical Magazine* 35.5 (1977), pp. 1269–1287. ISSN: 00318086. DOI: 10.1080/14786437708232952.

[55] Liang Fu and C. L. Kane. "Topological insulators with inversion symmetry.pdf". In: *Phys. Rev. B* 76 (2007).

[56] Shunsuke Fukami and Hideo Ohno. "Magnetization switching schemes for nanoscale three-terminal spintronics devices". In: *Japanese Journal of Applied Physics* 56.8 (2017). ISSN: 13474065. DOI: 10.7567/JJAP.56.0802A1.

[57] Antoine Georges et al. "Dynamical mean-field theory of strongly correlated fermion systems and the limit of infinite dimensions". In: *Reviews of Modern Physics* 68.1 (1996). ISSN: 1526498X. DOI: 10.1002/ps.5074.

[58] Barun Ghosh et al. "Low-energy type-II Dirac fermions and spin-polarized topological surface states in transition-metal dichalcogenide NiTe2". In: *arXiv* 100.19 (2019), p. 195134. ISSN: 23318422. DOI: `10.1103/PhysRevB.100.195134`. arXiv: `1908.04099`. URL: `https://doi.org/10.1103/PhysRevB.100.195134`.

[59] Feliciano Giustino. *Materials Modelling using Density Functional Theory: Properties and Predictions*. Oxford University Press, 2014.

[60] E. V. Gomonay and V. M. Loktev. "Spintronics of antiferromagnetic systems". In: *Low Temperature Physics* 40.1 (2014), pp. 17–35. ISSN: 1063777X. DOI: `10.1063/1.4862467`.

[61] O Gorochov et al. "Transport properties, magnetic susceptibility and Mössbauer spectroscopy of Fe0.25NbS2 and Fe0.33NbS2". In: *Philosophical Magazine B* 43.4 (1981), pp. 621–634. DOI: `10.1080/01418638108222164`.

[62] I. E. Graboy et al. "HREM study of epitaxially stabilized hexagonal rare earth manganites". In: *Chemistry of Materials* 15.13 (2003), pp. 2632–2637. ISSN: 08974756. DOI: `10.1021/cm021315b`.

[63] Dominik Gresch et al. "Z2Pack: Numerical implementation of hybrid Wannier centers for identifying topological materials". In: *Physical Review B* 95.7 (2017), pp. 1–24. ISSN: 24699969. DOI: `10.1103/PhysRevB.95.075146`. arXiv: `1610.08983`.

[64] Sinéad M. Griffin. "From the Early Universe to the Hubbard Hamiltonian in the Hexagonal Manganites". PhD thesis. ETH Zurich, 2014. ISBN: 9783905826111. URL: `https://www.research-collection.ethz.ch/handle/20.500.11850/88357`.

[65] Sinéad M. Griffin et al. "Defect Chemistry as a Crystal Structure Design Parameter: Intrinsic Point Defects and Ga Substitution in InMnO3". In: *Chemistry of Materials* 29.6 (2017), pp. 2425–2434. ISSN: 15205002. DOI: `10.1021/acs.chemmater.6b04207`.

[66] M. J. Grzybowski et al. "Imaging Current-Induced Switching of Antiferromagnetic Domains in CuMnAs". In: *Physical Review Letters* 118.5 (2017), pp. 1–5. ISSN: 10797114. DOI: `10.1103/PhysRevLett.118.057701`. arXiv: `1607.08478`.

[67] Yuzheng Guo, Stewart J. Clark, and John Robertson. "Electronic and magnetic properties of Ti2O3, Cr2O3, and Fe2O3calculated by the screened exchange hybrid density functional". In: *Journal of Physics Condensed Matter* 24.32 (2012). ISSN: 09538984. DOI: `10.1088/0953-8984/24/32/325504`.

[68] M V Gvozdikova, P-E Melchy, and M E Zhitomirsky. "Magnetic phase diagrams of classical triangular and kagome antiferromagnets". In: *Journal of Physics: Condensed Matter* 23.16 (2011), p. 164209. DOI: `10.1088/0953-8984/23/16/164209`. URL: `https://doi.org/10.1088{\%}2F0953-8984{\%}2F23{\%}2F16{\%}2F164209`.

[69] Shannon C. Haley et al. "Half-magnetization plateau and the origin of threefold symmetry breaking in a triangular frustrated antiferromagnet". In: 2 (2020), pp. 1–6. arXiv: `2002.02960`. URL: `http://arxiv.org/abs/2002.02960`.

[70] Shannon C. Haley et al. "Half-magnetization plateau and the origin of threefold symmetry breaking in an electrically-switchable triangular antiferromagnet". In: *Physical Review Research* 2.182 (2020), pp. 1–14. DOI: `10.1103/PhysRevResearch.2.043020`. arXiv: `2002.02960`. URL: `http://arxiv.org/abs/2002.02960`.

[71] M. Z. Hasan and C. L. Kane. "Colloquium: Topological insulators". In: *Reviews of Modern Physics* 82.4 (2010), pp. 3045–3067. ISSN: 00346861. DOI: `10.1103/RevModPhys.82.3045`.

[72] Lars Hedin. "On correlation effects in electron spectroscopies and the GW approximation The Table of Contents and more related content is available On correlation effects in electron spectroscopies and the GW approximation". In: 489 (1999).

[73] Jochen Heyd, Gustavo E. Scuseria, and Matthias Ernzerhof. "Hybrid functionals based on a screened Coulomb potential". In: *Journal of Chemical Physics* 118.18 (2003), pp. 8207–8215. ISSN: 00219606. DOI: `10.1063/1.1564060`.

[74] Motoaki Hirayama et al. "Topological Dirac nodal lines and surface charges in fcc alkaline earth metals". In: *Nature Communications* 8.111 (2017). ISSN: 20411723. DOI: `10.1038/ncomms14022`.

[75] P. Hohenberg and W. Kohn. "Inhomogenous Electron Gas". In: *Physical Review* 136.3B (1964), pp. 864–870. ISSN: 0378620X. DOI: `10.1007/BF01198136`.

[76] Jin Hu et al. "Evidence of Topological Nodal-Line Fermions in ZrSiSe and ZrSiTe". In: *Physical Review Letters* 117.1 (2016), pp. 1–7. ISSN: 10797114. DOI: `10.1103/PhysRevLett.117.016602`. arXiv: `1604.06860`.

[77] Jin Hu et al. "Transport of Topological Semimetals". In: *Annual Review of Materials Research* 49 (2019), pp. 207–252. ISSN: 15317331. DOI: `10.1146/annurev-matsci-070218-010023`.

[78] F. T. Huang et al. "Delicate balance between ferroelectricity and antiferroelectricity in hexagonal InMnO3". In: *Physical Review B - Condensed Matter and Materials Physics* 87.18 (2013), pp. 2–5. ISSN: 10980121. DOI: `10.1103/PhysRevB.87.184109`.

[79] Fei-ting Huang et al. "Duality of Topological Defects in Hexagonal Manganites". In: *Phys. Rev. Lett.* 113.DECEMBER (2014), p. 267602. ISSN: 0031-9007. DOI: `10.1103/PhysRevLett.113.267602`.

[80] Huaqing Huang and Feng Liu. "A Unified View of Topological Phase Transition in Band Theory". In: *Research* 2020 (2020), pp. 1–7. ISSN: 2639-5274. DOI: `10.34133/2020/7832610`.

[81] Huaqing Huang, Shuyun Zhou, and Wenhui Duan. "Type-II Dirac fermions in the PtSe 2 class of transition metal dichalcogenides". In: *Physical Review B* 94.12 (2016), pp. 1–6. ISSN: 24699969. DOI: `10.1103/PhysRevB.94.121117`. arXiv: `1607.07965`.

[82] Huaqing Huang et al. "Topological nodal-line semimetals in alkaline-earth stannides, germanides, and silicides". In: *Physical Review B* 93.20 (2016), pp. 1–6. ISSN: 24699969. DOI: 10.1103/PhysRevB.93.201114. arXiv: 1605.04050.

[83] Patrick Huang and Emily A. Carter. "Advances in correlated electronic structure methods for solids, surfaces, and nanostructures". In: *Annual Review of Physical Chemistry* 59 (2008), pp. 261–290. ISSN: 0066426X. DOI: 10.1146/annurev.physchem.59.032607.093528.

[84] Z. Huang et al. "Coupling between the ferroelectric and antiferromagnetic orders". In: *Physical Review B - Condensed Matter and Materials Physics* 56.5 (1997), pp. 2623–2626. ISSN: 1550235X. DOI: 10.1103/PhysRevB.56.2623.

[85] Yejin Huh, Eun Gook Moon, and Yong Baek Kim. "Long-range Coulomb interaction in nodal-ring semimetals". In: *Physical Review B* 93.3 (2016), pp. 1–8. ISSN: 24699969. DOI: 10.1103/PhysRevB.93.035138. arXiv: 1506.05105.

[86] Yejin Huh, Eun Gook Moon, and Yong Baek Kim. "Long-range Coulomb interaction in nodal-ring semimetals". In: *Physical Review B* 93.3 (2016). ISSN: 24699969. DOI: 10.1103/PhysRevB.93.035138. arXiv: 1506.05105.

[87] Fritz Hulliger and Eva Pobitschka. "On the magnetic behavior of new 2H-NbS2-type derivatives". In: *Journal of Solid State Chemistry* 1.2 (1970), pp. 117–119. ISSN: 0022-4596. DOI: https://doi.org/10.1016/0022-4596(70)90001-0. URL: http://www.sciencedirect.com/science/article/pii/0022459670900010.

[88] Federico Iori, Matteo Gatti, and Angel Rubio. "Role of nonlocal exchange in the electronic structure of correlated oxides". In: *Physical Review B - Condensed Matter and Materials Physics* 85.11 (2012), pp. 1–10. ISSN: 10980121. DOI: 10.1103/PhysRevB.85.115129. arXiv: arXiv:1201.3308v1.

[89] A. Jain et al. "The Materials Project: A materials genome approach to accelerating materials innovation". In: *APL Materials* 1.1 (2013). DOI: 10.1063/1.4812323.

[90] Y. J. Jin et al. "Ferromagnetic Weyl semimetal phase in a tetragonal structure". In: *Physical Review B* 96.20 (2017), pp. 2–6. ISSN: 24699969. DOI: 10.1103/PhysRevB.96.201102.

[91] David C Johnston. "Influence of uniaxial single-ion anisotropy on the magnetic and thermal properties of Heisenberg antiferromagnets within unified molecular field theory". In: *Phys. Rev. B* 95.9 (2017), p. 94421. DOI: 10.1103/PhysRevB.95.094421. URL: https://link.aps.org/doi/10.1103/PhysRevB.95.094421.

[92] T. Jungwirth et al. "Antiferromagnetic spintronics". In: *Nature Nanotechnology* 11.3 (2016), pp. 231–241. ISSN: 17483395. DOI: 10.1038/nnano.2016.18. arXiv: 1509.05296. URL: http://dx.doi.org/10.1038/nnano.2016.18.

[93] T Jungwirth et al. "The multiple directions of antiferromagnetic spintronics". In: *Nature Physics* 14.3 (2018), pp. 200–203. ISSN: 1745-2481. DOI: 10.1038/s41567-018-0063-6. URL: https://www.nature.com/articles/s41567-018-0063-6.

[94] C. L. Kane and E. J. Mele. “Quantum Spin hall effect in graphene”. In: *Physical Review Letters* 95.22 (2005), pp. 1–4. ISSN: 00319007. DOI: `10.1103/PhysRevLett.95.226801`. arXiv: `0411737 [cond-mat]`.

[95] M. Kasuya et al. “Optical spectra of Y1-xCaxVO3: Change of electronic structures with hole doping in Mott-Hubbard insulators”. In: *Physical Review B* 47.11 (1993), pp. 6197–6202. ISSN: 01631829. DOI: `10.1103/PhysRevB.47.6197`.

[96] Youngkuk Kim et al. “Dirac Line Nodes in Inversion-Symmetric Crystals”. In: *Physical Review Letters* 115.3 (2015), pp. 1–9. ISSN: 10797114. DOI: `10.1103/PhysRevLett.115.036806`. arXiv: `1504.03807`.

[97] A. V. Kimel et al. “Laser-induced ultrafast spin reorientation in the antiferromagnet TmFeO3”. In: *Nature* 429.6994 (2004), pp. 850–853. ISSN: 00280836. DOI: `10.1038/nature02659`.

[98] R. D. King-Smith and David Vanderbilt. “Theory of polarization of crystalline solids”. In: *Physical Review B* 47.3 (1993), pp. 1651–1654. ISSN: 01631829. DOI: `10.1103/PhysRevB.47.1651`.

[99] K. V. Klitzing, G. Dorda, and M. Pepper. “New method for high-accuracy determination of the fine-structure constant based on quantized hall resistance”. In: *Physical Review Letters* 45.6 (1980), pp. 494–497. ISSN: 00319007. DOI: `10.1103/PhysRevLett.45.494`.

[100] Mahito Kohmoto and Yong-shi Wu. “Diophantine equation for the three-dimensional quantum Hall effect”. In: *Physical Review B* 45.23 (1992), pp. 488–493.

[101] W. Kohn and L. J. Sham. “Self-Consistent Equations Including Exchange and Correlation Effects”. In: *Physical Review* 140.4A (1965), pp. 1133–1138.

[102] N. B. Kopnin, T. T. Heikkilä, and G. E. Volovik. “High-temperature surface superconductivity in topological flat-band systems”. In: *Physical Review B - Condensed Matter and Materials Physics* 83.22 (2011), pp. 1–4. ISSN: 10980121. DOI: `10.1103/PhysRevB.83.220503`. arXiv: `1103.2033`.

[103] G. Kresse and J. Furthmüller. “Efficient iterative schemes for ab initio total-energy calculations using a plane-wave basis set”. In: *Physical Review B* 54.16 (1996), pp. 11169–11186. ISSN: 0163-1829. DOI: `10.1103/PhysRevB.54.11169`. arXiv: `0927-0256(96)00008 [10.1016]`. URL: `http://link.aps.org/doi/10.1103/PhysRevB.54.11169`.

[104] D. Kriegner et al. “Multiple-stable anisotropic magnetoresistance memory in antiferromagnetic MnTe”. In: *Nature Communications* 7 (2016), pp. 1–7. ISSN: 20411723. DOI: `10.1038/ncomms11623`. arXiv: `1508.04877`.

[105] Shiji Krishnan et al. “Two-photon assisted excited state absorption in multiferroic YCrO3nanoparticles”. In: *Chemical Physics Letters* 529 (2012), pp. 59–63. ISSN: 00092614. DOI: `10.1016/j.cplett.2012.01.047`. URL: `http://dx.doi.org/10.1016/j.cplett.2012.01.047`.

[106] B Van Laar, H M Rietveld, and D J W Ijdo. "Magnetic and crystallographic structures of MexNbS2 and MexTaS2". In: *Journal of Solid State Chemistry* 3.2 (1971), pp. 154–160. ISSN: 0022-4596. DOI: `https://doi.org/10.1016/0022-4596(71)90019-3`. URL: `http://www.sciencedirect.com/science/article/pii/0022459671900193`.

[107] Stephan Lany. "Band-structure calculations for the 3d transition metal oxides in GW". In: *Physical Review B - Condensed Matter and Materials Physics* 87.8 (2013), pp. 1–9. ISSN: 10980121. DOI: `10.1103/PhysRevB.87.085112`.

[108] Changhoon Lee et al. "Magnetic structure of (C5H12N)CuBr3: Origin of the uniform Heisenberg chain behavior and the magnetic anisotropy of the Cu2+ (S = 1/2) ions". In: *RSC Advances* 6.27 (2016), pp. 22722–22727. ISSN: 20462069. DOI: `10.1039/c5ra26341g`.

[109] H. Li. "ARPES measurements on Dirac nodal-line Semimetal TiRhAs". In: *APS E01:00008*. 2019.

[110] Jiaheng Li et al. "Topological semimetals from the perspective of first-principles calculations". In: *Journal of Applied Physics* 128.19 (2020). ISSN: 10897550. DOI: `10.1063/5.0025396`. URL: `https://doi.org/10.1063/5.0025396`.

[111] Ronghan Li et al. "Weyl Ferroelectric Semimetal". In: (). arXiv: `arXiv:1610.07142v1`.

[112] Tian Liang et al. "Ultrahigh mobility and giant magnetoresistance in the Dirac semimetal Cd3As2". In: *Nature Materials* 14.3 (2014), pp. 280–284. ISSN: 1476-1122. DOI: `10.1038/nmat4143`. arXiv: `1404.7794`. URL: `http://www.ncbi.nlm.nih.gov/pubmed/25419815{\%}5Cnhttp://dx.doi.org/10.1038/nmat4143`.

[113] Tian Liang et al. "Ultrahigh mobility and giant magnetoresistance in the Dirac semimetal Cd3As2". In: *Nature Materials* 14.3 (2015), pp. 280–284. ISSN: 14764660. DOI: `10.1038/nmat4143`. arXiv: `1404.7794`.

[114] a. I. Lichtenstein, V.I. Anisimov, and J. Zaanen. "strong interactions: Orbital ordering". In: *Physical Review B* 52.8 (1995), pp. 5467–5471.

[115] Thorben Linneweber et al. "Exchange couplings for Mn ions in CdTe: Validity of spin models for dilute magnetic II-VI semiconductors". In: *Physical Review B* 95.4 (2017), pp. 1–10. ISSN: 24699969. DOI: `10.1103/PhysRevB.95.045134`. arXiv: `1607.00231`.

[116] Arielle Little et al. "Three-state nematicity in the triangular lattice antiferromagnet Fe1/3NbS2". In: *Nature Materials* (2020). ISSN: 14764660. DOI: `10.1038/s41563-020-0681-0`.

[117] Z K Liu et al. "A stable three-dimensional topological Dirac semimetal Cd3As2". In: *Nature Materials* 13.7 (2014), pp. 677–681. ISSN: 1476-1122. DOI: `10.1038/nmat3990`. arXiv: `1310.0391`. URL: `http://www.ncbi.nlm.nih.gov/pubmed/24859642{\%}5Cnhttp://www.nature.com/doifinder/10.1038/nmat3990`.

[118] Z K Liu et al. “Topological Dirac Semimetal , Na 3 Bi”. In: *Science* 343.February (2014), pp. 864–867. ISSN: 0036-8075.

[119] Th Lonkai et al. “Development of the high-temperature phase of hexagonal manganites”. In: *Physical Review B - Condensed Matter and Materials Physics* 69.13 (2004), pp. 1–10. ISSN: 01631829. DOI: 10.1103/PhysRevB.69.134108.

[120] Christoph Loschen et al. “First-principles LDA+U and GGA+U study of cerium oxides: Dependence on the effective U parameter”. In: *Physical Review B - Condensed Matter and Materials Physics* 75.3 (2007), pp. 1–8. ISSN: 10980121. DOI: 10.1103/PhysRevB.75.035115.

[121] Thomas Lottermoser et al. “Magnetic phase control by an electric field”. In: *Nature* 430.May (2004), pp. 541–544. ISSN: 0028-0836. DOI: 10.1038/nature02673.. URL: http://www.nature.com/nature/journal/v430/n6999/abs/nature02728.html.

[122] Kazimierz Lukaszewicz and Jaroslawa Karut-Kalicinska. “X-Ray Investigations of the Crystal Structure and Phase Transitions of YMnO3”. In: *Ferroelectrics* 7.1 (1974), pp. 81–82. ISSN: 15635112. DOI: 10.1080/00150197408237954.

[123] J. M. Luttinger and J. C. Ward. “Ground-state energy of a many-fermino system. II”. In: *Physical Review* 118.5 (1960), p. 1417. ISSN: 16130073. DOI: 10.1017/CBO9781107415324.004. arXiv: arXiv:1011.1669v3.

[124] B. Q. Lv et al. “Experimental discovery of weyl semimetal TaAs”. In: *Physical Review X* 5.3 (2015), p. 031013. ISSN: 21603308. DOI: 10.1103/PhysRevX.5.031013. arXiv: 1502.04684.

[125] Gerald D. Mahan. *Many-Particle Physics*. Third. Kluwer Academic/Plenum Publishers, 2000.

[126] Ramaprasad Maiti, Soumen Basu, and Dipankar Chakravorty. “Journal of Magnetism and Magnetic Materials Synthesis of nanocrystalline YFeO 3 and its magnetic properties”. In: *Journal of Magnetism and Magnetic Materials* 321.2009 (2010), pp. 3274–3277. DOI: 10.1016/j.jmmm.2009.05.061.

[127] A. Manchon and S. Zhang. “Theory of nonequilibrium intrinsic spin torque in a single nanomagnet”. In: *Physical Review B - Condensed Matter and Materials Physics* 78.21 (2008), pp. 1–4. ISSN: 10980121. DOI: 10.1103/PhysRevB.78.212405.

[128] A. Manchon and S. Zhang. “Theory of spin torque due to spin-orbit coupling”. In: *Physical Review B - Condensed Matter and Materials Physics* 79.9 (2009), pp. 1–9. ISSN: 10980121. DOI: 10.1103/PhysRevB.79.094422.

[129] A. Manchon et al. “Current-induced spin-orbit torques in ferromagnetic and antiferromagnetic systems”. In: *Reviews of Modern Physics* 91.3 (2019). ISSN: 15390756. DOI: 10.1103/RevModPhys.91.035004. arXiv: 1801.09636.

[130] M. Mandal and Ravi Singh. "Emergent superconductivity by re doping in type -II Weyl semimetal NiTe2". In: *arXiv* x (2020), pp. 1–6. ISSN: 23318422. DOI: 10.1088/1361-648x/abd8f3. arXiv: 2009.08690.

[131] Eran Maniv. "Private communication". In: *private communication* (2020).

[132] Eran Maniv et al. "Antiferromagnetic switching driven by the collective dynamics of a coexisting spin glass". In: *Science Advances* 7.2 (2021), pp. 1–7. ISSN: 23318422. arXiv: 2008.02795.

[133] S Mankovsky et al. "Electronic and magnetic properties of 2H-NbS2 intercalated by 3d transition metals". In: *Physical Review B* 94.18 (2016), p. 184430. DOI: 10.1103/PhysRevB.94.184430. URL: https://link.aps.org/doi/10.1103/PhysRevB.94.184430.

[134] S. Mankovsky et al. "Electronic and magnetic properties of 2H-NbS2 intercalated by 3d transition metals". In: *Physical Review B* 94.18 (2016), pp. 1–8. ISSN: 24699969. DOI: 10.1103/PhysRevB.94.184430. arXiv: 1607.05738.

[135] Sajedeh Manzeli et al. "2D transition metal dichalcogenides". In: *Nature Reviews Materials* 2 (2017). ISSN: 20588437. DOI: 10.1038/natrevmats.2017.33.

[136] Richard L. Martin and Francesc Illas. "Antiferromagnetic exchange interactions from hybrid density functional theory". In: *Physical Review Letters* 79.8 (1997), pp. 1539–1542. ISSN: 10797114. DOI: 10.1103/PhysRevLett.79.1539.

[137] N. Marzari and D. Vanderbilt. "Maximally Localized Generalized Wannier Functions for Composite Energy Bands". In: *Physical Review B* 56.20 (1997), p. 22. ISSN: 0163-1829. DOI: 10.1103/PhysRevB.56.12847. arXiv: 9707145 [cond-mat]. URL: http://link.aps.org/doi/10.1103/PhysRevB.56.12847{\%}5Cnhttp://arxiv.org/abs/cond-mat/9707145.

[138] Nicola Marzari et al. "Maximally localized Wannier functions: Theory and applications". In: *Reviews of Modern Physics* 84.4 (2012), pp. 1419–1475. ISSN: 00346861. DOI: 10.1103/RevModPhys.84.1419. arXiv: 1112.5411.

[139] C R Michel, C C Luhrs, and A Cha. "Synthesis of crystalline YCoO 3 perovskite via sol gel method". In: *Materials Letters* 58 (2004), pp. 716–718. DOI: 10.1016/j.matlet.2003.07.001.

[140] J. E. Moore and L. Balents. "Topological invariants of time-reversal-invariant band structures". In: *Physical Review B - Condensed Matter and Materials Physics* 75.12 (2007), pp. 1–4. ISSN: 10980121. DOI: 10.1103/PhysRevB.75.121306. arXiv: 0607314 [cond-mat].

[141] Joel Moore. "Topological insulators: The next generation". In: *Nature Physics* 5.6 (2009), pp. 378–380. ISSN: 17452481. DOI: 10.1038/nphys1294.

[142] Takahiro Moriyama et al. "Spin torque control of antiferromagnetic moments in NiO". In: *Scientific Reports* 8.1 (2018), pp. 1–6. ISSN: 20452322. DOI: `10.1038/s41598-018-32508-w`. arXiv: `1708.07682`. URL: `http://dx.doi.org/10.1038/s41598-018-32508-w`.

[143] Arash A. Mostofi et al. "An updated version of wannier90: A tool for obtaining maximally-localised Wannier functions". In: *Computer Physics Communications* 185.8 (2014), pp. 2309–2310. ISSN: 00104655. DOI: `10.1016/j.cpc.2014.05.003`. arXiv: `0708.0650`. URL: `http://dx.doi.org/10.1016/j.cpc.2014.05.003`.

[144] Arash A. Mostofi et al. "wannier90: A tool for obtaining maximally-localised Wannier functions". In: *Computer Physics Communications* 178.9 (2008), pp. 685–699. ISSN: 00104655. DOI: `10.1016/j.cpc.2007.11.016`. arXiv: `0708.0650`.

[145] Shuichi Murakami. "Phase transition between the quantum spin Hall and insulator phases in 3D: Emergence of a topological gapless phase". In: *New Journal of Physics* 9 (2007). ISSN: 13672630. DOI: `10.1088/1367-2630/9/9/356`. arXiv: `0710.0930`.

[146] Shuichi Murakami. "Phase transition between the quantum spin Hall and insulator phases in 3D: emergence of a topological gapless phase". In: *New Journal of Physics* 10.2 (2008), p. 029802. ISSN: 1367-2630. DOI: `10.1088/1367-2630/10/2/029802`.

[147] N Nagaosa. "A new state of Quantum Matter". In: *Science* 318 (2007), pp. 758–759. ISSN: 20950470. DOI: `10.1007/s11467-020-1035-8`.

[148] Nityan L Nair et al. "Electrical switching in a magnetically intercalated transition metal dichalcogenide". In: *Nature Materials* (2019), pp. 1–5. ISSN: 1476-4660. DOI: `10.1038/s41563-019-0518-x`. URL: `https://www.nature.com/articles/s41563-019-0518-x`.

[149] Madhab Neupane et al. "Observation of a three-dimensional topological dirac semimetal phase in high-mobility cd3 as2". In: *Nature Communications* 5.May (2014), pp. 1–8. ISSN: 20411723. DOI: `10.1038/ncomms4786`.

[150] Madhab Neupane et al. "Observation of topological nodal fermion semimetal phase in ZrSiS". In: *Physical Review B* 93.20 (2016), pp. 1–6. ISSN: 24699969. DOI: `10.1103/PhysRevB.93.201104`. arXiv: `1604.00720`.

[151] *No Title*. URL: `https://www.wavemetrics.com/` (visited on 12/21/2018).

[152] Doi Nobuhide and Tazuke Yuichi. "Spin Glass Phases in 2H-FexNbS2". In: *Journal of the Physical Society of Japan* 60.11 (1991), pp. 3980–3981. DOI: `10.1143/JPSJ.60.3980`.

[153] K. Olejnik et al. "THz electrical writing speed in an antiferromagnetic memory". In: *Science Advances* 4.March (2018), pp. 1–9. ISSN: 23318422. arXiv: `1711.08444`.

[154] T Ono et al. "Magnetization plateau in the frustrated quantum spin system Cs2CuBr4". In: *Phys. Rev. B* 67.10 (2003), p. 104431. DOI: `10.1103/PhysRevB.67.104431`. URL: `https://link.aps.org/doi/10.1103/PhysRevB.67.104431`.

[155] Danel Orobengoa et al. "AMPLIMODES: Symmetry-mode analysis on the Bilbao Crystallographic Server". In: *Journal of Applied Crystallography* 42.5 (2009), pp. 820–833. ISSN: 00218898. DOI: `10.1107/S0021889809028064`. arXiv: `1708.02002`.

[156] S. A. Parameswaran et al. "Probing the chiral anomaly with nonlocal transport in three-dimensional topological semimetals". In: *Physical Review X* 4.3 (2014), pp. 1–12. ISSN: 21603308. DOI: `10.1103/PhysRevX.4.031035`. arXiv: `1306.1234`.

[157] John P Perdew, Kieron Burke, and Matthias Ernzerhof. "Generalized Gradient Approximation Made Simple". In: *Physical Review Letters* 77.18 (1996), pp. 3865–3868. ISSN: 0031-9007. DOI: `10.1103/PhysRevLett.77.3865`. arXiv: `0927-0256(96)00008 [10.1016]`.

[158] John P. Perdew, Matthias Ernzerhof, and Kieron Burke. "Rationale for mixing exact exchange with density functional approximations". In: *Journal of Chemical Physics* 105.22 (1996), pp. 9982–9985. ISSN: 00219606. DOI: `10.1063/1.472933`.

[159] John P. Perdew and Wang Yue. "Accurate and simple density functional for the electronic exchange energy: Generalized gradient approximation". In: *Physical Review B* 33.12 (1986), pp. 8800–8802. ISSN: 01631829. DOI: `10.1103/PhysRevB.33.8800`. arXiv: `1011.1669`.

[160] John P. Perdew et al. "Erratum: Atoms, molecules, solids, and surfaces: Applications of the generalized gradient approximation for exchange and correlation (Physical Review B (1993) 48, 7, (4978))". In: *Physical Review B* 48.7 (1993), p. 4978. ISSN: 01631829. DOI: `10.1103/PhysRevB.48.4978.2`.

[161] J. M. Perez-Mato, D. Orobengoa, and M. I. Aroyo. *Mode crystallography of distorted structures*. Vol. 66. 5. 2010, pp. 558–590. ISBN: 0108767310. DOI: `10.1107/S0108767310016247`.

[162] Petar Popčević et al. "Electronic transport and magnetism in the alternating stack of metallic and highly frustrated magnetic layers in Co$_{1/3}$NbS$_2$". In: (2020). arXiv: `2003.08127`. URL: `http://arxiv.org/abs/2003.08127`.

[163] B. Radisavljevic et al. "Single-layer MoS2 transistors". In: *Nature Nanotechnology* 6.3 (2011), pp. 147–150. ISSN: 17483395. DOI: `10.1038/nnano.2010.279`.

[164] Catherine R. Rajamathi et al. "Weyl Semimetals as Hydrogen Evolution Catalysts". In: *Advanced Materials* 29.19 (2017), pp. 1–6. ISSN: 15214095. DOI: `10.1002/adma.201606202`.

[165] Nirat Ray and Umesh V Waghmare. "Coupling between magnetic ordering and structural instabilities in perovskite biferroics: A first-principles study". In: *Physical Review B - Condensed Matter and Materials Physics* 77.13 (2008), pp. 1–10. ISSN: 10980121. DOI: `10.1103/PhysRevB.77.134112`. arXiv: `0704.1251`.

[166] J. Roy-Montreuil et al. "Analyse de l'ordre dans les arseniures MM'As". In: *Annales de Chimie* 9 (1984).

[167] A. W. Rushforth et al. "Anisotropic magnetoresistance components in (Ga,Mn)As". In: *Physical Review Letters* 99.14 (2007), pp. 1–4. ISSN: 00319007. DOI: `10.1103/PhysRevLett.99.147207`.

[168] Hasan Sadat Nabi and Rossitza Pentcheva. "Energetic stability and magnetic coupling in (Cr1-xFe x)2O3: Evidence for a ferrimagnetic ilmenite-type superlattice from first principles". In: *Physical Review B - Condensed Matter and Materials Physics* 83.21 (2011), pp. 2–6. ISSN: 10980121. DOI: `10.1103/PhysRevB.83.214424`.

[169] Leslie M. Schoop, Florian Pielnhofer, and Bettina V. Lotsch. "Chemical Principles of Topological Semimetals". In: *Chemistry of Materials* 30.10 (2018), pp. 3155–3176. ISSN: 15205002. DOI: `10.1021/acs.chemmater.7b05133`. arXiv: `1804.10649`.

[170] Luis Seabra and Nic Shannon. "Competition between supersolid phases and magnetization plateaus in the frustrated easy-axis antiferromagnet on a triangular lattice". In: *Physical Review B* 83.13 (2011), p. 134412.

[171] P Sengupta et al. "Nonmonotonic field dependence of the Neel temperature in the quasi-two-dimensional magnet [Cu(HF2)(pyz)2]BF4". In: *Physical Review B* 79.6 (2009), p. 60409. DOI: `10.1103/PhysRevB.79.060409`. URL: `https://link.aps.org/doi/10.1103/PhysRevB.79.060409`.

[172] M Singh, J Callaway, and C S Wang. "Calculation of g and g for iron and nickel". In: *Physical Review B* 14.3 (1976), p. 1214.

[173] Jairo Sinova and Tomas Jungwirth. "Surprises from the spin Hall effect". In: *Physics Today* 70.7 (2017), pp. 38–42. ISSN: 00319228. DOI: `10.1063/PT.3.3625`.

[174] Jairo Sinova et al. "Spin Hall effects". In: *Reviews of Modern Physics* 87.4 (2015), pp. 1213–1260. ISSN: 15390756. DOI: `10.1103/RevModPhys.87.1213`.

[175] J.C. Slonczewski. "Current-driven excitation of magnetic multilayers". In: *Journal of Magnetism and Magnetic Materials* 159 (1996), pp. L1–L7. ISSN: 10226680. DOI: `10.4028/www.scientific.net/AMR.873.865`.

[176] L. Šmejkal et al. "Electric Control of Dirac Quasiparticles by Spin-Orbit Torque in an Antiferromagnet". In: *Physical Review Letters* 118.10 (2017), pp. 1–5. ISSN: 10797114. DOI: `10.1103/PhysRevLett.118.106402`. arXiv: `1610.08107`.

[177] Libor Šmejkal et al. "Topological antiferromagnetic spintronics". In: *Nature Physics* 14.3 (2018), pp. 242–251. ISSN: 17452481. DOI: `10.1038/s41567-018-0064-5`.

[178] I. V. Solovyev, M. V. Valentyuk, and V. V. Mazurenko. "Magnetic structure of hexagonal YMnO 3 and LuMnO 3 from a microscopic point of view". In: *Physical Review B - Condensed Matter and Materials Physics* 86.5 (2012), pp. 1–2. ISSN: 10980121. DOI: `10.1103/PhysRevB.86.054407`.

[179] Alexey A. Soluyanov et al. "Type-II Weyl Semimetals". In: *Nature* 527.7579 (2015), pp. 495–498. ISSN: 0028-0836. DOI: `10.1038/nature15768`. arXiv: `1507.01603`. URL: `http://arxiv.org/abs/1507.01603{\%}0Ahttp://dx.doi.org/10.1038/nature15768`.

[180] Ivo Souza, Nicola Marzari, and David Vanderbilt. "Maximally localized Wannier functions for entangled energy bands". In: *Physical Review B* 65.3 (2001), p. 035109. ISSN: 0163-1829. DOI: `10.1103/PhysRevB.65.035109`. arXiv: `0108084 [cond-mat]`. URL: `http://www.mendeley.com/research/introduction-maximallylocalized-wannier-functions-1/{\%}5Cnhttp://link.aps.org/doi/10.1103/PhysRevB.65.035109`.

[181] Nicola A. Spaldin and Manfred Fiebig. "The Renaissance of Magnetoelectric Multiferroices". In: *Science* 309.July (2005), pp. 391–392. ISSN: 0036-8075.

[182] Julia A. Steinberg et al. "Bulk Dirac points in distorted spinels". In: *Physical Review Letters* 112.3 (2014), pp. 1–5. ISSN: 00319007. DOI: `10.1103/PhysRevLett.112.036403`.

[183] M D Sundararajan et al. "Mössbauer studies of FexNbS2 (x= 0.25, 0.33 and 0.5)". In: *Journal of Physics and Chemistry of Solids* 44.8 (1983), pp. 773–777.

[184] Takuya Susuki et al. "Magnetization Process and Collective Excitations in the S=1/2 Triangular-Lattice Heisenberg Antiferromagnet Ba3CoSb2O9". In: *Phys. Rev. Lett.* 110.26 (2013), p. 267201. DOI: `10.1103/PhysRevLett.110.267201`. URL: `https://link.aps.org/doi/10.1103/PhysRevLett.110.267201`.

[185] Y. Suzuki, T., Ikeda, S., Richardson, J.W., Yamaguchi. "Magnetic Structure of Fe_1/3NbS2". In: *Proceedings of the Fifth International Symposium on Advanced Nuclear Energy Research*. 1993, pp. 343–346.

[186] L E Svistov et al. "Quasi-two-dimensional antiferromagnet on a triangular lattice RbFe(MoO4)2". In: *Phys. Rev. B* 67.9 (2003), p. 94434. DOI: `10.1103/PhysRevB.67.094434`. URL: `https://link.aps.org/doi/10.1103/PhysRevB.67.094434`.

[187] Masashi Takigawa and Frédéric Mila. "Magnetization Plateaus". In: *Introduction to Frustrated Magnetism: Materials, Experiments, Theory*. Ed. by Claudine Lacroix, Philippe Mendels, and Frédéric Mila. Berlin, Heidelberg: Springer Berlin Heidelberg, 2011, pp. 241–267. ISBN: 978-3-642-10589-0. DOI: `10.1007/978-3-642-10589-0_10`. URL: `https://doi.org/10.1007/978-3-642-10589-0{\_}10`.

[188] D. Tewelderbrhan and A. A. Balandin. ""Graphene-Like" exfoliation of atomically-thin films of Bi2Te3 and related materials: applications in thermoelectrics and topological insulators". In: *ECS Trans.* 33 (2010), pp. 103–117.

[189] Gerhard Theurich and Nicola A Hill. "Self-consistent treatment of spin-orbit coupling in solids using relativistic fully separable ab initio pseudopotentials". In: *Physical Review B* 64.7 (2001), p. 073106. ISSN: 0163-1829. DOI: `10.1103/PhysRevB.64.073106`. URL: `http://link.aps.org/doi/10.1103/PhysRevB.64.073106`.

[190] Florian Thöle, Andriani Keliri, and Nicola A. Spaldin. "Concepts from the linear magnetoelectric effect that might be useful for antiferromagnetic spintronics". In: *Journal of Applied Physics* 127.21 (2020), p. 213905. ISSN: 0021-8979. DOI: 10.1063/5.0006071.

[191] Wenchao Tian et al. "The property, preparation and application of topological insulators: A review". In: *Materials* 10.7 (2017). ISSN: 19961944. DOI: 10.3390/ma10070814.

[192] Atsushi Togo and Isao Tanaka. "First principles phonon calculations in materials science". In: *Scripta Materialia* 108 (2015), pp. 1–5. ISSN: 13596462. DOI: 10.1016/j.scriptamat.2015.07.021. URL: http://dx.doi.org/10.1016/j.scriptamat.2015.07.021.

[193] J. Tominaga et al. "Ferroelectric Order Control of the Dirac-Semimetal Phase in GeTe-Sb2Te3Superlattices". In: *Advanced Materials Interfaces* 1.1 (2014), pp. 1–7. ISSN: 21967350. DOI: 10.1002/admi.201300027.

[194] Fabien Tran and Peter Blaha. "Accurate band gaps of semiconductors and insulators with a semilocal exchange-correlation potential". In: *Physical Review Letters* 102.22 (2009), pp. 5–8. ISSN: 00319007. DOI: 10.1103/PhysRevLett.102.226401.

[195] Maximilian Trescher et al. "Quantum transport in Dirac materials: Signatures of tilted and anisotropic Dirac and Weyl cones". In: *Physical Review B - Condensed Matter and Materials Physics* 91.11 (2015), pp. 1–6. ISSN: 1550235X. DOI: 10.1103/PhysRevB.91.115135. arXiv: 1501.0403.

[196] A A Tsvetkov et al. "Structural, electronic, and magneto-optical properties of YVO 3". In: *Phys. Rev. B* 69.075110 (2004), pp. 1–11. DOI: 10.1103/PhysRevB.69.075110.

[197] B. Van Laar, H. M. Rietveld, and D. J.W. Ijdo. "Magnetic and crystallographic structures of MexNbS2 and MexTaS2". In: *Journal of Solid State Chemistry* 3.2 (1971), pp. 154–160. ISSN: 1095726X. DOI: 10.1016/0022-4596(71)90019-3.

[198] David Vanderbilt and R. D. King-Smith. "Electric polarization as a bulk quantity and its relation to surface charge". In: *Physical Review B* 48.7 (1993), pp. 4442–4455. ISSN: 01631829. DOI: 10.1103/PhysRevB.48.4442. arXiv: arXiv:1011.1669v3.

[199] J. Vidal et al. "False-positive and false-negative assignments of topological insulators in density functional theory and hybrids". In: *Physical Review B - Condensed Matter and Materials Physics* 84.4 (2011), pp. 1–4. ISSN: 10980121. DOI: 10.1103/PhysRevB.84.041109. arXiv: 1101.3734.

[200] P Wadley et al. "Electrical switching of an antiferromagnet". In: *Science* 351.6273 (2016), pp. 587–590. ISSN: 0036-8075, 1095-9203. DOI: 10.1126/science.aab1031. URL: https://science.sciencemag.org/content/351/6273/587.

[201] P. Wadley et al. "Spintronics: Electrical switching of an antiferromagnet". In: *Science* 351.6273 (2016), pp. 587–590. ISSN: 10959203. DOI: 10.1126/science.aab1031. arXiv: 1503.03765.

[202] Xiangang Wan et al. "Topological semimetal and Fermi-arc surface states in the electronic structure of pyrochlore iridates". In: *Physical Review B - Condensed Matter and Materials Physics* 83.20 (2011), pp. 1–9. ISSN: 10980121. DOI: 10.1103/PhysRevB.83.205101.

[203] Xiangang Wan et al. "Topological semimetal and Fermi-arc surface states in the electronic structure of pyrochlore iridates". In: *Physical Review B - Condensed Matter and Materials Physics* 83.20 (2011), pp. 1–9. ISSN: 10980121. DOI: 10.1103/PhysRevB.83.205101. arXiv: 1007.0016.

[204] Lei Wang, Thomas Maxisch, and Gerbrand Ceder. "Oxidation energies of transition metal oxides within the GGA+U framework". In: *Physical Review B* 73 (2006). ISSN: 19405901. DOI: 10.1103/PhysRevB.73.195107.

[205] Zhijun Wang et al. "Three-dimensional Dirac semimetal and quantum transport in Cd 3As2". In: *Physical Review B - Condensed Matter and Materials Physics* 88.12 (2013), pp. 1–6. ISSN: 10980121. DOI: 10.1103/PhysRevB.88.125427. arXiv: arXiv:1305.6780v1.

[206] Zhijun Wang et al. "Time-Reversal-Breaking Weyl Fermions in Magnetic Heusler Alloys". In: *Physical Review Letters* 117.23 (2016), p. 236401. ISSN: 10797114. DOI: 10.1103/PhysRevLett.117.236401. arXiv: 1603.00479. URL: https://doi.org/10.1103/PhysRevLett.117.236401.

[207] Hongming Weng, Xi Dai, and Zhong Fang. "Topological semimetals predicted from first-principles calculations". In: *Journal of Physics Condensed Matter* 28.30 (2016). ISSN: 1361648X. DOI: 10.1088/0953-8984/28/30/303001. arXiv: 1603.04744.

[208] Hongming Weng, Xi Dai, and Zhong Fang. "Topological semimetals predicted from first-principles calculations". In: *Journal of Physics: Condensed Matter* 28.30 (2016), p. 303001. ISSN: 0953-8984. DOI: 10.1088/0953-8984/28/30/303001. arXiv: 1603.04744. URL: http://arxiv.org/abs/1603.04744{\%}5Cnhttp://stacks.iop.org/0953-8984/28/i=30/a=303001?key=crossref.66f56dd447895c87cb3d13ca9d3a2595.

[209] Hongming Weng et al. "Topological node-line semimetal in three-dimensional graphene networks". In: *Physical Review B - Condensed Matter and Materials Physics* 92.4 (2015), pp. 1–8. ISSN: 1550235X. DOI: 10.1103/PhysRevB.92.045108. arXiv: arXiv:1411.2175v1.

[210] Hongming Weng et al. "Weyl semimetal phase in noncentrosymmetric transition-metal monophosphides". In: *Physical Review X* 5.1 (2015), pp. 1–10. ISSN: 21603308. DOI: 10.1103/PhysRevX.5.011029. arXiv: 1501.00060.

[211] A Wiedenmann et al. "A neutron scattering investigation of the magnetic phase diagram of FeI2". In: *Journal of Magnetism and Magnetic Materials* 74.1 (1988), pp. 7–21. ISSN: 0304-8853. DOI: https://doi.org/10.1016/0304-8853(88)90143-6. URL: http://www.sciencedirect.com/science/article/pii/0304885388901436.

[212] S. A. Wolf et al. “Spintronics: A spin-based electronics vision for the future”. In: *Science* 294.5546 (2001), pp. 1488–1495. ISSN: 00368075. DOI: 10.1126/science.1065389.

[213] Quan Sheng Wu et al. “WannierTools: An open-source software package for novel topological materials”. In: *Computer Physics Communications* 224 (2018), pp. 405–416. ISSN: 00104655. DOI: 10.1016/j.cpc.2017.09.033. arXiv: 1703.07789.

[214] Shan Wu and Robert J Birgeneau. “No Title”. In: *unpublished* (2021).

[215] Chunqiang Xu et al. “Topological Type-II Dirac Fermions Approaching the Fermi Level in a Transition Metal Dichalcogenide NiTe2”. In: *Chemistry of Materials* 30.14 (2018), pp. 4823–4830. ISSN: 15205002. DOI: 10.1021/acs.chemmater.8b02132.

[216] S.-Y. Xu et al. “Discovery of a Weyl Fermion semimetal and topological Fermi arcs”. In: *Science* 349.6248 (2015), pp. 613–617. ISSN: 0036-8075. DOI: 10.1126/science.aaa9297. arXiv: 1502.03807. URL: http://www.sciencemag.org/content/early/2015/07/15/science.aaa9297.

[217] Mingzhe Yan et al. “Lorentz-violating type-II Dirac fermions in transition metal dichalcogenide PtTe2”. In: *Nature Communications* 8.1 (2017), pp. 1–6. ISSN: 20411723. DOI: 10.1038/s41467-017-00280-6. arXiv: 1607.03643. URL: http://dx.doi.org/10.1038/s41467-017-00280-6.

[218] Bohm Jung Yang and Naoto Nagaosa. “Classification of stable three-dimensional Dirac semimetals with nontrivial topology”. In: *Nature Communications* 5 (2014). ISSN: 20411723. DOI: 10.1038/ncomms5898. arXiv: 1404.0754.

[219] Imseok Yang, Sergej Y. Savrasov, and Gabriel Kotliar. “Importance of correlation effects on magnetic anisotropy in Fe and Ni”. In: *Physical Review Letters* 87.21 (2001), pp. 216405–1–216405–4. ISSN: 10797114. DOI: 10.1103/PhysRevLett.87.216405. arXiv: 0107063 [cond-mat].

[220] Jonathan R. Yates et al. “Spectral and Fermi surface properties from Wannier interpolation”. In: *Physical Review B - Condensed Matter and Materials Physics* 75.19 (2007), pp. 1–12. ISSN: 10980121. DOI: 10.1103/PhysRevB.75.195121. arXiv: 0702554 [cond-mat].

[221] Mengxing Ye and Andrey V Chubukov. “Half-magnetization plateau in a Heisenberg antiferromagnet on a triangular lattice”. In: *Physical Review B* 96.14 (2017), p. 140406.

[222] Mengxing Ye and Andrey V Chubukov. “Quantum phase transitions in the Heisenberg J1-J2 triangular antiferromagnet in a magnetic field”. In: *Phys. Rev. B* 95.1 (2017), p. 14425. DOI: 10.1103/PhysRevB.95.014425. URL: https://link.aps.org/doi/10.1103/PhysRevB.95.014425.

[223] S. M. Young et al. “Dirac semimetal in three dimensions”. In: *Physical Review Letters* 108.14 (2012), pp. 1–5. ISSN: 00319007. DOI: 10.1103/PhysRevLett.108.140405. arXiv: 1111.6483.

[224] Rui Yu et al. "Topological Node-Line Semimetal and Dirac Semimetal State in Antiperovskite Cu3PdN". In: *Physical Review Letters* 115.3 (2015), pp. 3–7. ISSN: 10797114. DOI: `10.1103/PhysRevLett.115.036807`. arXiv: `1504.04577`.

[225] Wing Chi Yu et al. "Nonsymmorphic cubic Dirac point and crossed nodal rings across the ferroelectric phase transition in LiOsO3". In: *Physical Review Materials* 2.051201 (2018), pp. 1–8. DOI: `10.1103/PhysRevMaterials.2.051201`. arXiv: `1804.09389`. URL: `http://arxiv.org/abs/1804.09389`.

[226] Shirata Yutaka et al. "Quantum Magnetization Plateau in Spin-1 Triangular-Lattice Antiferromagnet Ba3NiSb2O9". In: *Journal of the Physical Society of Japan* 80.9 (2011), p. 93702. DOI: `10.1143/JPSJ.80.093702`. URL: `https://doi.org/10.1143/JPSJ.80.093702`.

[227] J Železný et al. "Relativistic Neel-Order Fields Induced by Electrical Current in Antiferromagnets". In: *Physical Review Letters* 113.15 (2014), p. 157201. DOI: `10.1103/PhysRevLett.113.157201`. URL: `https://link.aps.org/doi/10.1103/PhysRevLett.113.157201`.

[228] J. Železný et al. "Spin-orbit torques in locally and globally noncentrosymmetric crystals: Antiferromagnets and ferromagnets". In: *Physical Review B* 95.1 (2017), pp. 1–18. ISSN: 24699969. DOI: `10.1103/PhysRevB.95.014403`. arXiv: `1604.07590`.

[229] Jakub Zelezny. *Linear Response Symmetry*. 2017.

[230] Jakub Zelezny. *Wannier Linear Response*. 2018.

[231] Jakub Železný et al. "Spin-Polarized Current in Noncollinear Antiferromagnets". In: *Physical Review Letters* 119.18 (2017), pp. 1–7. ISSN: 10797114. DOI: `10.1103/PhysRevLett.119.187204`. arXiv: `1702.00295`.

[232] Haijun Zhang et al. "Topological insulators in Bi2Se3, Bi2Te3 and Sb2Te3 with a single Dirac cone on the surface". In: *Nature Physics* 5.6 (2009), pp. 438–442. ISSN: 1745-2473. DOI: `10.1038/nphys1270`. arXiv: `1405.2036`. URL: `http://www.nature.com/doifinder/10.1038/nphys1270`.

[233] Weifeng Zhang et al. "Giant facet-dependent spin-orbit torque and spin Hall conductivity in the triangular antiferromagnet IrMn3". In: *Science Advances* 2.9 (2016). ISSN: 23752548. DOI: `10.1126/sciadv.1600759`.

[234] Y J Zhang et al. "Light-Emitting Transistor". In: 344.May (2014), pp. 725–729.

[235] Chong Gui Zhong et al. "First-principles studies of the magnetic structure and exchange interactions in the frustrated multiferroic YMnO3". In: *Journal of Magnetism and Magnetic Materials* 321.9 (2009), pp. 1260–1265. ISSN: 03048853. DOI: `10.1016/j.jmmm.2008.11.005`.

[236] Alex Zunger and Marvin L. Cohen. “First-principles nonlocal-pseudopotential approach in the density-functional formalism: Development and application to atoms”. In: *Physical Review B* 18.10 (1978), pp. 5449–5472. ISSN: 01631829. DOI: `10.1103/PhysRevB.18.5449`.